Late Holocene coastal evolution and palaeoseismology in the southern region of the Jalisco subduction zone, México.

JESUS EMMANUEL BUSTAMANTE-FERNANDEZ

LATE HOLOCENE COASTAL EVOLUTION AND PALAEOSEISMOLOGY IN THE SOUTHERN REGION OF THE JALISCO SUBDUCTION ZONE, MÉXICO.

Jesús Emmanuel Bustamante Fernández

Thesis submitted in partial fulfilment of the requirements for the degree

Doctor of Philosophy

in

Physical Geography

at

the Department of Geography

2022

Abstract

The Pacific coast of Mexico is a region with a rapid rate of urbanization. Parallel to this coast lies the Mexican subduction zone, where great earthquakes (Mw > 8.0) have produced catastrophic impacts over the last decades. Our knowledge about the seismicity of this megathrust fault is limited by earthquake instrumental records, which extend back to the last ~120 years. This time span is too short to know the spatial and temporal recurrence of great earthquakes because of their highly variable recurrence, which commonly extends to several hundreds of years. In this sense, this study aims to contribute to our understanding of the long-term seismicity in the southern region of the Jalisco subduction zone, where the Rivera plate subducts beneath the North American plate. This research is innovative in the context of Mexican palaeoseismology as this is the first microfossil-based investigation that estimates coseismic land-level changes to infer past earthquake ruptures.

Tidal wetland deposits from the coastal plain of the Marabasco river were investigated using fossil diatoms, sediment geochemistry, sediment grain size and X-ray computed tomography (CT) images. Using the criteria to identify the stratigraphic signature of palaeoearthquakes, imprinted in this type of sedimentary systems, two abrupt stratigraphic contacts reveal a sudden increase of salinity conditions, suggesting a rapid land-level change, attributed to coseismic subsidence. Based on a Bayesian age-depth models, using ^{14}C and ^{137}Cs dates, the ages of these two events, 1995 ± 2 AD and 1914 ± 50 AD, allowed to correlate them with the earthquakes occurred in 1995 (Mw 8.0) and 1932 (Mw 7.8).

The stratigraphic signature of the 1932 and 1995 earthquakes serve as analogues, to investigate Late Holocene deposits, ^{14}C dated between 2350 and 955 cal. yr BP, to find evidence of coseismic land-level changes and infer variable rupture modes. Five probable palaeoearthquakes were identified, three events (1710-1541; 1265-1183; and 1111-1023 cal. yr BP) suggest coastal subsidence and only two events (1820 - 1657 and 1269-1219 cal. yr BP) coastal uplift. These land-level changes patterns confirm a trend of shallow ruptures, producing coastal subsidence. Nonetheless, evidence of coseismic uplift suggests deeper and likely wider earthquakes ruptures. The implications of these findings highlight the importance of geological evidence to better understand the long-term seismicity of the Mexican subduction zone, as earthquake ruptures over millennial time scales may differ from those witnessed in the last centuries.

Table of contents

CHAPTER 6

LATE HOLOCENE COASTAL UPLIFT AND SUBSIDENCE DURING MEGATHRUST EARTHQUAKES IN THE JALISCO SUBDUCTION ZONE, MEXICO.

CHAPTER 7

SUMMARY AND FUTURE OUTLOOK

List of figures

List of tables

Statement of Copyright

Acknowledgements

I am profoundly grateful to my supervisors Ian Shennan, Sarah Woodroffe and Jerry Lloyd for their guidance and advice. These last four years were quite challenging and without your support, this research project would not have been possible. For me, it was a great pleasure to learn from the big names within the palaeo sea-level community. You contributed profoundly to make my experience at Durham University better.

This research project would not been possible without the financial support of various institutions. First, I want to thank the Mexican government, which founded my PhD studies through the CONACYT's scholarship. I want to acknowledge the financial support to carry out fieldwork provided by the Department of Geography and Hatfield College of Durham University, Santander funding, The Micropaleontological Society, The Quaternary Research Association and the Estuarine and Coastal Sciences Association. Additionally, the financial support of the Natural Environment Research Council Grant-in-kind, which helped me to obtain radiocarbon measurements.

My deepest thanks to the researchers Patricia Mendez and José Ramón Hernández Santana, from the Institute of Geography of UNAM, for helping me with the fieldwork logistics in Mexico City. Fieldwork would not be possible without the fabulous team: Andrea Mancera, Emilio Saavedra and Adrián Ciprés.

I also want to thank to the laboratory staff at the Department of Geography of Durham University, which provided a lot of help and good moments during those long days processing samples. Thanks Chris, Neil, Eleanor, Kathryn, Martin, Amanda, Michael, and Mervyn. My deepest gratitude to Kathy Woods, who was very supportive during every single year of my PhD.

From the Department of Geography, special thanks to my colleagues and mentors Juliet Sefton, Ed Garrett, Muyeol Yung (my lab-, office- and flatmate), Brendan O'neill, Louise Callard and Louise Best. Your extraordinary knowledge about palaeoenvironmental studies facilitated some aspects of this research project.

Thanks for all those who made my life in the Durham a better place to live during the last four to five years: Maria de Falco, Valentina Vignieri, Ishiba, Andrea Silva, Naomi Wilmshurst, Oscar Ochoa, Carlos Ferrandon, Paticio Orden, Brian Kostadinov, Polo Cuspinera, Charlotte Mitchell, Joe Goodier, Rhys Jenkins, Alex Jardine, Tobi Roylands, Felipe Napoleoni, Gopi K. Basyal, Samprada Pradhan and many more who were present during those amazing days in Durham.

Thank you Cath Navarro for all your support in the toughest months of my PhD.

Las but not least, thanks to my family for always standing behind me, providing all the support to reach my dreams.

CHAPTER 1

INTRODUCTION

1.1. Rationale

Subduction zones are compressional tectonic systems, where plate convergence form thrust faults that extend hundreds to thousands of kilometres, hereafter referred to as megathrust faults (**Figure 1.1**). Along megathrust faults, the rupture of the brittle lithosphere can produce slip on the plate interface of several meters in a single event (e.g. Koketsu et al., 2011), releasing large amounts of energy and causing the most devasting earthquakes on Earth (McCalpin & Carver, 2009a; Pacheco et al., 1992; Scholz, 2002; Ye et al., 2018). Megathrust earthquakes are characterised by their size, which is a function of their magnitude. A single earthquake rupture can extend hundreds to thousands of kilometres along-strike and tens of kilometres downdip (e.g. Lay, 2005).

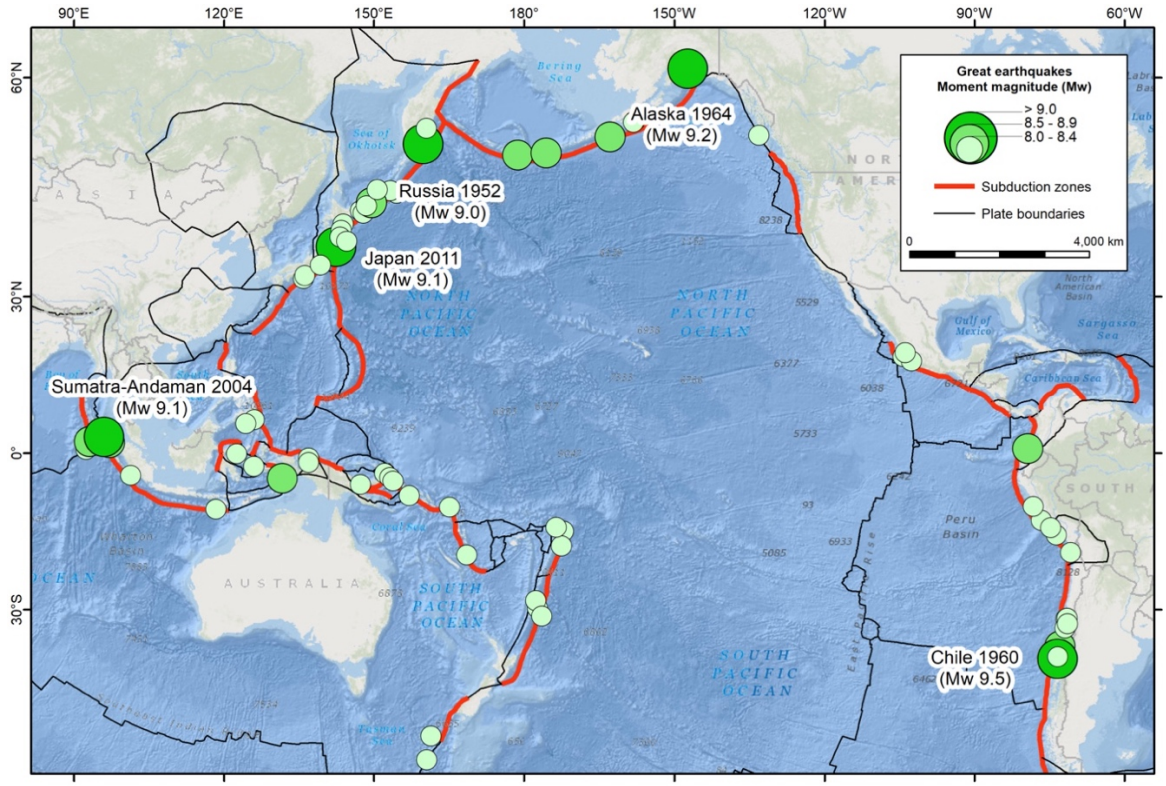

Figure 1.1. *Map of the spatial distribution of subduction zones and great megathrust earthquakes (Mw > 8.0) in the Pacific basin, occurred since 1900 (Data from USGS global earthuake catalogue. Base map source: Esri. World Topographic Map. http://www.arcgis.com).*

Offshore of the Mexican Pacific coast, from southern Nayarit to Chiapas (~1,800 km), lies the Mexican subduction zone, where two oceanic plates (Rivera and Cocos) subduct beneath the North American plate (Error! Reference source not found.). The Mexican subduction zone has produced great earthquakes, moment magnitudes (M_w) > 8.0, accompanied by tsunamis. The most catastrophic megathrust earthquake occurred on the 19th September, 1985. This earthquake (M_w 8.1) ruptured the Cocos-North American plate contact, offshore the coast of Michoacán, producing 6,000 casualties; 30,000 people injured; 3,300 damaged buildings and 36,000 destroyed buildings, with a total cost of the damage of 4.1 billion US dollars (Bitrán Bitrán, 2014).

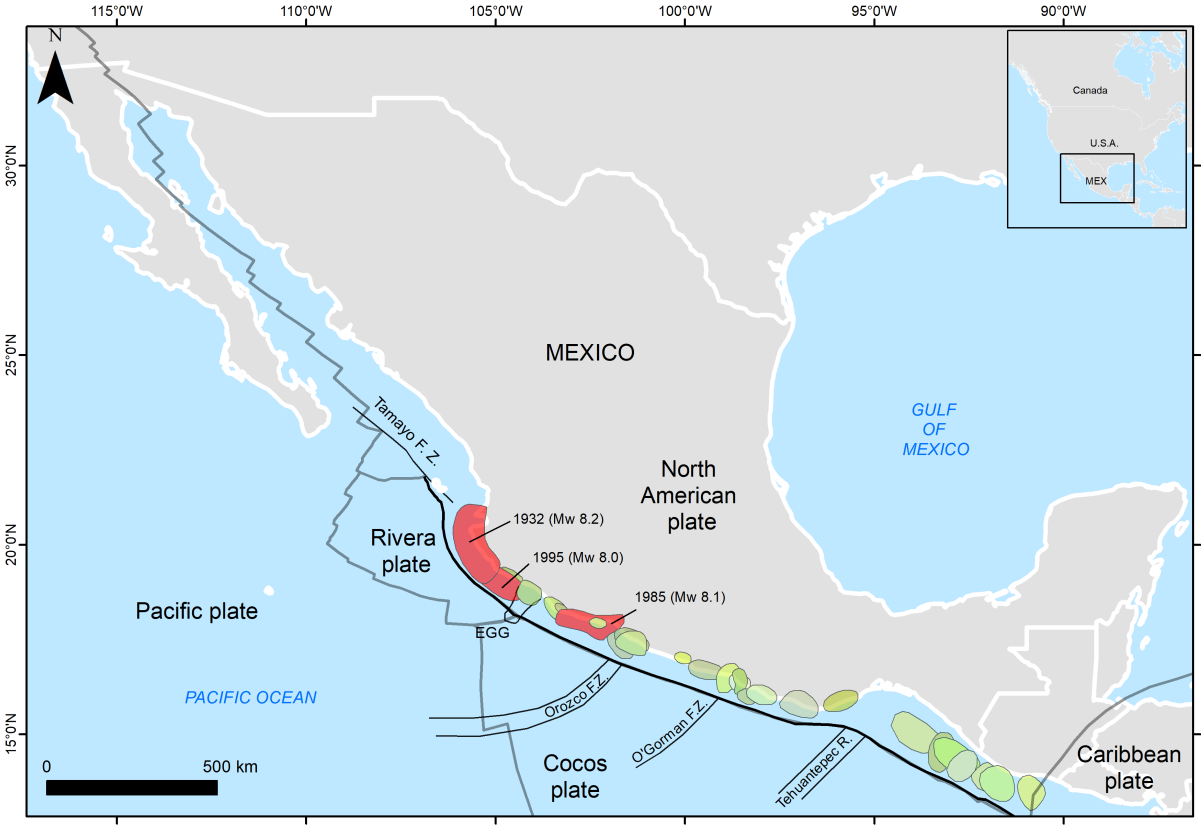

***Figure 1.2**. Spatial distribution of megathrust earthquakes in Mexico since 1904. Green ellipses represent earthquake ruptures of large events (M_w > 6.5). Red ellipses indicate ruptures of the great earthquakes (Mw > 8.0). The thick black line in the Pacific Ocean represents the trench of the Mexican subduction zone (Source: Kostoglodov & Pacheco, 1999).*

Currently, the Mexican Pacific coast is a region of rapid growth guided by tourist and port activities (e.g. Muñoz Sevilla et al., 2019; Padilla y Sotelo et al., 2009). The constant flow of national and international tourism contributes significantly to the local and regional GDPs of coastal cities in Bahía de Banderas, Nayarit; Puerto Vallarta,

Jalisco; Zihuatanejo and Acapulco, Guerrero; and Puerto Escondido and Huatulco, Oaxaca (e.g. Guardado Marín, 2009; Márquez González & Sánchez Crispín, 2007; Silva, 2012). The ports of Manzanillo, Lázaro Cárdenas, and Salina Cruz are essential nodes of global markets, strongly connected to the Eastern Asian and North American markets. (API Manzanillo, 2012; API Salina Cruz, 2016; Connell et al., 2015). These ports are important hubs for goods movement and transportation. For example, only the Port of Manzanillo moves more than 45% of the entire country's containerised cargo products; and it connects with industries in central México that contribute to more than 65% of the national GDP (API Manzanillo, 2012). Therefore, megathrust earthquakes represent a significant hazard that threat coastal communities and local to national economies.

Since the advent of instrumentation in earthquake seismology, ~100 years ago (e.g. Agnew, 2002; Di Giacomo et al., 2015), earthquake catalogues have intended to understand seismic patterns from global to local scales (Heuret et al., 2011; Kelleher et al., 1974; Ruff & Kanamori, 1980; Scholz & Campos, 1995). Earthquake catalogues assist mitigation plans, as these records provide evidence of local seismicity in terms of the magnitudes and frequency of large events. Nonetheless, the time span of earthquake instruments is too short to know the real pattern of seismicity of a particular region because the recurrence of great megathrust earthquakes extends to several hundreds of years. Hence, instrumental records are incapable of covering the whole spectrum of seismicity. Murray-Wallace and Woodroffe (2014) highlight the fact that the perceived tectonic stability of a coastal region is strongly constrained by the spatial and temporal scales of observation. In this context, it is important to extend the relatively short instrumental record back in time using proxy reconstructions of great earthquakes to understand the spatial and temporal behaviour of megathrusts along the Mexican subduction zone and being able to be better prepared during future events.

1.2. Statement of the problem and research aim.

Palaeoseismological investigations of subduction zones study the geological record of coastal systems to reveal the occurrence of prehistorical and preinstrumental earthquakes. These investigations aim to assess the impacts, sizes, and recurrence of the greatest earthquakes occurred in the past. Due to the greatest earthquakes are

catalogued as low-frequency events, based on human time scales, their occurrence in modern times favoured palaeoseismological investigations as they offer the unique opportunity to investigate their expression in the local geology, acting as analogues to reveal the presence, or even absence, of past earthquakes.

Instrumental earthquake records in Mexico date back to the first decade of the previous century (Alcántara et al., 2012; Pérez-Campos et al., 2018). Within this period, three great earthquakes occurred in 1932 (M_w 8.2), 1985 (M_w 8.1) and 1995 (M_w 8.0, **see fig 1.2**), offering the opportunity to investigate and used their geological signature as a modern analogue to extend the seismic record into the Holocene. Bodin & Klinger (1986) investigated the geological signature of the 1985 earthquake along the coast of Michoacán. Through the analysis of coralline algae mortality, Bodin & Klinger (1986) quantified the magnitude of coastal uplift along-strike. Goguitchaichvili et al. (2013) and Ramírez-Herrera et al., (2012) investigated the sedimentary signature of the tsunami deposit produced by this earthquake. For the 1932 and 1995 earthquakes, geological evidence exists only for their tsunami deposits (e.g. Castillo-Aja et al., 2019; Černý et al., 2015; Ramírez-Herrera et al., 2016), geological records of crustal deformation, either subsidence or uplift along-strike, is inexistent. Consequently, this investigation seeks to fulfil this research gap.

Due to the rupture and tsunami of the 1995 earthquake are better constrained and more documented than the 1932 earthquake (e.g. Filonov, 1997; Tena-Colunga et al., 1997), the coast adjacent to this earthquake rupture offers the opportunity to find its geological signature to characterise it and use it as a modern analogue for its predecessors. Hence, the overarching aim of this thesis is to use coastal sediments to reconstruct a centennial to millennial-scale record of past megathrust earthquakes along the southernmost region of the Rivera-North American subduction zone, in western Mexico.

1.3. Research questions and objectives

This following research questions and objectives guide the structure of this thesis:

- **Did the 1995 M_w 8.0 earthquake leave a sedimentary signature in coastal intertidal wetlands of the Mexican Pacific?**

The 1995 earthquake was instrumentally well-constrained and GPS and tide gauge data show along-strike coastal subsidence. Therefore, the research objectives are:

a) To identify a coastal wetland that experienced significant coseismic subsidence during the 1995 earthquake.
b) To characterise the physical and chemical composition of the sediments that indicate this coseismic subsidence.
c) To develop a diatom-based method to quantify coseismic subsidence caused by the 1995 earthquake.

- **Can we use coastal sediments from Estero Potrero Grande to constrain earthquake ruptures preceding the 1995 earthquake?**

Earthquake ruptures before the 1995 earthquake are not well-constrained due to the limitations of early instruments deployed across the Mexican territory. Hence geological records present an opportunity to constrain the ruptures of early instrumentally recorded and historical earthquakes. Hence, I aim to:

a) To investigate the sedimentary signature of early (pre-1995 AD) instrumentally recorded earthquakes along the Rivera-North America plate boundary.
b) To reconstruct the magnitude of coseismic land-level changes associated with the earthquakes identified.

- **What is the long-term behaviour of the Rivera-North America megathrust fault?**

The most recent megathrust earthquakes along the Rivera subduction zone have only produced coastal subsidence (Cumming, 1933; Hutton et al., 2001; Melbourne et al., 1997). However, geological evidence contradicts this statement as coastal landforms along the coast of Jalisco shows evidence of abrupt coastal uplift in the Holocene, likely produced coseismically (Castillo-Aja et al., 2019; Ramírez-Herrera et al., 2004). Coseismic uplift implies deeper and likely wider earthquake ruptures in Holocene times. Thus, the objectives of this research question are:

a) To investigate the late Holocene evolution of the coast adjacent to the Rivera-North American plate boundary.

b) To investigate trends and patterns in land-level changes associated with palaeoearthquakes.

1.4. Research approach

1.4.1. The earthquake deformation cycle

The compressive behaviour of subduction zones makes of megathrust earthquakes part of a cycle, due to the relative movement of tectonic plates. The frictional properties of the seismogenic zone promote locking on the fault, with heterogeneous strain accumulation over time and space (Wang et al., 2012). When the seismogenic zone reaches its maximum capacity to accumulate tectonic strain, the megathrust fails in a catastrophic manner, causing slip on the fault, producing earthquakes (Dixon & Moore, 2007). These processes produce gradual and abrupt patterns of crustal deformation.

Gradual crustal deformation, which lasts hundreds of years, occurs during the interseismic stage (Error! Reference source not found.**A**), when the interplate boundary (seismogenic zone) is locked and loading tectonic strain. During this stage, horizontal compressive stress in the shallow lithosphere produces the shortening of the overriding plate, causing horizontal and vertical deformation (Govers et al., 2017). Vertical deformation produces a region of subsidence over the locked seismogenic zone and a region of uplift, inland from the lower limit of the locked zone (Govers et al., 2017). Vertical deformation gradually spreads out from the locked zone, mostly confined between the trench and a backstop (~ 300-600 km), with the amplitude decreasing with time (Govers et al., 2017; Wang, 2007).

Abrupt crustal deformation occurs during the coseismic stage, when the interplate contact (seismogenic zone) slips and releases the accumulated tectonic strain (Error! Reference source not found.**B**), producing the relaxation of the overriding plate. During this stage, which lasts seconds to minutes, the overriding plate experiences elastic rebound, creating a region of uplift, located immediately above the slip area, and a. region of subsidence, located outside the areas of slip. The transition between the uplift and subsidence region is near the surface projection of the down dip end of the fault rupture, which is named as the hinge line (Govers et al., 2017). In coastal regions, coseismic deformation is commonly observed as abrupt land-level changes, either uplift (fall in sea level) or subsidence (rise in sea level). The direction and magnitude

of coseismic land-level changes depends on the relative position of the coast with respect to the slip area (McCalpin & Carver, 2009b; Rovere et al., 2016). Consequently, variable coseismic land-level changes, either uplift or subsidence, and their magnitude are indicative of down-dip rupture variations, which can be used to infer the width and depth of past earthquake ruptures.

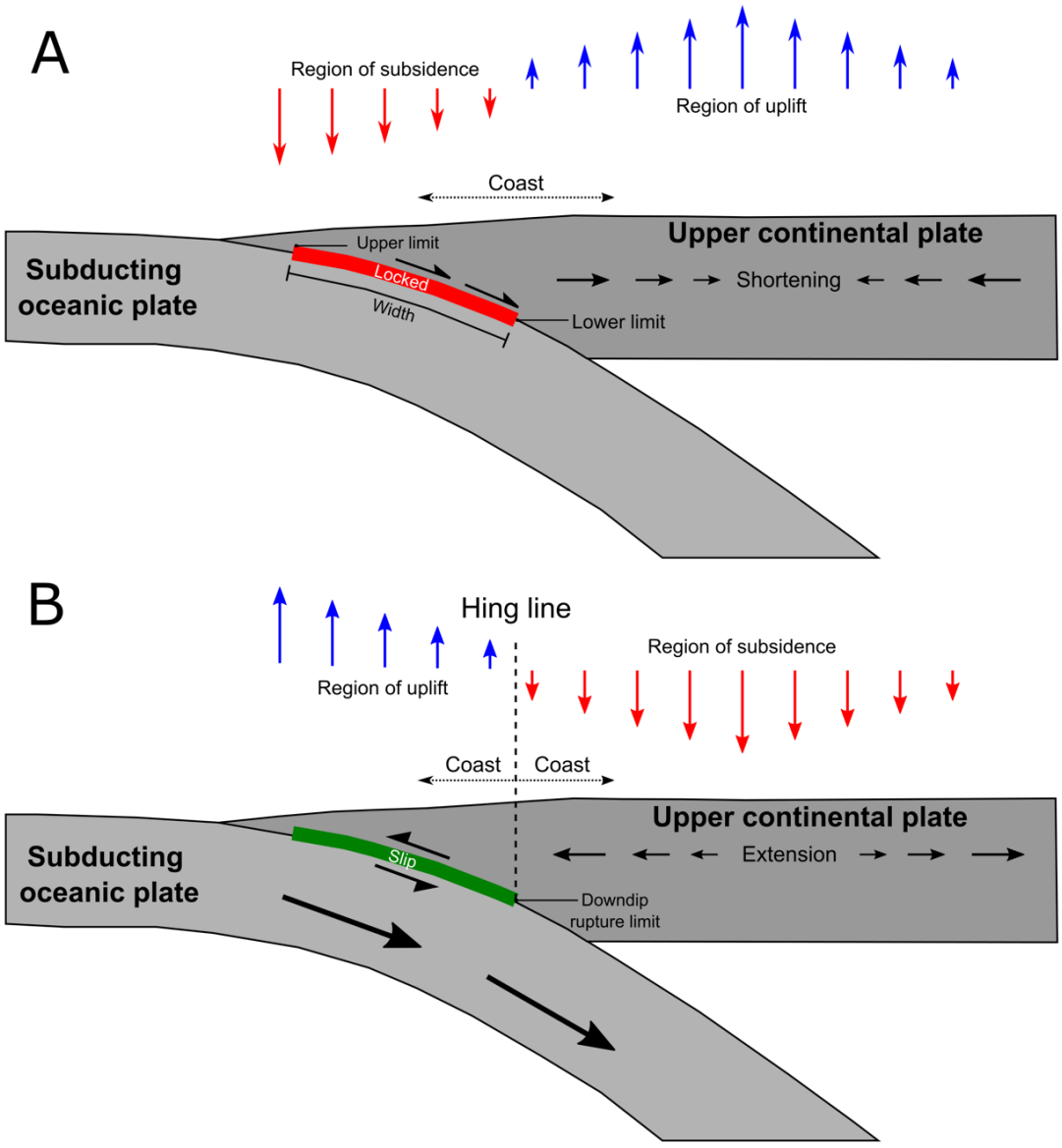

***Figure 1.3**. Schematic representation of crustal deformation during the earthquake deformation cycle. **A**) Interseismic stage. **B)** Coseismic stage (McCalpin & Carver, 2009a; Pacheco et al., 1993; Wang et al., 2012).*

1.4.2. The coastal paleoseismology framework

Palaeoseismology aims to determine the location, timing, and size of prehistoric earthquakes using geologic evidence created during individual events (McCalpin & Nelson, 2009). In subduction zones, the regional deformation of the overriding plate during an earthquake creates such evidence, which along coastal regions is seen as abrupt subsidence or uplift, whose expression is imprinted in the local geomorphology (e.g. Kelsey et al., 2015; Monecke et al., 2015) and stratigraphy (e.g. Shennan et al., 1999; Zong et al., 2003). Crustal deformation offshore may displace the water mass lying on it producing a tsunami (Okal & Newman, 2001; Polet & Kanamori, 2002; Sugawara, 2020), whose depositional and erosional features along the coast also provide geological evidence of past earthquakes. This section offers a review of these two different, but complementary approaches used in coastal palaeoseismology studies.

1.4.2.1. Land-level changes as evidence of megathrust earthquakes.

Coseismic subsidence or uplift along the coast produce an increase or decrease of marine conditions, respectively, modifying abruptly the dominant patterns of sedimentation. Coastal sedimentary systems, particularly intertidal wetlands, archive these abrupt land-level changes as stratigraphic unconformities, here referred as coseismic contacts, which are used as evidence of past earthquakes (Atwater, 1987; Long & Shennan, 1998; Peterson & Darienzo, 1991a).

Coseismic contacts mark abrupt alternations between peat or soils and mud, whose stratigraphic sequence depends on the type of land-level change. A coseismic contact produced by subsidence consists of buried peat or soils overlaid abruptly by mud; while coastal uplift is stratigraphically expressed as mud overlaid abruptly by soils. In intertidal wetlands, peat or soils represent the upper and middle intertidal zones, where highly organic sediments correspond to saltmarsh deposits, in temperate and polar regions (Allen, 2000; Ward, 2020), and mangrove deposits, in (sub-) tropical regions (Krauss et al., 2008). Mud sediments, represent lower intertidal and sub-tidal zones, where clastic sediments dominate, forming tidal flats (e.g. Furukawa et al., 1997; Furukawa & Wolanski, 1996; Rahman & Plater, 2014).

The lithology of coseismic contacts represents the initial diagnostic of past earthquakes. However, other processes may imprint a similar signature in the stratigraphy of intertidal wetlands. In this sense, the interpretation of past earthquakes based on the lithostratigraphy is not sufficient to discriminate its origin and the use of sea-level indicators permit to assess the suddenness and magnitude of change, which is one of the main stratigraphic features used to discriminate a seismic origin (e.g. Nelson et al., 1996; Shennan et al., 2016).

Kemp et al. (2017) define sea-level indicators as those biological assemblages, chemical signatures, and physical features with a known relationship to tides and elevations relative to tidal datums. The most common proxies used as sea-level indicators correspond to microfossil groups, such as diatoms (Dura et al., 2016; Dura & Hemphill-Haley, 2020; Hocking et al., 2017; Horton & Sawai, 2010; Watcham et al., 2013), foraminifera (e.g. Hawkes et al., 2010; Kemp et al., 2013, 2018; Sabean, 2004), and pollen (e.g. Ellison, 1989; Engelhart et al., 2007; Hughes et al., 2002). Quantification of coseismic land-level changes using microfossils is grounded on the development of transfer functions, which operate by modelling statistically the relationship between modern species assemblages, in response to a specific environmental variable (Birks, 2005; Sachs et al., 1977), which in this case corresponds to elevation related to a specific tidal datum. The resulting function is used to calibrate the fossil assemblages to estimate the variable of interest, which corresponds to palaeoelevations (Barlow et al., 2013). This approach forms the backbone of modern coastal palaeoseismology.

After systematic analyses of stratigraphic sequences from multiple coastal wetlands along the coast adjacent to the Cascadia subduction zone, Nelson et al. (1996) established a set of criteria that guide coastal palaeoseismological studies. This set of criteria was reinforced and complemented by evidence from multiple sites adjacent to the Alaska-Aleutian subduction zone (Shennan et al., 2016). Subsequently, six essential attributes of sediments contribute to identify coseismic contacts in the stratigraphy of intertidal wetlands:

- **Suddenness of submergence or emergence**. Stratigraphic contacts must demonstrate dramatic shifts in lithology and macro/microfossil content associated

to abrupt transitions of tidal sub-environments (Atwater, 1987; Long & Shennan, 1994).

- **Amount of submergence or emergence**. Microfossil assemblages and vegetation communities provide evidence of the direction and magnitude of land-level changes, through reconstruction of palaeoelevations bracketing a coseismic contact (e.g. Shennan et al., 2016).
- **Lateral extent of coseismic contacts**. Coseismic contacts should be continuous and consistent over areas of some metres or kilometres within the same site under investigation (e.g. Briggs et al., 2014).
- **Synchroneity of submergence-emergence**. Evidence of a synchroneity is achieved using dating methods. Correlation among sites indicates the occurrence of a regional event. Synchroneity provides an insight into the rupture length, which is an approach used to estimate earthquake palaeomagnitudes (e.g. Darienzo, 1991; Leonard et al., 2010).
- **Tsunami concurrent with submergence or emergence**. In subduction zones, the most prominent palaeoseismic evidence comes from the recognition of tsunami deposits (Scholz, 2014). Evidence of tsunami deposits is a strong indicator of a megathrust earthquake, particularly when it occurs in conjunction with uplift or subsidence.
- **Liquefaction concurrent with submergence or emergence**. Earthquake induced ground shaking promotes liquefaction, which is the transformation of a saturated granular material from a solid to liquefied state, due to increased porewater pressure (Obermier et al., 2005).

This set of criteria serve as a guideline to identify great earthquakes (M_w 8.0) imprinted in the stratigraphy of tidal wetlands. However, not all megathrust earthquakes cause significant land-level to produce a geological record in tidal wetlands. This is in part due to the features of past earthquake ruptures and the local geomorphological and sedimentary conditions. In this sense, it is important, when possible, to assess the response of the coast during variable earthquake magnitudes and different coastal settings to understand, what McCalpin & Nelson (2009) refer as, the creation and preservation thresholds. These thresholds permit to establish the detection limits under different earthquake scenarios (e.g. Brader et al., 2021). For example, after widespread investigations of tidal wetlands along the Alaska-Aleutian subduction

zone, Shennan et al. (2016) conclude that the detection limit of tidal wetlands correspond to 10 – 15% of the great diurnal tidal range.

When coseismic land-level changes are small, and close to their detection limit to be discriminated from non-tectonic processes, their sedimentary signature can be misinterpreted and the real rate of seismicity for a particular region may be either overestimated or underestimated. In this sense, Shennan et al. (2016) stress the use of a combination of the following palaeoseismic indicators: 1) The stratigraphic contact should show evidence of its lateral continuity; 2) sudden elevation change should be coherent in multiple sites along the stratigraphic contact; and 3) elevation changes from multiple sites need to indicate the same sign rather a random distribution of values above and below zero. This suggests that exhaustive field investigations within a single estuary or a tidal basin are required to confirm, or rule out, a coseismic origin when land-level changes are small. This argument is grounded on the response of tidal wetlands to non-tectonic processes, whose stratigraphic signature that may resemble a coseismic origin, do not have a regional expression and their sedimentary signature is normally highly localized in tidal wetlands (e.g. Nelson et al., 1998).

This research framework was developed using sediments from estuaries along the Pacific coast of North America (Alaska, Canada, and USA). This region of the Pacific basin hosts meso- and macrotidal coastal wetlands, dominated by salt marshes (Whitfield & Elliott, 2011). Here, different sea-level proxies have been tested to assess their reliability to reconstruct past earthquakes (e.g. Bender et al., 2015, 2015; Engelhart, Horton, Nelson, et al., 2013; Hawkes et al., 2010; Hong et al., 2021; Hughes et al., 2002; Kemp et al., 2013; Nelson & Kashima, 1993; Sawai et al., 2016; Watcham et al., 2013). Given the similarities of tidal wetlands, this research framework was used in palaeoseismic investigations in Chile and Japan (e.g. Brader et al., 2021; Garrett et al., 2013, 2015; Hocking et al., 2017; Sawai, 2001; Sawai et al., 2004; Sawai & Nasu, 2005). However, it is important to know whether this framework works equally in different coastal settings, such as the Mexican Pacific coast, where microtidal coasts hosts mangroves and tropical saltmarshes, which face specific challenges due to the poor preservation of microfossils (e.g. Martin et al., 1995) and the lack of reliable datable material (e.g. Sefton et al., 2022). Hence, it is vital to test the applicability of this framework to know how this approach can be adapted.

1.4.2.2. Tsunami deposits as evidence of megathrust earthquakes.

In coastal settings where coseismic land-level changes are not recorded, due to the local geomorphology or the relative position of the coast to the megathrust fault, geological records of tsunamis represent the alternative approach to investigate past megathrust earthquakes (e.g. Fujiwara et al., 2020; Garrett et al., 2016; Sawai, 2020). Evidence of past tsunamis involves the study of depositional and erosional features related to tsunami inundation (Spiske, 2020). Nonetheless, the most suitable evidence to investigate past tsunamis correspond to anomalous deposits in back-barrier lowlands, where allochthonous sediments are easily recognized and better preserved in the lithostratigraphy (Dawson et al., 2020).

A barrier represents a range of emergent depositional landforms, mainly composed by sand, which is separated from the mainland coast by a bay, lagoon, lake, pond or wetlands (Masselink et al., 2011). Back-barrier wetlands are excellent sediment traps of incoming tsunami waves, which carry sand material from the barrier, contrasting with the background sedimentation of fine-grained silt and clay sediments, often rich in organic matter (Dawson et al., 2020). If these wetlands record coseismic land-level changes, an anomalous sand deposit is bracketed by peat and mud, depending on the magnitude and trend of vertical deformation (e.g. Dura et al., 2017). However, when there is not any record of land-level changes, a tsunami deposit is observed as a sandy layer bracketed by deposits corresponding to the background sedimentation (e.g. Nelson et al., 2015; Witter et al., 2019).

Multiple analytical methods permit to investigate and infer some characteristics of past tsunamis. Grain size allow to identify the number of sedimentary beds associated to different stages of inundation and energy of the flow and backflow of past tsunamis (e.g. Switzer & Jones, 2008). Microfossil assemblages permit to identify the source of sediments (e.g. Dura & Hemphill-Haley, 2020; Hemphill-Haley, 1996). Geochemistry also permits to identify the source of sediments, based on the absolute and relative concentrations of major, minor and trace elements (e.g. Chagué, 2020; Chagué-Goff et al., 2011, 2017). Mineral assemblages permit to infer different modes of sediment transport and hydrodynamics (e.g. Costa et al., 2015; Jagodziński et al., 2012; Nakamura et al., 2012). Magnetic properties can reveal sediment provenance and the energy of past events (e.g. Bógalo et al., 2017; Černý et al., 2015; Goguitchaichvili et

al., 2013). The development of novel techniques such as X-ray computed tomography imaging favoured the identification of physical features of tsunami deposits (e.g. Falvard & Paris, 2017; Paris, 2020).

After worldwide investigations of Holocene and recent tsunami events, field and laboratory evidence favoured the establishment of some criteria that guide the identification of past tsunamis in the sedimentary record (e.g. Dominey-Howes et al., 2006; Morton et al., 2007; Peters & Jaffe, 2010; Switzer & Jones, 2008). These criteria include evidence of:

- **Lateral extent of a sand deposit**. Tsunamis are high-energy events of large-scale inundations, whose deposits are commonly observed as continuous or almost continuous deposits of sand over large areas impacted (Kempf et al., 2017).
- **Basal unconformity**. The characteristic of the basal contact demonstrates the energy associated with the deposit.
- **Presence of intraclasts**. Tsunami waves can erode the muddy substrate, producing fine grained clasts of soft sediments, which are incorporated within the tsunami deposit as rip-up clasts (Ishizawa et al., 2018; Wilson et al., 2014)
- **Normally graded sediments**. During the tsunami high-speed flow, coarser grains with higher settling velocities are deposited first, followed by fine grains with lower settling velocities (Wilson et al. 2014).
- **Landward fining sequence**. Sediment grain size of tsunami sediments fine landward from the shore as tsunami waves are unable to load coarse sediments due to they lose energy when they move landwards (Dominey-Howes et al., 2006).
- **Presence of a mud cap**. A mud cap represents the deposition of fine sediments from suspended material, resulting from a change of flow velocity (Kelsey et al., 2005; Wilson et al., 2014).
- **Macrofossils**. Organic material eroded, transported and settled following the deposition by the tsunami is commonly present within the tsunami deposit or capping the top (Kelsey et al., 2005; Wilson et al., 2014).
- **Biostratigraphy**. The presence of marine or coastal microfossils provide evidence of a marine incursion in coastal wetlands (Dura & Hemphill-Haley, 2020; Hemphill-Haley, 1996).

The reconstruction of long-term sequences of subduction zone earthquakes, simply based on tsunami deposits, is challenged by the fact that other processes such as volcanic eruptions, submarine and terrestrial landslides and the impact of extra-terrestrial objects can also produce tsunami waves (Sugawara, 2020). Hence, tsunamis might not be produced locally by a megathrust earthquake. Additionally, when sedimentological evidence is present in the geological record, it turns out challenging to differentiate it from the background sedimentation or from the imprint of other extreme-wave events, such as storm-surge deposits (Costa et al., 2021). To overcome these difficulties, geological evidence of tsunami deposits accompanying sudden subsidence or uplift provides unquestionable evidence of a past megathrust earthquakes in coastal areas adjacent to a subduction zone.

1.5. Geological evidence of past earthquakes in the Jalisco subduction zone.

Geological investigations of past earthquakes along the coasts of Jalisco and Colima are scarce and irregularly distributed (**fig. 1.4**). Sites investigated concentrate in the southern region of this subduction segment, from Punta Careyes (19.43°N, 105.02°W) to the Cuyutlán Lagoon (18.89°N, 104.03°W). Although, early geological investigations focus on evidence of crustal deformation, most of these investigations aim to reconstruct long-term sequences of past earthquakes through the study of tsunami deposits.

Ramírez-Herrera et al. (2004) investigated the features of emerged landforms at five sites along 40 km of the Jalisco coast, from Punta Farallón to Barra de Navidad (**R-I in fig. 1.4B**), to find evidence of Holocene crustal deformation. This study can be considered as the first geological investigation in this subduction segment that aimed to find coastal evidence of tectonic activity during the Holocene. Tidal notches near the mouth of the Cuitzmala river and within the Barra de Navidad lagoon were levelled and dated. The tidal notch near Cuitzmala is ~4.5 ± 0.2 m msl. The ^{14}C age of this notch, 1262 ±51 yr. BP, was estimated using in situ red algae. The notch in Barra de Navidad is 0.9 ± 0.2m msl. Using oyster shells, ^{14}C results show anomalous values (109% of modern carbon) and the age of this notch was not obtained (Ramírez-Herrera et al. (2004). These emerged landforms were interpreted as probable evidence of coastal uplift, likely caused by earthquakes, due to the presence of in-situ dead organisms inside these landforms.

The first sedimentological study of tsunami deposits was carried out by Ramírez-Herrera et al. (2014), using deposits from the Estuary Palo Verde in Colima (**R-II in fig. 1.4B**). This site is 30 km southeast from Manzanillo bay. Ramírez-Herrera et al. (2014) found two anomalous sand deposits in a trench, dug in the back portion of the coastal barrier. Sediment geochemistry, magnetic properties, granulometry and diatom assemblages suggest that these two sand beds were deposited by tsunamis. Based on ^{14}C ages, Ramírez-Herrera et al. (2014) concluded that the oldest sand bed was deposited between 1346 AD and 1256 AD; and the shallowest deposit corresponds to a tsunami occurred in 1932 AD. At the same site (**R-V in fig. 1.4B**), Bógalo et al. (2017) investigated these two deposits using a broad range of magnetic properties as proxies to confirm their tsunami origin.

Ramírez-Herrera et al. (2016) studied the stratigraphy, at a trench scale, at the site El Tecuán (**R-III in fig. 1.4B**), which is ~60 km northwest from Manzanillo bay. At this site four sand beds with sharp basal contacts extend laterally over 100 m inland from the trench. The magnetic properties of these deposits took Ramírez-Herrera et al. (2016) to conclude that they correspond to tsunami deposits. Using downcore ^{210}Pb and three ^{14}C ages, the youngest deposit, dated 1935 ± 11 AD, was correlated to an earthquake in 1932. Although the individual ages of the former deposits were not constrained, Ramírez-Herrera et al. (2016) concluded that these beds were deposited after the 15th century.

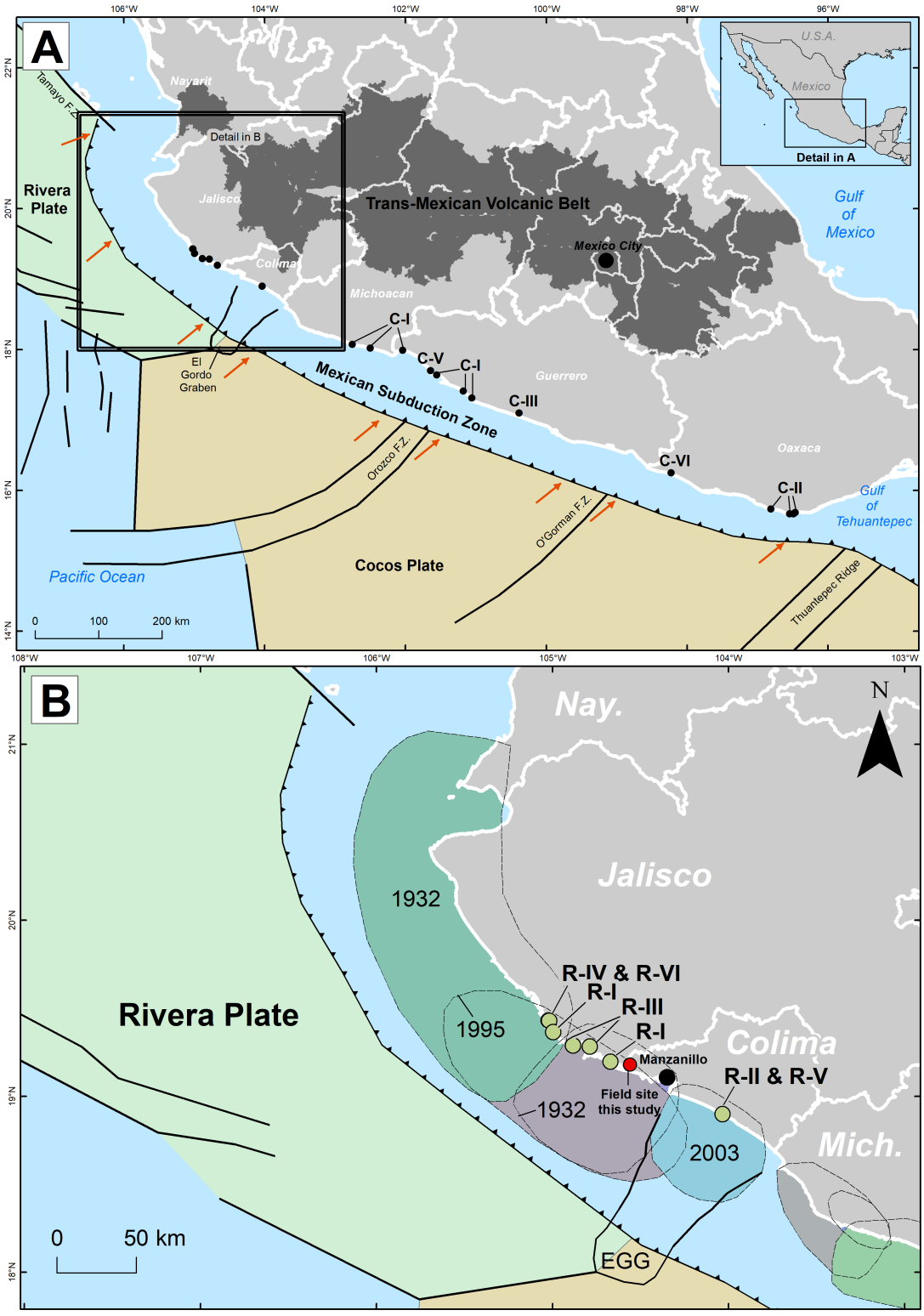

***Figure 1.4**. Geological investigations of past earthquakes and tsunamis in the Mexican Pacific coast. **A)** Distribution of geological records within the Cocos plate domain, including: C-I: Bodin & Klinger, 1986; C-II: Ramírez-Herrera & Orozco, 2002; C-III: Ramírez-Herrera et al., 2007; C-IV: Ramírez-Herrera et al., 2009; C-V: Ramírez-Herrera et al., 2012; C-VI: Ramírez-Herrera et al., 2020. **B)** Sites of studies within Rivera plate domain: R-I: Ramírez-Herrera et al., 2004, R-II: Ramírez-Herrera et al., 2014, R-III: Ramírez-Herrera et al., 2016, R-IV: Černý et al., 2015, R-V: Bógalo et al., 2017, R-VI: Castillo-Aja et al., 2019.*

Ten kilometres southeast from the El Tecuán site, Ramírez-Herrera et al. (2016) also investigated the stratigraphy of the coastal plain at La Manzanilla (**R-III in fig. 1.4B**). The site investigated is ~100 m inland from the shore. Ramírez-Herrera et al. (2016) found one anomalous sand bed that extends laterally over 80 m inland from the trench. This unit shows an erosional basal contact, rip-up clasts, and soft deformation features at the base of the unit. The age of this event was estimated based on one ^{14}C age, ~380 cal. yr BP, from the bottom of the sequence. Due to the stratigraphic position of the deposit, the authors interpreted this layer as a tsunami deposit produced by the 1932 earthquake.

Tsunami deposits were investigated by Castillo-Aja et al. (2019) and Černý et al. (2015) at Las Salinas lagoon, behind the cliffs of Punta Careyes (**R-V and R-VI in fig. 1.4B**). Černý et al. (2015) found evidence of one anomalous sand bed deposited within 50 cm below the land surface. Černý et al. (2015) measured the magnetic properties of this deposit at a trench scale, looking at its lateral variability. Based on ^{210}Pb and ^{137}Cs concentrations, Černý et al. (2015) concluded that this anomalous deposit occurred within the last 110 years, and its origin is likely to be associated with the tsunami occurred in 1932.

Castillo-Aja et al. (2019) extended the record of Las Salinas site. Deposits from a 90 cm deep trench reveal four anomalous beds with abrupt basal contacts composed by coarse sand with shell fragments and some clay mottles. Based on microfossils assemblages, the authors established their marine origin and interpreted them as potential tsunami deposits. Based, on archaeomagnetic dating using pottery samples, Castillo-Aja et al. (2019) dated the oldest event and correlated it with the earthquake of 1563 AD, which according to Suter (2019) this is the first historically recorded earthquake for this subduction zone. The three youngest events were dated using ^{210}Pb and ^{137}Cs concentrations. Castillo-Aja et al. (2019) indicated that the sequence of the deposits correspond to the megathrust earthquakes in 1900, 1932 and 1995.

This review of geological investigations along the coasts of Jalisco and Colima, to investigate past earthquakes is constrained by onshore evidence produced by the most recent earthquakes. Coastal sediments reveal the widespread evidence of tsunami deposits associated to the earthquakes occurred in 1932 and 1995. Although historical records of past megathrust earthquakes and tsunamis are well documented

(Castillo-Aja & Ramírez-Herrera, 2017; Suter, 2019), only a few sites correlate the geological evidence with historical earthquakes (e.g. Castillo-Aja et al., 2019). This is in part due to the restrictions and challenges of the dating methods, which limit the unambiguous reconstruction of past earthquakes. In conclusion, as the existing fragmented spatial and temporal evidence of geological records along this coast the long-term behaviour of this megathrust fault remains unknown. It is in this context, in which this thesis aims to contribute.

1.6. Thesis structure

This thesis consists of three chapters of results, which act as independent but methodologically related studies. The research presented in **Chapter 4** "Quantifying coseismic coastal subsidence caused by the 1995 Colima-Jalisco (M_w 8.0) earthquake using coastal stratigraphic sequences" was designed to develop the methodological approach based on fossil diatoms, in order investigate the potential of this coast to quantify coseismic land-level changes. The outcome of the methodological approach developed here was tested using geodetic instrumental observations during the 1995 earthquake.

Based on the methodological development of Chapter 4, I investigated the evidence of early instrumental earthquakes. The **Chapter 5 "**Coastal subsidence caused by the 1932 (Mw 7.8) megathrust earthquake and other marine incursions on the Jalisco-Colima coast, México" was designed to understand the response of the coast, either subsidence or uplift, during early instrumental earthquakes to constrain these ruptures.

Lastly, in the **Chapter 6** "Late Holocene coastal uplift and subsidence during megathrust earthquakes in the Jalisco subduction zone, México" I aimed to extend the records and find evidence of palaeoearthquakes. In this chapter, I interpreted the Late Holocene evolution of the coast, which is unknown, to understand the different types of earthquake signatures in a rapid evolving coastal system and reconstruct long-term sequences of past seismic event.

Chapter 7 summarises the results to frame wider significance of this study in the context of earthquake hazard assessment along the Mexican pacific.

CHAPTER 2

STUDY AREA

2.1. Introduction

The study area belongs to the coastal plain of the Marabasco river, which is the political boundary of the states of Jalisco and Colima. This site corresponds to the southern sector of the tectonic domain of the subducting Rivera plate. This chapter includes a general context of the tectonic and environmental setting of the study area that hosts the field sites, where sediment core samples were collected.

2.2. Seismotectonic setting

The central Pacific coast of Mexico is an active tectonic margin dominated by subduction of Rivera and Cocos plates (**fig 2.1A**). The morphological expression of this margin is the Middle America Trench, which lies ~ 3000 km from central Mexico to Costa Rica (Bartolome et al., 2016; Dañobeitia et al., 2016). In the northernmost sector of the Middle America Trench, from the Tamayo Fracture Zone to the El Gordo Graben, lies the subducting segment of the Rivera-North American plates, here named as the Jalisco Subduction zone.

The Rivera plate is a relative young microplate originated ~10 Ma ago, when the Cocos plate began its fragmentation (DeMets & Traylen, 2000; Manea et al., 2013). The Rivera plate begins to subduct at a dip angle of 7 ± 1º, reaching and abrupt dip angle of 65º at 100 km depth (Bartolomé et al., 2011; Dañobeitia et al., 2016). The subduction of the Rivera Plate is characterized by a more northerly trajectory than the adjacent Cocos Plate (Dañobeitia et al., 2016). In this sense, the trench-normal component of convergence of the Rivera plate progressively increases towards the south (Manea et al., 2013). Hence, plate subduction is associated with counter-clockwise rotation, resulting in an increase rate of convergence from north to south, from ~2 to ~5 cm yr^{-1}, respectively (Dañobeitia et al., 2016; Kostoglodov & Bandy, 1995; Manea et al., 2013; Suter, 2019).

Regional thrust mechanisms indicate a shallow trend seismicity, 15 – 20 km depth, (Abbott & Brudzinski, 2015). Linking this dominant pattern with the characteristics of this subduction zone, such as: 1) the dipping angle of the Rivera slab and 2) the width

of this continental margin, 80 km wide on average (W. L. Bandy & Mortera, 2012), most of the instrumental earthquakes ruptured offshore. However, Currie et al. (2002) point out that along the Mexican subduction zone, megathrust earthquakes can rupture at depths confined to ~30 km, which in the context of this subduction zone megathrust earthquakes ruptures can extend further inland, bringing the seismic source below the coast (**fig 2.1B**).

In the last century, local instrumentation recorded the occurrence of four large to great earthquakes in the Jalisco subduction zone (**fig. 2.1B**). The largest earthquake occurred offshore the coast of Jalisco on the 3rd of June 1932 (Mw 8.2). This event was followed fifteen days later (18th of June, 1932) by a Mw 7.8 earthquake that ruptured the southern part of the Jalisco subduction zone (Currie et al., 2002; Núñez-Cornú et al., 2016). These two events ruptured different but adjacent parts of the plate interface (S. K. Singh et al., 1985). The hypocentre of the first earthquake (1932-I) was located at a depth of 16 km, with its rupture propagated NW for about 220 km, within a width 75 - 80 km (Okal & Borrero, 2011; S. K. Singh et al., 1985). Estimations of coseismic slip are between 2.4m (Eissler & McNally, 1984) and 4.5 m (Okal & Borrero, 2011). This disparity of values is explained by the occurrence of four sub events that ruptured different asperities (S. K. Singh et al., 1985). The hypocentre of the second earthquake (1932-II) was 16 km depth, offshore the coast of Manzanillo (S. K. Singh et al., 1985). The length and width of this second event are 60 and 80 km, respectively (S. K. Singh et al., 1985).

The second largest earthquake during the instrumental period occurred on the 9th of October 1995 (Mw 8.0). This earthquake's rupture initiated at a depth of 15-20 km, offshore the Manzanillo's bay, and it propagated for along 150 km length to the northwest, near the Chamela's bay (Abbott & Brudzinski, 2015; Hutton et al., 2001; Ortiz, Kostoglodov, et al., 2000). Seismological data suggest that coseismic slip focused principally from 0-30 km downdip at depths of 3-13 km (Hutton et al., 2001). The maximum slip was 5 m at 15 km depth (Melbourne et al., 1997).

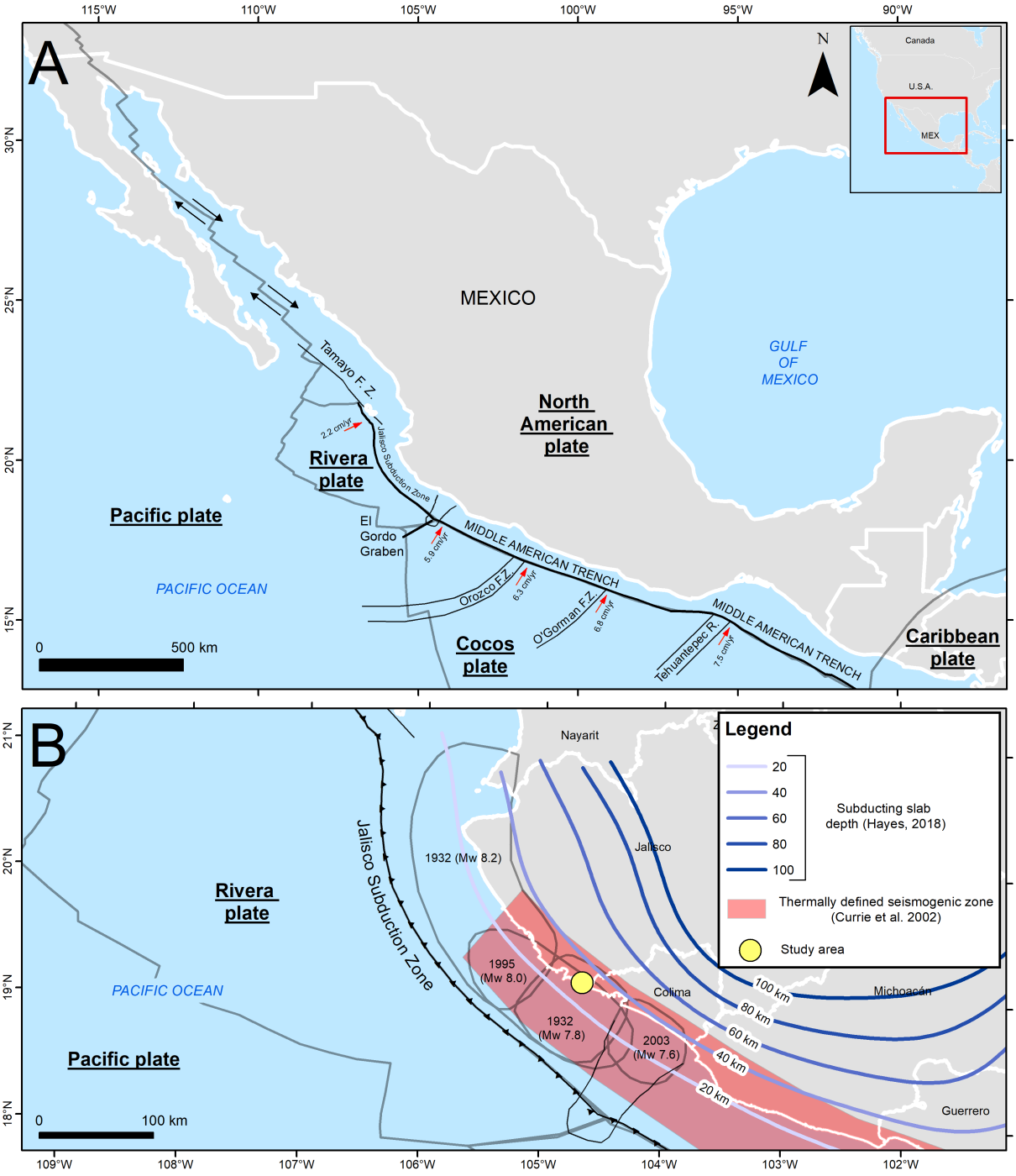

Figure 2.1.A *Tectonic setting of the Mexican Pacific coast. Red arrows represent the direction of the subducting plates, numbers indicate the rate of convergence* ***B)*** *Seismotectonic context of the Jalisco subduction zone. The geometry of the subducting Rivera plate is represented by blue coloured contours. Black ellipses represent megathrust earthquakes of the last 120 years..*

The most recent megathrust earthquake occurred on 22nd of January 2003. This event ruptured near the triple junction of Rivera-Cocos-North American plates, extending to the western half of El Gordo Graben, which is thought to constitute a barrier for along-strike propagation of large subduction thrust earthquakes in this region (Schmitt et al.,

2007). The hypocentral depth of this event was 10 km (Gómez-González et al., 2010). The rupture initiated at a depth of 15-25 km and propagated up and downdip, NNE-SSW (Yagi et al., 2004). Due to this rupture propagated mainly in the dip direction, the along strike length of the rupture area is significantly shorter than its down-dip width (Yagi et al., 2004). The rupture extended from 9 km to 40km depth, and the effective rupture area was estimated to be 40 x 80 km (Schmitt et al., 2007; Yagi et al., 2004). The maximum magnitude of coseismic slip was 2 m, at 24 km depth (Schmitt et al., 2007).

Geophysical models suggest that a rupture of the entire seismogenic zone is equivalent to an earthquake Mw 8.1 - 8.3 (Hutton et al., 2001; S. K. Singh & Lermo, 1985). These scenarios consider a rupture length of ~300 km across the whole contact of the Rivera-North American plate, with uniform coseismic slip < 5 m (Hutton et al., 2001). Under this scenario, these models suggest a recurrence interval which spans 100 - 200 years (Eissler & McNally, 1984; Hutton et al., 2001).

2.3. Geology & Geomorphology

The central portion of the Mexican Pacific coast is part of the physiographic unit known as Sierra Madre del Sur, which forms a west to east widening forearc segment with exposures of the Late Cretaceous to early Miocene arc-magmatic record (Morán-Zenteno et al., 2018). The study area (**fig 2.2**) is in the northern region of the Sierra Madre del Sur, within the sub-province known as Sierras de la costa de Jalisco y Colima (Coastal ranges of Jalisco and Colima). The inland landscape is characterised by high to medium fault-block mountains and highly dissected hills (Hernández Santana et al., 1995; Méndez Linares et al., 2007; Ramírez-Herrera et al., 2004; Ramirez-Herrera & Urrutia-Fucugauchi, 1999). The coastal landscape shows sparse low plains with lagoons and estuaries, alternated with small hills promontories that extend to the coastline formic coastal cliffs, which shelter narrow beaches and coastal barriers (Méndez Linares et al., 2007; Ramirez-Herrera & Urrutia-Fucugauchi, 1999).

The study site corresponds to the coastal plain of the Marabasco river. This plain is surrounded by high-relief (**fig. 2.2**), composed by intrusive igneous rocks Granite-Granodiorite and Granodiorite-Diorite, formed during the Mesozoic and early Cenozoic (Rosales Franco & Camargo Soto, 2019). These igneous rocks form small, < 400

masl, and medium hills, 400 – 800 masl, highly incised by fluvial activity (Hernández Santana et al., 1995; Méndez Linares et al., 2007).

Quaternary deposits include alluvial, paludal and littoral sediments. Alluvial deposits, composed by silt and sand, are associated to the Marabasco river. This river is the main fluvial system found within the study site. The basin of the Marabasco river is composed by the intrusive igneous rocks, occupying an area of 2,034 km^2 (Jiménez Román, 1980). The Marabasco river forms an extensive deltaic plain, which is sheltered, from wave action, by a coastal barrier formed by littoral deposits. This barrier is 500 m wide, and it is formed by a sequence of beach ridges and dune chains, > 5 m high (Méndez Linares et al., 2007).

Paludal deposits dominate on both flanks of the Marabasco river's deltaic plain. On the west flank, these deposits lay parallel to the coastal barrier and they are associated to the coastal lagoon Barra de Navidad. On the east flank, paludal deposits form a large wetland that extends from the back-barrier to the foot of the hills. This extensive area is known as Estero Potrero Grande, which is part of the Marabasco River estuary due to a series of creeks connect the wetland with this river's mouth (**fig. 2.2**).

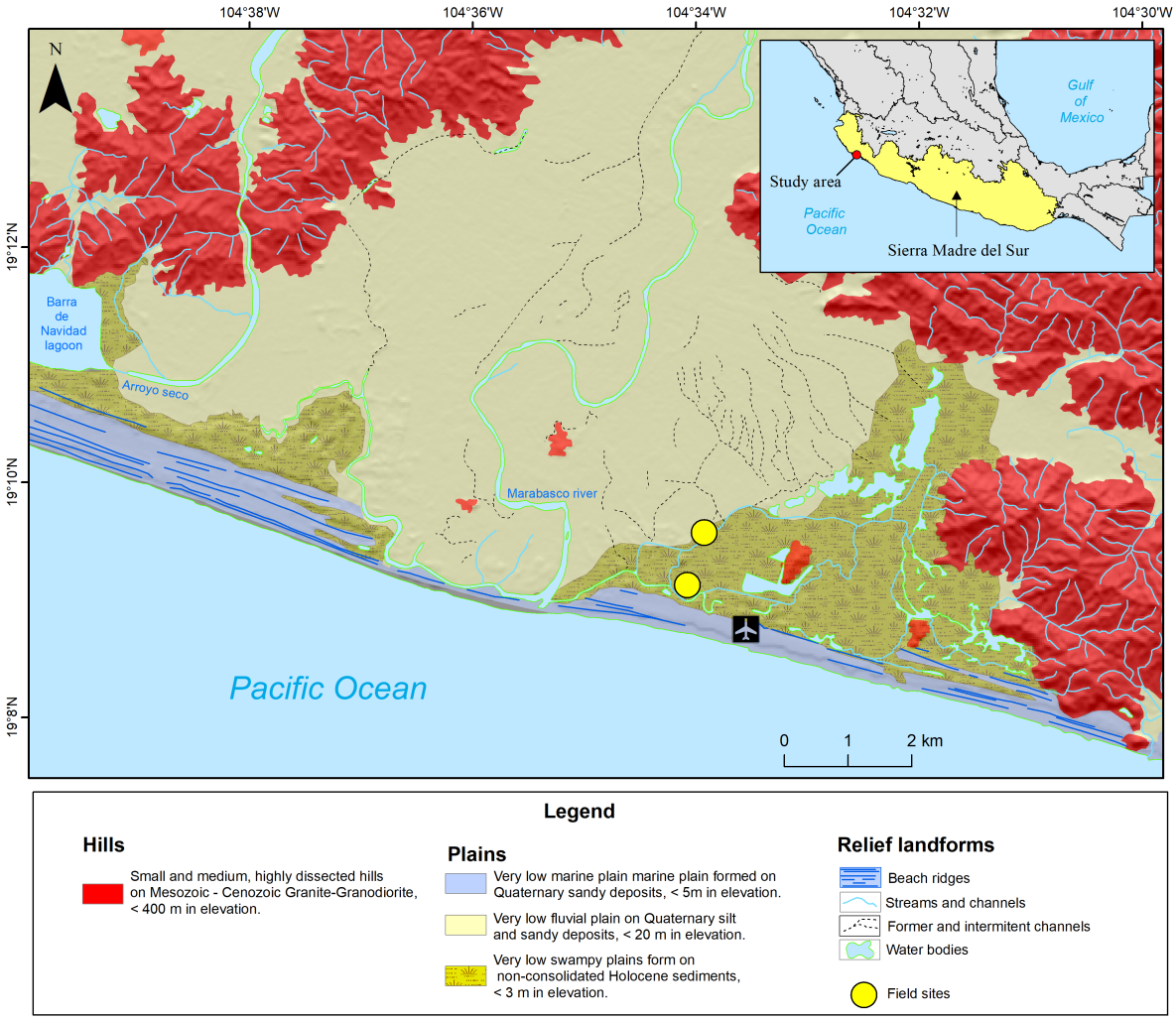

***Figure 2.2**. Geology and geomorphology of the Marabasco river coastal plain.*

2.4. Climate

The climate of this region is tropical wet-dry (García, 1964; Vidal Zepeda et al., 2007). This climate is characterised by a wet season, which extends from May to October, being the wettest months July and August (García, 1964; Jiménez Román, 1980; Vidal Zepeda, 2005). The Marabasco river's basin experiences a mean precipitation of ~10 mm in May, reaching a maximum level in August, up to 300 mm (Jiménez Román, 1980). The second half of the year is conditioned by an extended dry season, between November and April, with the driest months in February and March (García, 1964; Jiménez Román, 1980; Vidal Zepeda, 2005). The temperatures remain stable throughout the year, fluctuating between 18.5º C and 28.4º C (Jiménez Román, 1980).

2.5. Tides and coastal processes

Based on the tidal datums from the nearest tide gauge, ~28 km south, at the Manzanillo's port (**table 2.1**), this coast is classified as microtidal (SMN., 2021). The Mean Range of Tide is 0.536 m, this corresponds to the difference in height between the Mean High Water (MHW) and Mean Low Water (MLW). The Great Diurnal tidal range is 0.731 m, corresponding to the difference in height between the Mean Higher High Water (MHHW) and Mean Lower Low Water (MLLW). Most waves along the region are < 1 m high, with 50% arriving from the southeast (Gonzalez-Vazquez et al., 2014).

As fluvial discharges vary significantly during the year, the Marabasco river is an intermittent stream and its estuarine conditions change over the year (De la Lanza Espino et al., 2013; Jiménez Román, 1980). During the dry season the mouth of the river remains closed due to long-shore currents build a bar in the river's mouth, and the back-barrier wetland becomes a coastal lagoon, with minimum influence of tides.

Nonetheless, during the wet season the Marabasco river increases its discharges and the river's mouth is breached, amplifying the tidal signal in this wetland. During extreme storms and hurricanes, coastal breaching also occurs in low-lying sites along the barrier. Nonetheless, these inlets are ephemeral, and they close a few days after these events, due to weak fluvial or tidal flows.

Table 2.1*.Tidal datums of the Manzanillo tide gauge (Source: SMN., 2021).*

Datum		**Metres (m)**
Extreme High Water	EHW	0.848
Mean Higher High Water	MHHW	0.333
Mean High Water	MHW	0.272
Mean Tide Level	MTL	0.005
Mean Low Water	MLW	-0.264
Mean Lower Low Water	MLLW	-0.398

2.6. Field site: Estero Potrero Grande

Two sites were investigated in 2018 and 2019 (**fig. 2.3**). These sites belong to the coastal wetland Estero Potrero Grande, which extends over an area of ~20 km^2, for along 5 km, from the inland foothills to the back-barrier (see fig. 2.2). This wetland contrasts with the rest of other coastal wetlands along the coast of Jalisco, where agriculture and livestock activities have produced intensive modifications.

Estero Potrero Grande is a brackish, lentic and shallow wetland, dominated by halophyte vegetation, including the plant species *Batis maritima* and *Distichlis spicata* (INEGI, 1975). These two species are found frequently in saltmarshes and mangrove swamps (Hill et al., 2018; Lonard et al., 2011). Along the Mexican coasts, *Batis maritima* and *Distichlis spicata* dominate the upper intertidal zones. These two saltmarsh species emplace in the transition zone from mangroves to saltpans. Other dominant species within this wetland is the invasive species *Phragmites australis.* This wetland grass becomes dominant in the inland portions of this site, showing the transition towards a freshwater wetland.

The 2018 site is ~1 km from the Manzanillo international airport. Historically, this site has been struck by storms and hurricanes producing significant morphological changes near the Marabasco river's mouth and other low-lying areas long the coastal barrier that shelters the back-barrier wetland. Hence, to avoid the signature of storms and hurricanes, imprinted in the local stratigraphy, the main criteria for site selection was to work on a site far from the river's mouth and other ephemeral inlets. Hence, boreholes of the 2018 site are >1 km inland from the shoreline and >2.5 km away from the river's mouth. Boreholes are in an area adjacent to a creek channel that cut the coastal plain in a north-northeast direction. This meandering channel connects the estuary with the back-barrier wetland and the tidal signature is still observed at this site. Therefore, only the boreholes adjacent to this creek channel were chosen to represent the local stratigraphy, as they are sensitive to changes in the estuarine conditions, caused by extreme events. The stratigraphy of this site is summarised in Chapters 4 and 5. These sediments reveal the signature of earthquakes occurred in the last century.

The 2019 site was chosen following the same criteria stated in the previous paragraph. This field site is ~2 km from the Marabasco river's mouth and 0.5 km inland from the shoreline. Even though the 2019 site is closer to the shoreline, the wide coastal barrier,

~400 m, does not show evidence of breaching during the most recent major hurricanes. Thus, only the most extreme events were imprinted in the stratigraphy of this site. Boreholes of the 2019 site are adjacent to a creek channel that cut the coastal plain in a shore-normal direction. At this site, vegetation is spare due to the presence of ponding water caused by the presence of abandoned fish tanks, where aquaculture activities took place in past decades. Sediments collected from this site correspond to Late Holocene deposits used to find evidence of palaeoearthquakes (Chapter 5).

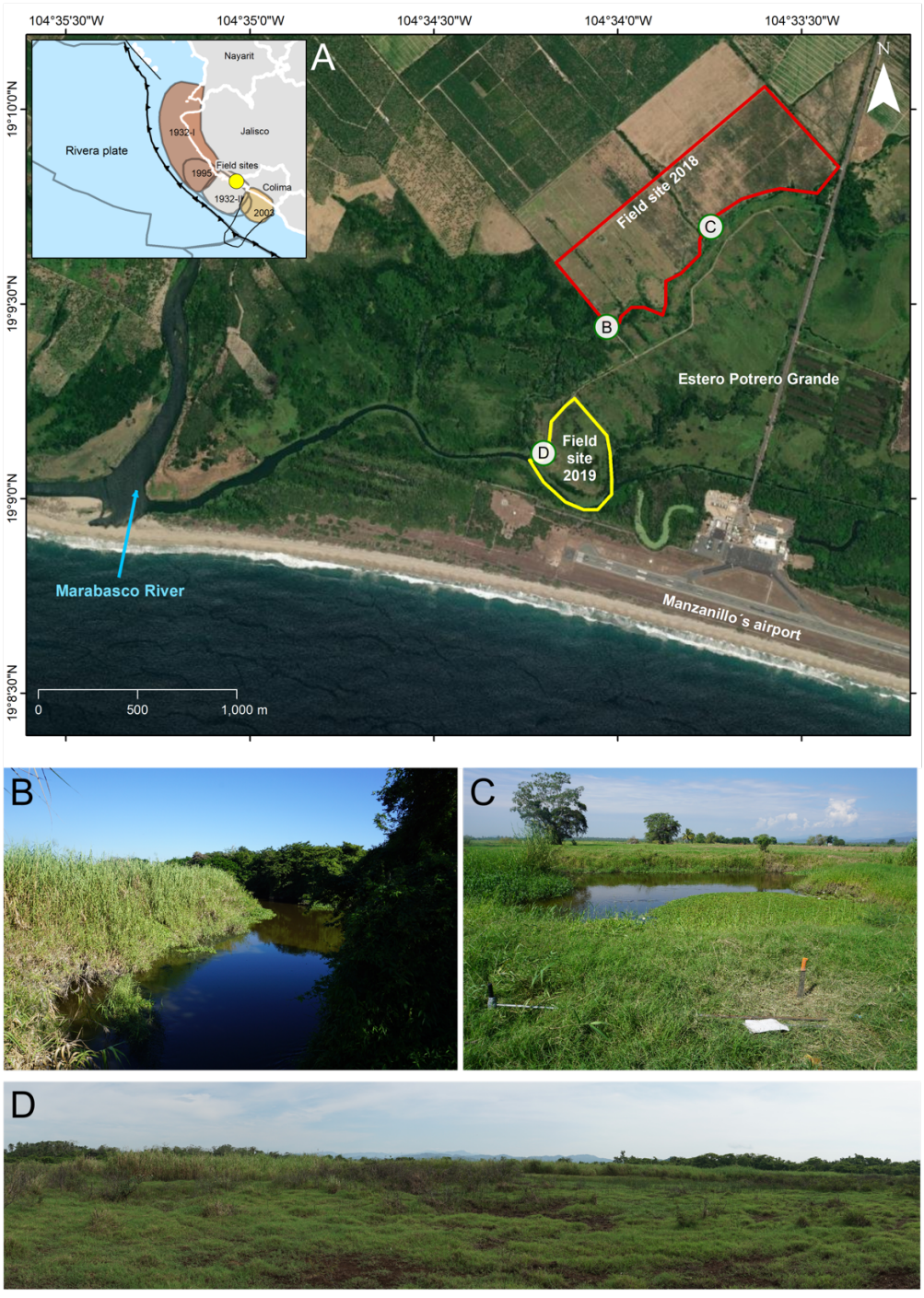

Figure 2.3. Location of field sites in the wetland Estero Potrero Grande.

CHAPTER 3

RESEARCH METHODS

3.1. Fossil stratigraphy

The stratigraphy of wetland sediments was investigated using hand-driven coring devices. In the field site investigated in 2018, sediments reconnaissance and retrieval for laboratory analyses was undertaken using a 2.5 cm diameter gouge corer. Sediments from the 2019 site were retrieved using a 5.2 cm “Russian” peat corer. Sediments were described in the field, based on their macroscopic components, using as guideline the Troels-Smith (1955) classification scheme for unconsolidated sediments. In order to discriminate the nature of stratigraphic changes, transitions between stratigraphic units, here referred as stratigraphic contacts, were classified as abrupt (< 0.5 cm) or gradual (> 0.5 cm). These contacts were used to correlate the stratigraphic units, based on their stratigraphic position and depths.

Boreholes were surveyed using the Leica NA700 automatic level. Elevations were referenced to the INEGI geodetic benchmark V0614 to obtain the orthometric heights relative to the North American Vertical Datum 1929 (NAVD29). Samples taken for laboratory analyses were sampled in 50 cm long sections with an overlap of 5 cm between core sections. Hence, twin boreholes were drilled, 1 m apart, to ensure the integrity of the sedimentary sequences. Sediment samples were stored in round PVC tubes and wrapped in plastic liners.

3.2. Non-destructive methods.

3.2.1. X-ray Computed Tomography (CT)

Immediately on arrival to the laboratory, core sections were scanned using non-destructive methods to image, at high resolution, the physical characteristics of the sediments. Core sections were vertically scanned using the Geotek X-ray computed tomography (CT) imaging system. The x-ray was set up at 128.99 kV and 245.7 mA. The vertical resolution is 6 mm (70 pixels) per scanning, with a pixel resolution of 86.87 µm. The CT image was post-processed using the 'Image J' software (Abràmoff et al., 2004) to enhance the contrast, identify and characterise the stratigraphic contacts.

3.2.2. Geochemistry

Core sections were scanned with the Geotek Multi-Sensor Core Logger (MSCL-XRF) to obtain geochemical composition of sediments and identify salinity changes, reflected by elemental log-ratios. The Geotek XRF scanner has an X-ray tube with an Rh-anode with a collimator. For light elements (e.g. Al, Ca, Cl, Co, Fe, K, S, Si and Ti), the X-ray voltage was 10 kV and the X-ray current 0.130 mA, while for heavier elements (e.g. Zr, Br, Mo, Rb, Sr and Zn), the settings were 30 kV and 0.500 mA. Output data is in counts per second (cps)

Only for Chapters 4 and 5, elemental log-ratios were used to support the identification of salinity changes downcore. Three independent ratios were built using as denominator the elements Sulphur (S), Bromine (Br) and Calcium (Ca), and as numerator the element Zinc (Zn). Elements S, Br and Ca show high concentrations in seawater and marine sediments (Chagué, 2020; Chagué-Goff et al., 2017a; Rothwell & Croudace, 2015), while Zn is a terrestrial element present in fluvial waters and sediment along the Mexican Pacific, and specifically in the Marabasco river (Marmolejo-Rodríguez et al., 2007; Martinez et al., 2014). Consequently, greater influence of marine conditions in the wetland is reflected by the increase of the S/Zn, Br/Zn and Ca/Zn ratios. On the other hand, a decrease of these ratios would suggest either less influence of marine conditions or more influence of fluvial discharges.

In addition to elemental measurements, the XRF scanner produces two measurements of energy scattering, incoherent and coherent (Burnett et al., 2011). Incoherent scattering occurs when the energy of the incident X-rays is much greater than the energy binding electrons to the atom nucleus, producing deviating the energy with some loss of energy (Woodward & Gadd, 2019). Coherent scattering occurs when primary X-rays interact with material and are deviated without losing energy (Liu et al., 2013). Incoherent scattering relates with elements with low atomic numbers such as H, C, N and O, which are abundant in organic matter (Croudace et al., 2006; Woodward & Gadd, 2019). Consequently, inc/coh ratio is an indicator of organic content in sediments (Burnett et al., 2011; Chawchai et al., 2016; Giralt et al., 2011; Liu et al., 2013; Woodward et al., 2018; Woodward & Gadd, 2019). In Chapters 4 and 5, the inc/coh log-ratio was built to investigate changes in the presence or absence of

organic content in the sediment matrix. High values of this ratio suggest higher content of organic sediments, whereas lower values suggest a reduction.

3.3. Grain size analysis

Sediment grain size analyses were carried out at 1 cm intervals. This proxy was used to identify the sedimentological signature of high energy events but also to interpret the background sedimentation. Bulk sediment pre-treatment followed the HCl + H_2O_2 method found in Vaasma (2008). To avoid flocculation, 2 ml of sodium hexametaphosphate ($(NaPO_3)_6$) was added to each sample before the analysis. Samples were analysed using a Beckman Coulter LS 13 320 Laser Diffraction Particle Size Analyser. The analyser was set up to average the observations for 90 seconds three times. The output contains the volume of material within a range from 0.04 µm up to 2000 µm in 165 classes. The results were processed through the GRADISTAT extension in MS Excel (Blott & Pye, 2001) to obtain the fraction of sand, silt and clay, as well as the most important parameters of the grain size distributions (Folk & Ward, 1957).

3.4. Diatom analyses

Fossil diatoms were used to reconstruct palaeoenvironmental changes and quantify land-level changes. From each core section, 0.5 g of sediment was subsampled and oxidised using 15 ml of concentrated (20%) hydrogen peroxide (H_2O_2) to remove organic material. Samples were not centrifuged to avoid frustule breakage. Duplicated slides with low and high material concentrations were mounted on slides using Naphrax. Around 200 diatom valves were identified using an oil-immersion microscope with a magnification of 1,000x.

Species identification followed the catalogues of Mexican coastal diatoms (López Fuerte et al., 2010; López-Fuerte et al., 2013; López-Fuerte & Siqueiros Beltrones, 2016; Novelo et al., 2007; Siqueiros Beltrones et al., 2005; Siqueiros-Beltrones et al., 2020). Halobian classes were assigned based on Denys, (1991); Hartley et al. (1996); Vos & de Wolf (1993); Hocking et al. (2017); Horton et al. (2007); and Shennan et al. (2016). Salinity classes were assigned as polyhalobous (marine species), mesohalobous (brackish species), oligohalobous-halophile (freshwater species

stimulated at low salinity); and oligohalobous-indifferent (freshwater species that tolerate low salinity; Dura et al., 2016; Horton & Sawai, 2010). Final counts were transformed into relative abundance (%) and grouped according to their halobian classes.

3.4.1. Palaeoelevation estimations and quantification of land-level changes

Many palaeoseismological investigations employ fossil diatoms to quantify the magnitude of coseismic land-level changes across multiple earthquakes cycles (e.g. Garrett et al., 2013; S. Hamilton & Shennan, 2005, 2005; Hocking et al., 2017; Shennan et al., 2016; Shennan & Hamilton, 2010). This approach relies upon the development of diatom-based transfer functions. Elevations are obtained as a standardised water-level index (SWLI), which are the normalised units of elevation used to reduce variations in tidal range, when surface sediments to build a training set are sampled across multiple sites (Kemp & Telford, 2015). Given the limitations of this study to carry out fieldwork to build a diatom-based transfer function, palaeoelevations from the fossil record were estimated indirectly.

This method aims to use the cumulative percentage of brackish and marine diatoms to calculate palaeoelevations. Shennan et al. (2016) demonstrated the existing relationship between the cumulative percentage of brackish and marine diatoms and their corresponding palaeoelevations (**fig. 3.1A**). This relationship was chosen to be modelled statistically and estimate palaeoelevations indirectly as it offers the possibility to use a well-constrained and a published dataset, which can also support future investigations. In this sense, I used two datasets (**fig. 3.1**), one from Alaska (Shennan et al., 2016) and one from Chile (Hocking et al., 2017). These datasets contain two variables: 1) the cumulative percentage of brackish and marine fossil diatoms and 2) palaeoelevations in SWLI units, obtained through a diatom-based transfer function. I used these variables to build a simple linear regression model for each dataset. I used the percentage of marine and brackish species, is the independent variable (X), and their corresponding SWLI values, act as the dependent variable (Y).

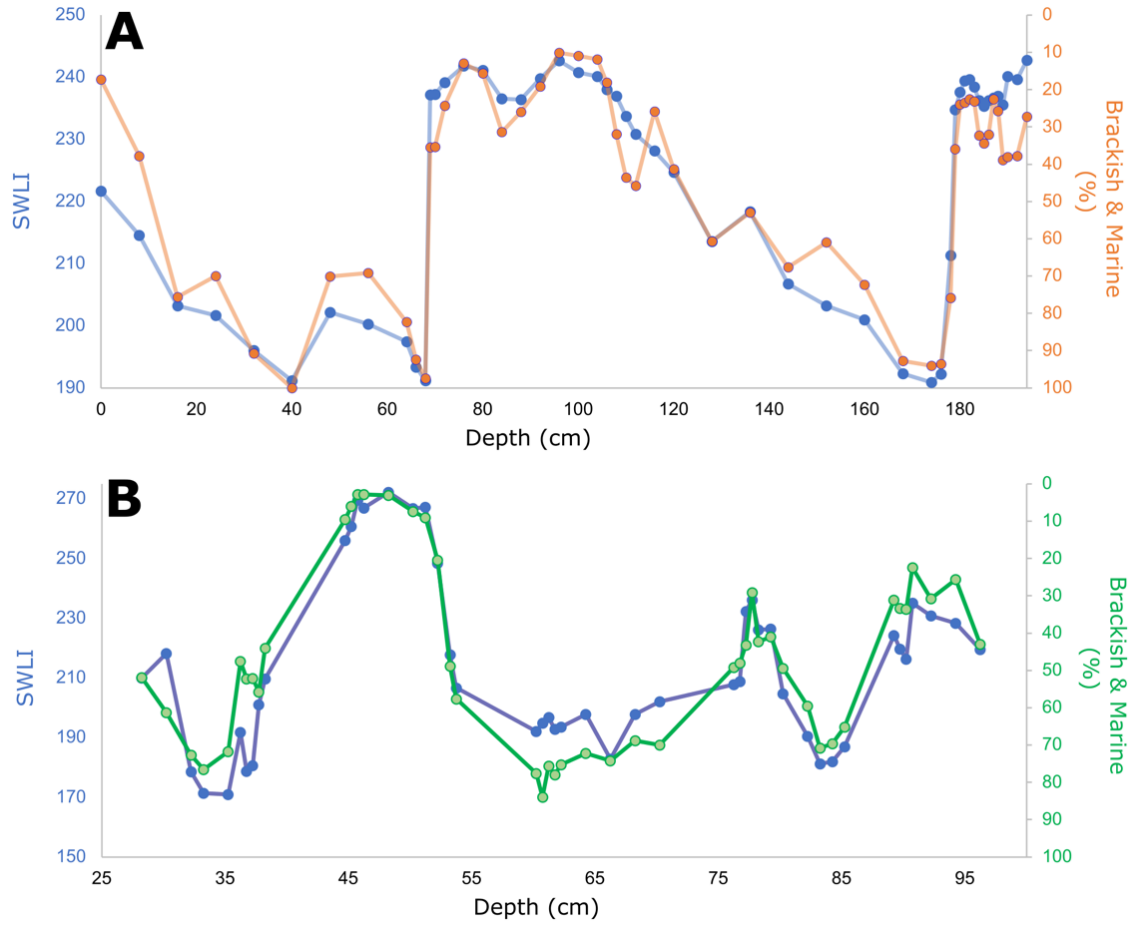

Figure 3.1. *Plots showing the relationship between the percentage of brackish and marine diatoms and palaeoelevations (SWLI). A) Samples from Alaska (Shennan et al. 2016); B) Samples from Chile (Hocking et al., 2017).*

The intercept (α) and slope *(β*) of these linear models (Model 1 for the Alaska dataset and Model 2 for the Chile dataset) were used to estimate the mid-point of palaeoelevations, based on the percentage of brackish and marine diatoms of the fossil record from the Mexican Pacific. The output, in SWLI units, was then transformed into meters based on the vertical difference of MHHW (200 SWLI) and MTL (100 SWLI), using the water level datums from the tide gauge in Manzanillo (see **table 2.1**).,

Palaeoelevations (m) were referenced to the Mean Higher High Water (MHHW). Thus, palaeoelevations are either above (+ m MHHW) or below the MHHW (-m MHHW). The indicative meaning of these two tidal zones was then classified as the upper and lower intertidal zone, respectively. Following Hemphill-Haley (1993), the reference water level (RWL) of the upper intertidal zone was constrained by the MHHW and the

Extreme High Water (EHW), and the RWL of the lower intertidal zone is constrained by the MHHW and the Mean Tide Level (MTL), see **table 2.1** for the elevations reference.

The total elevation error estimate (e_e) of the palaeoelevation reconstructions is obtained following Shennan (2015). The error of the regression model is incorporated, corresponding to the confidence intervals of the linear regression (e_1), and the half the indicative range of each sample (e_2), using the following equation:

$$e_e = \sqrt{e_1^2 + e_2^2}$$

Lastly, the amount of coseismic land-level change across the stratigraphic contact was obtained from the height difference of the samples below and above each contact. Following Garrett et al. (2013) the uncertainty of coseismic deformation ($CD_{uncertainty}$) is obtained using the error previous to the event (E_{pre}) and the error post the event (E_{post}):

$$CD_{uncertainty} = \sqrt{(E_{pre}\,\text{error})^2 + (E_{post}\,\text{error})^2}$$

3.5. Chronology

3.5.1. Radiocarbon dating

Plant macrofossils were subsampled from core sediments to obtain mass spectrometry (AMS) radiocarbon (^{14}C) dates. Bulk sediment was subsampled and washed with deionised water using a 500 µm sieve. Detrital fragments were retained and carefully examined using a binocular microscope to select datable material. Leaves and seeds were picked as dead material, which is rapidly buried after death and not easily transported, reducing the presence of outliers or age reversals in the chronostratigraphic sequences. Samples were submitted to the SUERC and Beta-Analytic laboratories.

3.5.2. Caesium-137 (^{137}Cs)

^{137}Cs is a short-living radionuclide (half-life = 30.17 years), whose environmental presence is solely from nuclear fission, which resulted from atmospheric nuclear weapons testing (Drexler et al., 2018). ^{137}Cs was initially incorporated in sediments

when fallout began in 1952 ± 2 AD, but it was not until 1963 ± 1 AD when measurable global fallout occurred (Corbett & Walsh, 2015; Drexler et al., 2018). A second large input of ^{137}Cs corresponds to the the nuclear accident of Chernobyl in 1986, which predominantly affected the Northern hemisphere (Corbett & Walsh, 2015).

Downcore concentrations of ^{137}Cs permit to establish a chronological control for sediments deposited during the second half of the twentieth century. When concentration values surpass the detection limit for the equipment used, the onset of ^{137}Cs can be established (e.g. Kemp et al., 2012). The onset is frequently used as the first chronological marker that indicates the beginning of ^{137}Cs fallout in 1952 ± 2 AD (e.g. DePaolis et al., 2021; Haltia et al., 2021; Shennan et al., 2014; Zong et al., 2003). A second, and a more robust, temporal marker corresponds to the peak of ^{137}Cs concentrations, which represents the year of maximum ^{137}Cs fallout in 1963 ± 1 AD (e.g. Briggs et al., 2014; Witter et al., 2019; Zong et al., 2003). Some sites, predominantly in Europe, can detect a second peak of ^{137}Cs concentrations, which serves as a third temporal marker, linked to the Chernobyl incident in 1984 AD (e.g. Haltia et al., 2021). In this study, downcore concentrations of ^{137}Cs were measured to establish, when possible, the beginning (^{137}Cs onset) and maximum fallout (^{137}Cs peak) as chronological controls.

Concentrations of ^{137}Cs were measured by gamma spectrometry. Samples were oven-dried and ball-milled. The fine powder was weighed and deposited in a 4 cm long plastic tube. The tubes were covered with a rubber cap and sealed with wax. The samples were analysed by an Ortec Gamma well detector, with the gamma-ray energy 32keV.

3.5.3. Age-depth models

To constrain the age of the stratigraphic contacts, ^{14}C and ^{137}Cs were used to build multiple age-depth models using the *P_sequence* in OxCal (Bronk Ramsey, 1995, 2001). The *P_sequence* is a Bayesian age-depth model that permits interpolating and constraining ages, considering a variable random sedimentation rate (Ramsey, 2008). Because of the variable age range of the core sediments, age-depth models include composite chronologies. Hence, in OxCal the calibration curves used are the IntCal20

(Reimer et al., 2020) and the post-bomb atmospheric curve, Bomb21NH2 (Hua et al., 2021).

CHAPTER 4

QUANTIFYING COSEISMIC COASTAL SUBSIDENCE CAUSED BY THE 1995 COLIMA-JALISCO (M_W 8.0) EARTHQUAKE USING COASTAL STRATIGRAPHIC SEQUENCES

ABSTRACT

The coast between the states of Jalisco and Colima was struck in 1995 by a Mw 8.0 megathrust earthquake, produced by a wide rupture along the Rivera and North American plates contact. This earthquake caused widespread subsidence, 6 to 20 cm, along the coast adjacent to this rupture. Some minutes after this earthquake a tsunami, with a maximum run-up of 5 m, struck the coast, flooding up to 500 m inland. The availability of seismic instruments, GPS stations, tide gauges and field-based reports, allowed to constrain the features of this earthquake and its accompanying tsunami. Consequently, this seismic event permits to investigate its sedimentary signature to reveal the characteristics of onshore coastal deposits after an earthquake of this magnitude, which serves as a modern analogue to reconstruct past earthquakes of similar or even larger magnitudes. Within the rupture area of this earthquake lies the coastal wetland Estero Potrero Grande. This coastal site experienced coseismic subsidence and the impacts of this tsunami. In this study, sediments beneath this wetland were collected to find evidence of the 1995 earthquake. Within the shallowest 28 cm depth below the land-surface, a bed of organic silt is overlaid abruptly by grey silt for along 1 km. Using ^{137}Cs concentrations in sediments and a Bayesian age-depth model, the age range of this stratigraphic contact is 1990 – 2002 (2σ), with a mean age 1995 ± 2AD (1σ). The elemental log-ratios S/Zn, Br/Zn and Ca/Zn reveal an abrupt increase of salinity conditions across this stratigraphic contact suggesting a rapid increase of marine water influence in this wetland. Diatom assemblages confirm this abrupt change, and diatom-based palaeoelevation models revealed subsidence within the range 6.38 ± 27 cm and 11.0 ± 28 cm. Sediment grain size data confirms the occurrence of a high energy event concurrent with subsidence, what likely represents the sedimentary signature of the tsunami produced by the 1995 earthquake.

4.1. Introduction

On the 9th October, 1995, in western Mexico, the interface between the subducting Rivera plate and the overriding North America plate (**fig. 4.1**) ruptured seismically, producing a devastating earthquake M_w 8.0. This great earthquake caused strong ground shaking across the states of Nayarit, Jalisco, Colima and Michoacán (Zobin & Ventura-Ramirez, 1998). Based on the Modified Mercalli Intensity Scale, this earthquake was classified as a violent earthquake, from the Tenacatita Bay to Manzanillo Bay (Carrillo-Martínez, 1997). The city of Manzanillo witnessed the collapse of several buildings and structural damage to roads, railways, airports, ports and other types of vital infrastructure, causing significant disruption to the local and regional economy (e.g. Tena-Colunga et al., 1997). Official figures show that more than 30,000 people were affected, and 58 lost their lives (CENAPRED, 2014).

Approximately fifteen minutes after this earthquake, the coasts of Jalisco and Colima were struck by a tsunami wave, with a run-up of 5 m (Borerro et al., 1997). This tsunami was described as a surge that impacted mostly the Tenacatita Bay (Borerro et al., 1997; Castillo-Aja & Ramírez-Herrera, 2017), where seawater penetrated as far as 500 m inland, causing floods between 2 and 4 m high in the towns of La Manzanilla and Boca de Iguanas (Borerro et al., 1997; Castillo-Aja & Ramírez-Herrera, 2017; Filonov, 1997).

The 1995 Colima-Jalisco earthquake is the second largest instrumentally recorded seismic event along the Rivera-North American plate domain. This event occurred 63 years after the 1932 M_w 8.2 event. The 1995 Colima-Jalisco earthquake was the first earthquake whose coseismic deformation was recorded instrumentally, using the local network of Global Positioning System receivers (e.g. Hutton et al., 2001; Melbourne et al., 1997), which began operation only some months before this event occurred (DeMets et al., 1995). Geodetic observations allowed to constraint some of the features of the earthquake rupture, such as its length, width, depth, as well as the magnitude and the spatial distribution of coseismic slip (Hjörleifsdóttir et al., 2018; Hutton et al., 2001; Melbourne et al., 1997). In addition to geodetic data, observations from local seismic data (Pacheco et al., 1997); teleseismic data (Courboulex et al., 1997; Escobedo et al., 1998; Hjörleifsdóttir et al., 2018; Mendoza & Hartzell, 1995),

macroseismic data (Zobin & Ventura-Ramirez, 1998); coseismic sea-level change observations (Ortiz, Kostoglodov, et al., 2000) and field data post-event (Trejo-Gómez et al., 2015) aided to constrain rupture features.

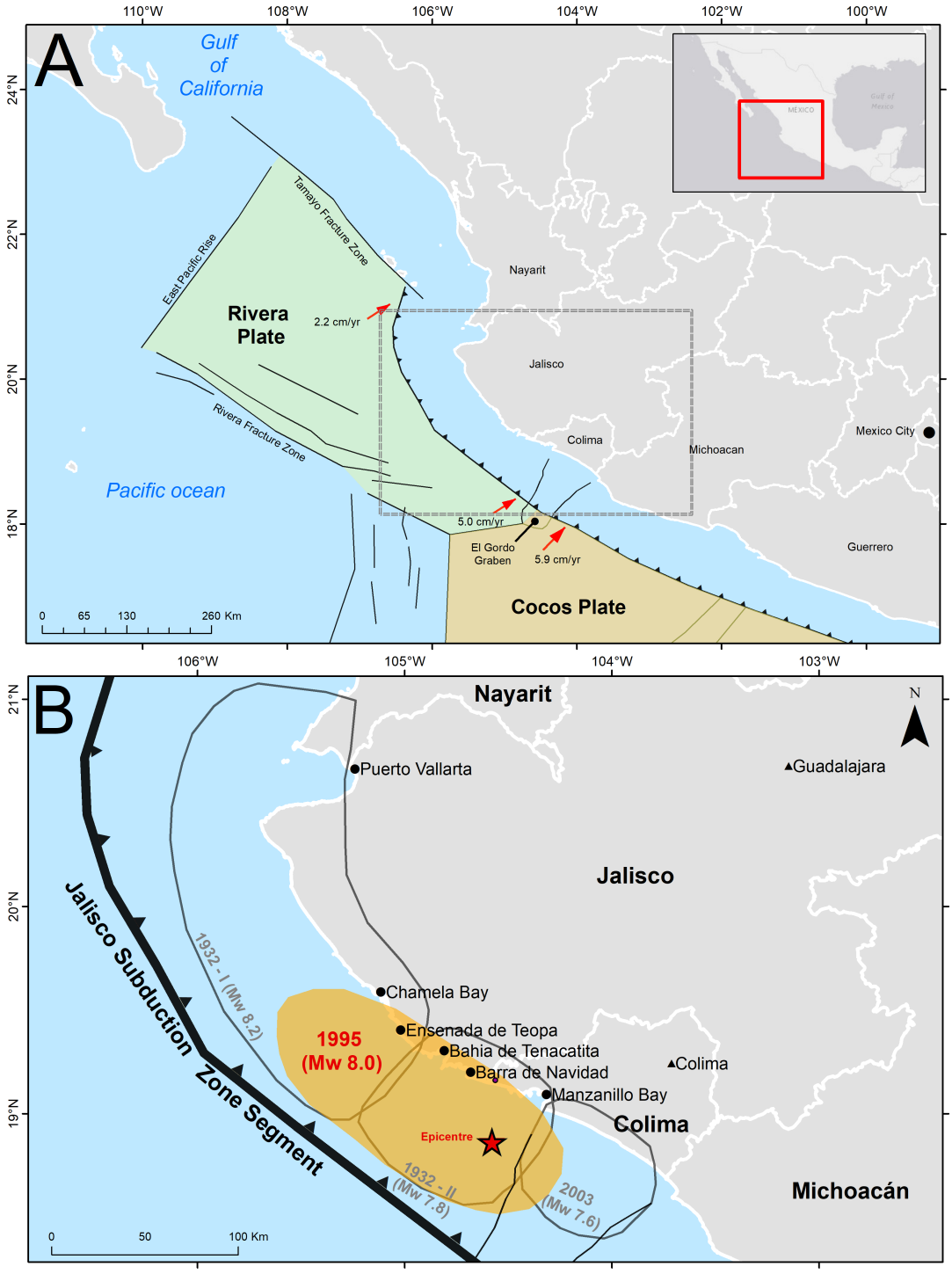

***Figure 4.1**. A) Map showing the seismotectonic context of western Mexico. B) Map showing the ruptured areas of megathrust earthquakes, highlighting in orange the ruptured area during the 1995 earthquake. The epicentre is represented by the red star (from Kostoglodov & Pacheco 1999).*

Despite the adverse effects caused by this earthquake, its occurrence provides the unique opportunity to investigate its sedimentary fingerprint, which serves as a modern analogue to identify past earthquakes of similar or larger magnitudes (e.g. Dura et al., 2017; Garrett et al., 2015; Monecke et al., 2008; Shennan et al., 2014). The overarching aim of this study is to investigate the sedimentary records of the 1995 Colima-Jalisco earthquake, using a range of sedimentological, geochemical and microfossil techniques. The main objective is to develop a diatom-based quantitative approach to estimate the magnitude of coseismic deformation. This is the first study along the Mexican subduction zone, which focuses on quantifying coseismic deformation using intertidal sediments and fossil diatoms.

4.2. Features of the 1995 Colima-Jalisco Mw 8.0 earthquake.

The epicentre of the 1995 earthquake (18.864°N 104.579°W) was ~40 km south of the coastal city Manzanillo (**fig. 4.2**). The seismic slip propagated northwest for ~150 km, offshore of Chamela Bay (Abbott & Brudzinski, 2015; Hutton et al., 2001; Ortiz, Kostoglodov, et al., 2000). Most of the seismic slip was within the 18 km depth (Melbourne et al., 1997; Mendoza & Hartzell, 1995; Ortiz, Kostoglodov, et al., 2000). Based on the extension of this rupture, it overlaps the 1932-II M_w 7.8 earthquake rupture entirely and it overlaps only the southern half of the 1932-I M_w 8.2 earthquake rupture (see **fig. 4.1;** Azúa et al., 2002; Núñez-Cornú et al., 2016).

Coseismic slip distribution of the 1995 earthquake was not uniform (Melbourne et al., 1997; Mendoza & Hartzell, 1995; Ortiz, Kostoglodov, et al., 2000). According to rupture models, the slip concentrated in three regions (**fig. 4.2**): 1) near the epicentre, 2) offshore Barra de Navidad and 3) offshore Chamela Bay (Courboulex et al., 1997; Hutton et al., 2001; Masterlark et al., 2001). Near the epicentre, the maximum slip was 1-2 m, and it was mostly as shallow as 8 km depth (Melbourne et al., 1997; Mendoza & Hartzell, 1995). Offshore Chamela, the maximum slip was between 4 and 5 m, at depths up to 15 km (Hutton et al., 2001; Melbourne et al., 1997; Mendoza & Hartzell, 1995). These sites correspond to areas where spread the major asperities (Dominguez Rivas et al., 1997).

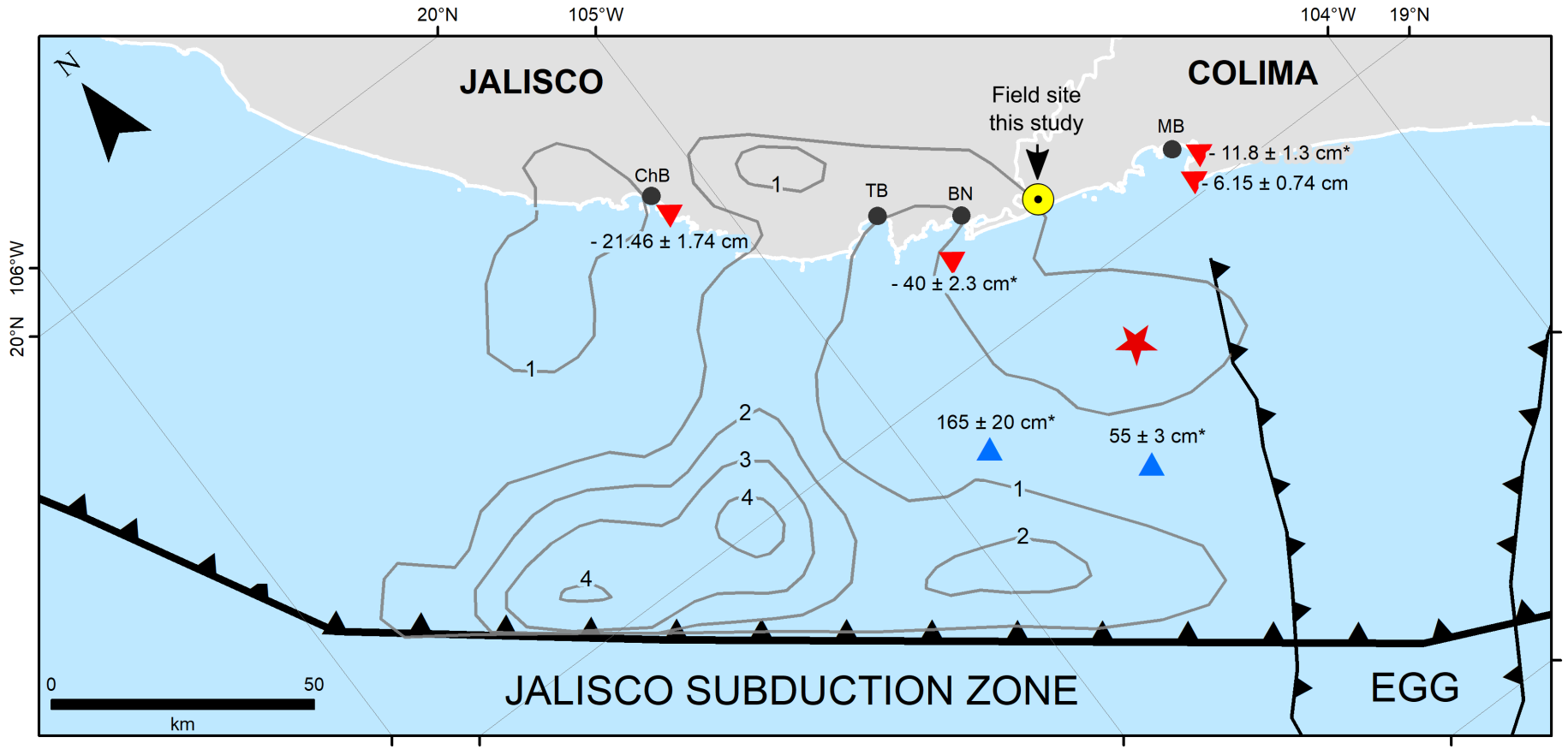

***Figure 4.2**. Map showing the features of the 1995 Mw 8.0 earthquake. The red star shows the epicentre of this earthquake. Grey contours indicate slip distribution and magnitude estimated through inversion of teleseismic data (Mendoza & Hartzell, 1995). Blue triangles show the site that recorded coseismic uplift. Inverted red triangles show the location of instruments that recorded coseismic subsidence. Coseismic deformation values with * were taken from Ortiz et al. (2000), the rest of the values from Hutton et al. (2001). Coastal towns: ChB = Chamela Bay; TB = Tenacatita Bay; BN: Barra de Navidad; MB: Manzanillo Bay.*

The magnitude of coseismic slip is spatially coincident with the magnitude of coseismic land-level changes. Geodetic instruments recorded widespread coastal subsidence along the rupture (**fig. 4.2**). Near the epicentre, in Manzanillo, GPS data recorded the smallest amount of coastal subsidence, 6.15 ± 0.74 cm (Hutton et al., 2001), whereas the maximum subsidence, 21.46 ±1.74 cm, was recorded at Chamela Bay (Hutton et al., 2001). Sea-level data from a tide gauge at Manzanillo Harbour also recorded coastal subsidence of 11.8 ± 1.3 cm (Ortiz, Kostoglodov, et al., 2000). Additionally, in the central part of the rupture area, a pressure gauge located ~7 km offshore Barra de Navidad recorded coseismic subsidence of 40 ± 2.3 cm (Ortiz, Kostoglodov, et al., 2000).

4.3. Results.

4.3.1. Lithostratigraphy

Eleven boreholes were manually drilled in an area adjacent to a SW-NE channel in the Marabasco River alluvial plain (**fig. 4.3**). The distance of the field site to the shoreline ranges from 1.3 to 2.2 km; and the distance to the mouth of the Marabasco river is 2.6 to 3.6 km. From all these cores analysed, only five sites show a coherence in the stratigraphy and sediment units were correlated successfully. The deposits are composed of a basal sand layer with rare fragments of angular and rounded gravel followed by a sequence of four stratigraphic couplets of organic-rich silt overlaid by grey lenses of silt. In this paper, the focus is on the shallowest couplet, which is expected to reflect the stratigraphic signature of the 1995 earthquake, which is the most recent seismic event of the region.

The shallowest couplet was mapped over ~1 km, in five boreholes (**fig. 4.3D**), parallel to the tidal creek. This couplet extends as far as 2 km inland, always in areas adjacent to the creek. In core MAR001 (19.158°N, 104.567°W), the shallowest contact is at 25 cm depth, consisting of a dark brown silty clay with humified organic matter overlaid abruptly by grey silt with spare roots. Approximately 380 m northeast, at MAR004 (19.159°N, 104.564°W), the same brown silt organic unit is overlaid abruptly at 23 cm depth by a grey mud lens. At MAR005 (19.160°N, -104.564°W), the stratigraphic boundary occurs at 28 cm, where silt abruptly replaces a horizontal bed of black organic silt with herbaceous remains. At MAR010 (19.163°N,104.560°W) and

MAR009 (19.163°N,104.56°W), this couplet is found at 21.5cm and 26 cm depth respectively, and it shows an underlying black organic silt bed overlaid abruptly by a grey bed of grey silt. The core retrieved for detailed analysis corresponds to the site MAR005 (Error! Reference source not found. **D**).

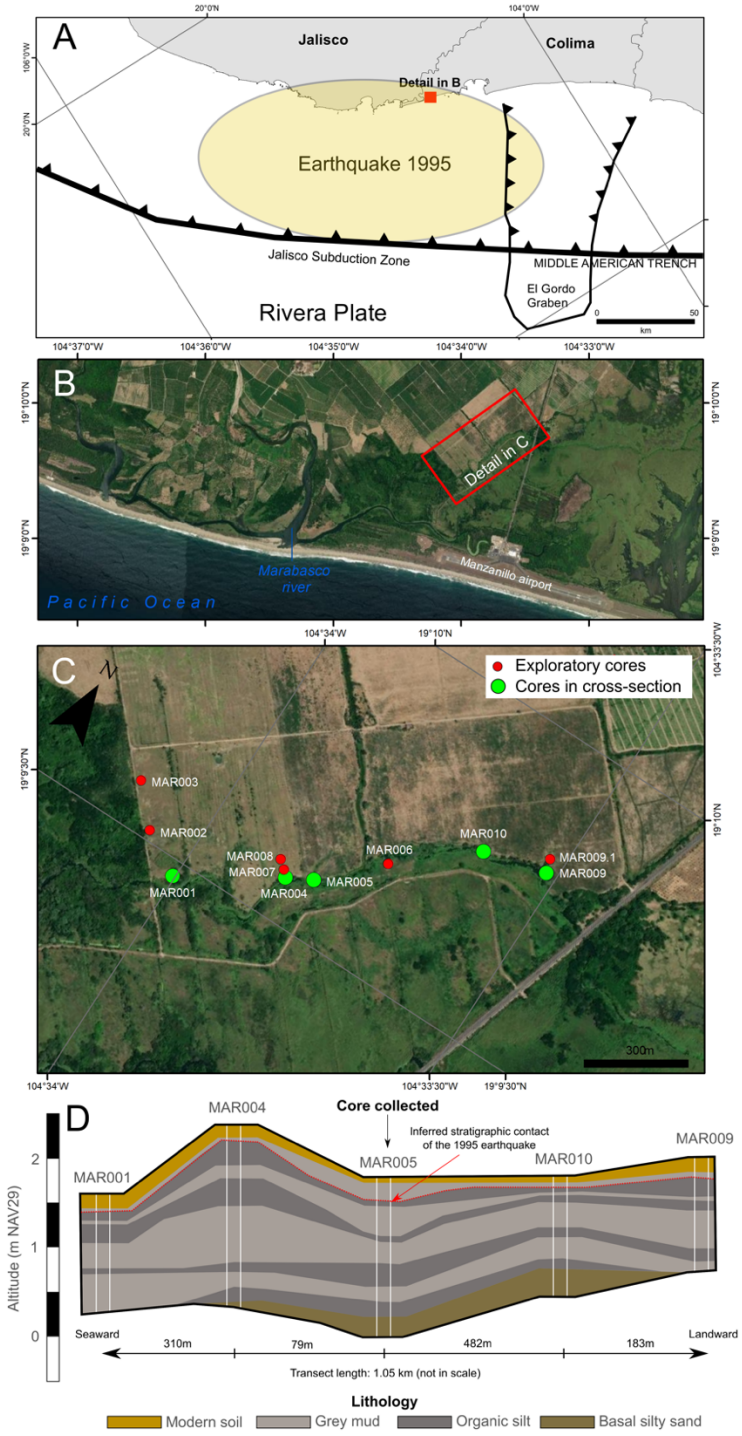

***Figure 4.3**. Summary of the stratigraphy of the coring sites sampled in 2018. (Source of base map, satellite image from ESRI [http://www.arcgis.com)](http://www.arcgis.com)*

4.3.2. Chronology

Downcore concentrations of ^{137}Cs, from 0 to 108 cm, fluctuate between 0 and 1.78 mBq g^{-1} (**fig. 4.4**). From 80 cm upwards in the core, concentrations exceed the detection limit (0.5 mBq g^{-1}), showing a first peak at 72 cm (1.58 ±1.22 mBq g^{-1}). The peak of concentrations centred at 68 cm (1.79 ± 0.99 mBq g^{-1}), above this depth concentrations decrease monotonously to the top of the core.

Based on this profile, the onset of ^{137}Cs cannot be established accurately because at 80 cm ^{137}Cs concentrations are above the detection limit but the lower limit of the uncertainty extends below this threshold. At 76 cm, the midpoint of ^{37}Cs and its uncertainties are well above the detection limit. However, the interval in sampling, 4 cm, increases the degree of error to identify the onset accurately (e.g. Zong et al. 2003). Hence, following Witter et al. (2019) sediments above 80 cm are considered to be deposited during 1950s.

Regarding the the fallout peak (1963 ± 1 AD), it was established at 68 cm depth, where the mid-point of concentrations and its uncertainties reach the highest concentrations, extending above the detection limit. The identification of the peak of ^{137}Cs concentrations, 1963 ± 1 AD, at 68 cm confirms the sallowest stratigraphic contact, at 20 cm in this core, was produced between 1963 and 2018.

To estimate the age of this contact, in OxCal the inputs to build the age-depth model include a *C_Date*(1963) at 68 cm, representing the year of maximum fallout, and a C_Date(2018) at 0 cm depth, representing the year of the land-surface at the time of sampling.

The output of the interpolation in OxCal (**fig. 4.4**) suggests a mean sedimentation rate of 1.23 ± 0.01 cm yr^{-1}. Within this depth range, no significant changes in sediment particle size occur, suggesting that this rate of sedimentation is constant. The estimated age, based on this age-depth model, is 1990 – 2001 AD (2 σ); with a mean age at 1995 ± 2 AD (1 σ).

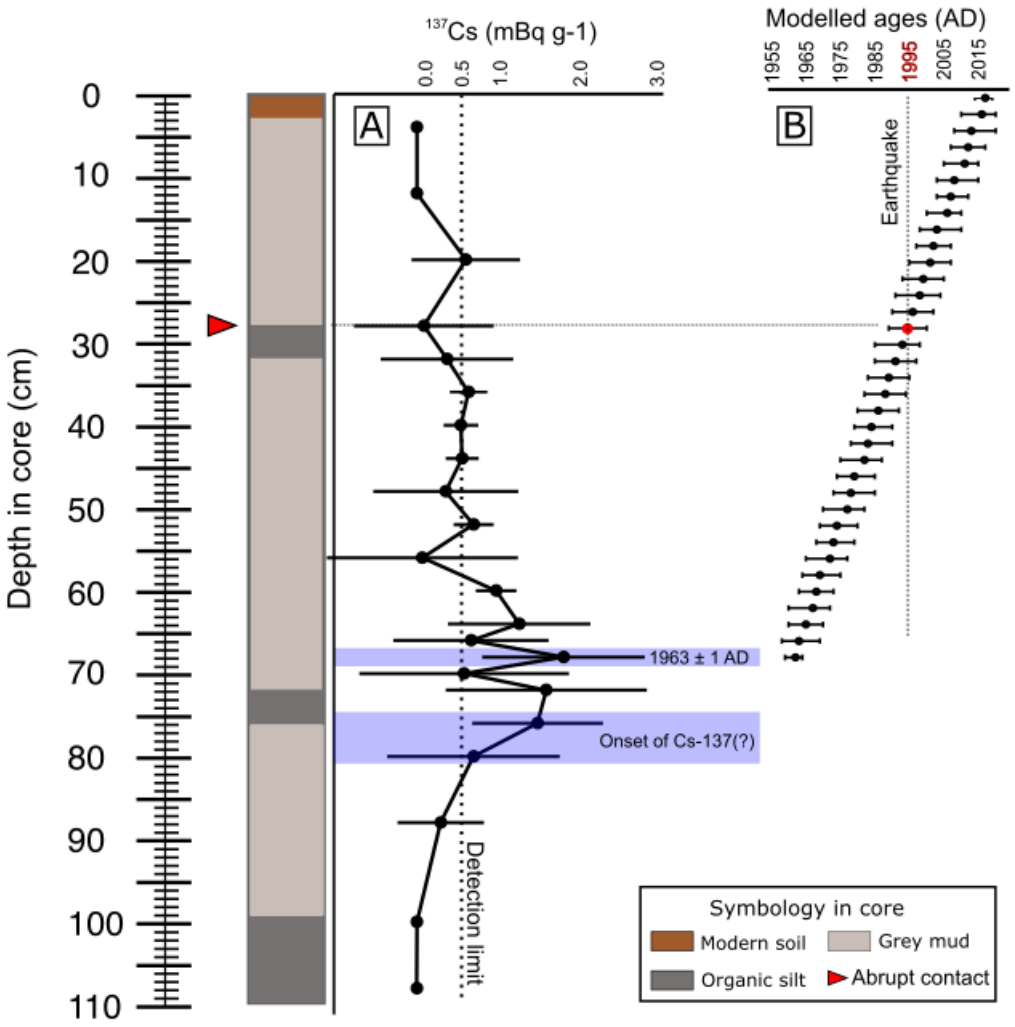

***Figure 4.4**. Chronological control of the 1995 earthquake. A) Downcore concentrations of 137Cs, showing the maximum concentration at 60 cm depth, here interpreted as the maximum fallout in 1963 AD. B) Age-depth model from OxCal interpolated at every 2 cm*

4.3.3. Core imaging and geochemistry.

The results from core MAR005 using non-destructive methods provide evidence of the abruptness and attributes of the shallowest couplet. In core MAR005, the stratigraphic contact is abrupt, and it is at 28 cm. Although, in this core section, the contact is slightly tilted, it shows its abruptness (**fig. 4.4**). Based on CT images, the underlying unit appears in dark tones in the black and white image (B&W) and blue-green tones in the coloured CT image. This underlying organic unit is ~5 cm thick. On the other hand, the overlying minerogenic unit, appears in light grey tones and yellow to red tones in CT images.

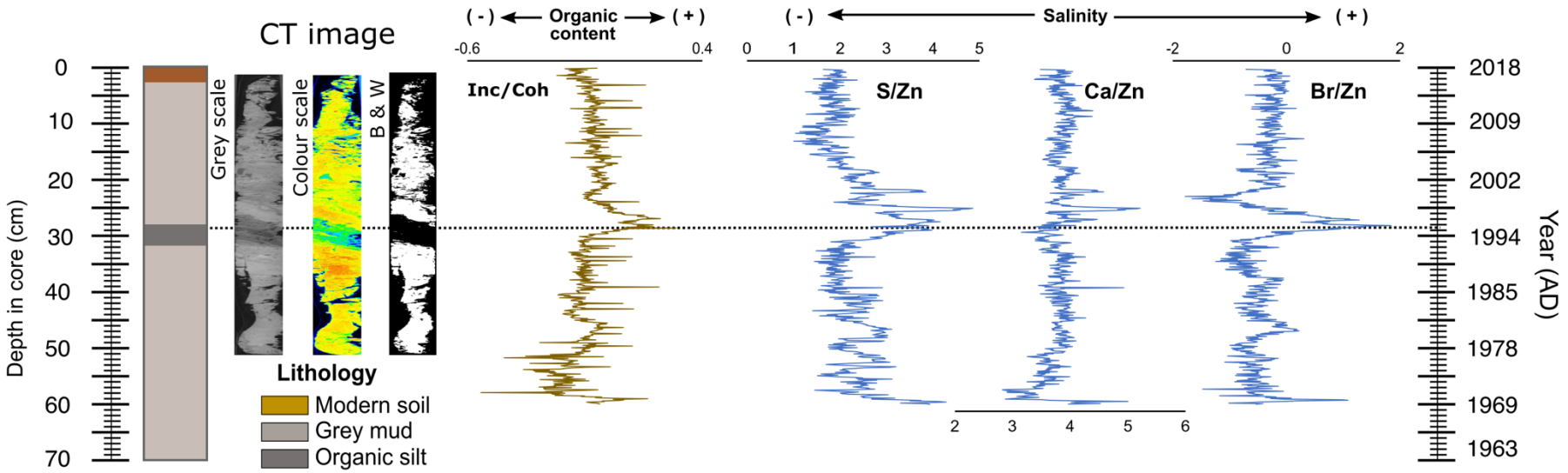

***Figure 4.5**. Core scanning imaging of core MAR005. The results of the Computer Tomography (CT) in grey scale, in false colour and black and white, as well as the four ratios built from the XRF data. Incoherence/Coherence (Inc/Coh) is the ratio that indicates changes in the content of organic matter, an increase of the ratio suggest increase of organic content, whereas a decrease of the ratio suggest a reduction of organic content. The ratios S/Zn, Ca/Zn and Br/Zn are the three ratios used to identify abrupt changes in salinity associated to an increase or decrease of marine waters in the wetland.*

The inc/coh ratio, as the organic content proxy, is relatively low and slightly below 0 from 60 to 30 cm. At 30 cm depth, the inc/coh ratio begins to increase gradually, reaching a maximum at 28 cm. Between 28 – 27 cm, this ratio shows a constant abrupt decrease, reaching the minimum value at 24 cm. From 24 cm to the top of the core, the inc/coh ratio shows a monotonous decrease.

Zn-normalized palaeosalinity ratios (S, Br, and Ca), from 50 cm upwards show a monotonous behaviour (**fig. 4.4**) without significant fluctuations (S/Zn from 1.4 to 31, Ca/Zn from 3.4 to 4.9, Br/Zn from -1.2 to 0.2). Around 30 cm, only S/Zn and Br/Zn ratios show a minimum increase, to reach a significant peak at 28 cm (S/Zn = 3.9, Br/Zn = 1.8). Even though, the ratio Ca/Zn shows a small change at 28 cm, upwards in the core, Ca/Zn shows a constant increase. Above 28 cm, these three ratios kept fluctuating within relatively high values in comparison to their background value ranges. It is at 24 cm depth, where the ratios decrease to values similar to those below the stratigraphic contact. From 24 cm to the top of the core, these ratios return to a monotonous behaviour.

4.3.4. Sediment Grain Size Analysis

Below the stratigraphic contact, variations in mean grain size do not show any significant sedimentological change (Error! Reference source not found.). From 70 to 29 cm depth sediments are classified as poorly sorted fine silt (mean 7.9 -6.3ϕ). The grain size distributions are unimodal. The percentage of sand content at these depths is very low (4 - 7%). At 28 cm depth, there is a slight but abrupt increase of sand content (26%). The grain size distribution of this sample moves towards the coarse fraction, as shown by the mean and deciles D10 and D90. The sample at 28 cm depth is classified as fine sand (mean = 5.77 ϕ), very poorly sorted and polymodal. This anomalous bed of coarse sediment is less than 0.5 cm thick, and it was not visible by eye or in the core images. Above 28 cm depth, the percentage of sand decreases abruptly (~0%) and sediments turn back to fine silt.

A biplot with the mean and sorting coefficient clearly shows the departure of the sample at 28 cm from the rest of the samples from the upper 70 cm of the core. Biplots allow to identify anomalous deposits, associated to unusual patterns of sedimentation (e.g. Hamilton et al., 2019; Lario et al., 2002; Tanner, 1991).

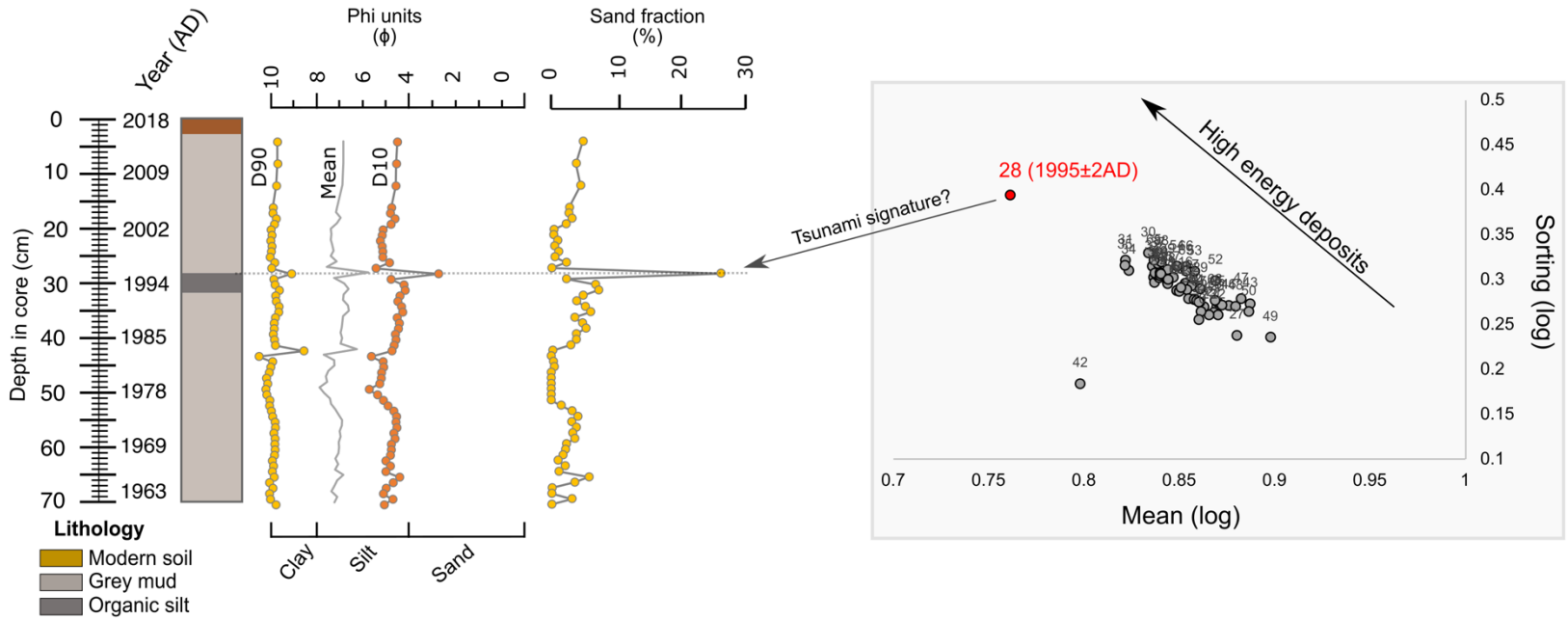

***Figure 4.6**. Downcore fluctuations of the mean and deciles D10 and D90 obtained from the particle size distributions (PSD) and the fractions (%) of sand. Panel on the right shows the biplot of the mean and sorting parameter.*

4.3.5. Model development for palaeoelevation calculation.

The simple linear regression models to obtain palaeoelevation show a negative relationship between the variable of brackish and marine diatom species and palaeoelevations SWLI unit. (**fig. 4.7**). This negative relationship responds to the SWLI values, as 100 SWLI represents Mean Tide Level (MTL), suggesting higher influence of marine conditions, and 200 SWLI represents Mean Higher High Water (MHHW), suggesting lower influence of marine conditions. Hereafter Model 1 (M1) corresponds to the Alaska dataset, and Model 2 (M2) to the Chile dataset.

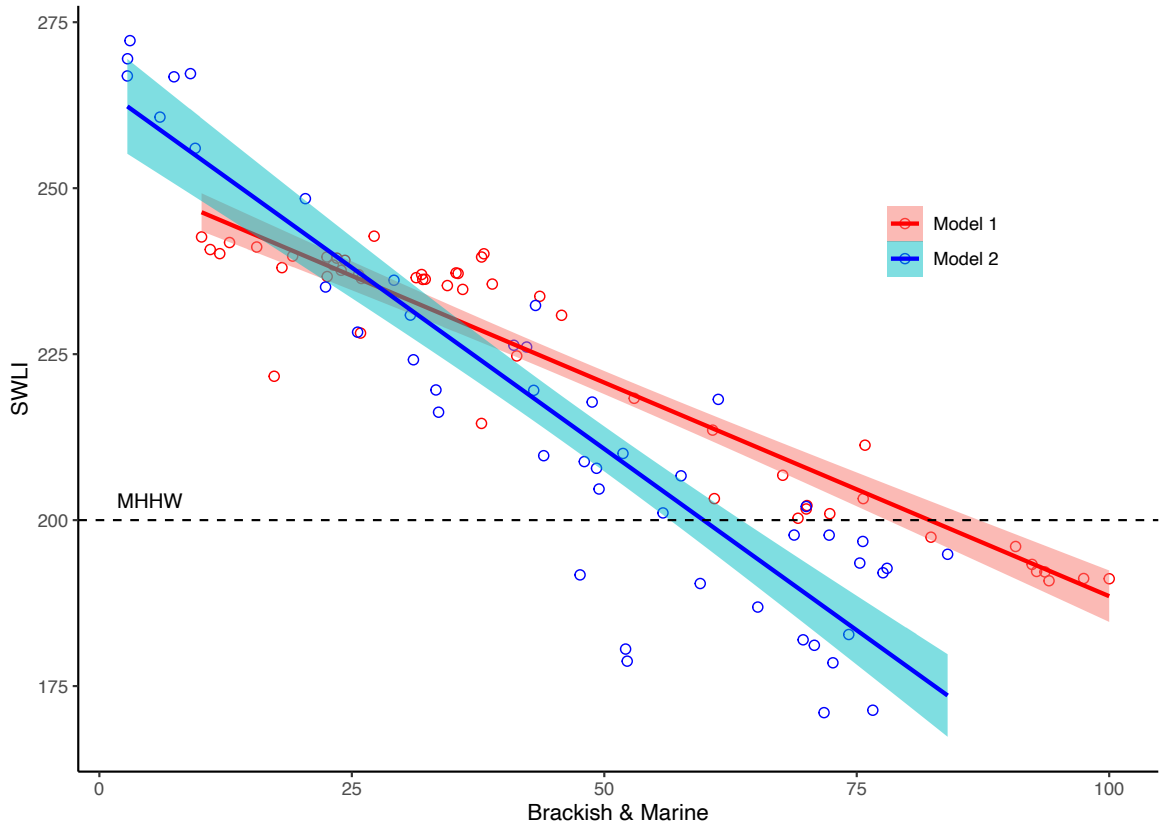

***Figure 4.7**. Linear regression models to estimate palaeoelevations. Red dots correspond to the dataset from Alaska (Shennan et al. 2016) and blue dots correspond to the dataset from Chile (Hocking et al., 2017). The red thick line corresponds to the linear regression model using the dataset from Alaska (M1). The Blue thick line corresponds to the linear regression model using the dataset from Chile (M2) The shadow bands, bracketing the linear models, represent the confidence interval of each linear regression model.*

The overall regression of both models is statistically significant (p-value < 0.05), showing good overall fit (R^2 > 0.8).

***Table 4. 1**. Parameters of the linear regression models.*

	R^2	α	*β*
Model 1	0.89	252.89	-0.64
Model 2	0.84	265.35	-1.09

Each observation downcore is referenced to meters either above or below the MHHW. Depending on their relative position, m MHHW, two intertidal zones were established (**table 4.2**) with their Reference Water Level and Indicative Range calculated, following Khan et al. (2017) .

***Table 4.2**. Indicative meaning established to estimate error terms of palaeoelevations.*

Intertidal zone	Reference Water Level (RWL)	Indicative range (IR)
Upper	(MHHW + EHW)/2 = 0.591 m	MHHW - EHW = 0.52 m
Lower	(MTL + MHHW)/2 = 0.169 m	MTL - MHHW = 0.33 m

The total elevation errors (ee) for each part of the intertidal zone, considering the error of the regression models (e1) and half their reference water level (e2) are summarized in **table 4.3.**

***Table 4.3**. Summary of total elevation error for each intertidal zone.*

	Intertidal zone	*e1*	*e2*	*ee*
Model 1	Upper	0.04 m	0.26 m	± 0.26 m
	Lower	0.04 m	0.17 m	± 0.17 m
Model 2	Upper	0.08 m	0.26 m	± 0.27 m
	Lower	0.09 m	0.17 m	± 0.18 m

4.3.6. Diatom analyses

A total of 183 diatom species were identified in samples analysed, with species accounting for >5% in at least 5 samples illustrated in **figure 4.8**. Diatom assemblages show a mix between freshwater, brackish and marine taxa. Below the 28 cm stratigraphic contact from 57 to 34 cm depth, freshwater diatoms dominate the

assemblages, reaching up to up to 90% of the assemblages. The dominant species are *Luticola mutica* (> 30%) and *Diadesmis confervaceae* (> 50%). Palaeoelevation reconstructions, based on models 1 and 2 indicate that the site reached a maximum elevation ~0.2 m above MHHW in this lower section of the core.

Within the 3 cm below the stratigraphic contact (29 - 32 cm), there is an increase of *Halamphora submontana* (5 – 17%). Within this depth range, diatom assemblages suggest an upper intertidal paleoenvironment immediately before the 1995 event. The elevation below the contact is 0.12 ± 0.26m MHHW, predicted by Model 1, and 0.12 ± 0. 27 m MHHW predicted by Model 2.

At 28 cm depth, there is a spike of *C. meneghiniana* (> 15%), which is concurrent with the spike of sand fraction, S/Zn and Br/Zn. Above the 28 cm contact, diatoms show an abrupt increase in marine and brackish species. The sum of these two classes reach up to 50% of the total assemblage. Palaeoelevation models 1 and 2 show a drop in the land level, Model 1 indicating a ground level altitude of +0.07±0. 26 m MHHW and Model 2, +0.03 ±0. 27 m MHHW. Hence, these reconstructions suggest land-level change of -0.06 ± 0. 26 m (model 1) and -0.11 ± 0. 27 m (model 2), and an abrupt change from the upper to the lower intertidal zones, where the marine species *Nitzschia grossestriata* (18%) and *Paralia sulcata* (11%) are the dominant.

Four centimetres above the stratigraphic contact, from 24 cm depth to the top of the core, diatoms show a shift to freshwater dominated assemblage (> 70%). The species *N. fonticola, G. affine and H. submontana* illustrate this transition. Although, *H. submontana* is the species that dominate the sediments to the top of the core.

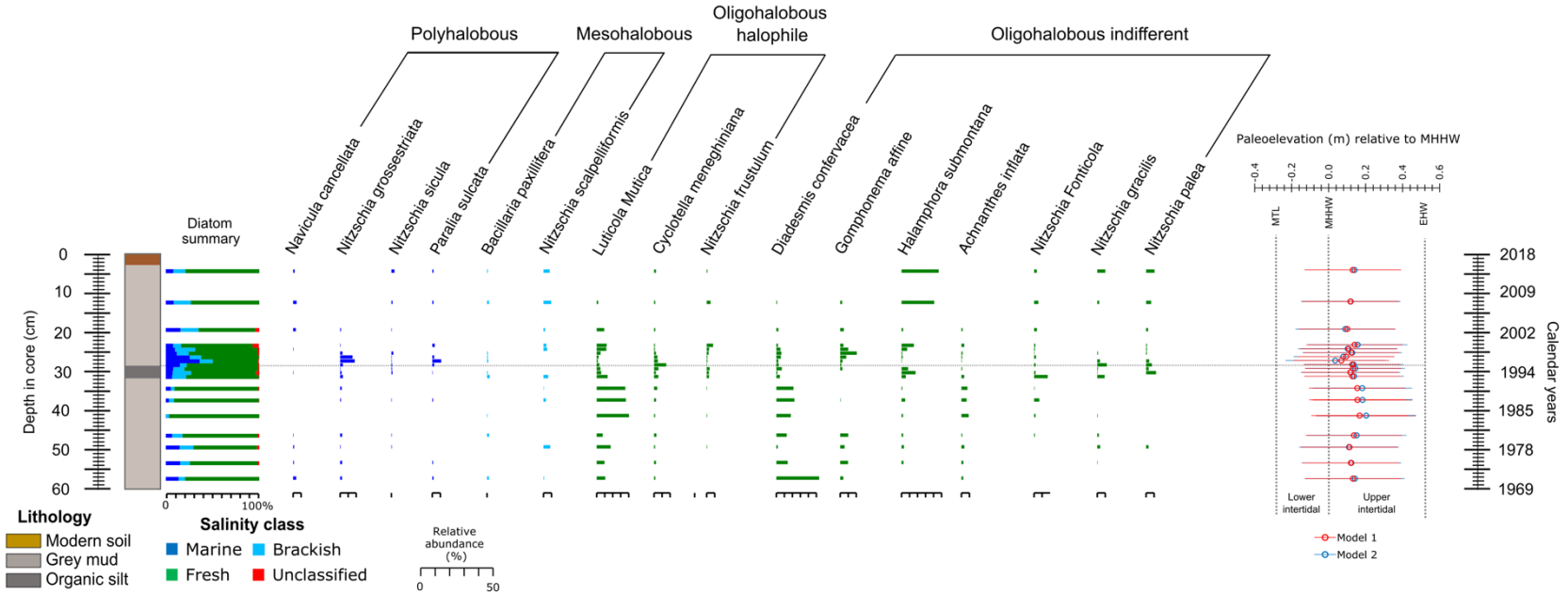

Figure 4.8. *Biostratigraphy and palaeoelevations of the top 60 cm of the core MAR005. Diatom species here shown correspond to species > 5%, which appear in more than 5 samples. The classification of species is based on the halobian classification, whereas the summary classifies all the species between marine, brackish, and freshwater species. The panel on the end right shows palaeoelevation changes across the contact obtained from the linear models.*

4.4. Discussion

The coast of Jalisco and Colima was struck in 1995 by a M_w 8.0 earthquake produced by a ~150 km rupture along the Jalisco subduction zone. Geodetic records demonstrate that the coast adjacent to the earthquake rupture experienced subsidence, 0.06 - 0.2 m (Hutton et al., 2001; Melbourne et al., 1997; Ortiz, Kostoglodov, et al., 2000). Within the region of subsidence lies the coastal wetland Estero Potrero Grande, whose stratigraphy was investigated in 2018 to find evidence of coastal subsidence during the 1995 earthquake.

The stratigraphy beneath this wetland shows a sequence of four minerogenic beds abruptly overlying organic sediments, which resemble the sedimentary signature of coastal subsidence produced by great megathrust earthquakes (e.g. Atwater, 1987; Dura et al., 2011; Nelson et al., 1996; Shennan et al., 1998). Due to the 1995 earthquake was the latest great megathrust earthquake that hit this coast, the shallowest organic-minerogenic couplet might be the signature of this event. Hence, this discussion focuses on the sedimentological properties of this contact to confirm its coseismic origin.

The first step consisted of finding the stratigraphic position of 1995 AD in the core MAR005, using downcore concentrations of the radioisotope ^{137}Cs. At 68 cm depth, the downcore profile of ^{137}Cs shows its maximum activity. According to studies of ^{137}Cs concentrations in wetland sediments across the North American region, the maximum activity of ^{137}Cs in sediments represents the year of maximum fallout, 1963 AD (Corbett & Walsh, 2015; Drexler et al., 2018). The position of this chronohorizon indicates that those sediments above it deposited during the last 55 years, resulting in a sedimentation rate of 1.23 ± 0.01 cm yr^{-1}. This rate of sedimentation is more than four times higher than the sedimentation rate in coastal lagoons along the Mexican Pacific (Ruiz-Fernández & Hillaire-Marcel, 2009), and it is comparable with those settings highly influenced by fluvial discharges (e.g. Ruiz-Fernández et al., 2002). Assuming this relatively high rate of sedimentation, the shallowest stratigraphic couplet at 28 cm depth was dated within the range 1990 – 2001 AD (2σ). This age range not only brackets the year of the earthquake in 1995, but the interpolated mean age is 1995 ± 2 AD (1σ), based on the age-depth model.

In order to confirm the coseismic origin of this stratigraphic couplet, the criteria proposed by Nelson et al. (1996) and Shennan et al. (2016) serves as the guide. The criteria to fulfil in this study includes: 1) lateral extent of organic-mud couplets, 2) abruptness of submergence across the couplets, 3) amount of submergence and 4) tsunami evidence.

Field data provides evidence to determine the lateral extent of this contact. Considering the distinctive characteristics of the lithofacies bracketing the contact, their depths and stratigraphic position, it was possible to correlate the stratigraphic contact along the coring transect (e.g. Nelson et al., 1998). The underlying unit is similar in all cores, being a highly humidified organic silty unit with fragments of plants. This organic bed is relatively thin, ~ 5 cm thick, in all cores. This underlying unit was clearly differentiated from its overlying sediments, due to the abrupt reduction of organic content, and turning into a grey silty layer. Regarding the depths and stratigraphic position of this contact, it is constrained within 21 - 28 cm depth for along 1 km, being the shallowest contact below the modern land surface. It means that the contact corresponds to the latest great event that produced this stratigraphic signature.

The second criterion, suddenness of submergence, was fulfil using CT scanning image, geochemical composition, and diatom assemblages. CT scanning images reveal the abrupt transition from organic to silt sediments. Even though, the contact is tilted in core MAR005, the abruptness of change is evident. Following the classification of stratigraphic contacts in palaeoseismic studies, either sharp (10 mm) or abrupt (1 mm; Nelson et al. 2008), this stratigraphic contact would fall within the category of abrupt.

Relative concentrations of the elements Ca, S and Br aid to reveal submergence. The relative and absolute high concentrations of these elements is indicate of marine incursions in coastal wetlands, associated to either gradual (e.g. Figueroa-Rangel et al., 2016), or abrupt sea-level changes caused by hurricanes (e.g. Bianchette et al., 2016, 2017), earthquakes and tsunamis (e.g. Ramirez-Herrera et al., 2007; Ramírez-Herrera et al., 2012, 2014). The log-ratios S/Zn, Ca/Zn and Br/Zn show an abrupt increase above the stratigraphic contact, with high values within the overlying grey silty unit. This increase indicates the high influence of marine conditions, what confirms the abrupt submergence of the land.

Another line of evidence of abrupt submergence corresponds to diatom assemblages. As mentioned before, the species *L. mutica, D. confervaceae* and H. submontana dominate the assemblages preceding the stratigraphic contact. The epipelic species *L. mutica* is commonly found in upper intertidal zones along the Pacific coast of North America (e.g. Hong et al., 2021; Sawai et al., 2016a). *D. confervaceae* is a benthic freshwater species commonly found in shallow lentic freshwater systems (Jaramillo et al., 2021; Lezilda Carvalho Torgan & Cristiane Bahi Dos Santos, 2008; Szabó et al., 2004; Vélez et al., 2006). Lastly, H. submontana dominates in fluvially dominated environments (Cocquyt et al., 2019; Compère, 1984; Qingmin et al., 2015). These species suggest that land-level below the stratigraphic contact was likely in the upper intertidal zone, > MHHW.

Above the stratigraphic contact, the abrupt increase of marine diatoms, including the species N. *grossestriata* and *P. sulcata*, confirm submergence. *N. grossestriata* is a dominant species in fringing mangroves and shallow subtidal environments across Mexican coastal wetlands (e.g. Martínez-López, 2004; Siqueiros-Beltrones et al., 2017). On the other hand, P. *sulcata* is a planktonic marine species (McQuoid & Hobson, 1998; McQuoid & Nordberg, 2003; Vos & de Wolf, 1993; Zong, 1997), interpreted as an indicator of shallow brackish-marine estuarine conditions (Chagué-Goff et al., 2002). *P. sulcata* has also been associated to events of shoreline retreat (McQuoid & Hobson, 1998; McQuoid & Nordberg, 2003). This rapid increase of these species implies an abrupt land-level change, associated to coastal subsidence.

The third criterion corresponds to the amount of submergence. According to the qualitative characteristics of diatom species, the coast could transition from the upper intertidal zone (>MHHW) to the lower intertidal zone (<MHHW). Diatom-based palaeoelevations suggest a land-level change of -6.38 ± 26 cm and -11.0 ± 27 cm. Taking into considerations the magnitude of subsidence recorded by GPS stations adjacent to this study's field site, there is an agreement between the diatom-based subsidence here reported, and the magnitude of subsidence recoded by GPS devices deployed along the coast. In Manzanillo, ~ 30 km south from this study site, the magnitude of subsidence was 6.15 ± 0.74 cm (Hutton et al., 2001). Whereas at Chamela Bay, ~70 km northwards from this study field site, GPS data recorded subsidence of 21.46 ± 1.74 cm. (Hutton et al., 2001).

The spatial pattern of subsidence along the coast parallel to the rupture shows an increase from south to north, (**fig. 4.9**). According to rupture models, this pattern of deformation is driven by the distribution of coseismic slip along-strike. The minimum amount of coseismic slip, ~ 1m, is near the epicentre, located offshore the Manzanillo Bay (**fig. 4.9**). On the other hand, the maximum amount of coseismic slip on the fault plane is offshore the Chamela bay, ~ 4 m. Offshore the Estero Potrero Grande, the magnitude of coseismic slip was 2 m. Hence the diatom-based magnitude of subsidence here estimated seems to be spatially coherent and according to the amount of coseismic slip occurred near this study's field site.

Years after coseismic subsidence, the diatomological record shows a rapid return to freshwater conditions. Palaeoelevation models show that by 1999 ± 1 AD (1 σ), land-level was near its pre-earthquake position. This relatively rapid recovery of land-level can be explained by the combination of post-seismic land-level change and local sedimentation. Geodetic observations demonstrate that some years after the earthquake the coast adjacent to the 1995 earthquake's rupture, reversed the pattern of coseismic deformation and the coast experienced uplift due to those processes associated to the post-seismic stage (Hutton et al., 2001). In addition to coastal uplift, the relatively high rate of sedimentations could contribute to infilling the accommodation space, allowing the land surface to emerge quickly and transitions to a freshwater environment again.

The last criterion to fulfil corresponds to tsunami evidence accompanying subsidence. Sandy deposits are commonly the key sedimentary evidence to identify the occurrence of past tsunamis. In the wetland Estero Potrero Grande, when undertaking field sampling along the coring transect, there was not visible evidence of sandy deposition. However, laboratory results from sediment grain size analysis and geochemistry show a thin (<1 cm) sandy lamina at the stratigraphic contact accompanied by an abrupt increase of salinity conditions (**fig. 4.9**). However, diatom assemblages do not show an evident increase of neither brackish nor marine species accompanying this deposit.

If this sand deposit is the signature of the tsunami accompanying the 1995 earthquake, its thickness is likely to be product of the height of the tsunami run-up, the local geomorphology, and the distance of the coring sites from the shoreline. The tsunami run-up at this site, was documented to be ~4 m (Borerro et al., 1997). Due to higher

elevations of the frontal chain of dunes, >5 m, field evidence indicate that this tsunami only flooded the beach fronting the sandy barrier, without evidence of beach barrier overtopping (Borerro et al., 1997). Hence, the tsunami probably penetrated the back-barrier wetland through low-lying areas, such as the mouth's river and other inlets. Numerical models indicate that tsunami waves, ~5 m, can penetrate as far as at 1 km inland in similar settings along the Mexican Pacific coast (e.g. Corona & Ramírez-Herrera, 2012; Farreras et al., 2007; Sanchez & Farreras, 1987). If the 1995 tsunami reached the coring site, 1 – 2 km from the shoreline, the complex network of creek channels, naturally makes it to lose its energy, reducing its capacity to pick up coarse sediments while the wave was moving inland. Hence, this thin deposit might indicate the landward limit of tsunami deposition, only identified in adjacent areas to the channels. Deposits of similar thickness also occurred in the landward limit of tsunami deposits, where sandy beds can be as thin as < 1 cm thick (e.g. Chagué-Goff et al., 2015b; DePaolis et al., 2021; Garrett et al., 2013; Moore et al., 2006; Paris et al., 2007; Takashimizu et al., 2012).

Because this deposit is associated to a marine incursion, as palaeosalinity ratios demonstrate, and considering its synchroneity with abrupt subsidence around 1995 AD, the tsunami accompanying this great earthquake was most likely the event that deposited these sandy sediments. However, more sedimentary evidence need to be collected in other sites across this wetland to corroborate this hypothesis.

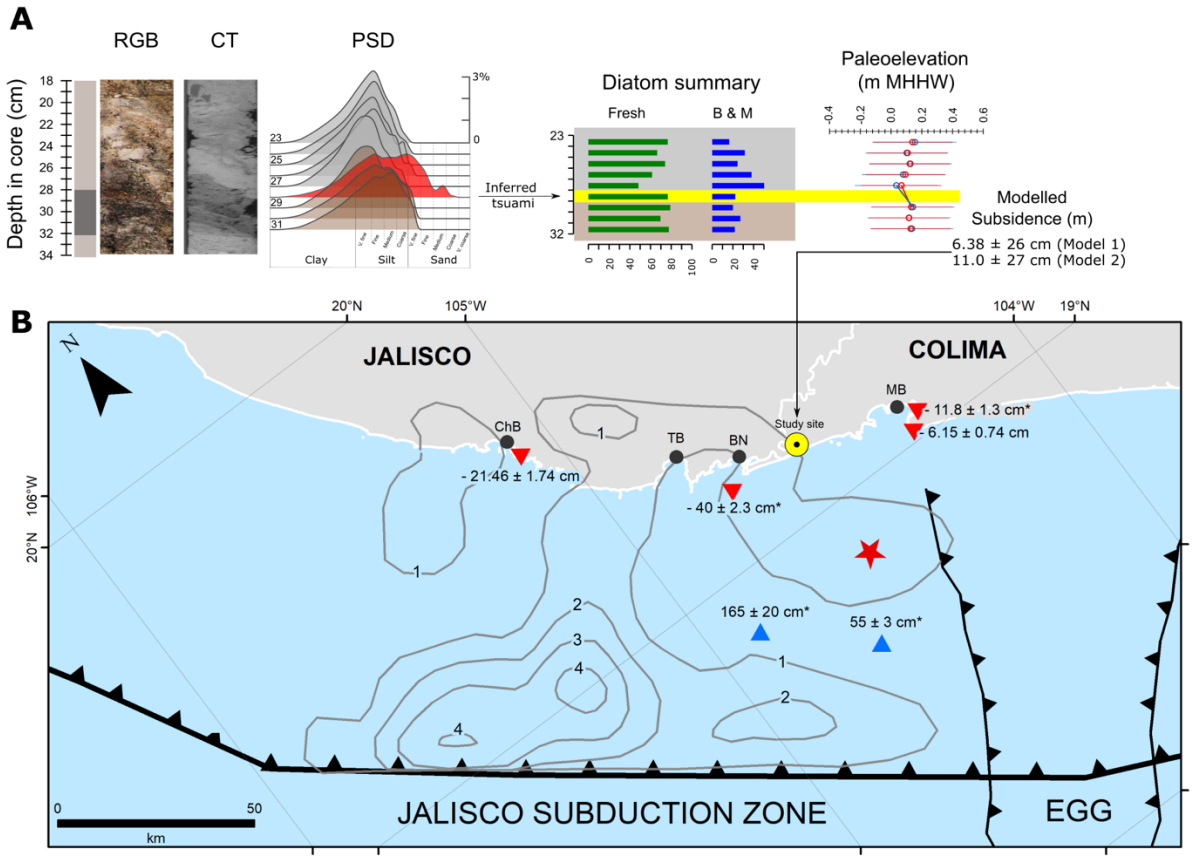

Figure 4.9. *Summary of the stratigraphic evidence of the 1995 Mw 8.0 earthquake.* ***A)*** *Showing the results of the laboratory procedures. From left to right is: the high resolution photograph in colour (RGB); the image in grey scale of the computed tomography (CT) scanning; the particle size distributions (PSD) bracketing the stratigraphic contact; the summary of diatoms; and lastly palaeoelevation changes across the stratigraphic contact followed by the amount of coseismic deformation.* ***B)*** *Spatial distribution of coseismic deformation. Green circle shows the location and amount of coastal subsidence obtained in this study. In order to cross-compare my estimations with the instrumental records, the units here used are in centimetres (cm). Red circles show areas that recorded subsidence, and blue circles represent those areas that recorded coseismic uplift. Simple values of coseismic deformation were obtained from Hutton et al. (2001), *** obtained from Ortiz et al. (2000).*

4.4.1. Alternative mechanisms of creation

Clastic-rich sediments overlying abruptly organogenic sediments can result of other hydro/morphodynamic processes. Changes in the tide levels induced by storms and morphological alterations of inlets or river mouths can deposit fine to coarse marine and coastal sediments to the lower reaches of estuaries (Goslin & Clemmensen, 2017; Nelson et al., 1998; Otvos, 2011; Peterson & Darienzo, 1991b). In addition to the 1995 earthquake, between 1990 – 2001 AD, two major hydrometeorological events possibly produced the stratigraphic sequence here analysed. These two events occurred in 1992, Hurricane Winifred, and 1993, Hurricane Calvin.

Hurricane Winifred made landfall as a category 2 in Manzanillo, roughly 30 km south from Estero Potrero Grande. Before hitting the coast, this event reached a maximum category of 3, offshore the coast of Michoacán, producing winds up to 185 km/hr (NHC, 1992). Most of the damages concentrated around the borders of the Colima and Michoacán states, ~100 km south from the study site (NHC, 1992). On the other hand, Hurricane Calvin reached a maximum category of 2, making landfall ~ 50 km northwest from the study field site (NHC, 1993). The wind speed reached up to 175 km/h, producing water levels up to 4.8 m, as combination of waves and storm surge (NHC, 1993). Damages concentrated mainly in the low-lying areas southwards the coast of Manzanillo (NHC, 1993). Near Estero Potrero Grande, official reports do not mention significant damages (Hernández et al., 2013).

Considering the similarities of these two hurricanes, storm-induced water levels were most likely <5 m. During events of this magnitude, wave overtopping, and coastal breaching is unlikely to occur at this site because the heights of frontal dunes are higher than 5 m amsl. Geospatial datasets (Landsat-5 images courtesy of the U.S. Geological survey) do not show evidence of coastal breaching after the occurrence of such events. Nonetheless, the mouth of the Marabasco river is the only landform along the coastal barrier showing evidence of breaching. This suggests that inland penetration of marine waters and sediments could occur throughout the river's mouth.

Only during storms and hurricanes, the mouth of the Marabasco river is breached as consequence of high-water levels produced primarily by fluvial discharges. These high water levels are consequence of cumulative precipitation within the catchment, which accumulates and drains before the arrival of a storm or hurricane to the coast (e.g. Elwany et al., 1998; McSweeney et al., 2017). Ah this stage, fluvial outflow becomes the dominant hydrological flux, followed by storm surges and storm waves, (e.g. Rich & Keller, 2013). This hydrological behaviour reduces the capacity of waves and storm surges to transport and deposit sediments far inland throughout the river's mouth. Considering the distance of the coring sites to the river's mouth, > 2.5 km, deposition of marine sediments is unlikely to occur during this type of meteorological events, considering the complex geometry of creek channels cutting the wetland.

If these two hurricanes produced significant morphological changes in the river's mouth, the wetland Estero Potrero Grande could have experienced an amplification of

tides and an increase of marine and brackish sedimentation. However, in wave-dominated coasts, breached barriers are short-lived due to the lack of sustained inlet flows (Rich & Keller, 2013; Seminack & McBride, 2018). Some days to weeks after great storms or hurricanes, the mouth of the Marabasco river is frequently blocked as consequence of the strong longshore drift, which begins to gradually build a bar due to the exceedance of sediments delivered by fluvial activity. Diatomological and geochemical evidence show a long-lasting environmental change, which might not reflect a temporary marine incursion. In conclusion, the data here shown using the criteria to identify earthquakes in the sedimentary record take us to conclude that the origin of this stratigraphic contact was most likely the earthquake and tsunami in 1995 AD.

4.4.2. The signature of the 1995 M_w 8.0 earthquake as a modern analogue.

The occurrence of the 1995 earthquake offered the unique opportunity to investigate its sedimentary fingerprint and constrain it with instrumental and historical records. This evidence serves as the modern analogue of this subduction segment to better understand and identify past earthquakes.

4.4.2.1. Coseismic subsidence preserved in tropical saltmarshes.

The first research objective of this chapter was to identify a tidal wetland adjacent to the 1995 earthquake rupture that experienced significant coseismic subsidence to investigate the sedimentary record of this event. Understanding the spatial features of this earthquake rupture and the coastal process and systems allowed to tackle the first objective.

The model of the spatial distribution of coseismic slip along-strike (**see fig. 4.9**) shows a heterogeneous rupture of the 1995 earthquake, showing three large asperities offshore the Manzanillo Bay, Barra de Navidad lagoon and Chamela Bay, which experienced coseismic slip of 1, 2 and 4 m, respectively (Mendoza & Hartzell, 1995). GPS receivers show evidence of coastal subsidence from Manzanillo Bay and Chamela Bay, 6.15 ± 0.74 cm and 21.46 ± 1.74 cm respectively (Hutton et al., 2001; Melbourne et al., 1997).The spatial distribution of coseismic slip allowed to investigate

the geomorphology of this coastal stretch to identify wetlands that could record coseismic subsidence.

Along this coastal segment, from Manzanillo to Chamela, the coast is predominantly rocky, with high cliffs intercalated with pocket beaches (e.g. Méndez Linares et al., 2007; Ramirez-Herrera & Urrutia-Fucugauchi, 1999). Coastal wetlands, which were the main target in this investigation, are scarce and sheltered by coastal barriers. Most of these wetlands receive little or no influence of tides due to the absence of estuaries and inlets. However, in the central portion of the rupture lies the Estero Potrero grande, which is one of the few wetlands along the coast of Jalisco, tidally influenced, as it is adjacent to the Marabasco river estuary. Estero Potrero Grande is adjacent to the asperity offshore Barra de Navidad and it is a large wetland dominated by tropical saltmarshes, which occupies the upper portions of the tidal zone, interacting with mangrove ecosystems (e.g. Méndez Linares et al., 2007).

Field evidence demonstrated that this wetland is highly sensitive to record small changes in tide levels, ~0.1m, as subsidence was clearly expressed in the stratigraphy over a 1 km transect. But it also demonstrated to be sheltered by the sand barrier to avoid the signature of storms and minor hurricanes. The sensitivity of this wetland to record small land-level changes is likely product of its microtidal conditions, which favour the establishment of subtidal environments at narrow elevation ranges that can respond more dramatically to subtle changes in tide levels (Barlow et al., 2013).

4.4.2.2. The physical and chemical expression of subsidence in a tropical saltmarsh

The second objective of this research was to characterise the physical and chemical composition of the sediments that indicate this coseismic subsidence. Evidence of coseismic subsidence in temperate wetlands consists of peat soils overlaid abruptly by mud. In Estero Potrero Grande, evidence of subsidence consists of a thin black layer of organic silt overlaid abruptly by mud. The organic unit differs largely from the typical peat soils due to the hydrological conditions controlled by the regional climate. Estero Potrero Grande undergoes intense dry conditions during half of the year, favouring the fluctuations of groundwater and evaporation of ponding water, causing dissection (Edwards, 1978; Ontiveros-Cuadras et al., 2021; Páez et al., 2022; Yáñez-

Arancibia et al., 2014). Consequently, organic matter decays faster than sites permanently waterlogged. However, the preservation of subsidence imprinted in the lithostratigraphy is well preserved due to the high rate of sedimentation, which increases coastal aggradation and estuary infilling (e.g. Méndez Linares et al., 2007).

Considering that freshwater conditions predominantly influence this wetland, Zn-normalized elemental ratios (S, Br and Ca) favour identifying palaeosalinity changes. Geochemistry data revealed the abrupt increase of marine conditions above the stratigraphic contact produced by the 1995 earthquake. These three independent proxies reinforce the utility of XRF-based palaeosalinity indicators in palaeoseismic investigations along the Mexican Pacific coast (Figueroa-Rangel et al., 2016; Ramírez-Herrera et al., 2009, 2012, 2014).

Sediment grain size revealed the occurrence of a thin layer of coarse sediments with a relatively high percentage of sand (~30%), which is attributed to the tsunami that accompanied the 1995 earthquake. Due to the thickness of this deposit, < 0.5 cm, this invisible layer of coarse sediments was not identified in the coring transect. The sampling strategy of sediment grain size analysis in this study, at every 1 cm, demonstrates the importance of the sampling resolution to reveal imperceptible patterns of sedimentation.

4.4.2.3. Testing the diatom-based method to quantify coseismic subsidence

The last objective of this research was to develop a diatom-based method to quantify coseismic subsidence caused by the 1995 earthquake. This investigation demonstrated the advantage of using sediments from the wetland Estero Potrero Grande to the reconstruction of land-level changes, as they preserve well fossil diatoms. Previous studies of megathrust earthquakes along the Mexican Subduction Zone have noticed the poor preservation of microfossils in coastal deposits, including mangrove areas, motivating the use of alternative proxies (e.g. Ramírez-Herrera et al., 2016; Ramírez-Herrera et al., 2012, 2014).

Diatom assemblages demonstrated their sensitivity to record coastal subsidence. The magnitude of subsidence obtained based on the method here developed proved to be spatially congruent with observations obtained from GPS receivers. The magnitude of

subsidence based on Model 1 and Model 2 corresponds to 9% and 11% of the great diurnal tidal range (MHHW - MLLW) respectively. This value is similar to what Shennan et al. (2016) established for Alaska wetlands as the minimum threshold to discriminate land-level changes caused by megathrust earthquakes. However, it is important to consider that these values might vary because the tidal datums to estimate the great diurnal range correspond to the tide gauge at Manzanillo Bay, which is ~30 km southeast from this study site.

These tidal datums also control the error terms, which are higher than subsidence values. The large errors (0.26 – 0.27 m) are controlled by the decision to use the Extreme High-Water datum as the upper limit for the indicative range of the upper intertidal zone. This datum is highly influenced by non-tidal extreme water levels recorded by the Manzanillo tide gauge, which might be associated to ocean and hydrometeorological events. Even though, for locations with low land-level changes, the error terms of reconstructed elevations are expected to be larger than the modelled subsidence (Brader et al. 2021), constraining better the indicative ranges at a local scale would permit to reduce these error terms in future palaeoseismological investigations.

An alternative approach to estimate palaeoelevations in this study considered to use of the transfer functions built by Shennan et al. (2016) in Alaska and Hocking et al. (2017) in Chile. Nonetheless, as diatom-based transfer functions use species assemblages in relation to the elevations, the use of a transfer function built with diatoms from temperate environments might produce poor modern analogues to estimate palaeoelevations using diatom assemblages from tropical environments. Considering that local factors exert a control on diversity and distribution of diatoms species, large discrepancies may exist between diatoms in temperate and tropical regions (e.g. Soininen & Teittinen, 2019). For example, the marine species N. grossestriata is abundant in the Mexican Pacific and in this study, N. grossestriata was the indicative species of coastal subsidence during the 1995 earthquake. Nonetheless, the datasets of Alaska and Chile do not contain this species. Hence, the adoption of a diatom-based transfer function from temperate coastal wetlands remains unsuitable in a tropical context. The approach adopted here should not necessarily substitute the

development of locally based transfer functions and future investigations need to test these results.

4.5. Conclusions.

The 1995 M_w 8.0 Colima-Jalisco earthquake produced widespread subsidence along the coast adjacent to this earthquake rupture. Within this area lies the coastal wetland Estero Potrero Grande, whose sediments beneath show evidence of abrupt environmental changes caused by coastal coseismic subsidence. Within the upper 30 cm depth, there is an abrupt sedimentary change of an organic-rich layer of sediment that is overlaid abruptly by grey silt for along ~1 km, in an area adjacent to a creek channel that connects the wetland with the mouth of the Marabasco river.

Using ^{137}Cs profiling to build a Bayesian age-depth model, the age of this stratigraphic contact (event) was dated 1990 – 2001AD (2σ); with a mean age 1995 ± 2AD (1σ). Sediment geochemistry, using the log-ratios Ca/Zn, S/Zn and Br/Zn, demonstrate an abrupt increase of salinity conditions above the contact. Diatom assemblages confirm that such increase of salinity conditions represent an abrupt transition from a freshwater to a marine/brackish environment, most likely produced by coastal subsidence. Using a diatom-based quantitative approach to identify the magnitude of subsidence, this coast experienced a land-level change of -6.38 ± 26 cm and -11.0 ± 27 cm. The magnitude of this land-level change is congruent with geodetic instrumental observations during the earthquake. Lastly, sediment grain size analysis show evidence of a millimetre-scale coarse deposit, which is inferred to be the stratigraphic signature of a high energy event, most likely to be caused by the 5 m high tsunami that followed this earthquake. The stratigraphic record of the 1995 earthquake and its tsunami in sediments of the wetland Estero Potrero Grande serve as modern analogues to investigate former earthquakes in this region.

CHAPTER 5

COASTAL SUBSIDENCE CAUSED BY THE 1932 (M_W 7.8) MEGATHRUST EARTHQUAKE AND OTHER MARINE INCURSIONS ON THE JALISCO-COLIMA COAST, MÉXICO

ABSTRACT

Deposits of the coastal wetland Estero Potrero Grande, located in the southern segment of this subduction zone, record the stratigraphic signature of the 1995 earthquake, which is preceded by three events, or stratigraphic contacts, that resemble coastal subsidence and one event that resemble coastal uplift. Using field evidence, diatom assemblages, geochemistry and X-ray computed tomography (CT) images it was possible to discriminate the origin of these contacts. Based on the criteria to identify past earthquakes in tidal settings and using the signature of the 1995 as an anologue of past events, only one of four stratigraphic contacts was likely produced coseismically. This contact shows evidence of a possible tsunami deposit and subsidence (0.09 ± 26 to 0.15 ± 0.27 m). A Bayesian age-depth model, based on ^{14}C ^{137}Cs dates, estimate the age of this event at 1914 ± 50 cal. A.D. Given the sedimentological properties of this event, the M_w 7.8 earthquake in 1932 is the event that most likely produced such stratigraphic record. These finding help to constrain the parameters of this megathrust earthquakes, e.g. width and depth, considering that earthquakes occurred before the M_w 1995 events are poorly constrained instrumentally.

5.1 Introduction

The Jalisco Subduction Zone, is a tectonically active margin, where plate subduction controls the high rate of seismicity and regional tectonic deformation (Bandy et al., 1999; Dañobeitia et al., 2016; Manea et al., 2013; Ramírez-Herrera & Urrutia-Fucugauchi, 1999). Earthquake catalogues, compiled since the nineteenth century, demonstrate the potential of this megathrust fault to produce large (M_w 7.0 – 7.9) and great earthquakes ($M_w \geq 8.0$; e.g. Sawires et al., 2019; Singh et al., 1981; Suárez et al., 2020). The largest events recorded by local seismic instruments occurred in 1932 (M_w 8.2 and M_w 7.8), 1995 (M_w 8.0) and 2003 (M_w 7.6). The epicentres, depths, widths, lengths, as well as the distributions of coseismic slip of the 1995 and 2003 earthquakes (**fig 5.1**) were estimated accurately due to the vast information available from seismographs, GPS receivers and tide gauges (e.g. Courboulex et al., 1997; Filonov, 1997; Hjörleifsdóttir et al., 2018; Hutton et al., 2001; Melbourne et al., 1997a; Ortiz, Kostoglodov, et al., 2000; Trejo-Gómez et al., 2015). Whereas the estimation of earthquake parameters preceding the 1995 earthquake was limited by local and teleseismic data.

Local seismic data correspond to the Mexican seismic network, which began operations in 1910 (Alcántara et al., 2012; Pérez-Campos et al., 2018). Teleseismic data correspond to seismic instruments deployed worldwide, which are in operations since the nineteenth century. Teleseismic data permitted to estimate the time, location of epicentres and magnitude of great earthquakes (Sawires et al., 2019; Singh et al., 1981; Suárez et al., 2020). However, several studies demonstrate that the locations of epicentres, obtained through teleseismic data, are some tens to more than one-hundred kilometres north-east from their true position (Cruz & Wyss, 1983; Hjörleifsdóttir et al., 2016; Singh et al., 1985; Singh & Lermo, 1985). This inaccuracy brings the epicentres of megathrust earthquakes far inland from the coastline and outside the seismogenic zone (e.g. Cruz & Wyss, 1983; Okal & Borrero, 2011). Earthquake ruptures estimated by early instrumental earthquakes also present inaccuracies, e.g. 1932, as they were estimated through the analysis of aftershocks distributions (e.g. Singh et al., 1985). As it was demonstrated after some of the most recent earthquakes, aftershocks concentrate in areas of low-slip regions, either inside or outside the rupture area, and only a few aftershocks occur in areas of maximum

slip (Das & Henry, 2003; Mendoza & Hartzell, 1988). Consequently, earthquake areas estimated through the analysis of aftershocks distributions only approach the real areas of slip (e.g. Bilek & Engdahl, 2007; Das & Henry, 2003; Mendoza & Hartzell, 1988).

Knowing the exact location and the extension of past earthquake ruptures is essential for the local earthquake hazard assessment, as these parameters are crucial to approximate to the maximum size expected and the recurrence period of megathrust earthquakes. Hence, considering that coseismic land-level changes might reveal earthquake locations, rupture lengths, widths, and depths (e.g. Govers et al., 2017; Thatcher & Rundle, 1984), quantifying the response of the coast during early instrumental earthquakes along the Jalisco subduction zone is necessary. In this sense, stratigraphic markers represent the unique opportunity to quantify coseismic land-level changes of early instrumentally recorded earthquakes.

Coastal sediments beneath the wetland Estero Potrero Grande record the signature of subsidence caused by the 1995 earthquake. Field evidence shows stratigraphic sequences beneath this event resemble its sedimentary fingerprint. These sequences might represent episodes of coseismic land-level changes during multiple earthquake deformation cycles. This study investigates the sedimentological properties of sediments deposited before the 1995 earthquake to reveal their origin, likely coseismic, and quantify the magnitude and patterns of land-level change to constrain past earthquake ruptures.

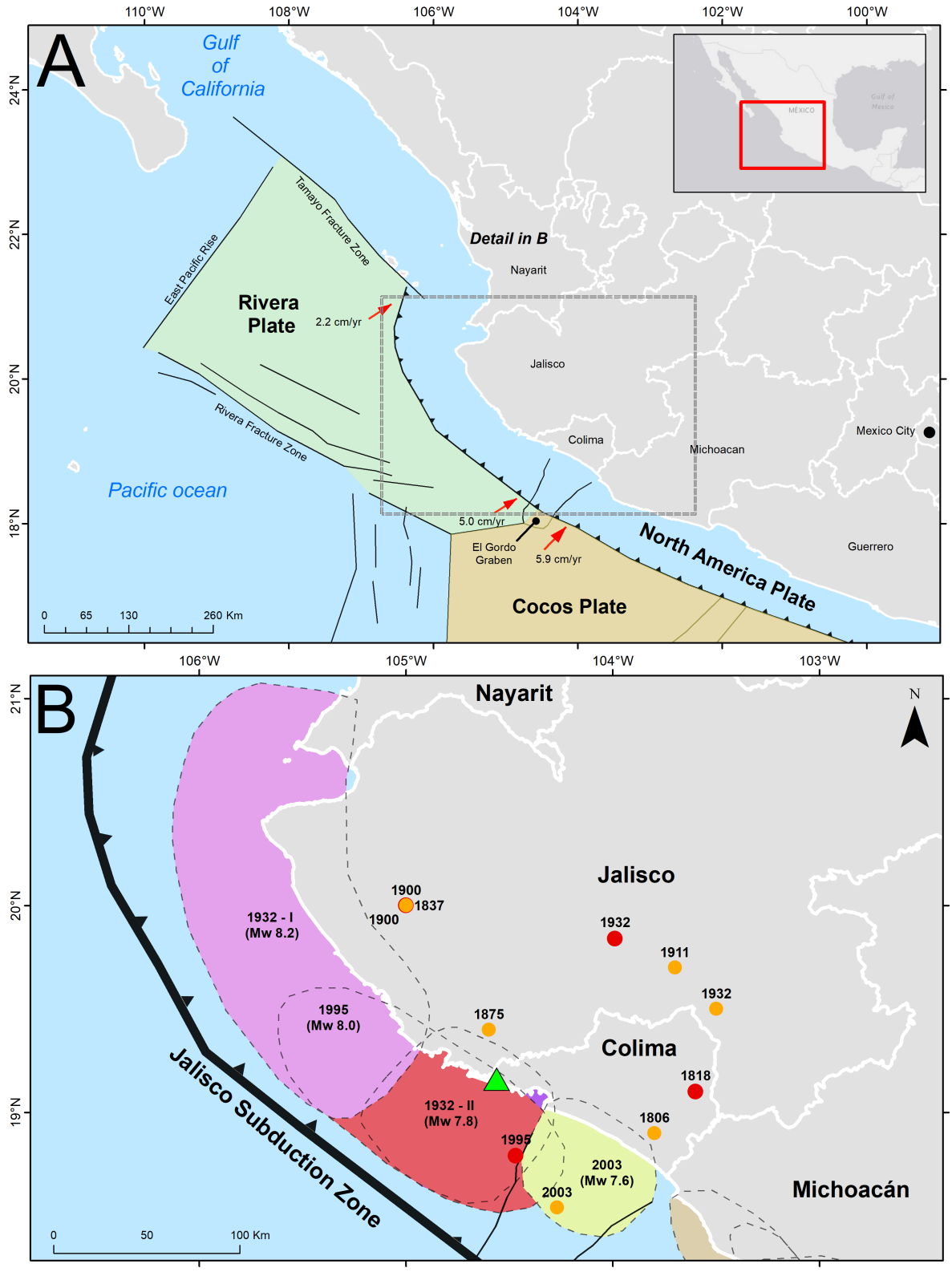

Figure 5.1. *Spatio-temporal framework of seismicity along the Jalisco Subduction Zone. Orange dots show the epicentres of large (Mw 7.0 – 7.9) earthquakes. Red dots show the epicentre location of great (Mw > 8.0) earthquakes since the nineteenth century (Sawires et al., 2019). Ellipses in colour are the rupture areas of earthquakes recorded by local instruments since 1910 (Kostoglodov & Pacheco, 1999). The green triangle shows the location of the field site of this study.*

5.2 Results

The stratigraphy here summarized (**fig 5.2**) corresponds to the coring site 2018, where the evidence of the 1995 earthquake was collected. The bottom of the stratigraphic column consists of grey to brownish organic silty sand. Sediments are very poorly sorted and dominantly polymodal. The highest content of sand, 37%, is in the deepest section of the coring transect. Sediments show normal grading, and fine to medium silt replaces coarse silt in the upper part of this basal unit. This uppermost part contains angular to rounded gravel, smaller than 5 cm in diameter, which gradually increases in density towards the top of this basal unit. This basal unit extends up to 3 m below the modern surface. At this depth, the unit was impenetrable by hand-driven coring.

Within the basal unit, freshwater diatoms dominate the assemblages, >50% (**fig 5.3**). The planktonic species *Cyclotella meneghiniana* (27%) is the most common species, showing a spike in the upper section of the basal unit. The benthic freshwater species *Halamphora submontana* and *Nitzschia fonticola* became dominant towards the upper part of the basal sand.

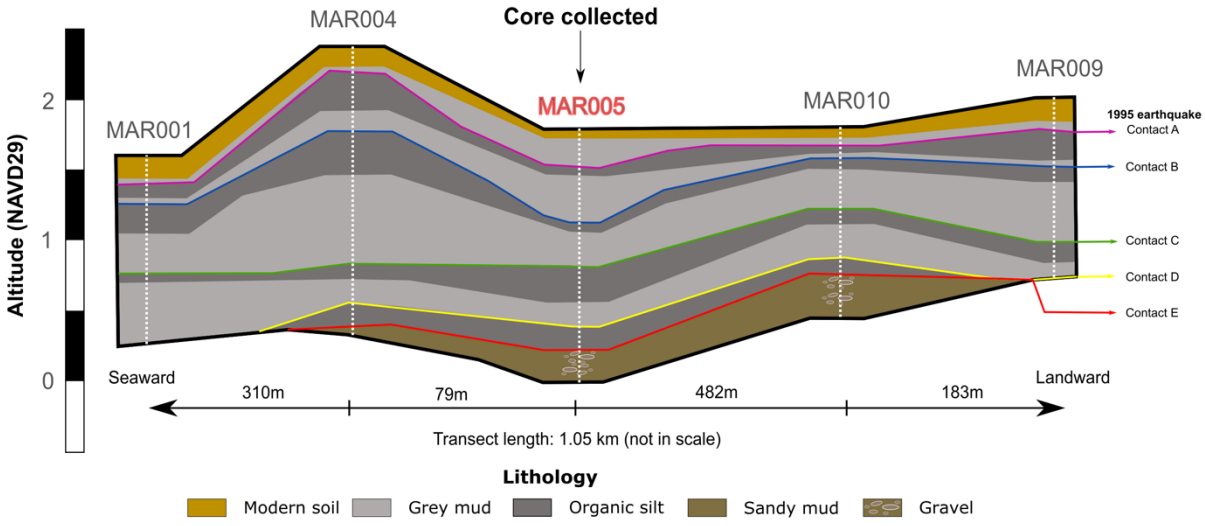

***Figure 5.2**. Cross-section of the Estero Potrero Grande site. The borehole chosen to retrieve the samples for further laboratory analyses was MAR005 (1.79 m NAVD29).*

The XRF-based organic content proxy reaches its minimum values within the basal sand, inc/coh = 0.7, showing an average rate of change of 1% upwards in the core

(**fig 5.4**). Salinity ratios reach their minimum values within this basal unit, S/Zn = 0.7 and Br/Zn = -1.6 but showing a constant increase towards the upper part of the unit at 6% and 2%, respectively.

The basal unit is overlaid abruptly by a dark grey organic bed with wood fragments (< 5 cm) and undifferentiated organics. This unit contains thin laminations (<1 cm) of very poorly sorted medium to fine silt. The percentage of sand reduces to < 10%. This stratigraphic transition is referred to as Contact E. This stratigraphic contact was identified ~500 m along the transect ,within a depth range of 108 - 200 cm, below the surface.

In the core MAR005, Contact E is at 153 cm depth. Immediately above the contact, there is an increase of freshwater taxa (> 70%), represented by *Nitzschia fonticola* (4 - 14%) and *Halampohora submontana* (6 – 9%). The brackish species *Nitzschia scalpelliformis* (7 – 19%) also increases above Contact E, although brackish species remain below 20%.

XRF-based salinity indicators show a gradual and steady increase across the Contact E. The percentage of change of S/Zn is 10% and Br/Zn is 4%. The inc/coh ratio shows also show an abrupt increase of 5% across this contact.

Within the organic-rich unit overlying Contact E, the organic content proxy inc/coh shows a rate of change of 1%, reaching a maximum value inc/coh = 1.2 at 137 cm depth. Within this organic-rich unit, freshwater diatoms keep relatively constant (> 60%), and the species *Nitzschia fonticola* (>10%), *Halamphora submontana* (> 20%), and *Cyclotella meneghiniana* (>10%) still dominate the assemblages. Salinity indicators, S/Zn and Br/Zn show a rate of change of 6% and 3%, respectively.

At 138 cm depth in core MAR005, this organic bed is overlaid abruptly by a light grey coarse silt. This abrupt transition is named Contact D. This contact was mapped between depths 94 - 183 cm below the surface for along the ~500 m, from MAR004 to MAR010 (fig).

Above Contact D, in the core MAR005, there is a 3 cm bed of a very poorly sorted coarse silt, with a 34% sand fraction. This spike of coarse sediments is accompanied

by an abrupt increase of the ratios S/Zn and Br/Zn, whose relative concentrations increase by 43% and 102%, respectively. Diatom assemblages do not change their composition within this bed of coarse silt. Nonetheless, 6 cm above the stratigraphic contact, the percentage of brackish and marine species peak to >70% of the total assemblage. The most common species are *Paralia sulcata* (10%) and *Nitzschia sicula* (10%), as well as brackish species such as *Bacillaria paxillifer* (12%).

Roughly 15 cm above Contact D, the content of herbaceous and wood fragments begin to rise. The inc/coh ratio showed an increase of 15% at this depth. Sediments gradually turn into fine silt, very poorly sorted, with low sand content (~10%). Freshwater diatoms reach again ~60% of the total assemblage within this organic silt. The dominant species are *Cyclotella meneghiniana* (> 10%), *Nitzschia frustulum* (5 – 14%) and *Nitzschia palea* (5%). The rate of change of salinity ratios is zero, with values fluctuation around 3.4 for S/Zn, and 0.5 for Br/Zn.

Along the coring transect, between 55 and 155 cm depth, this organic unit shows an abrupt increase of the minerogenic fraction. This stratigraphic transition is labelled as Contact C. In the core MAR005, Contact C is at 99 cm depth. The overlying sediments are classified as very poorly sorted coarse silt, with a slight increase of sand (~20%). Salinity ratios show a sharp decrease, whose amount of change is -21% for S/Zn and –90% for Br/Zn. The inc/coh ratios also show a constant change across the transect, at a -2% rate on average.

Diatom assemblages below Contact C show a gradual increase of marine and brackish species, where *Paralia sulcata* (10 – 22%) is the most common species. Above this contact, the abundance of marine and brackish diatoms peak at 50%. The dominant species are *Paralia sulcata* (>15%), *Nitzschia sicula* (>5%) and *Bacillaria paxillifer (5 – 10%).*

The grey silt overlying Contact C remains as poorly sorted fine silt with a gradual increase of highly humified herbaceous fragments. The content of sand is < 5%. This organic silt unit extends along the whole coring transect. This increase of organic sediments is accompanied by an increase in freshwater diatoms, which reach up to 60% of the total assemblage. The common species are *Halamphora submontana* (10 – 20%), *Achnanthes inflata (*6 – 14%*), Nitzschia gracilis* (5 -10%) and *Cyclotella*

meneghiniana (5 - 10%). Between 24 and 71 cm depth, this organic unit is overlaid abruptly by a grey silt bed. This transition, here referred to as Contact B, varies in its abruptness, being more abrupt in the central boreholes.

In the core MAR005, Contact B is at 71 cm depth. It is characterised by the presence of vegetation in vertical position, which is represented by the inc/coh ratio showing its peak (inc/coh = 1.2) a few centimetres above the stratigraphic contact. This contact shows a very thin deposit, < 1cm, of a very poorly sorted fine sand. Diatom assemblages are mixed in this deposit, slightly dominated by freshwater taxa. However, above the contact, *Nitzschia grossestriata* (> 5%) and *Paralia sulcata* (5 - 15%) are the most common diatom species. Marine and brackish species together sum up to >25% of the assemblage. Salinity ratios S/Zn and Br/Zn remain relatively stable below Contact B, then increase abruptly above the contact with a rate of change of 78% and ~200%, respectively.

Upwards in the stratigraphy is the signature of the 1995 earthquake, Contact A, which was described in the previous Chapter.

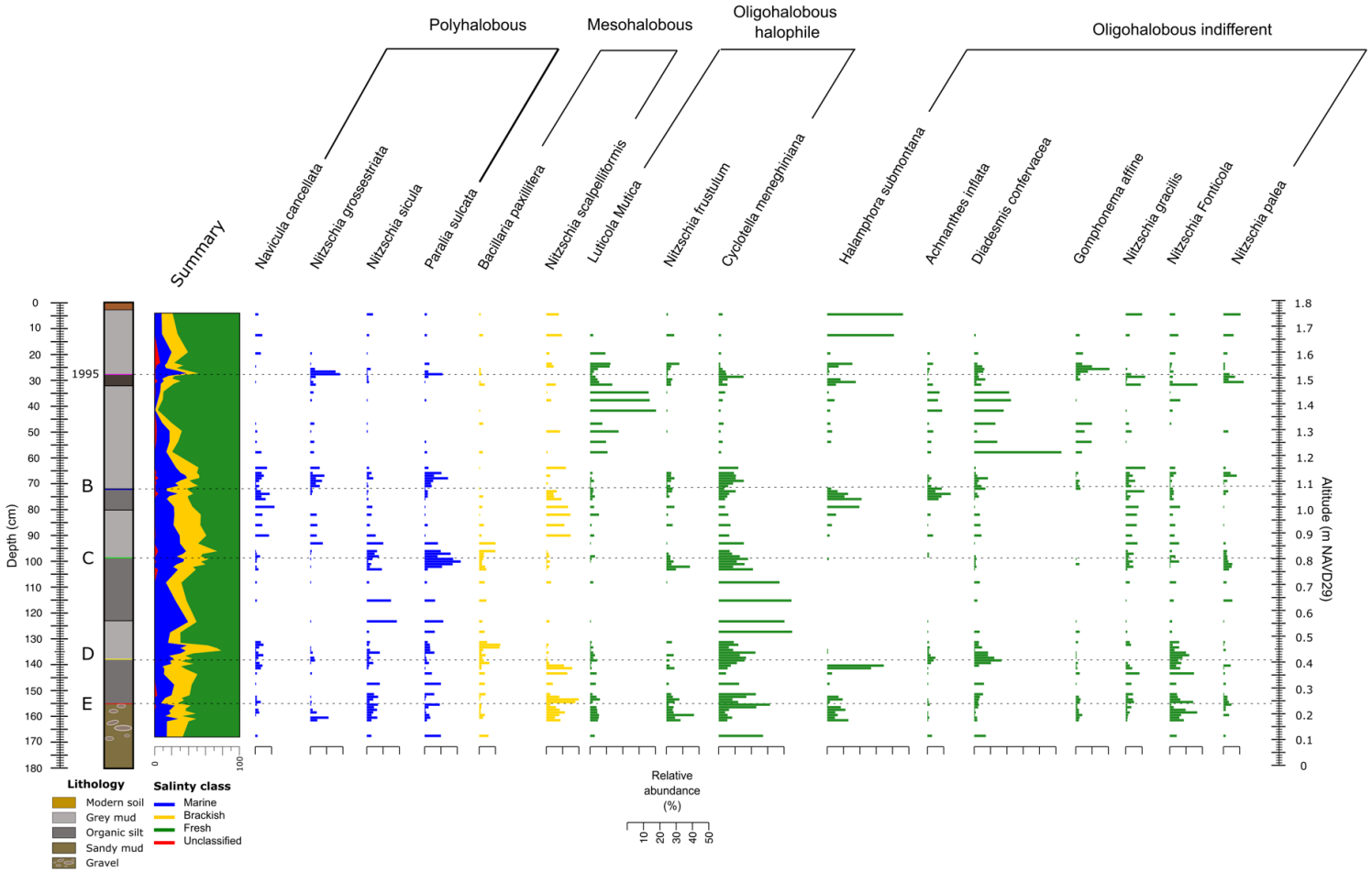

Figure 5.3. *Biostratigraphy of core MAR005. This diagram shows only those species > 5% in at least five samples. Halobian classification of species considered polyhalobous, mesohalobous, oligohalobous halophile and oligohalobous indifferent. Note that the summary of salinity classes left-hand side of the plot classifies polyhalobous species as marine, mesohalobous species as brackish and oligohalobous-halophile and -indifferent as freshwater species.*

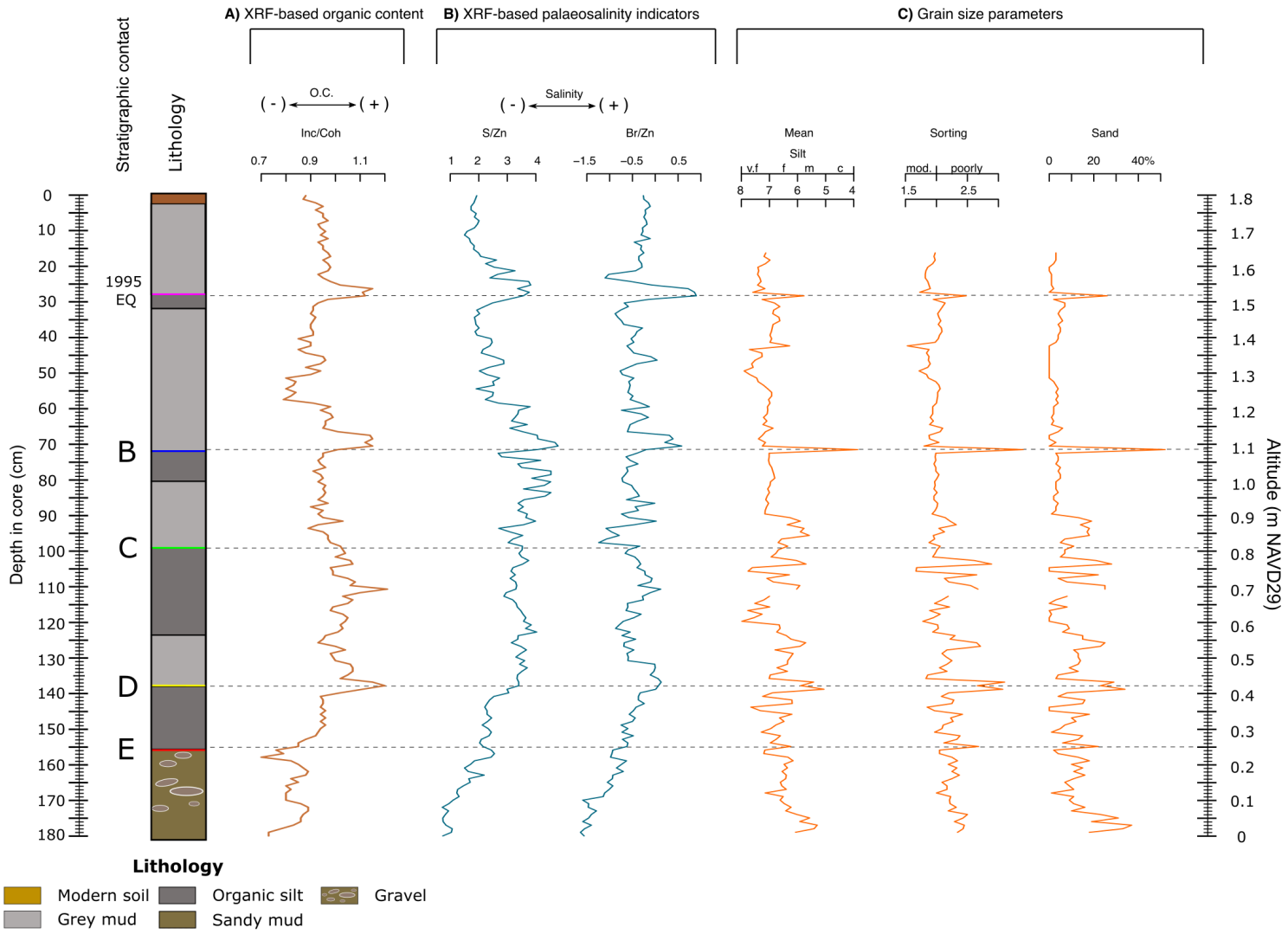

Figure 5.4. *Downcore fluctuations of proxies to identify palaeoenvironmental changes across the stratigraphic contacts.*

5.2.1. Diatom-based palaeoelevation changes.

Palaeoelevations, relative to the Mean Higher High Water (m MHHW), of the core MAR005 (fig. 5.5) fluctuate between +0.01 ± 0.26 m and +0.17 ± 0.26 m MMHW in Model 1 (M1) and between -0.06 ± 0.26 m and +0.20 ± 0.26 m MHHW, according to Model 2 (M2). The magnitude and trends of land-level change across the stratigraphic contacts is summarised in ***table 5.1***.

Table 5.1*. Land-level changes across the stratigraphic contacts A to D in core MAR005.*

	Contact E	Contact D	Contact C	Contact B
Model 1	+0.03 ± 0.26 m	- 0.09 ± 0.26 m	-0.02 ± 0. 26 m	-0.02 ± 0. 26 m
Model 2	+0.05 ± 0.27 m	- 0.15 ± 0. 27 m	-0.04 ± 0. 27 m	-0.04 ± 0. 27 m

Within this basal unit palaeoelevations vary between +0.07 ± 0.26 m and +0.11 ± 0. 26 m MHHW, according to Model 1 (M1), and between +0.04 ± 0. 26 m and +0.11 ± 0. 26 m MHHW, based on Model 2 (M2). Across the Contact E there is a low change of palaeoelevation, from +0.9 ± 0. 26 to +0.12 ± 0. 26 m MHHW (M1) and from +0.7 ± 0. 26 to +0.12 ± 0. 26 m MHHW (M2).

Between Contacts E and D, palaeoelevations oscillate between +0.07 ± 0. 26 m MHHW and +0.12 ± 0. 26 m MHHW (M1) and +0.03 ± 0. 26 m MHHW and +0.12 ± 0. 26 m MHHW (M2). Across Contact D, palaeoelevation models indicate a change from +0.10 ± 0. 26 m MHHW to +0.01 ± 0. 26 m MHHW (M1) and from +0.08 ± 0. 26m MHHW to -0.06 ± 0. 26 m MHHW (M2).

Between Contacts D and C, palaeoelevations fluctuate between +0.01 ± 0.26 m MHHW and +0.11 0. 26 m MHHW (M1) and -0.06 ± 0. 26 MHHW and +0.11 ± 0. 26 MHHW (M2). Across the stratigraphic Contact C, palaeoelevations indicate a change from +0.06 ± 0. 26 MHHW to +0.04 ± 0. 26 m MHHW (M1), and from +0.03 ± 0. 26 m MHHW to -0.01 ± 0. 26 m MHHW (M2).

Between the stratigraphic Contacts C and B, palaeoelevations vary from +0.03 ± 0. 26 m MHHW and +0.09 ± 0. 26 m MHHW (M1) and -0.03 ± 0. 26 m MHHW and +0.08 ± 0. 26 m MHHW. (M2). The depths bracketing the Contact A indicate a land-level change from +0.09 ± 0. 26 m MHHW to +0.07 ± 0. 26 m MHHW (M1); and from +0.07 ± 0.26 m MHHW to +0.04 ± 0.26 m MHHW (M2).

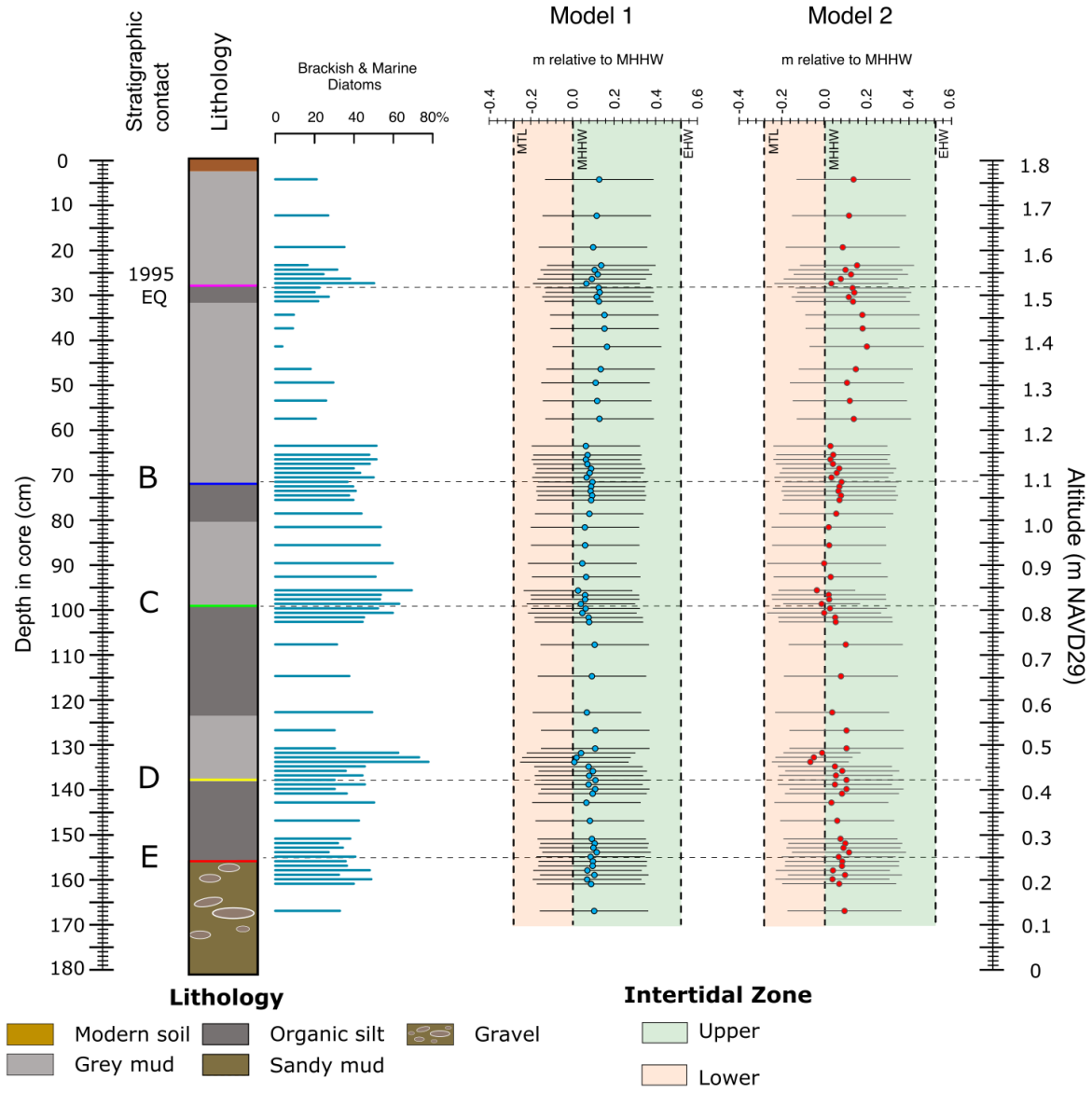

***Figure 5.5**. Diatom-based palaeoelevation changes of the core MAR005*

5.2.2. Chronology and timing of the stratigraphic contacts.

Downcore concentrations of Caesium-137 (^{137}Cs), detailed in the previous chapter, and six accelerator mass spectrometry (AMS) radiocarbon (^{14}C), summarised in **table 5.2,** were used. to estimate the ages of the stratigraphic contacts, B to E

Table 5.2. *Radiocarbon dates of core MAR005 indicating calibrated and modelled dates after the age-depth model in OxCal.*

								P_sequence **modelled ages (years A.D.)**			
Core_ID	**Lab Code**	**Depth in core (cm)**	**$\delta^{13}C$ (‰)**	**^{14}C enrichment (% Modern ±1σ)**	**^{14}C Age (years B.P. ±1σ)**	**Calibration curve**	**Calibrated age range (years A.D. ±2σ)**	**Age range (±2σ)**	**Median**		**Agreement Index**
									Mean (±1σ)		
MAR005_1	SUERC-90540	67	-29.2	124.9 ± 0.58	Modern	BOMB 21 NH2	1959-1984	1959 -1975	1964 ± 3	1964	60.2
MAR005_2	SUERC-90541	68	-29.6	131.56 ± 0.61	Modern	BOMB 21 NH2	1961-1981	1958-1968	1963 ± 2	1963	53.4
MAR005_5	SUERC-90542	98.5	-30.2	100.51 ± 0.46	Modern	BOMB 21 NH2	1946-2018	1948-1959	1953 ± 2	1954	124.2
MAR005_6	SUERC-90543	99.5	-28.4	100.63 ± 0.47	Modern	BOMB 21 NH2	1950 -2014	1948-1958	1952 ± 11	1953	108.1
MAR005_8	Beta - 535426	129.5	26.5	97.66 ± 0.36	190 ± 30	INTCAL 20	1649-1950	1743-1955	1922 ± 45	1938	93.8
MAR005_9	SUERC-90544	155.5	-28	98.44 ± 0.46	126 ± 37	INTCAL 20	1674-1944	1684-1945	1865 ± 69	1888	104.1

The input of the Bayesian age-depth model in OxCal consists of six ^{14}C dates. Two ^{14}C dates input as R_Date(), because they were reported as conventional radiocarbon ages. Four ^{14}C dates input as R_F14C(), because they were reported with an excess of ^{14}C. Two absolute dates, which correspond to the ^{137}Cs peak, , i.e. 1963 AD, and the stratigraphic contact of the 1995 earthquake, 1995 AD, were input as C_Date(). Three boundaries, corresponding to contacts B to D, were input as Boundaries(). The calibration curves used were Bomb21NH2 (Hua et al., 2021) and IntCal20 (Reimer et al., 2020), as Mix_Curves(). Lastly, the chosen parameter *k* was 0.05.

The output of the age-depth model (**fig. 5.6**) shows an overall agreement index of 76.5. This score indicates a good fit of the output model, considering that the index should be higher than 60 to be considered as an acceptable model (Bronk Ramsey, 1995). In terms of Individual indices, only one sample is below the threshold of 60% (**table 5.2)**. The output of this is model was used to estimate the ages of each stratigraphic contact, which are summarized in **table 5.3.**

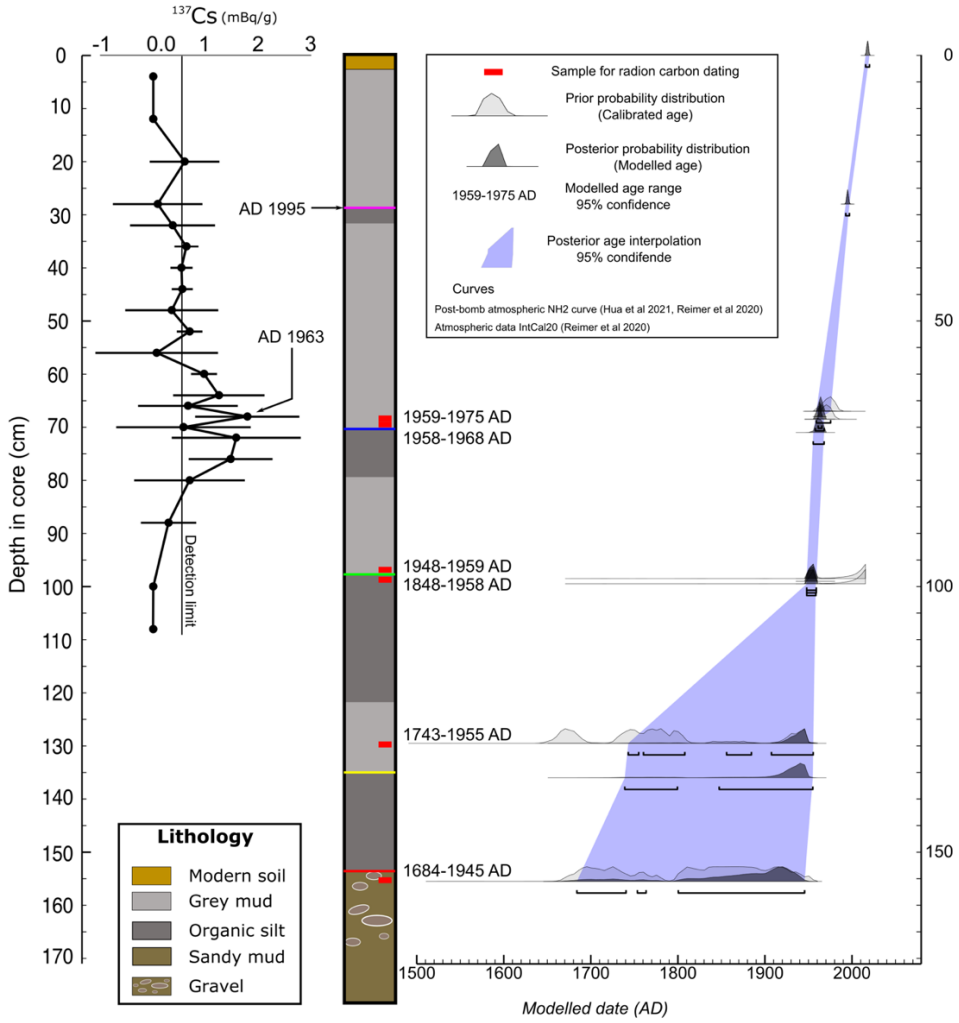

***Figure 5.6**. Chronology of the core MAR005. Age control includes down-core concentrations of ^{137}Cs, radiocarbon dates, and the age-depth model's output.*

***Table 5.3.** Estimated ages for the stratigraphic contacts B to E, obtained from the P_sequence model in OxCal.*

Contact	Depth (cm)	Mean (1 σ, cal. yr A.D.)	Median (cal. yr A.D.)	Age range (2 σ, cal. yr AD)
B	71	1962 ± 3	1962	1955 – 1968 (95.4%)
C	99	1953 ± 2	1953	1948 – 1959 (95.4%)
D	136	1914 ± 50	1932	1739 – 1799 (5.7%) 1847 – 1955 (89.8%)
E	155	1865 ± 69	1888	1684 – 1740 (9.3%) 1753 – 1763 (1.3%) 1800 – 1955 (84.9%)

5.3 Discussion

The stratigraphy beneath the coastal wetland Estero Potrero Grande has the potential to record the signature of great megathrust earthquakes (M_w > 8.0), as proved with the sedimentary signature of the 1995 tsunamigenic earthquake. The deposits associated with this earthquake satisfy the criteria proposed by Nelson et al. (1996) and Shennan et al. (2016) to identify the sedimentary evidence of megathrust earthquakes imprinted in low-energy coastal environments. These criteria are now used to test the origin of the four abrupt stratigraphic contacts (**table 5.4**) that precede the 1995 earthquake (Contacts B to E) in this coastal site.

***Table 5.4**. Criteria applied to the stratigraphic contacts of Estero Potrero Grande to assign a potential coseismic origin.*

Contact	1) Lateral extent of the couplet (m)	2) Abruptness of subsidence or uplift	3) Magnitude of subsidence (-) or uplift (+).	4) Tsunami evidence	Coseismic origin
B	1000	Gradual to Abrupt	-0.02 ± 0.26 m (M1) -0.04 ± 0.27 m (M2)	Yes (?)	Unlikely
C	1000	Abrupt	-0.02 ± 0.26 m (M1) -0.04 ± 0.27 m (M2)	No	Unlikely
D	500	Abrupt	- 0.09 ± 0.26m (M1) - 0.15 ± 0.27 m (M2)	Yes	Most likely
E	500	Abrupt to gradual to gradual	+0.03 ± 0.26 m (M1) +0.05 ± 0.27 m (M2)	No	Unlikely

Field data permitted to assess the lateral extension of the stratigraphic contacts. CT scanning images, geochemistry and fossil diatoms allowed us to identify and quantify the abruptness of change, either subsidence or uplift. Grain size analysis helped to identify high energy deposits, possibly associated with tsunamis. Diatom-based palaeoelevation models permitted to quantify the magnitude of land-level change. Lastly, the chronology of the record based on ^{14}C and ^{137}Cs dating is used to correlate the age of the stratigraphic contacts with instrumentally recorded earthquakes along the Jalisco subduction zone. This summary is in **figure 5.7**.

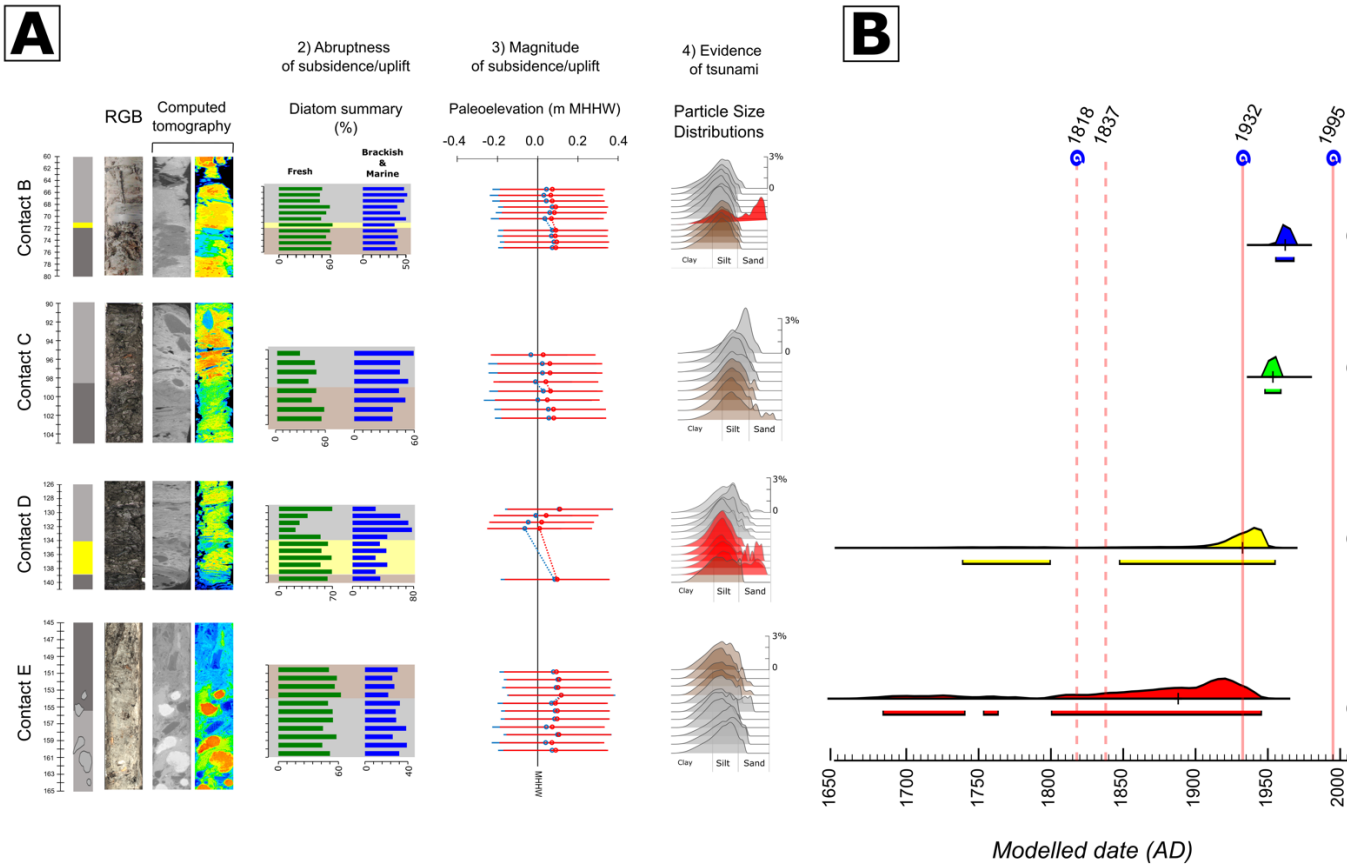

***Figure 5.7**. Summary of the stratigraphic contacts using multiple proxies and the criteria to satisfy a coseismic origin. **A)** From left to right, high-resolution photographs (RGB), X-ray CT-scans in greyscale and false colour. Summary of diatoms, grouping brackish and marine together. Palaeoelevation changes were obtained from Model 1 (red) and Model 2 (blue). Particle size distributions in red represent samples inferred as high energy deposits, possibly tsunami deposits. **B)** Probability distributions obtained from the age-depth model for contacts B to E. Horizontal bars below the distributions show dates at 95% confidence. Vertical black lines crossing the bottom of the distributions show the median value. Vertical red lines indicate the timing of great megathrust earthquakes (Mw ≥ 8.0) along the Jalisco Subduction Zone recorded by seismic instruments (Sawires et al., 2019; S. Singh et al., 1981; Suárez et al., 2020). Thick lines are those earthquakes recorded by instruments deployed across the Mexican territory since 1910. Dashed vertical lines show the timing of earthquakes obtained from teleseismic datasets*

before 1910. Blue symbols next to the year indicate the occurrence of documented tsunamis (taken from Castillo-Aja & Ramírez-Herrera, 2017).

5.3.1. Contact E.

Contact E is the oldest event, dated to 1684-1955 cal. AD (2-sigma). This contact shows a lateral continuity over ~ 500 m along the coring transect. One of the characteristics of this contact is the spatial difference of the contact abruptness. This transition is more abrupt in inland cores, e.g. MAR010, than in the central cores, e.g. MAR005 (**fig. 5.8**). Contact E shows an underlying silty sand with gravel, overlaid abruptly by an organic-rich unit. In tectonically active coasts, this type of sequence is the signature of coastal coseismic uplift, showing a rapid transition from marine/brackish environments, either subtidal or lower intertidal environments, to freshwater environments, either upper intertidal or supratidal environments (e.g. Sawai, 2001a, 2001b; Shennan, 2009; Shennan et al., 2014).

Diatom assemblages show that the underlying unit of Contact E is freshwater palaeoenvironment with a high content of the planktonic freshwater species, e.g. *Cyclotella meneghiniana.* This species is commonly associated with estuarine environments, highly influenced by freshwater discharges (Zong et al., 2006). Other benthic species include *Halamphora submontana and Nitzschia fonticola. H. submontana* is a species commonly associated with riverine environments (Cocquyt et al., 2019; Leira & Sabater, 2005; Qingmin et al., 2015), and *N. fonticola* occurs in high saltmarshes (e.g. Sherrod, 1999). These two benthic species are common beneath the stratigraphic contact, and they increase in abundance immediately above Contact E. The magnitude of land-level change is low (+0.03 ± 0.26 m and +0.05 ± 0.27 m) to assert that this stratigraphic contact was produced by an episode of coastal uplift.

Palaeoenvironmental conditions suggest a change in freshwater conditions without clear evidence of brackish or marine fluctuations. Indeed, the salinity ratios S/Zn and Br/Zn reach their lowest values below the contact, suggesting the dominance of Zn, which is an element abundant in the Marabasco river (Marmolejo-Rodríguez et al. 2007). Consequently, the process that could originate this contact is most likely associated to a change of the hydraulic regime of this channel.

The morphology of this channel is part of a network of channels linked to the back-barrier deltaic system of the Marabasco river. Along the Mexican Pacific coast, these morphologies represent abandoned tributaries (De la Lanza Espino et al., 2013). Holocene sequences of deltaic environments show that abandoned paleochannels are often characterised by an underlying matrix of sand or muddy sand, enriched with gravel, which is overlaid by finer sediments with increased organic content, with a gradual disappearance of the sand fraction (e.g. Gugliotta et al., 2021; Thom, 1967; Toonen et al., 2012). The lithology of the Contact E shows an underlying basal unit with coarse sediments, silty sand with gravel, and the dominance of freshwater diatoms species. The reduction of gravel and sand above the contact, accompanied by the establishment of vegetation and benthic freshwater diatom species, likely represents the reduction of fluvial activity and possibly the abandonment of the channel. Hence Contact E represents a palaeoenvironmental change linked to the Marabasco river.

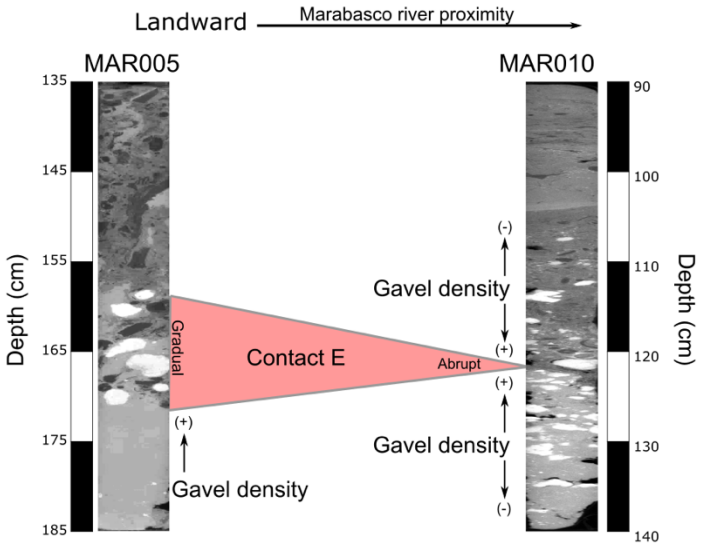

***Figure 5.8**. Sedimentary features of Contact E in cores MAR005 and MAR010. This figure shows the differences in the degree of the abruptness of the contact. Light grey colour on the bottom represents basal unit rich in sand content, white dots and circles represent gravel, and dark grey colours above the contact show an organic-rich unit.*

5.3.2. Contact D

Contact D was identified in three of five cores (MAR004, 005 and 010), showing a lateral continuity over ~ 500 m. An abrupt change characterises this contact from the organic-rich silt overlaid by a coarse silt unit.

Diatom assemblages and geochemistry show an abrupt transition from freshwater to marine/brackish conditions (**fig. 5.9**). Below the contact, within the organic unit, *H. submontana* and *N. fonticola* indicate a dominantly freshwater environment. Above the contact, the benthic species *N. grossestriata* and *N. cancellata* show an increase of marine influence. These two species are associated with lower intertidal environments in tropical (e.g. Horton et al., 2007) and temperate regions (e.g. Hemphill-Haley, 1996; Sawai et al., 2016). Litho-, bio and chemo-stratigraphic changes indicate that coastal subsidence is likely the mechanism that produced Contact D. According to Models 1 and 2, the magnitude of subsidence was between 0.09 ± 0.26 m and 0.15 ± 0.27 m. This subsidence was established six centimetres above the contact because of the 3 cm bed of coarse silt, rich in sand, immediately above Contact D.

This bed of coarse sediments deposited immediately above Contact D suggests a high-energy event, whose sedimentary features an abrupt basal contact, similar in all cores; 2) a 3 to 1 cm bed of coarse silt with high content of sand; 3) a 2 cm muddy cap overlying this coarse deposit; 4) evidence of rip-up clasts revealed by CT-scan images; 5) increase in salinity within this deposit, represented only by geochemistry indicators (Br/Zn and S/Zn), but not by diatoms; 6) normally graded sediments; 7) poorly sorted sediments; 8) lateral continuity over more than 400 m. These features satisfy some of the criteria commonly used in palaeotsunami studies to discriminate the origin of high energy deposits (Morton et al., 2007; Wilson et al., 2014). Hence, based on the physical and chemical composition of the sediments, this high energy event is associated with a high energy marine incursion, likely a tsunami.

Based on the age-depth model, the age of this contact is within the ranges 1739-1799 cal. AD (5.7%) and 1847-1955 cal. A.D. (89.8%). However, based on the shape of the probability distribution (**see fig. 5.7**), the most likely age range of Contact D is 1847 – 1955 cal. A.D. The mean age at 1σ is 1914 ± 50 cal. A.D. Its modelled median age is 1932 cal. A.D. The features of this indicate that Contact D is the sedimentary fingerprint of the M_w 7.8 earthquake occurred in 1932 A.D.

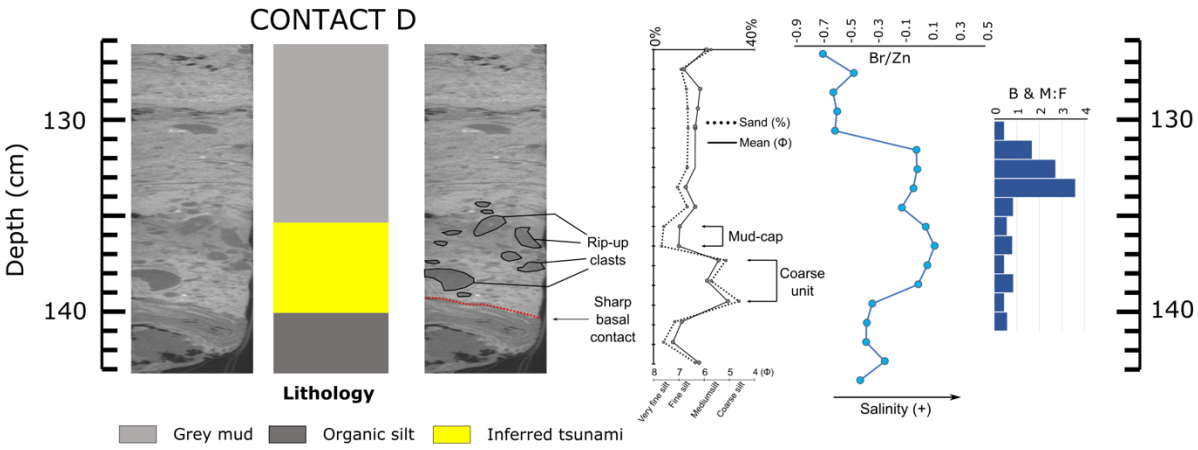

***Figure 5.9**. Sedimentological properties of Contact D. This diagram summarizes the physical features, chemical and biostratigraphic composition (ratio of Brackish + marine diatoms (%) / freshwater diatoms (%) of the tsunami of 1932.*

5.3.3. Contact C

This stratigraphic contact was mapped along the whole 1 km transect, showing a sequence of organic-rich silt overlain by silt. The underlying unit represents a freshwater environment dominated by the benthic species *N. frustulum* and *N. palea*. These two species are associated with upper intertidal and supratidal environments (e.g. Hocking et al., 2017; Roe et al., 2009). Geochemistry suggests an abrupt decrease in salinity above Contact C, shown by low values of S/Zn and Br/Zn ratios, which indicate an increase of Zn. Although, diatom assemblages show a gradual increase of brackish and marine conditions, some centimetres below the stratigraphic contact, with the marine species *P. sulcata* as the most common species. Palaeoelevation models show a relatively small land-level change of -0.02 ± 0.26 m (M1) and -0.04 ± 0.27 m (M2).

Based on the features of this contact, it is not possible to satisfy the criteria to assign a coseismic origin for Contact C. In fact, within the age range of this stratigraphic contact, 1948 – 1959 cal. AD, there are not records of earthquakes in the Jalisco subduction zone. Within this age range, the only non-tectonic event that could produce this stratigraphic signature is the hurricane category 4 hurricane occurred on the 27th October 1959 (Hagen et al., 2016).

This hurricane was the most destructive event of the 20th century that affected the Mexican's Pacific coast (Arreygue-Rocha & Cortés-Cortes, 2007; Hagen et al., 2016; Padilla Lozoya, 2007; Padilla Lozoya & Luna Montes, 1995; Patiño-Barragán et al., 2009). The landfall site was ~ 20 km south of the study site, at the Bays of Manzanillo-Santiago, where the wind speed reached 222 km/hr (Hagen et al., 2016; Patiño-Barragán et al., 2009). The damaged area extended ~120 km along the coast, from the south of Jalisco to the North of Michoacán (Hagen et al., 2016).

The abrupt decrease of the S/Zn and Br/Zn ratios above the contact indicate the higher release of the terrestrial element Zn. As the hurricane approached to the coast, it could produce high fluvial discharges, releasing fluvial sediments over this wetland. A strong line of evidence that supports this event-driven fluvial sedimentation is the abrupt increase in the sedimentation rate over the wetland. This could be caused by this hurricane (**fig. 5.10**). Below the stratigraphic contact, the sedimentation rate was below 1 cm/yr. Above Contact C, this rate of sedimentation shows a threefold increase, to reach a maximum value of 3.12 cm/yr.

The gradual increase of brackish and marine diatoms below and above the contact could be explained by morphological changes of the coastal barrier during the hurricane. Below the stratigraphic contact, the coastal barrier could breach due to the accumulated fluvial discharges during an event of such magnitude, allowing the wetland to have a greater influence of marine conditions. The peak of brackish and marine diatoms above the contact, possibly reflects wave run-up levels or storm surge levels that could exceeded the coastal barrier heights, producing overwash deposits, which could introduce sea water into the bays and estuaries behind barriers and spread it onto the marshes and shallow ponds behind it (e.g. Yao et al., 2020).

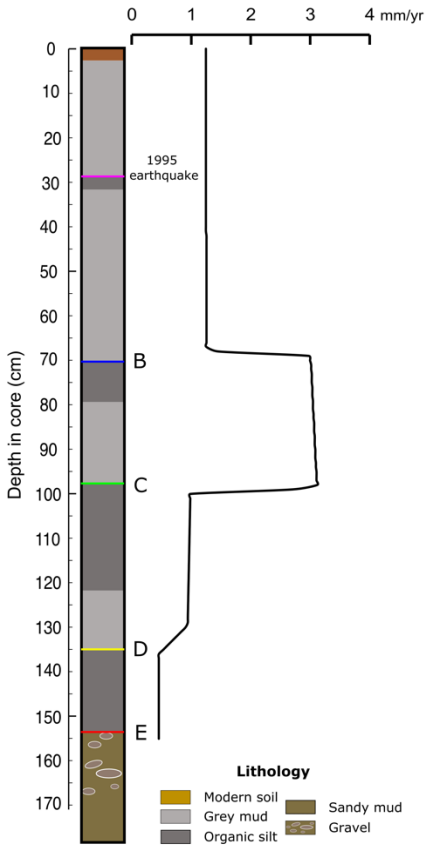

***Figure 5.10**. Sedimentation rate of core MAR005. The rapid increase of sedimentation at Contact C indicates the signature of the category 4 hurricane in 1959.*

5.3.4. Contact B

Contact B shows a transition from organic rich silt overlaid by silt. The contact was identified across the whole transect, being more abrupt and more clearly defined in cores MAR004, 005 and 010. The stratigraphic contact in cores MAR009 and MAR001 is less abrupt and less defined. Nonetheless, it was possible to map Contact B for ~1 km across the whole coring transect.

The underlying unit is a freshwater environment, where the benthic species *Halamphora submontana*, *Achnanthes inflata* and *Nitzschia gracilis* dominate the assemblages. Within the overlying silt unit, there is a slight increase of the marine species *Nitzschia grossestriata* and *Paralia sulcata.* While the presence of marine species such as *P. sulcata* and *N. grossestriata* suggests a significant increase in marine conditions, the actual increase in numbers of marine species is relatively small,

hence the palaeoelevation models suggest only minimal land level changes, -0.02 ±0.26 m MHHW (M1) and -0.04 ±0.27 m MHHW (M2).

The sedimentology across the contact shows a high energy event, illustrated by an increase of sand fraction, >50%. This coarse deposit is very thin, < 1 cm, to characterise its sedimentological properties. Even though the diatom assemblages do not show an increase in marine diatoms, within this sandy lamina, the geochemical composition (S/Zr and Br/Zr ratios) indicates an increase in salinity.

The evidence presented thus far is not sufficient to determine that this contact was caused by coastal subsidence during a megathrust earthquake. Specifically, because despite an increase in salinity conditions, represented by XRF-based salinity rations, diatom assemblages show a very small land-level change (< 0.05 m) and the environmental change is not long-lasting, as it occurred during the 1932 and 1995 earthquakes. Indeed, within the age range of this contact, 1955 – 1968 cal. AD (2σ), there is not any record of an earthquake in this subduction zone.

Alternative explanation of the origin of Contact B might be a storm, such as the 1959 hurricane, a local tsunami produced within the domain of the Cocos-North America plate, or a far-field tsunami produced in another subduction zone. However, in comparison to the sedimentological properties of the Contact C, a hurricane or a storm cannot be the process to explain the origin of this contact, due to the absence of evidence of a terrestrial input. Thus, a possible explanation is the occurrence of a tsunami produced in another subduction zone (**table 5.5**).

Table 5.5 *List of local and far-field tsunamis that struck the Mexican's Pacific coast between 1995 and 1968 AD.*

Event no.	Year	Earthquake Magnitude	Location	Maximum water height (m)	Water levels in Mexico		
					Site of maximum water height	Water height (m)	Water height at Manzanillo (m)
Local tsunamis							
1	1957	7.9	Guerrero, Mexico	1.3	Acapulco, Guerrero	1.3	No data
2	1962	7	Guerrero, Mexico	0.81	Acapulco, Guerrero	0.81	No data
3	1962	7.2	Guerrero, Mexico	0.34	Acapulco, Guerrero	0.34	No data
4	1965	7.8	Guerrero, Mexico	0.4	Acapulco, Guerrero	0.40	No data
Distant tsunamis							
1	1957	8.6	Andreanof Islands, Alaska, USA	32	Ensenada, Baja California	1.0	0.63
2	1960	9.5	Valdivia, Chile	25	Ensenada, Baja California	2.5*	1.32**
3	1960	6.8	Peru	9	Acapulco, Guerrero	0.13	No data
4	1964	9.2	Prince William Sound, Alaska, USA	51.8	Ensenada, Baja California	2.4*	1.2**
5	1965	8.7	Rat Islands, Alaska, USA	10.7	Salina Cruz, Oaxaca	0.46	0.27
6	1966	8.1	Peru	3	Salina Cruz, Oaxaca	0.24	No data
7	1968	8.2	Tokachi, Japan	6	Acapulco, Guerrero	0.43	0.4

National Geophysical Data Center (2022)

*CENAPRED (2005)

**Ortiz-Huerta et al. (2018).

The upper part of Table 4 summarises potential tsunami candidates produced by earthquakes in the Cocos-North America subduction zone between 1955 – 1968 AD. The largest tsunami was caused by the 1957 M_w 7.9 earthquake in Guerrero. This tsunami was only recorded by tide gauges in Acapulco, Guerrero and Salina Cruz, Oaxaca (Ortiz et al., 2000). This tsunami was not recorded in Manzanillo, the closest tide gauge to this study site. Hence, this tsunami is unlikely to be the event that produced the sand layer at Contact B.

From the list of distant tsunamis that struck the Mexican Pacific (**table 5.5.**), only the tsunamis of 1960 and 1964 were large enough to affect the coast near the field site. At Manzanillo, there is no data on the tsunami height caused by the 1960 earthquake in Chile. Nonetheless, tsunami modelling indicates a maximum height of 1.32 m (Ortiz-Huerta et al., 2018). Whereas tide gauge data for the 1964 tsunami recorded water height 1.2 m above sea level (CENAPRED, 2005). Due to the Contact B is below the maximum spike of ^{137}Cs concentrations in 1963 AD; hence the high energy event producing the sand at the contact is most likely associated with the 1960 tsunami from Chile. However, further field data is required to support this a conclusion.

5.3.5. Evidence of early instrumental earthquakes in Estero Potrero Grande.

The first objective of this chapter is to investigate the sedimentary signature of early instrumentally recorded earthquakes along the Jalisco subduction zone. From the four stratigraphic contacts that precede the signature of the 1995 earthquake in the coastal wetland Estero Potrero Grande, only Contact D fulfils the criteria to conclude that it was produced coseismically. The modelled-age for this event overlaps with the year 1932, when three earthquakes and their accompanying tsunamis occurred within the same month: 3rd June, 1932-I (M_w 8.2); 18th June, 1932-II (M_w 7.8); and 22nd June, 1932-III (M_w 6.9).

5.3.6. Constraining the rupture of the Mw 7.8 1932 earthquake.

Features of the earthquakes occurred in the are poorly understood, and their characteristics are not well constrained due to instrumental limitations during this period. For example, several studies using teleseismic data locate the epicentres of

the events 1932-I and 1932-II far inland and outside the seismogenic zone (**fig. 5.11**). Singh et al. (1985) indicate that the magnitude of error is more than 100 km.

However, rupture areas of the 1932-I and 1932-II earthquakes represent better the size and locations of these events. Nonetheless, these areas present their own limitations due to they were estimated through the analyses of aftershock distributions, using only few seismic stations across the Mexican territory (Singh et al., 1985). As mentioned in the introduction, aftershocks distribution only approach to the real areas of coseismic slip (e.g. Bilek & Engdahl, 2007; Das & Henry, 2003; Mendoza & Hartzell, 1988).

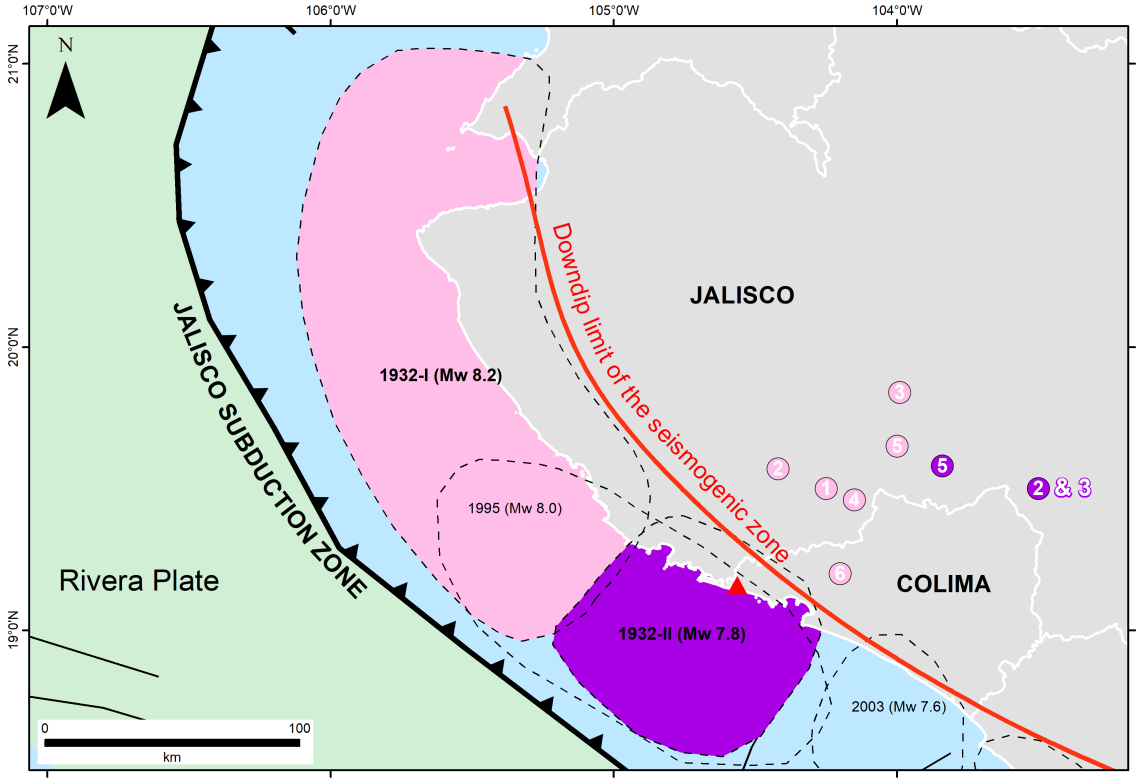

***Figure 5.11**. Location of the epicentres and rupture areas of the 1932 earthquakes. The earthquake 1932-I occurred on the 3rd June 1932, Mw 8.2. The earthquake 1932-II occurrend on the 18th June 1932. The epicentre of the 1932-I event is represented by pink circles, and the 1932-II event by purple circles. Epicentre locations were taken from the catalogue in Okal & Borrero (2011). White numbers inside pink and purple circles correspond to 1. Gutenber & Richter (1954); 2. Eissler & McNally (1984); 3. Singh et al., (1984); 4. Engdahl & Villaseñor (2002); 5. Okal & Borrero (2011); 6. International Seismological Summary. The ellipse in pink is the earthquake rupture of the 1932-I event, and the ellipse in purple is the earthquake rupture of the 1932-II event. The thick red line corresponds to the 40 km depth of the subducting slab (Hayes et al., 2018), corresponding to the intersection of the megathrust fault with the continental Moho, which corresponds to the down-dip limit of the seismogenic zone. The red triangle shows the location of this study's field site.*

In **figure 5.11**, the rupture areas of the 1932-I and 1932-II earthquakes extend to the downdip limit of the seismogenic zone. This rupture pattern took Singh et al. (1985) to conclude that both earthquakes rupture the entire seismogenic zone. A rupture of such characteristics would extend behind the coast, producing coastal coseismic uplift, as it occurred during deep earthquake ruptures of other events along the Mexican pacific (e.g. Bodin & Klinger, 1986; Ramírez-Herrera & Orozco, 2002). Field evidence post-event point out widespread coastal subsidence of 45 – 70 cm (Cumming, 1933). This pattern of coastal land-level change would suggest a shallow rupture, contradicting a rupture extending to the downdip limit of the seismogenic zone. This discrepancy between modelled rupture areas that imply coastal uplift (Singh et al., 1985) and field evidence that reveal coastal subsidence (Cumming, 1933) underpins the second objective of this research: to reconstruct the magnitude of coseismic land-level changes associated with early instrumental earthquakes.

The sedimentary evidence shown in this study reveals the occurrence of coastal subsidence during this event. Due to the location of the Estero Potero Grande wetland, the 1932-II M_w 7.8 earthquake is most likely the event responsible of this land-level change pattern. Diatom-based land-level changes show the magnitude of subsidence between 0.09 ± 0.26 m. and 0.15 ± 0.27 m, being slightly higher than the subsidence, using the same methodology, for the 1995 M_w 8.0 earthquake (0.06 ± 0.73 m. and 0.11 ± 0.74 m). If diatom-based land-level changes are accurate, an explanation of this difference is likely associated to the amount of coseismic slip, considering that this is a key parameter of that influences the magnitude of vertical coastal deformation. Geophysical models indicate that the amount of coseismic slip during the 1932-II (M_w 7.8) earthquake was 2.6 m (Okal & Borrero, 2011). This model assumes an homogeneous rupture for 88 km along-strike (Okal & Borrero, 2011). This magnitude of slip is higher than the magnitude of slip occurred, offshore Estero Potrero Grande, estimated during the 1995 earthquake, which is ~2 m (Melbourne et al., 1997; Mendoza & Hartzell, 1995).

Alternatively, sedimentary process during this earthquake can explain the higher magnitude of subsidence modelled for the 1932 earthquake (M_w 7.8). The wetland Estero Potrero Grande lies 30 km southeast from the rupture limit of the M_w 8.2 earthquake, which occurred fifteen days before the M_w 7.8. An isoseismic map of the

first earthquake demonstrates that the coastal plain of the Marabasco river, where Estero Potrero Grande extends, experienced intensities IX – X (Singh et al., 1985). This pattern of intensities indicate that very strong ground shaking affected this coastal plain. Seismic induced ground shaking promotes sediment compaction and liquefaction in soft sediments with high content of ground water (Obermeier, 2009). The sedimentological properties of basal sediments show the right conditions to favour compaction due to the high content of sand in a highly water saturated environment. Additionally, Estero Potrero Grande could also had experienced coseismic subsidence produced by the first earthquake, as GPS data show that coastal sites adjacent to the earthquake rupture during the Mw 8.0 earthquake of 1995 experienced vertical deformation ~5cm. Lastly, sediment reworking and erosion induced by the inferred tsunami could also amplified the estimated subsidence. However, future research is necessary within the same estuary to confirm these alternative mechanisms of creation.

5.3.7. Tsunami evidence of the 1932 earthquake.

The three earthquakes occurred in 1932 produced tsunamis of different magnitudes. In terms of size, the largest tsunami occurred after the earthquake 1932-I, with a run-up of 10 m, which affected the central part of the Jalisco coast, where the inundation penetrated as far as 8 km inland (Castillo-Aja & Ramírez-Herrera, 2017). The second-largest tsunami, < 9 m high, occurred after the M_w 6.9 1932-III earthquake (Corona & Ramírez-Herrera, 2012; Okal & Borrero, 2011). The worst effects of this tsunami affected 75 km along the south of the Colima coast (Corona & Ramírez-Herrera, 2012; Okal & Borrero, 2011). The smallest tsunami, <1.5 m, occurred after the 1932-II earthquake, which, according to historical data, did not produce significant damages, in comparison to the other two tsunamis (Castillo-Aja & Ramírez-Herrera, 2017; Okal & Borrero, 2011; A. Sanchez & Farreras, 1993). Based on the evidence in this study, it is difficult to indicate which of these three tsunamis left the coarse layer found in this site and more evidence need to be collected at this estuary.

5.4. Conclusion

This study investigated the stratigraphy beneath the Estero Potrero Grande coastal wetland, which preserves the sedimentary record of the 1995 (M_w 8.0) earthquake and

its associated tsunami. The main goal of the current study is to extend the record and find evidence of earlier earthquakes at this coastal site. The stratigraphy of Estero Potrero Grande has a sequence of three beds of silt overlying organic-rich sediments, which were possibly produced by coseismic subsidence, and one sequence of organic-rich sediments abruptly overlying muddy sand. In order to reveal the origin of these sedimentary contacts, diatoms, grain size analysis and geochemistry are used as the main proxies to infer abrupt environmental change. To correlate these contacts with past megathrust events, ^{14}C and ^{137}Cs were used to build a chronological model and estimate the age of the stratigraphic sequence.

From the results obtained in this study, I conclude that:

1) There is only one record, Contact D, associated with a megathrust earthquake, which is correlated with the M_w 7.8 earthquake that occurred on 18th June 1932.
2) Diatom-based palaeoelevation models indicate that during this event, the coast experienced subsidence between 0.09 ± 0.26 m and 0.15 ± 0.27 m.
3) The evidence of the 1932 earthquake is accompanied by a coarse deposit, which could be associated with the largest tsunami in 1932 that struck this coast on 6th June 1932.
4) Evidence of coastal subsidence reported here confirms the limitations of instrumental records during the first half of the twentieth century, suggesting that during the 1932 earthquakes, most of the coseismic slip was offshore, at least in the portion adjacent to the Estero Potrero Grande.
5) The evidence gathered in this study also shows the feasibility of this wetland to record changes associated with the hydrological conditions of the Marabasco River delta. For Contact E, the sedimentary changes suggest channel abandonment of a delta distributary in the lowermost portion of this sedimentary system.
6) The mechanism associated to the origin of Contact C is likely the major hurricane category 4 that struck this coast in 1959.
7) Lastly, the origin of Contact B is possibly associated with the distant tsunami that struck this coast in 1960, caused by the Valdivia M_w 9.5 earthquake in the south of Chile.

CHAPTER 6

LATE HOLOCENE COASTAL UPLIFT AND SUBSIDENCE DURING MEGATHRUST EARTHQUAKES IN THE JALISCO SUBDUCTION ZONE, MEXICO.

ABSTRACT

During the last century, megathrust earthquakes along the Jalisco subduction zone show persistent coastal subsidence, accompanied by tsunamis. This evidence indicates a dominant shallow rupture pattern, with their rupture downdip limit located offshore, causing subsidence, and their updip limit possibly near the trench, producing tsunamis. However, geophysical models indicate that the seismogenic zone extends inland, suggesting the likelihood of this subduction zone to produce earthquakes whose downdip limit can extend deeper, and consequently inland, causing coastal coseismic uplift. This study investigates Late Holocene coastal wetland sediments to understand the evolution of the coast and identify different patterns of coseismic land-level changes.

The results demonstrate the occurrence of two episodes of abrupt coastal uplift prior to 2350 – 2154 cal. yr BP and 1269 – 1219 cal. yr BP. The oldest event is accompanied by a tsunami deposit (S-II), which indicates a wide rupture, likely across the whole seismogenic zone. Additionally, the coast also experienced three episodes of subsidence in 1710-1541cal.yr BP, 1263 – 1151 cal. yr BP and 1108 – 995 cal. yr BP. These events are typical of shallow ruptures, similar to those earthquakes occurred in the last century. Only the event between dated at 1710 - 1541cal.yr BP reveals the occurrence of a high energy deposit associated to a tsunami deposit (S-I). This study demonstrates that different patterns of coastal coseismic land-level changes occurred in the Late Holocene, suggesting that instrumentally recorded earthquakes do not represent the different rupture scenarios and future earthquakes might be bigger.

6.1. Introduction

Onshore deposits on coasts adjacent to subduction zones provide evidence of abrupt coastal environmental changes produced by earthquakes. During megathrust earthquakes, coastal areas adjacent to earthquake ruptures frequently experience vertical land-level changes, causing abrupt changes of sea-level changes (e.g. Atwater, 1987; Hamilton & Shennan, 2005; Long & Shennan, 1994, 1998; Nelson et al., 1998; Pilarczyk et al., 2014; Shennan et al., 2016; Shennan & Hamilton, 2006; Zong et al., 2003). Across multiple earthquake cycles, some coastal areas can experience either coastal subsidence (e.g. Kelsey et al., 2002; Milker et al., 2016) or coastal uplift (e.g. Sawai, 2001; Sawai et al., 2002); whereas some others show alternated events of coastal subsidence and uplift during consecutive earthquake cycles (e.g. Briggs et al., 2014; Dura et al., 2017).

The direction of coseismic land-level changes, either subsidence or uplift, depends on the relative position of the coast with respect to the downdip limit of the megathrust fault rupture (Govers et al., 2017). In tectonic settings where the subducting plate is oceanic and the overriding plate is continental, uplifted regions concentrate above the ruptured areas, whereas regions of subsidence extend landward from the down-dip limit of the rupture (**fig. 6.1)**. The surface projection of the transition from coseismic uplift to subsidence, is referred to as the hinge line (Govers et al., 2017; Melbourne et al., 1997; Meltzner et al., 2006). Thus, coastal subsidence and uplift is diagnostic of the depth extent of faulting (Melbourne et al., 1997), which is a parameter that controls the size of earthquakes (Hyndman, 2007).

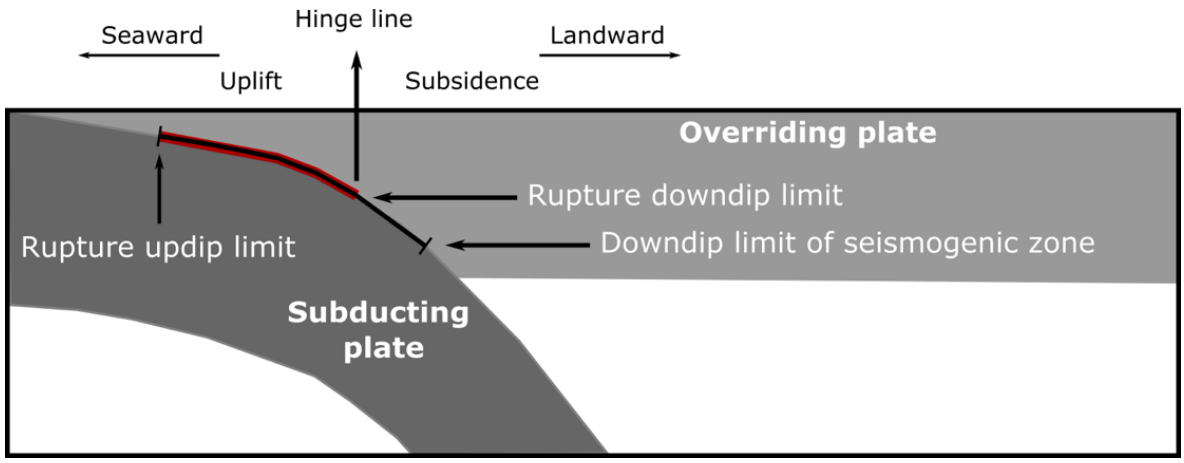

***Figure 6.1**. Cross-section of a subduction zone during a megathrust earthquake. The black line shows the seismogenic zone. The red line represents a hypothetical shallow rupture.*

Along the Jalisco subduction zone, megathrust earthquakes that occurred during the last century show a dominant trend of coastal subsidence caused by slip distributions constrained within 15 – 30 km depth along (Abbott & Brudzinski, 2015; Currie et al., 2002). This pattern of shallow seismicity was consistent during the largest earthquakes in 1932 Mw 8.2 and Mw 7.8 (Okal & Borrero, 2011), 1995 Mw 8.0 (Abbott & Brudzinski, 2015; Hutton et al., 2001; Masterlark et al., 2001) and 2003 Mw 7.6 (Schmitt et al., 2007; Yagi et al., 2004). This dominant trend of coastal subsidence suggests the hinge lines of these earthquakes were located offshore, and most of the coseismic slip was between the trench and the coast (Hutton et al., 2001; Melbourne et al., 1997; Schmitt et al., 2007).

Thermal models of the megathrust fault along the Jalisco subduction zone indicate that the seismogenic zone corresponds to the 350°C isotherm (**fig. 6.2**), being ~75 km wide, with its downdip limit located ~117 km from the trench (Currie et al., 2002). Considering the distance from the shoreline to the trench ranges from 65 to 120 km (Bandy & Mortera, 2012; Melbourne et al., 1997a; Ramírez-Herrera et al., 2004), the seismogenic zone extends beyond the coast and further inland (Currie et al., 2002).

Geological records along the Jalisco coast show evidence of sudden coastal uplift, likely caused by pre-instrumental earthquakes (Castillo-Aja et al., 2019; Ramírez-Herrera et al., 2004). Such evidence suggests different patterns of coseismic land-level changes over a longer timescale, as past earthquake ruptures can be deeper and consequently wider than the most recent earthquakes. The overarching aim of this chapter is to reconstruct the evolution of the coast during the late Holocene in order to identify variable land-level changes produced by megathrust earthquakes in the southern region of the Jalisco subduction zone to infer variable rupture modes.

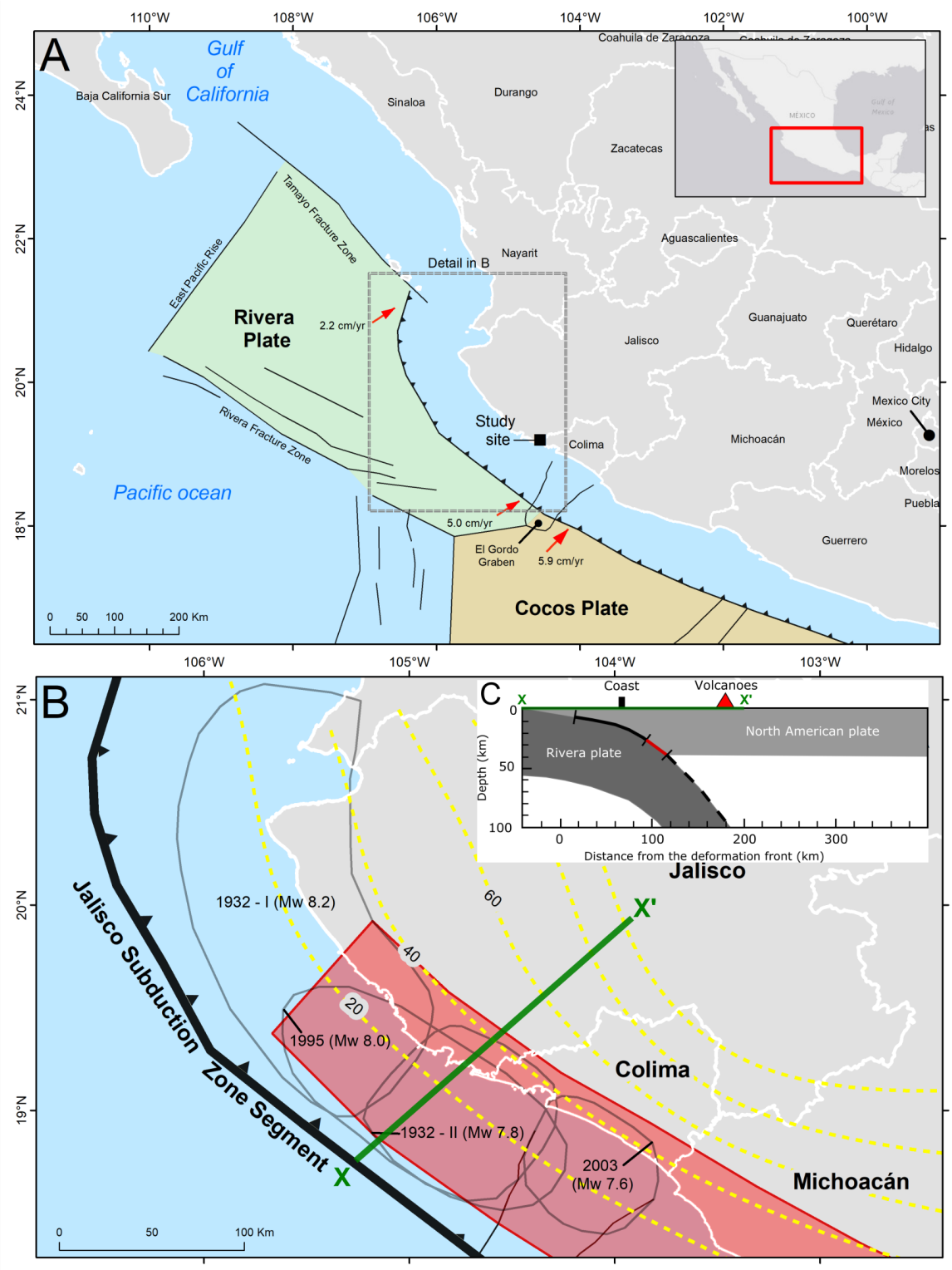

Figure 6.2. *Seismogenic zone of the Jalisco subduction zone. B) The red area shows the extension of the seismogenic zone (from Currie et al., 2002). Dashed yellow lines show depths of the subducting Rivera plate (Hayes et al., 2018). Black circles show the ruptured areas of megathrust earthquakes instrumentally recorded at the beginning of the twentieth century (Kostoglodov & Pacheco, 1999). C) Simplified diagram of the seismogenic region of the southern Jalisco subduction zone. The thick black line indicates the proposed seismogenic zone. The thick red line indicates the transition zone towards the Moho seismogenic zone limit (adapted from Currie et al., 2002).*

6.2. Results

6.2.1. Lithostratigraphy and sediment grain size

Wetland sediments were retrieved in 2019 from a shore-parallel coring transect (**fig. 6.3**), located behind the international airport of Manzanillo. The coring transect reveals three main stratigraphic units: lower, middle, and upper. The stratigraphy of the site is summarised in this section, based on field observations (**fig. 6.4)**, as well as the corresponding sediment grain sizes obtained from the core MAR19006 (**fig. 6.5)**.

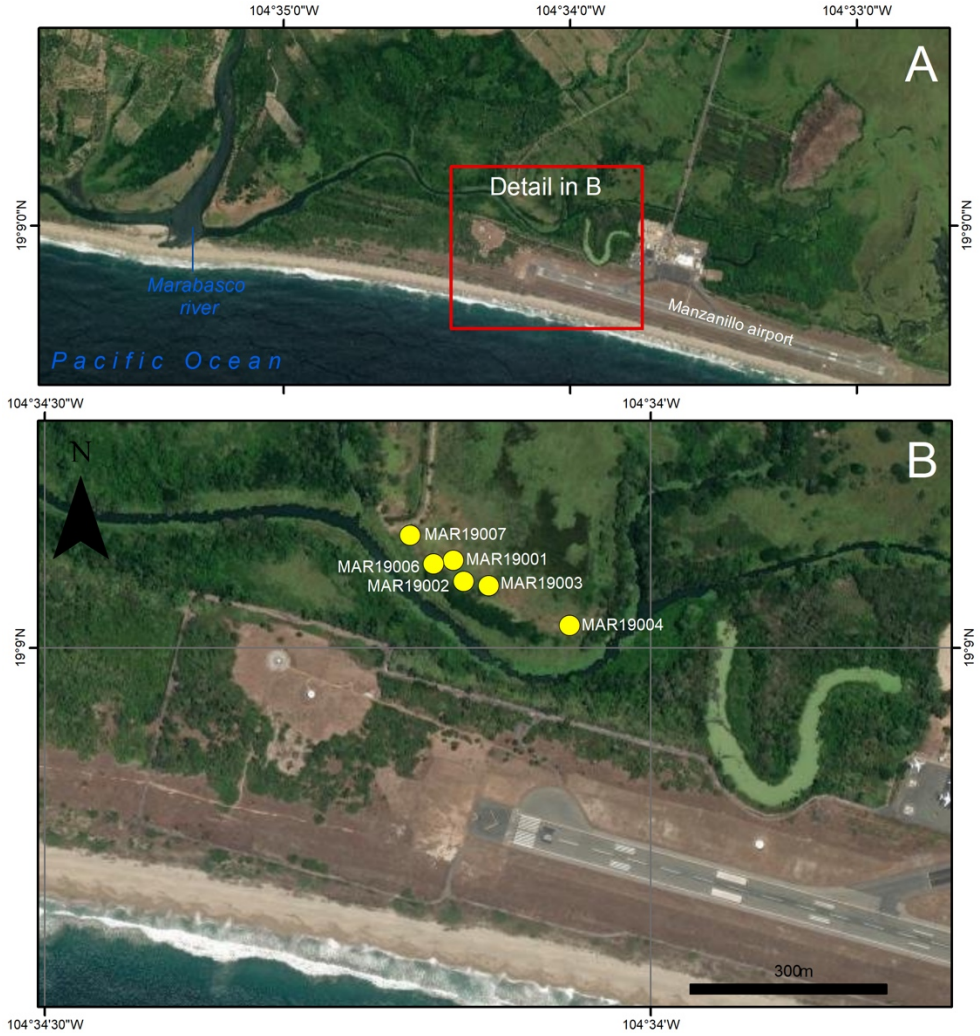

***Figure 6.3**. Location of the coring sites in the coastal wetland Estero Potrero Grande.*

The lower unit is a brown sandy mud with high content of undifferentiated organic debris. This unit was identified between 3.1 and 5 m depth. In most of the cores, we only sampled the upper 50 cm of this unit because it was impenetrable by hand-coring. However, cores MAR19007 and MAR19006 characterise the deepest portion of this

unit. Its lowermost portion (below ~3.7 m depth) is sandy mud, very poorly sorted and polymodal, with sand laminae (< 1 cm). The percentage of sand reaches 40%, but it gradually decreases up-core to reach less than 10%.

At ~4.2 m depth within the lower unit, a thin deposit of coarse sand overlies the lowest laminated organic sand. This deposit, here referred to as S-II, contains up to 40% sand, and is very poorly sorted and polymodal. This deposit has a sharp lower contact with the underlying laminated organic sand. It is between 2 and 4 cm thick, and it was mapped for 57 m along the core transect. Sediments overlying deposit S-II are still rich in sand (~30%) and undifferentiated organic debris; however, sand laminations are absent, suggesting an abrupt change in sedimentation at this point. Above deposit S-II the sediment begins to fine upwards, grading into poorly sorted, very fine silt.

Between 3.7 and 4.0 m (still within the lower unit) another coarse deposit, here named S-I, was identified. This deposit shows an abrupt increase in sand fraction, reaching up to 30%. This deposit is classified as very fine sandy silt, polymodal and very poorly sorted. In comparison with the deposit S-I, the basal contact of S-I is less sharp. Within this deposit, there are fragments of the worm shells *Vermicularia pellucida* and *Serpulorbis margaritaceous* (**fig. 6.5A**).

The upper portion of the lower stratigraphic unit is characterised by a gradual reduction in sand (< 20%), and the increase of poorly sorted and bimodal fine silt. Additionally, there is a gradual increase in paired bivalves of the genus *Mytilus* (**fig. 6.5B**). This change in sediment grain size is the transition to the middle stratigraphic unit .

This siliclastic unit with paired bivalves is abruptly replaced at ~3.2 m depth by peat with high content of wood fragments (~5 cm in length) and plant remains, as well as fine silt. Within this organic unit there is an abrupt reduction in bivalves. This stratigraphic transition is labelled as Contact J, and it is correlated along ~290 m of the coring transect.

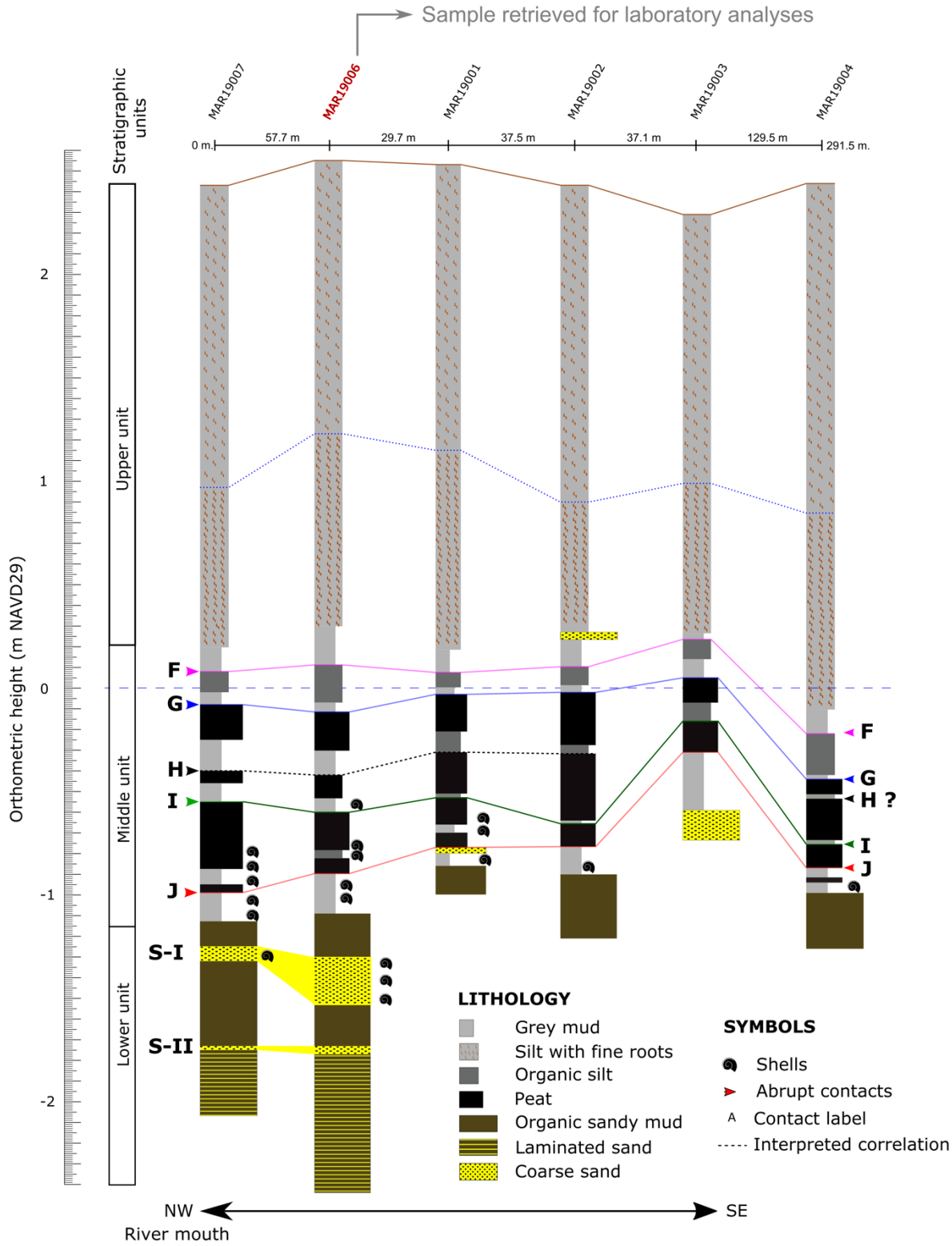

***Figure 6.4**. Summary of the stratigraphy of the coring transect at Estero Potrero Grande.*

This peat layer overlying Contact J is gradually replaced by grey silty clay. This siliclastic unit has increased occurrences of *Mytilus* spp and the gastropod *Neritina latissims* (**fig. 6.5C**). Upwards in the core, these fine sediments are gradually replaced

by brown peat with plant remains and wood fragments. The density of macrofossils is higher in the cores located at the NW end of the transect. At the opposite end of the transect, cores contain more humified organic matter. The peat is abruptly overlaid by a grey bed of medium silt, very poorly sorted, with a slight increase in sand (~10%). This silty unit contains fragments of broken shells in its basal portion. The stratigraphic transition is here referred to as Contact I, which was traced for ~290 m along the coring transect.

The minerogenic unit overlying Contact I is less than 10 cm thick. It gradually becomes a brown medium silt with ~50 % fragments of plants and wood. Between 2.1 and 3.0 m depth across the transect, this organic unit is sharply overlaid by a grey coarse silt with ~20 % sand. This stratigraphic contact is Contact H. The lateral continuity of Contact H is restricted to four cores located at the northwest end of the transect.

The minerogenic unit immediately above Contact H becomes progressively organic up core. This organic unit is on average 18 cm thick and is composed of plant fragments with occasional wood fragments (< 10%). In comparison with the previous organic units, this unit shows a higher minerogenic content (> 50%), classified as very unimodal and poorly sorted fine silt, with a little sand (< 1%). This organic silt is overlaid sharply by grey fine silt with occasional fine roots. This transition is Contact G, which is on average at 2.5 m depth within the cores and is traced along 290 m of the coring transect.

Up-core the grey silt above Contact G gradually grades into a dark grey organic silt with fragments of leaves and wood (< 1 cm). Between 1.4 and 2.7 m depth across the transect another grey fine silt with organic matter and occasional roots overlies abruptly this organic rich unit. This is Contact F, which is mapped across the whole coring transect.

Roughly 15 cm above Contact F, sediments are predominantly silt, with very fine roots, smaller than 0.5 cm. Upwards in the core until the modern land surface, there is not any stratigraphic change. These sediments are interpreted as infilling deposits of the former aquaculture ponds. These deposits are labelled as the upper stratigraphic unit.

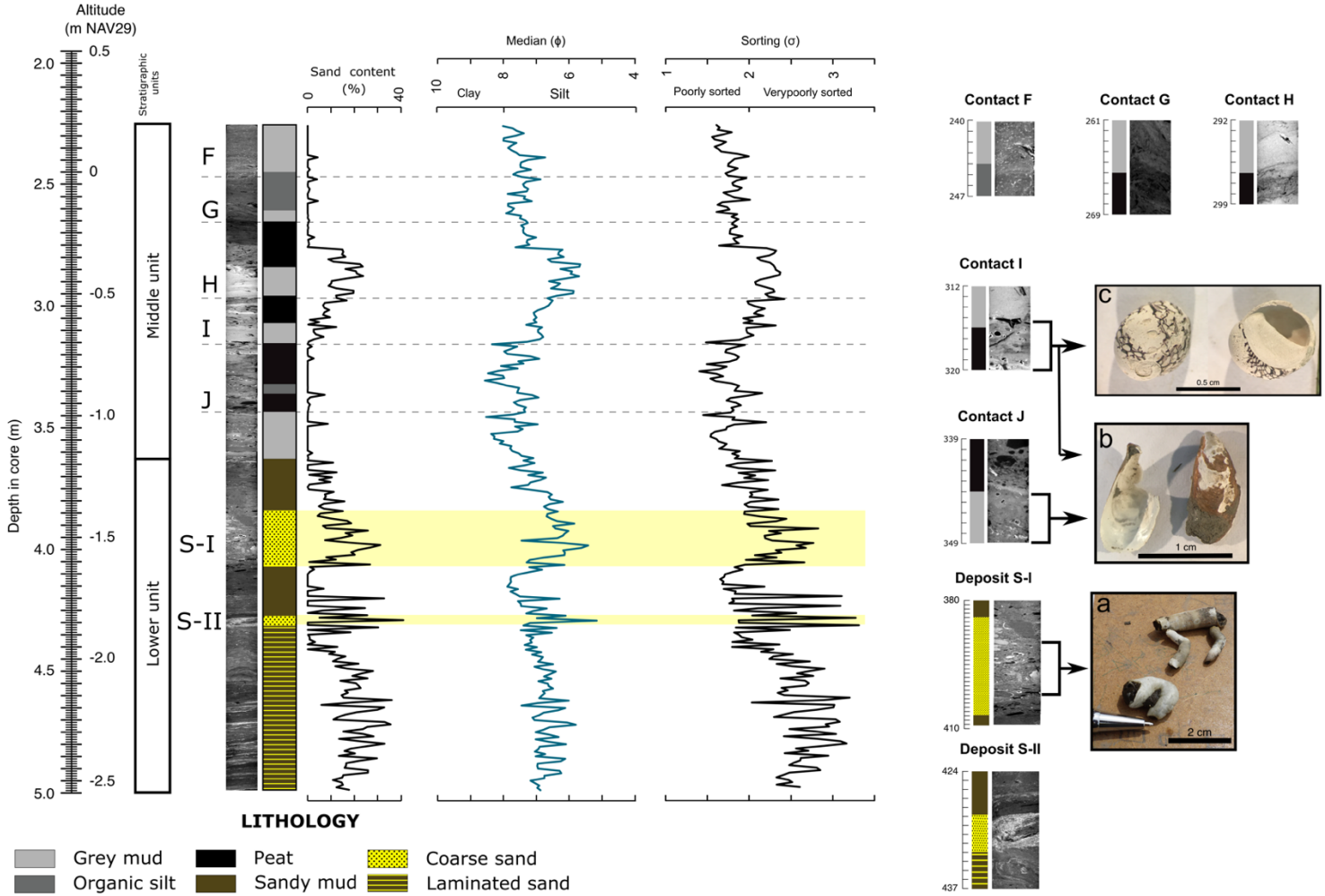

***Figure 6.5**. Downcore fluctuations in sediment grain size parameters. including CT images in grey scale of core MAR19006 and the position of stratigraphic contacts (with additional expanded images of contacts). Images of selected gastropods and bivalves also shown as follows: **a)** Fragments of Vermicularia pellucida and Serpulorbis margaritaceous found in the sand deposit S-II; **b)** Paired bivalves, Mytilus sp. found in the lowermost portion of the middle stratigraphic unit; **c)** Neritina latissimi found in the peat layers within the middle stratigraphic unit*

6.2.2. Biostratigraphy

There are 207 species of fossil diatoms identified in the core MAR19006. These diatom species correspond to marine (26%), brackish (22%), and freshwater species (47%). The summary of diatom assemblages considers only those species which abundances is > 5% in at least 5 of 266 samples (**fig. 6.6**). The description of the relative abundance of species focuses on the sand deposits S-I and S-II and across the contacts F to I.

The lowermost portion of the core MAR19006 shows a composition of diatoms, slightly dominated by freshwater species (~40%), e.g. *Cyclotella meneghiniana,* followed by brackish (~30%), e.g. *Cyclotella striata and Bacillaria paxillifer*, and lastly marine species (~30%), including *Paralia sulcata* and *Nitzschia grossestriata*. All these species are planktonic, with the exception of *N. grossestriata*.

Below the sand deposit S-II, between 4.6 and 4.35 m depth, benthic diatoms of all salinity classes begin to dominate the assemblages, e.g. *A. proteus, A. coffeaformis, N. fonticola, C. placentula*. Within the sand deposit S-II, although there is a mix of diatom species, the most common species is *N. grossestriata* (20%). Overlying the sand deposit S-II, the planktonic freshwater species *Cyclotella meneghiniana* (50%) dominates the assemblages.

Below the sand deposit S-I, sediments are still dominated by *C. meneghiniana* (24 – 42%), but with the increase of other freshwater species such as *Nitzschia fonticola* (3–10%) and *Cocconeis placentula var. euglypta* (5–7%). At 4.0 m depth, at the bottom of the sand deposit S-I, brackish species double their relative abundance, from ~20% to >40%. The most common species within the deposit S-I are *Tabularia fasciculata (10–17%) and Cyclotella striata (9–13%).*

Below Contact J, marine diatoms e.g. *Amphora proteus* (5 – 8%) and *Cocconeis pinnata* (4 – 7%); and brackish diatoms, e.g. *Cyclotella striata* (19 – 25 %) and *Bacillaria paxillifer* (4 – 9%), sum up to 70% of the assemblage. Above this contact, diatom assemblage shows an abrupt increase in freshwater species (Error! Reference source not found.), which reach up to 60% of the assemblages. The most common

species are benthic, such as *Nitzschia fonticola* (14 – 21%), *Cocconeis placentula* (4 - 8%), *Nitszchia dissipata* (1 – 7%) and the planktonic species *Cyclotella meneghiniana* (5 – 12%). Below the Contact I, the planktonic brackish species *C. striata* is dominant, reaching up to 53% of the total assemblage, followed by freshwater species, which sum up to ~40% of the total assemblage. The most common freshwater benthic species are *N. fonticola* (3 – 7%) and *C. placentula* (4 – 6%), and the planktonic species is *C. meneghiniana* (18 – 22%). Marine species below Contact I are on average ~20%, but their relative abundance increases abruptly up to 70% above this contact. The most abundant marine species overlying Contact I are planktonic, including *P. sulcata* (12 – 31%) and *C. litoralis* (15 – 22%), followed by the benthic marine species *N. grossestriata* (4 – 7%) and *C. pinnata* (4 – 6%).

Sediments below Contact H are characterised by brackish (~50%) and freshwater (30%) diatoms, including the planktonic species *C. Striata* (25 – 29%) and *C. meneghiniana* (4 – 27%), respectively. The overlying sediments show an abrupt increase of freshwater diatoms (up to 70%), being the most common species *C. meneghiniana* (26 – 49%), followed by the brackish planktonic species *C. striata* (17%) and *B. paxillifer* (10%).

As found below Contact G, diatom assemblages are predominantly freshwater species (45%), e.g. *C. placentula* (5 – 10%), *N. fonticola* (2 – 6%) and *C. meneghiniana* (2 – 6%). The most common brackish and marine species are *C. striata* (18 – 30%) and *C. pinnata* (1 – 8%), respectively. Above this contact, there is an increase of brackish species, from approximately 40% to > 60%. The most common species are *T. fasciculata* (13 – 15%), *R. gibberula* (5 -10%) and the planktonic species *C. striata* (13 – 51%).

The unit immediately below Contact F is dominated by freshwater diatoms (50 - 72%), dominated by *C. meneghiniana* (14 – 18%), *Cocconeis placentula* (4 – 7%), and lower numbers of the brackish species (~30%) including *B. paxillifer* (4 – 12%), *T. fasciculata* (3 – 8%) and *R. gibberula* (3 – 8%). Above the contact, there is an abrupt increase of brackish species (40%), e.g. *B. paxillifer* (6 – 26%) and *T. fasciculata* (5 – 8%); and marine species, including *P. sulcata* (7 – 12%) and *N. grossestriata* (1 – 5%).

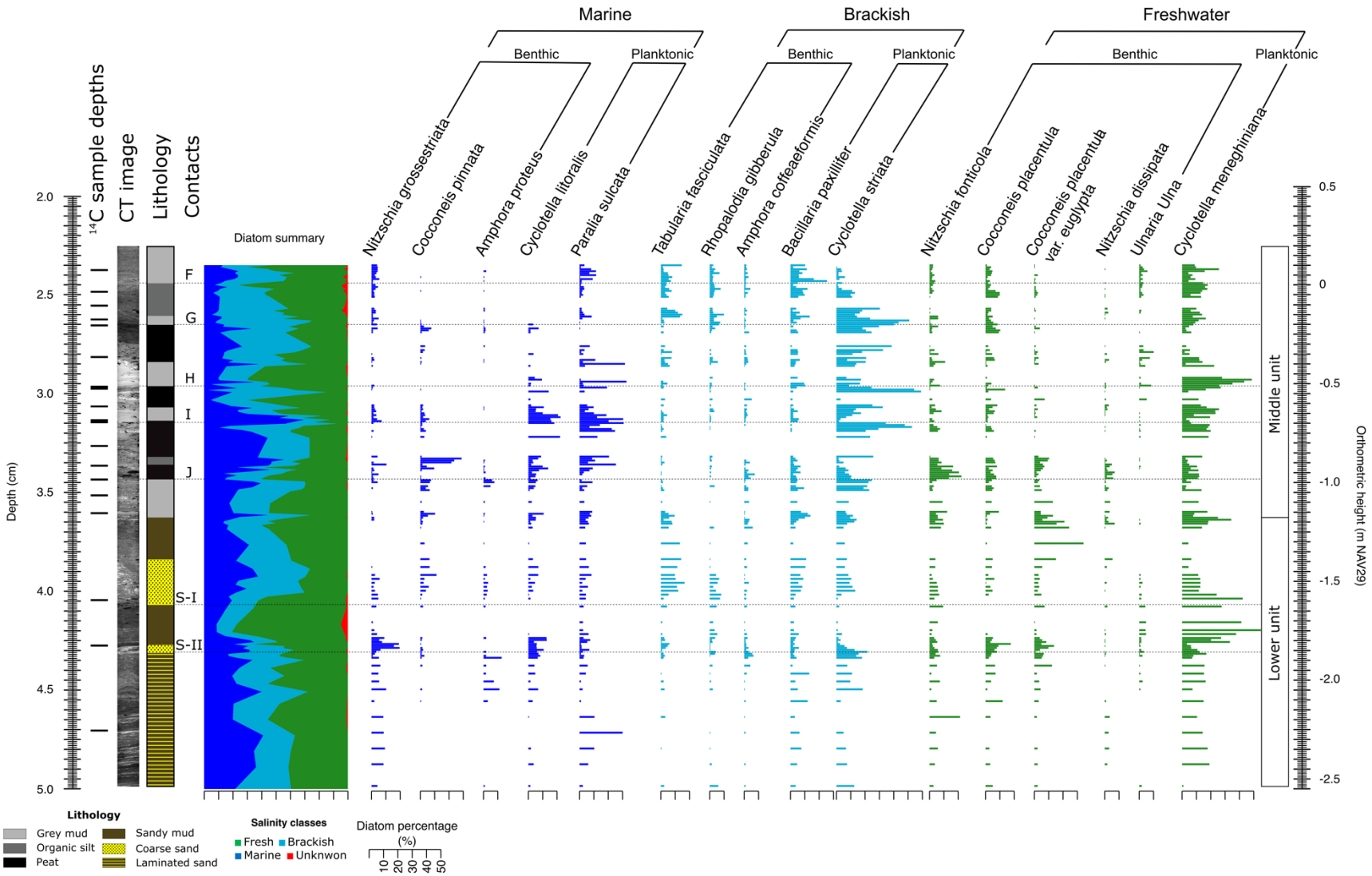

***Figure 6.6**. Biostratigraphy of the core MAR19006, showing diatom species that account for 5% of the total valves counted in at least 5 samples.*

6.2.3. Diatom-based palaeoelevation changes.

The sum of brackish and marine diatoms were used to estimate palaeoelevations using the linear models built in Chapter 2. To quantify land-level changes, only those samples bracketing the stratigraphic contacts F to J, between 3.29 - 2.35 m depth, were considered in this analysis. Palaeoelevations are relative to the Mean Higher High Water (m MHHW).

According to Model 1, hereafter referred as M1, palaeoelevations fluctuate between -0.02 and +0.12 m MHHW. On the other hand, palaeoelevations obtained from Model 2, or M2, oscillate between -0.11 and +0.13 m MHHW (**fig. 6.7**).

Below the Contact J, the sum of brackish and marine diatoms is ~70%. Hence palaeoelevations obtained from are +0.03 ± 0.26 m MHHW, M1, and -0.04 ± 0.27 m MHHW, M2. Above the Contact J, the percentage of brackish and marine diatoms decreases to ~40%, what suggest an increase of palaeoelevations, to +0.09±0.26 m MHHW (M1) and +0.07 ± 0.27 m MHHW (M2). The resulting land-level change of the is +0.06 ± 0.26 m (M1) and +0.11 ± 0.26 m (M2).

The percentage of brackish and marine diatoms below the Contact I is slightly higher than 60%. Palaeoelevation at these depths are +0.03 ± 0.26m MHHW (M1) and -0.03 ± 0.27 m MHHW (M2). Above this stratigraphic contact, the relative abundance of brackish and marine species increases abruptly, reaching 91% immediately above the contact. Thus, palaeoelevations decrease abruptly to -0.02 ± 0.26 m MHHW (M1) and -0.11 ± 0.27 m MHHW (M2). Subsequently, the land-level change is -0.05 ± 0.26 m (M1) and – 0.08 ± 0. 26 m (M2).

Regarding the Contact H, the percentage of brackish and marine diatoms underlying this contact are > 55%. Palaeoelevations below the contact are +0.05 ± 0.26 m MHHW (M1) and +0.01 ± 0.27 m MHHW (M2). Above Contact H, the sum of brackish and marine diatoms decreases gradually to reach 30% some centimetres above this contact. Thus, palaeoelevations are +0.09 ± 0.26 m MHHW (M1) and +0.07 ± 0.27 m MHHW (M2). This suggests a land-level change of +0.04 ± 0.26 (M1) and +0.06 ± 0.26 (M2).

The relative abundance of brackish and marine diatoms below Contact G is on average ~60%. Palaeoelevations, 1 cm below the contact, are +0.05 ± 0.26 m MHHW (M1) and +0.01 ± 0.27 m MHHW (M2). Above Contact G, the percentage of brackish and marine diatoms reach up to 65%, and new palaeoelevations are +0.04 ± 0.26 m MHHW (M1) and -0.02 ± 0.27 m MHHW (M2). Hence, the maximum land-level change recorded is -0.01 ± 0.26 (M1) and 0.03 ± 0.26 m (M2).

Lastly, below the Contact F, diatom assemblages show the relative abundance of brackish and marine diatoms ~30%, suggesting palaeoelevations +0.09 ± 0.26 m MHHW (M1) and +0.08 ± 0.27 m MHHW (M2). Above the contact, diatom species show an abrupt increase of brackish and marine species, which are >56%. Palaeoelevations above this contact reach +0.06 ± 0.26 m MHHW (M1) and +0.02 ± 0.27 m MHHW (M2). Consequently, land-level changes are -0.04 ± 0.26 m (M1) and -0.06 ± 0.26 m (M2).

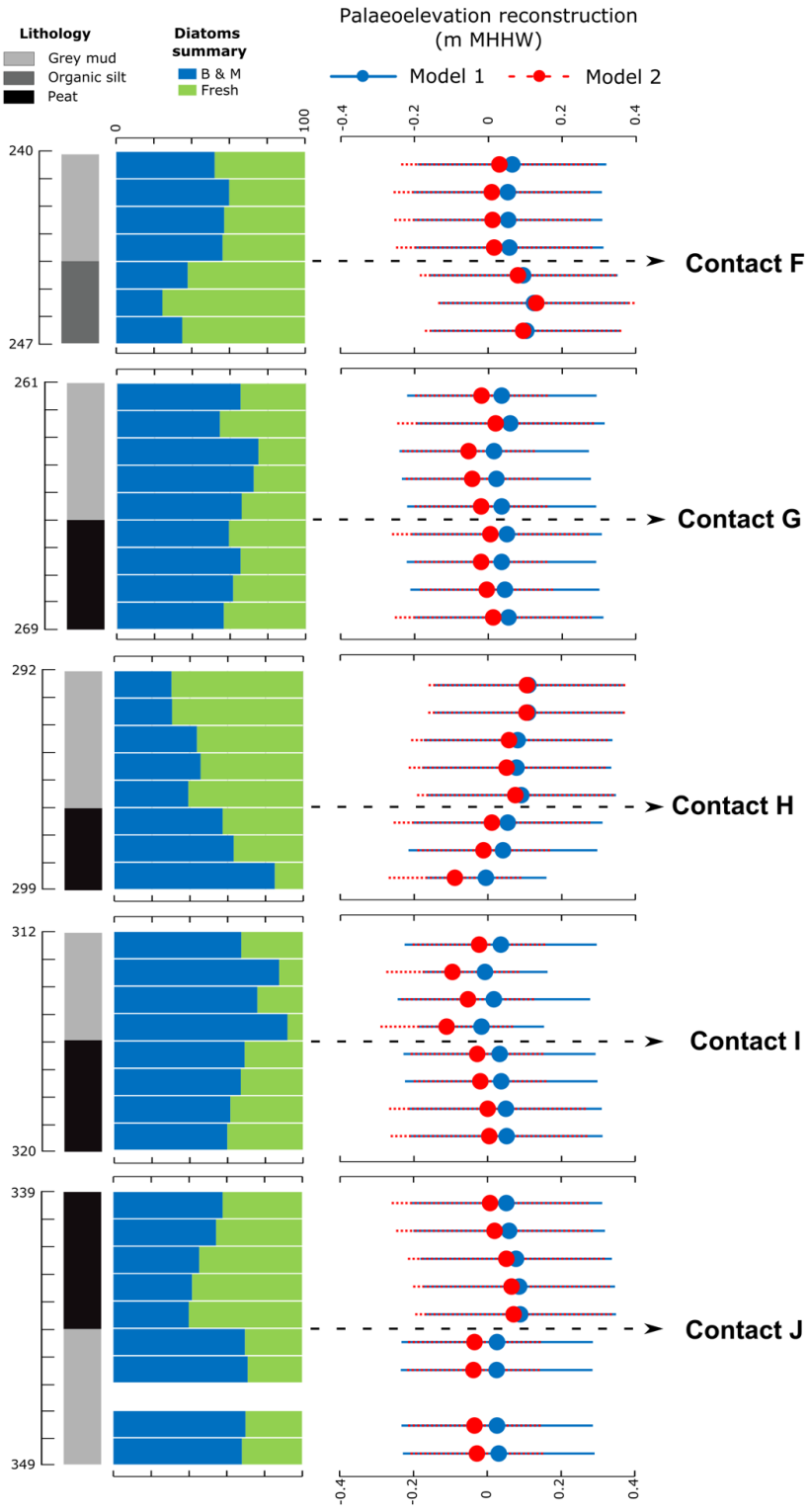

***Figure 6.7**. Palaeoelevation reconstructions of the stratigraphic contacts F to J, showing the summary of the percentage of brackish and marine diatoms, corresponding to the dependent variable in the linear model to estimate palaeoelevations, as developed in Chapter 2.*

6.2.4. Chronology

Nineteen samples were submitted for AMS radiocarbon dating (**table 6.1**). These samples were collected between 237 – 470 cm depth . All dated material consists of plant fragments, except for the sample SUERC-97315, which uses seeds of *Distichlis spicata*. All dates were included In the Bayesian age-depth model as no outliers were identified. The input in this model consisted of the parameter k = 1, and five boundaries, as *C_boundary* (), assigned in those depths where significant lithostratigraphic changes occur. The calibration curve was IntCal20 (Reimer et al., 2020).

***Table 6.1**. Radiocarbon sample results. Calibrated and modelled ages from OxCal.*

Stratigraphic position (cm)	Laboratory code	Sample number	IRMS $\delta^{13}C$ (‰)	^{14}C Enrichment (± 1σ % modern)	Conventional radiocarbon age (years BP ± 1σ)	Calibrated age range (2σ years BP)	*P_sequence* modelled age (2σ years BP)	Agreement index
237.50	SUERC-97334	MAR19006_19	-28.7	86.87 ± 0.26	1130.82 ± 37	1177-956	1108-955	114.2
248.50	SUERC-97330	MAR19006_18	-29.3	86.93 ± 0.26	1125.45 ± 37	1177-955	1112-995	103.3
255.5	SUERC-97329	MAR19006_17	-28.9	86.46 ± 0.26	1168.98 ± 37	1178-973	1111-1023	106.2
262.5	SUERC-97328	MAR19006_16	-27.9	86.71 ± 0.26	1145.94 ± 37	1178-958	1123-1050	79.4
265.5	SUERC-97327	MAR19006_15	-28.2	86.05 ± 0.25	1206.67 ± 37	1267-1000	1129-1059	117.3
281.5	SUERC-97326	MAR19006_14	-28.9	86.19 ± 0.25	1194.15 ± 37	1248-978	1176-1099	116.1
296.5	SUERC-97325	MAR19006_13	-26.8	85.24 ± 0.25	1282.49 ± 37	1293-1122	1235-1120	80.1
297.5	SUERC-97324	MAR19006_12	-29.9	85.65 ± 0.25	1244.26 ± 37	1275-1070	1235-1125	100.9
306.5	SUERC-97320	MAR19006_11	-29.9	84.86 ± 0.25	1318.44 ± 37	1300-1176	1247-1176	87.1
313.5	SUERC-97319	MAR19006_10	-27.0	86.1 ± 0.22	1202.28 ± 35	1260-1000	1263-1151	38.9
314.5	SUERC-97318	MAR19006_9	-27.7	85.56 ± 0.22	1253.09 ± 35	1280-1073	1264-1153	138.4
326.5	SUERC-97317	MAR19006_8	-28.0	85.49 ± 0.25	1259.02 ± 37	1284-1073	1265-1183	135.3
336.5	SUERC-97316	MAR19006_7	-28.3	85.09 ± 0.25	1296.76 ± 37	1296-1130	1265-1213	93.7
343.5	SUERC-97315	MAR19006_6	-23.6	85.88 ± 0.22	1222.4 ± 35	1270-1061	1269-1219	60.9
351.5	SUERC-97310	MAR19006_5	-27.4	85.58 ± 0.25	1250.74 ± 37	1278-1073	1275-1223	115.1
360.50	UCIAMS-244081	MAR19006_4			1295 ± 15	1285-1176	1285-1221	84.5
404.50	Beta-574923	MAR19006_B	-27.5		1700 ± 30	1697-1532	1623-1525	106.3
427.5	SUERC-97309	MAR19006_2	-27.4	80.08 ± 0.21	1784.87 ± 35	1746-1569	1820-1657	78.5
470.5	Beta- 574924	MAR19006_C	-28.4		2280 ± 30	2350-2157	2350-2154	88.1

The output of the *P_sequence* model using all of the ^{14}C data developed in Oxcal shows a good fit with an overall Agreement index of 67 (**fig. 6.8**). Based on these radiocarbon dates, core MAR19006 records the accumulation of sediments between 2350 and 956 cal. yr BP. Ages of the two lower sand deposits and the stratigraphic contacts A to E are reported as maximum ages, below the contact or deposit, and minimum ages, below the contact or deposit (**table 6.2**).

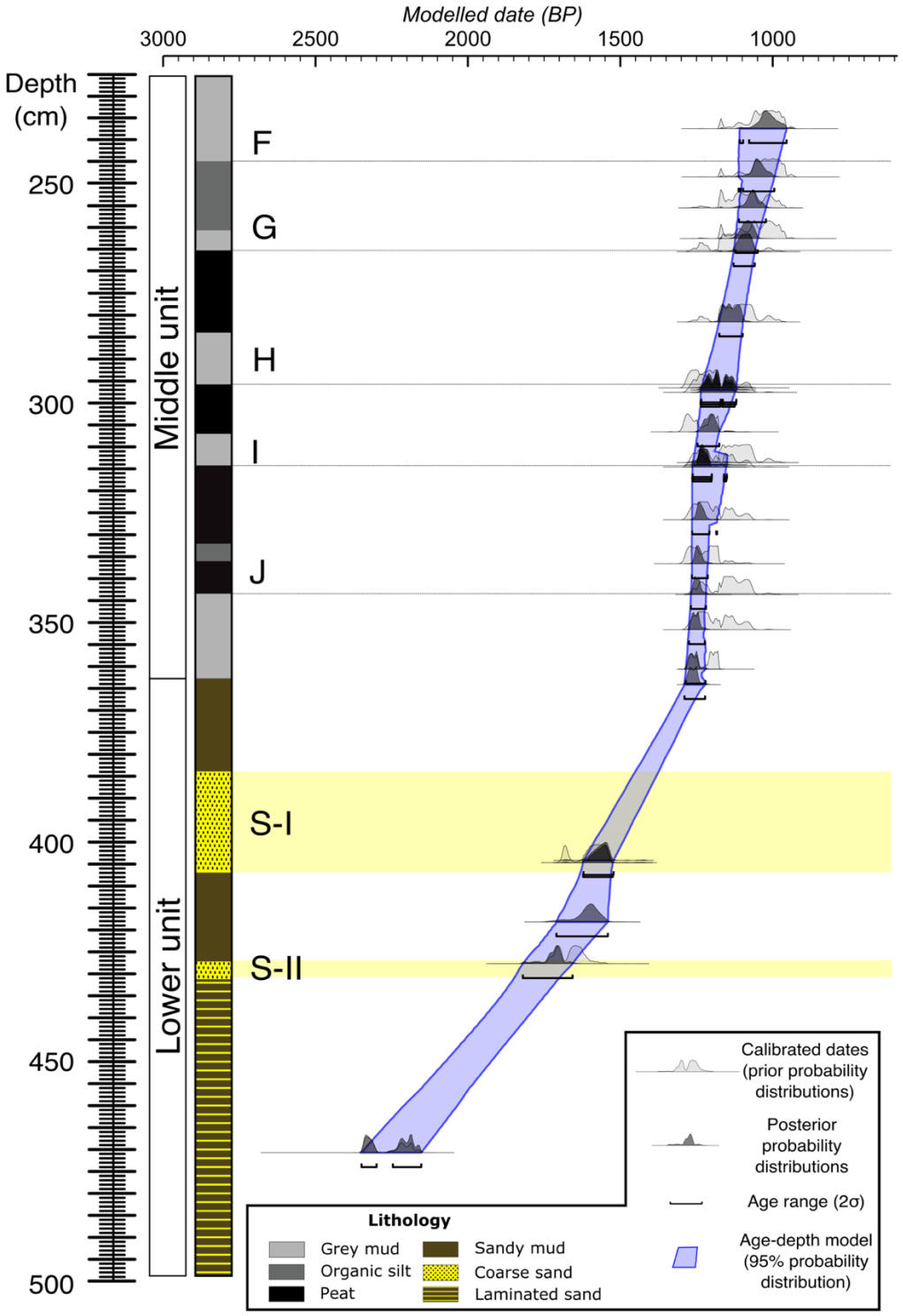

***Figure 6.8**. Output of the Bayesian age-depth model for the core MAR19006.*

***Table 6.2**. Radiocarbon ages for the sand deposits (S-I and S-II) and stratigraphic contacts F to J in core MAR19006. Maximum ages (Max) correspond to samples taken below each event. Minimum ages (Min) correspond to samples taken above each event.*

Deposit or contact	Age range (2σ, cal. yr BP)	
F	Min	1112-995
	Max	1111-1023
G	Min	1129-1059
	Max	1176-1099
H	Min	-----
	Max	1237-1121
I	Min	1264-1151
	Max	1265-1183
J	Min	1269-1219
	Max	-----
S-I	Min	-----
	Max	1710 - 1541
S-II	Min	1820 - 1657
	Max	-----

6.3. Discussion

In this discussion I give a palaeoenvironmental interpretation of the fossil record from the core MAR19006 to understand the coastal evolution between ~2500 and 955 cal. yr BP. I focus on the sedimentological properties associated to the deposits S-I and S-II (table 6.3) and contacts F to J (table 6.4), in order to reveal their origin, likely coseismic, associated to the Jalisco Subduction Zone.

6.3.1. Lower stratigraphic unit

The bottom of lower unit contains laminae of medium to coarse sand. The frequency and thickness of these sand laminae (< 0.5 cm) suggests periodic high energy deposition, possibly associated to storms. The age at the bottom of the stratigraphic section is 2502 - 2301 cal. yr BP. At this time, some coastal wetlands along the Mexican Pacific were already sheltered by coastal barriers and the shoreline was prograding (e.g. Bianchette et al., 2017; Caballero et al., 2005; Curray & Moore, 1963; Joo-Chang et al., 2015; Sirkin, 1985). However, between 2500 – 1700 cal. yr BP, the

Pacific coast experienced a period of high intensity El Niño-Southern Oscillation (ENSO; Barron & Anderson, 2011; Moy et al., 2002). Along the Mexican Pacific, strong ENSO is typically associated with warm conditions (e.g. Joo-Chang et al., 2015; Pérez-Cruz, 2006) and periods of increased storminess (e.g. Masters, 2006; Odériz et al., 2020). During strong ENSO, the North American Pacific coast beaches commonly face erosive conditions, providing sediments that infill estuaries and back-barrier basins (e.g. Masters, 2006). This period of storminess supports the hypothesis of storm deposition, represented by the sandy laminations at the bottom of the stratigraphy in this study site.

This period of frequent storms would promote coastal breaching and morphological alteration along the coastal barrier. Biostratigraphy at the bottom of the core sediments, show well-mixed diatom assemblages, ~30% each salinity class, with abundant planktonic species (e.g. *P. sulcata, C. striata, B. paxillifer* and *C. meneghiniana*). These conditions resemble an open estuary, where well-mixed diatom assemblages represent the constant exchange of fluvial and tidal fluxes (e.g. Zong et al., 2006). Hence, based on the diatom assemblages and sediment grain sizes, this site after 2500 cal. yr BP was most likely an open estuary highly influenced by recurrent storms.

Since 2110 - 1956 cal. yr BP, the sand laminae became thinner, and the content of sand decreases gradually to reach its minimum in 1899 – 1755 cal. yr BP. The gradual reduction of sand during this period was accompanied by increasing organic matter and the gradual establishment of benthic marine diatoms such as *A. proteus* and *N. grossestriata.* These two diatom species are associated with fringing mangroves of coastal lagoons in the northwest Mexican Pacific (Beltrones & Fuerte, 2006; Siqueiros-Beltrones et al., 2017). These sedimentological features suggest the gradual transition from an open estuary to a relatively calmer environment, likely a lagoonal estuarine environment. These conditions are coincident with the end of the strong ENSO period (~1700 cal. yr BP).

In this transient lagoonal estuarine palaeoenvironment, two anomalous sandy beds, S-I and S-II, were deposited. Their sedimentological properties indicate that both deposits are associated to high energy events. In order to reveal their origin, and considering the palaeoenvironmental characteristics, I rely on the stratigraphic criteria

used to identify (palaeo-) tsunami deposits in coastal lakes (e.g. Kelsey et al., 2005; Kempf et al., 2015, 2017). The stratigraphic criteria here considered (**table 6.3**) include:

1) the lateral extent of a sand deposit, obtained from correlation of sand deposits using field data.

2) Features of its basal contact, obtained from field evidence and CT scanned images for better resolution.

3) Presence of rip-up clasts revealed by CT scanned images.

4) Sediment grading, assessed by sediment grain sizes to infer finning upward structures.

5) Presence of a mud cap, evidenced by sediment grain size analyses.

6) Evidence organic debris revealed by CT scanned images.

7) Presence of marine diatoms, revealed by the analysis of diatom assemblages.

***Table 6.3**. Summary of the tested criteria for deposits S-I and S-II.*

Deposit	Lateral extent (m)	Basal contact	Rip-up clast	Fining upward	Mud cap	Organic debris
S-II	56	Sharp to erosional	✓	✓	✓	✓
S-I	56	Sharp	✓	✓	✖	✓

6.3.1.1 Deposit S-II

This deposit was mapped for around 56 m. In core MAR19006, S-II is a 5 cm thick bed of coarse sediments with a high content of sand (>40%). The depositional event was most likely a high-energy and high-velocity event, due to the signs of moderate erosion in its sharp basal contact, as well as the presence of an interbedded layer of mud with organic debris, which resemble rip-up clasts (**fig. 6.9**). Overlying S-II, a thin cap (~2 cm) of organic mud represents the abrupt change of flow velocity during deposition (e.g. Kelsey et al., 2005; Wilson et al., 2014). The content of organic debris within this

mud cap is more likely material reworked during the turbulent behaviour of the depositional event. The increase of marine and brackish diatom species, dominated by the marine species *N. grossestriata*, reveal the association of S-II with a marine incursion.

Based on the criteria used in this investigation to discriminate the tsunami origin of anomalous deposits in Estero Potrero Grande (**table 6.3**), the sedimentary features of S-II point out to a tsunami as the most probable event that deposited S-II. Indeed, the features of the sediments bracketing S-II show evidence of an abrupt change of the sedimentary and palaeoenvironmental conditions after the deposition of S-II, which were most likely produced by an abrupt land-level change.

Below the deposit S-II, C.T. scan images reveal the presence of highly laminated sediments, composed by sand interbedded with mud. These deposits were interpreted as the signature of an open estuary, highly influenced by tides and storm events. Immediately after the deposition of S-II, these laminated sediments disappear abruptly. This sudden and permanent change reveal an alteration of the dominant sedimentary processes. This change in the sedimentary regime is accompanied by an abrupt change of diatom assemblages, which reveal a sudden and long-lasting transition to a freshwater environment. The diatom species *C. meneghiniana,* which lives in the upper reach of estuarine environments (Zong et al., 2006), dominates the assemblages. These sedimentary and palaeoenvironmental change indicate the abrupt departure of the coring site from marine conditions, which can be explained by sudden coastal uplift. The same stratigraphic sequence was associated to coseismic uplift accompanied by a tsunami in a similar geomorphic context in New Zealand (e.g. Pizer et al., 2021).

Coastal uplift suggests that the earthquake rupture was beneath the coast. Evidence of the proximity of the coring site to the seismic source is revealed by the C.T. scan images. The underlying laminated unit shows patterns of deformed sediments, such as folded and vertically intruded structures. These patterns of sediment deformation resemble those produced by seismically-driven liquefaction, which occurs in water saturated deposits, rich in sand inter-bedded with mud (Owen & Moretti, 2011). This evidence of sediment liquefaction indicates the strong ground shaking due to the proximity of the coast to the seismic source.

Because S-II is associated to a marine incursion, an alternative hypothesis to explain its origin is associated to a storm surge driven by a tropical cyclone. The age-depth model indicates that this site did not experience the deposition an extreme wave event, like the deposit S-II, in a period of at least 500 years. This period doubles the average return period, ~300 years, of major tropical cyclones along the Mexican Pacific coast (Bianchette et al., 2022). The time of deposition of S-II (1820 - 1657cal. yr BP) corresponds to the last stage of a period of high storminess in the Mexican Pacific, influenced by ENSO. During the last stage of this period, evidence from the core MAR19006 suggest that this site experienced a gradual decrease of tidal and storm activity, most likely caused by an overall trend of coastal progradation that favoured the widening of the coastal barrier, isolating the coring site from shore processes. It is in this geomorphological context where S-II could be deposited by a storm.

Thus, if S-II was deposited during a tropical cyclone, this event should have produced an extraordinarily high storm surge that breached the coastal barrier, facilitating the penetration of waves in the back-barrier region to produce the sharp to erosive basal contact of S-II. This mechanism of deposition more likely produced significant geomorphological changes along the coastal barrier, such as breaching and overwash, producing an abrupt increase of marine and brackish conditions above the deposit S-II. However, storm surge deposits are frequently characterised by non-erosional basal contacts due to their lower inundation velocity (Switzer & Jones, 2008). Additionally, diatom assemblages overlying S-II do not show an increase of marine and brackish conditions above the deposit S-II. Instead, freshwater diatoms dominate the assemblages. Although extreme waves deposit can build sand ridges that isolate back-barrier wetlands or lagoons from marine conditions, this type of morphological changes are commonly associated to tsunami events (e.g. McCloskey et al., 2015; Yao et al., 2021).

The internal structure of S-II contain sand laminae abruptly interbedded with mud and organic debris. Storm deposits commonly present sand laminations (e.g. Morton et al., 2007; Switzer & Jones, 2008) produced by the rhythmic pattern of short-period inundation pulses (Goslin & Clemmensen, 2017; Switzer & Jones, 2008). Nonetheless, storm deposits hardly contain interbedded mud layers and organic debris (Morton et al. 2007).

The sedimentary features of S-II unconvincing to argue that a tropical cyclone deposited S-II. Hence, based on the sedimentary evidence associated to S-II and the features of the bracketing deposits, the most plausible mechanism of creation to explain the origin of S-II is a tsunami deposit that accompanied a megathrust earthquake, which more likely produced coastal uplift. Although, there is not any palaeoseismic record along the Mexican Pacific to correlate this event, dated 1820 – 1657 cal. yr BP, this sedimentary evidence strongly support this hypothesis.

6.3.1.2. Deposit S-I

After the deposition of S-II, during ~ 210 years (1710 – 1541 cal. yr BP), the coastal barrier that protects Estero Potrero Grande from marine action was in a steady state of progradation. This pattern of evolution is represented by the gradual and constant decrease of sand and the gradual increase of freshwater diatoms. Coastal progradation during this time was also inferred in the coast of Nayarit, ~400 km north-eastward from this study site, where the estimated rate of progradation was 3.0 – 3.2 m/yr (Curray & Moore, 1963). This indicates that Estero Potrero Grande gradually became in a low-energy and freshwater palaeoenvironment. It is in this geomorphological context when S-I was deposited.

The sedimentary features of S-I point out to a high-energy event as the mechanism of deposition. Its basal contact is sharp but without evidence of erosion, in comparison with the basal contact of S-II (**fig. 6.9**). However, the nature of the basal contact during high-energy events is associated to the distance of the site of deposition from the shoreline. Tsunami deposits in sites adjacent to the shoreline, show more erosive basal contacts than sites farther inland, where basal contacts are commonly sharper (e.g. Kempf et al., 2015).The departure of the coring site from the shoreline due to the prograding behaviour of the barrier before the deposition of S-I can explain the nature of the basal contact of the deposit S-I. Nonetheless, the presence of rounded to angular rip-up clasts, embedded in S-I, suggest an erosive behaviour of its depositional mechanism.

Diatom assemblages indicate that S-I corresponds to a marine incursion. These assemblages reveal an abrupt increase of marine and brackish species within this deposit (e.g. *N. grossestriata, A. proteus* and *C. pinnata)*. This hypothesis is

corroborated by the presence of shell hash and shell fragments of *Vermicularia pellucida* and *Serpulorbis margaritaceous*. These species of molluscs dominate the intertidal zone of the rocky coast of Jalisco and their fragments are frequently deposited along the beach (González Villarreal, 2005). Due to the distance of Estero Potrero Grande to the nearest rocky promontories is larger than 10 km, these shell fragments were possibly eroded from the beach and deposited in the back-barrier basin during the deposition of S-I. Indeed, the rounded edges of these shell fragments suggest reworking, possibly by wave action, before their deposition.

There is not any record of earthquakes occurred along the Pacific coast of Mexico during the time of deposition of S-I, around 1710 – 1541 cal. yr BP. Nonetheless, in the Nuxco lagoon, Guerrero, located ~400 km southeast from Estero Potrero Grande, Bianchette et al. (2022) found an anomalous deposit, 28 cm thick, of shell hash that is interpreted as a marine incursion, occurred ~1500 cal. yr BP. Although this is the median age of this deposit, the age range at 2-sgima overlaps with the deposit found in Estero Potrero Grande. Based on the size of the deposit of Nuxco lagoon, Bianchette et al. (2022) highlight that this is the most intense event occurred in Nuxco lagoon, since 3970 cal. yr BP. The origin of the deposit is still unresolved, as it is not clear whether it represents many depositional events during an active period of storminess, or the deposit corresponds to a single large event. If the same event produced a marine incursion in Estero Potrero Grande and the Nuxco lagoon, the mechanism of creation was a regional event that affected at least 400 km stretch of the coast. Thus, a local tsunamis or a large tropical cyclone, which commonly affect similar lengths of coasts (e.g. Morton et al., 2007), can explain their origin.

Tsunami models of the Mexican Pacific demonstrate that megathrust earthquakes can produce tsunami waves significantly large to produce high run-ups (>5 m) over hundreds of kilometres in regions adjacent to the earthquake ruptures (e.g. Hjörleifsdóttir et al., 2018; Núñez-Cornú et al., 2008; Ramírez-Herrera et al., 2020). Hence, the occurrence of a local tsunami can explain the origin of the deposit S-I in both the Estero Potrero Grande and the shell-rich layer in Nuxco lagoon. However, it is important to know whether this event was produced either in the domain of the Rivera plate, belonging to the Estero Potrero Grande site, or within the domain of the Cocos plate, where the Nuxco lagoon is located. In Estero Potrero grande, S-I is the

thickest deposit found in the stratigraphic record. This extraordinarily anomalous high energy event shows a high content of sand fraction, ~30%, and the presence of shell fragments that correspond to beach deposits deposited in the back-barrier basin of Estero Potrero Grande. In contrast, the shell-rich layer found in the Nuxco lagoon is characterised by the anomalously high-content of shell hash but with a low-content of sand. These contrasting features suggest that, if the same event produce these two anomalous deposits, the tsunami wave and the run-up were likely higher in Estero Potrero Grande, as the content of sand and beach material dominate this deposit in this site. Hence, the source of the tsunami was more likely closer to this site.

Another line of evidence that indicates the proximity of Estero Potrero Grande to the source of the tsunami corresponds to the qualitative features of the diatom assemblages after the deposition of S-I. The abrupt and the long-lasting increase of marine and brackish diatoms above this deposit could be explained by the drastic modifications of the local geomorphology produced by the tsunami, a permanent land-level change, or a combination of both. If a tsunami produced extensive geomorphological modifications along the barrier, i.e. breaching, these features were more likely reversed gradually in a short period of time, as long-shore currents frequently re-built sand bars in breached areas of coastal settings such as the Estero Potrero Grande (e.g. Yáñez-Arancibia et al., 2014). Hence, this lasting environmental change cannot entirely be explained by geomorphological changes. This permanent environmental change can be, alternatively explained by a land-level change, likely coastal subsidence, that favoured the increase and permanent shift to marine conditions after the deposition of S-I.

The occurrence of a tropical cyclone is the alternative mechanism to explain the deposition of S-I. This depositional process could be only explained by an extraordinary super storm because the background sedimentation and the rest of the stratigraphy does not show evidence of a deposit as thick as S-I, even during the period of high storminess. The composition of S-I, including the high content of sand and beach material, indicate that in a period of coastal progradation this cyclone was able produce significant overwash to deposit material eroded from the beach. This super storm had to be large enough to produce significant geomorphological changes along the barrier, mainly breaching, to explain the long-lasting change of diatom

assemblages. Lastly, this event had to be an anomalous tropical cyclone that occurred in a dry and warm climate period that extended between ~1600 and ~700 cal. yr BP (Curray & Moore, 1963; Joo-Chang et al., 2015; Metcalfe et al., 2000).

Given the correlation of S-I with the shell deposit found in the Nuxco lagoon, the origin of this cyclone was possibly southeast Guerrero, within the Easter Pacific warm pool (Misra et al., 2016). This cyclone could reach a high intensity offshore Nuxco to produce barrier breaching, favouring the deposition of the shelly bed with the low content of sand. Then, this cyclone displaced northwest for at least 400 km and once it was offshore Estero Potrero Grande, the intensity of the cyclone more likely peaked, producing overwash that deposited the eroded beach sediments in this study site.

The stratigraphic evidence from Estero Potrero Grande, the climate conditions of the region and the local geomorphology during the time of deposition, favour to conclude that the deposit S-I is most likely associated with a tsunami. This deposit not only fulfils the criteria used to discriminate the tsunami origin (**table 6.3**), but it also contain sedimentary structures that correspond only to tsunami deposits, such as the presence of rip-up clasts. The evidence here exposed also indicate the possible correlation of this deposit with coastal coseismic subsidence. However, more needs to be collected at different coastal locations to support the hypothesis here proposed.

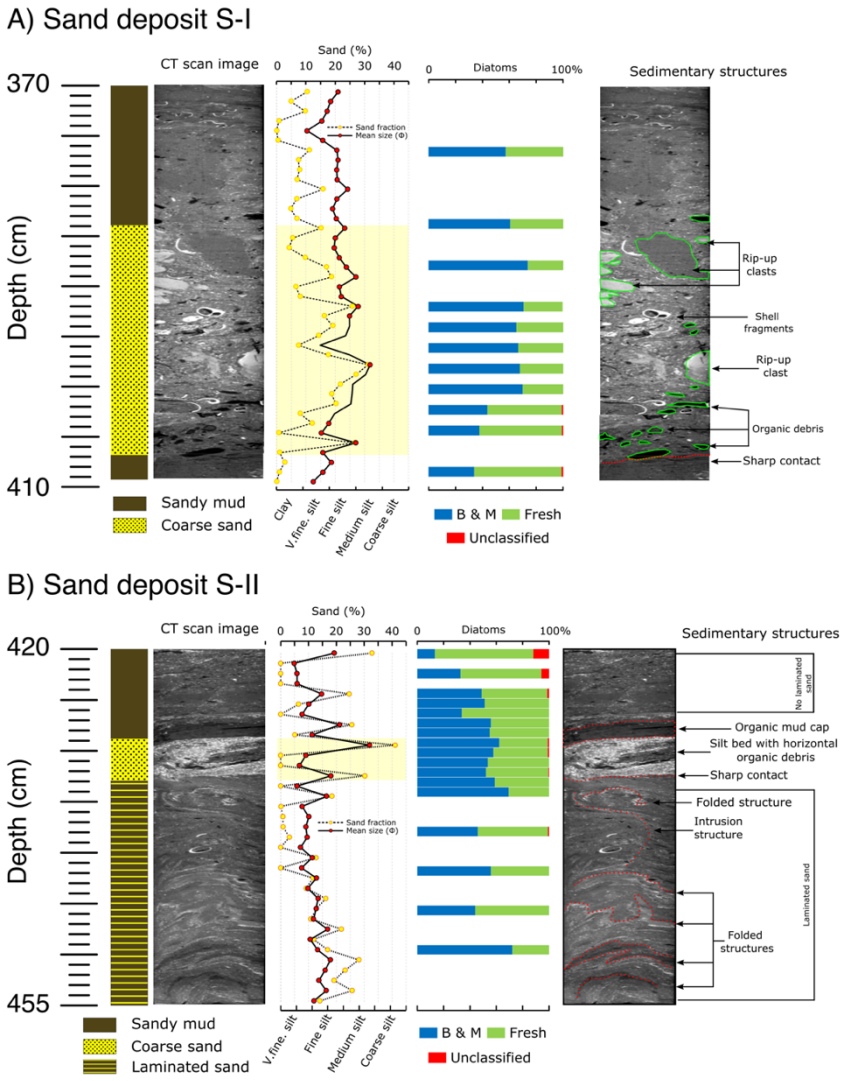

***Figure 6.9**. Sedimentary structures, litho- and biostratigraphic features of the sand deposits S-I and S-II.*

6.3.2. Middle stratigraphic unit.

The middle stratigraphic unit is typified by an increase in clay and fine silt. These fine sediments are accompanied by abundant paired bivalves in growth position. Diatom assemblages dominated by marine species, e.g. *A. proteus and C. pinnata*, and brackish species, such as *C. striata,* suggest a transition to a low intertidal environment, as these species dominate in mudflats adjacent to mangroves (e.g. López Fuerte et al., 2010). Similar clay-rich sediments dominate low intertidal areas and fringing mangrove regions of modern coastal lagoons in this region (e.g. Cabrera-Paez et al., 2020). As mentioned earlier, this stratigraphic unit shows abrupt alternations between minerogenic and peat or highly organic sediments, referred to as contacts F to J.

To determine whether these contacts were produced coseismically, their features are summarised in **table 6.4**, considering some of the criteria to identify earthquakes using sediments from tidal wetlands (Nelson et al., 1996; Shennan et al., 2016). The criteria include:

1) Lateral extent of peat over mud or mud over peat, suggesting uplift or subsidence respectively. This criterion is tested using field observations to correlate the lateral continuity of the stratigraphic contacts.

2) Suddenness of uplift or subsidence. This criterion is assessed by the abruptness of changes in the composition of diatom assemblages. For uplift there should be a change from marine and brackish to freshwater species. For subsidence there should be a change from freshwater to marine and brackish species.

3) Amount of uplift or subsidence. The magnitude of land-level changes across the stratigraphic contacts is estimated using the percentage of brackish and marine diatoms and the two linear models to give palaeoelevation changes.

4) Tsunami concurrent with subsidence or uplift. This criterion is assessed using sediment grain size and diatom assemblages.

***Table 6.4**. Summary of the stratigraphic contacts F to J using the criteria to identify earthquakes.*

Contact	Type of contact	Lateral extent (m)	Suddenness of change	Magnitude (m)	Tsunami	Coseismic origin
F	Silt over organic silt	280	Freshwater-brackish to brackish-marine	-0.04 ± 0.74 m (M1); -0.06 ± 0.75 m (M2)	No evidence	Likely
G	Silt over peat	280	Freshwater to marine/brackish	-0.01 ± 0.74 m (M1) -0.03 ± 0.63 m (M2)	No evidence	Unlikely
H	Silt over peat	125	Freshwater to freshwater	+0.04 ± 0.74 (M1) +0.06 ± 0.75 (M2)	No evidence	Unlikely
I	Silt over organic silt	280	Freshwater to brackish-marine	-0.05 ± 0.62 (M1) - 0.08 ± 0.48 m (M2)	No evidence	Likely
J	Peat over clay	280	Marine-brackish to freshwater	+0.06 ± 0.74 (M1) +0.11 ± 0.63 m (M2)	No evidence	Most likely

6.3.2.1. Contact J

This stratigraphic contact shows the abrupt change from an underlying clay with high content of marine and brackish diatoms, to an overlying freshwater peat. This contact was traced for along 280 m. Palaeoelevation models suggest uplift between 0.06 ± 0.26 m and 0.11± 0.27 m. Even though, one core, MAR001, shows evidence of a 2 cm sand deposit immediately below the peat layer it cannot be said confidently that there was a tsunami at the time of the event.

The age range of this contact, 1269 - 1219 cal. yr BP, corresponds the minimum age of this event, as the dated sample was within the overlying peat, 1 cm above the contact. Contact J correlates with the emerged tidal notches, near the mouth of the Cuitzmala river, 50 km to the northwest of the field site. Ramírez-Herrera et al. (2004) radiocarbon dated these tidal notches using situ algae to 1289 - 1069 cal. yr BP (1262 ± 51 yr BP). This is age range is very close to the age of Contact J. Although the origin of these notches is still unclear, Ramírez-Herrera et al. (2004) argue that the presence of in-situ intertidal organisms support the hypothesis of episodic uplift, most likely caused by a megathrust earthquake. All the sedimentary evidence here presented suggests that Contact J represents abrupt coastal uplift, which was very likely caused by a megathrust earthquake.

6.3.2.2. Contact I

Contact I is an abrupt transition from brown peat to grey silt, which is traced for 280 m along the cored transect. The diatoms suggest a change from upper intertidal to low intertidal environment across the contact. The models suggest a land-level change of -0.05 ± 0.26 m (model 1) and -0.08 ± 0.27 m (model 2). Above the contact there is no evidence of a tsunami, despite the slight increase in sand, which might be associated to tidal flooding. The low amount of land-level change questions whether the origin of this contact is coseismic. However, the abruptness of change in sediment composition indicates a significant change in the sedimentation process. Additionally, the abrupt increase of benthic marine diatoms above the contact confirms this sudden and long-lasting palaeoenvironmental change. Hence, this contact was most likely produced by coseismic subsidence.

The maximum (1265 – 1183 cal. yr BP) and minimum age (1264 – 1151 cal. yr BP) of the contact, taken from 1 cm below and above the contact are not correlated with any local or regional geological records of megathrust earthquakes, so it is not possible to correlate these observations with possible palaeoearthquakes.

6.3.2.3. Contact H

Contact H is defined by an abrupt transition from a slightly silty peat to a grey silt. Within the overlying silty unit there is a gradual increase in sand content, coarsening upwards. The correlation of Contact H was achieved tracing the overlying bed of coarser sediments. Contact H is only identified along 125 m of the cored transect.

Based on the lithology, this stratigraphic sequence might represent the signature of coastal subsidence, however diatom assemblages rule out this hypothesis. Below the contact there is an absence of benthic species, with planktonic diatoms suggesting a freshwater (e.g. *C. meneghiniana*) to brackish (e.g. *C. striata*) environment. Above the contact, the relative abundance of freshwater diatoms increase to 70%, where the planktonic species *C. meneghiniana* is dominant. The increase of sand fraction and freshwater planktonic diatoms above the Contact H, suggest potentially a change to a freshwater environment, driven by a fluvial discharge.

The age of this contact was obtained from two samples within the underlying organic unit. The age closest to the contact indicates a maximum age for the event of 1237 - 1121 cal. yr BP. This contact overlaps with the beginning of the Medieval Climate Anomaly, which is a Northern Hemisphere warm period between 1150 – 750 yr BP (Broecker, 2001). For the Cuyutlán lagoon, roughly 50 km south of the study site, this climatic event is marked by a high content of terrestrially-sourced minerogenic deposits, which are interpreted as fluvial deposits triggered by increased hurricane activity (Figueroa-Rangel et al., 2016). Contact H might represent this period with sediments above Contact H showing an increase of siliclastic sediments with a high content of freshwater diatoms, which may relate to intensification of fluvial activity during this period. This would have allowed more freshwater diatoms to survive in the Estero Potrero Grande lagoon and delivered more clastic sediment to this wetland from the Marabasco river.

6.3.2.4. Contact G

Contact G is marked by an abrupt transition from organic silt to a thin bed of silt and was traced across the entire coring transect. Diatoms suggest a change from freshwater to a brackish environment. There is no sedimentological evidence of a high energy event above this contact, but there is a spike of the planktonic brackish species *C. striata*, which indicates rapid incursion of marine waters. Palaeoelevation models suggest minor subsidence, between -0.01 ± 0.26 m (model 1) and -0.03 ± 0.27 m (model 2) immediately above the contact. Although, three cm above the contact, palaeoelevations reach a maximum land-level change of -0.04 ± 0.26 m (model 1) and -0.06 ± 0.27 m (model 2).

This contact has some features that makes it different to the rest of the peat-silt contacts. For example, the overlying minerogenic unit of this event is the thinnest across the coring transect. This would suggest a short-live change in sedimentary conditions. This minimum change in sedimentary conditions is also revealed in the diatom assemblages, which show an abrupt but relatively small increase in benthic and planktonic brackish species above the contact.

The maximum age of the contact, obtained from sampled material 1 cm below the contact gives an age range of 1176 – 1099 cal. yr BP. The minimum age, 3 cm above

the contact is 1129 – 1059 cal. yr BP. The minor amount of land-level change, the thinness of the overlying minerogenic unit and the lack of palaeoearthquakes dated around this time means that Contact G is unlikely to have a coseismic origin.

6.3.2.5. Contact F

This stratigraphic contact represents the abrupt transition from and underlying organic silt to an overlying silt bed. This sedimentary sequence indicate possible subsidence. Palaeoelevation models confirm it, showing a land-level change between of -0.04 ± 0.26 m, and -0.06 ± 0.27 m. These relatively small land-level changes indicate the transition from a freshwater-brackish palaeoenvironment, slightly above the MHHW, to a brackish-marine palaeoenvironment, slightly below the MHHW. Diatom assemblages above the stratigraphic contact show the increase of the marine species *N. grossestriata* and *P. sulcata*. These two species are the fossil record of coastal subsidence during the 1995 earthquake (**Chapter 2**).

The maximum age of this event, from 3 cm below the contact, is 1111 – 1023 cal. yr BP. The minimum age, 8 cm above the contact, is 1112 – 995 cal. yr BP. Around this time there is no evidence of palaeoearthquakes near this site, due to the lack of studies that cover this age range.

Despite the lack of palaeoearthquakes during this time along the coast and the small land-level change, the qualitative features of fossil diatom assemblages, such as the abruptness and long-lasting change can support the hypothesis that the coast experienced abrupt submergence, likely caused by coseismic subsidence.

6.3.3 Variable land-level changes during the Late Holocene earthquakes

Along the Jalisco subduction zone, megathrust earthquakes occurring in the last century produced coastal subsidence. Geodetic observations and rupture models demonstrate that past ruptures were shallower than 30 km depth (**table 6.5**). This rupture pattern caused coastal subsidence due to most of the coseismic slip concentrated between the trench and the coast. The aim of this chapter is to investigate whether coseismic coastal subsidence persists over earthquake deformation cycles in past centuries. This aim is grounded on the evidence that the seismogenic zone of this megathrust fault extends landward and earthquake ruptures deeper than 30 km depth can produce coastal uplift. Consequently, the size of the ruptures could be wider in comparison with those of the most recent earthquakes.

***Table 6.5**. Summary of the instrumentally recorded megathrust earthquakes along the Jalisco subduction zone occurred after 1910.*

Year	Moment magnitude (Mw)	Length (km)	Width (km)	Depth (km)	Coseismic slip (m)	Subsidence (m)	Source
1932-I	8.2	220	80	20	4.5	0.4 to 0.75‡	Trejo-Gómez et al., 2015; Okal & Borrero, 2011
1932-II	7.8	60	80	20	2.6	0.09 – 0.15†	
1995	8.0	150	60	20	Up to 4	0.06 to 0.20* 0.06 to 0.11††	Abbott & Brudzinski, 2015; Hutton et al., 2001; Masterlark et al., 2001
2003	7.6	40	70	30	Up to 2	0.01 - 0.06**	Schmitt et al., 2007; Yagi et al., 2004

‡ Land-level change obtained from historical records (Cumming, 1933).

† Land-level change obtained from geological records (Chapter 2 in this study)

†† Land-level change obtained from geological records (Chapter 1 in this study)

* Land-level changes obtained from GPS data (Hutton et al. 2001)

** Land-level changes obtained from GPS data (Schmitt et al. 2007)

6.3.4. Evidence of coseismic uplift

There are two clearly identifiable episodes of sudden uplift at Estero Potrero Grande. Sedimentary records suggest variable rupture patterns during these two events, which indicate variable rupture sizes. During the first event (S-II), occurred prior to 1820 – 1657 cal. yr BP, uplift and liquefaction evidence indicate that the downdip limit of the rupture extended inland of the coast, and most likely to the deepest portion of the

seismogenic zone. The tsunami deposit that accompanies this uplift event is indicative of the location of the updip limit of the rupture, which possibly extended near the trench to produce significant displacement of the ocean floor (Polet & Kanamori, 2002). A rupture of such dimensions would exceed the width of all earthquakes that occurred in the last century in this subduction zone.

Regarding the youngest uplift event (Contact J), 1269 – 1219 cal. yr BP, the coast emerged abruptly from the lower to upper intertidal zone. Geomorphological evidence of coastal uplift near the mouth of the Cuitzmala river was synchronous with the episodic emergence of the wetland Estero Potrero Grande. However, tidal notches in Cuitzmala were 4.5 – 4.7 m above MSL (Ramírez-Herrera et al., 2004). Considering their rate of uplift, 3 mm/yr, for the last 1300 years (Ramírez-Herrera et al., 2004), this set of notches may have experienced coseismic uplift in the order of 0.6 – 0.8 m. This amount of uplift is larger than the magnitude of uplift obtained in this study, 0.6 ± 0.26 m and 0.11 ± 0.27 m. This difference in the amount of land-level change could be explained by a heterogeneous rupture, including along-strike variations of coseismic slip on the fault or variable rupture depths along-strike. Heterogeneous ruptures occurred during the 1995 earthquake, where areas of large coseismic slip experienced larger subsidence (e.g. Hutton et al., 2001; Melbourne et al., 1997). However, more evidence along the coast would confirm variable magnitudes of uplift during this event.

The sedimentary evidence associated to this event, support the hypothesis of an earthquake rupture with the downdip limit extended inland. Nonetheless, the lack of tsunami deposition suggests that the updip limit did not reach the upper part of the seismogenic zone.

6.3.5. Limited evidence of coastal subsidence

In addition to coastal uplift, Late Holocene sediments reveal the occurrence of three episodes of abrupt increase in brackish and marine conditions, associated with the deposit S-I, and stratigraphic contacts I and F.

Deposit S-I shows clear evidence of marine incursion associated to a high-energy event, sharing similarities to tsunami deposits found in coastal lakes. Due to this event occurred when the site was below the lowest tide, lithology alone does not provide any

evidence of land-level change. As Brader et al., (2021) highlighted, with increasing water depth in the subtidal zone, lithology and biostratigraphy vary little with changes in sediment surface elevation. In this context, it was not possible to estimate land-level change. However, the abrupt and long-lasting increase of brackish and marine diatoms after this event, might suggest subsidence.

Contacts I and F also suggest subsidence, but palaeoelevation models indicate minor land-level changes, < -0.1 m. Quantitative analysis of fossil diatoms and transfer functions using sediments from tidal marshes in Chile, revealed a similar amount of coastal subsidence during the 2016 M_w 7.6 Chiloé earthquake (Brader et al., 2021). Along the coast adjacent to the Jalisco subduction zone, GPS datasets (e.g. Schmitt et al., 2007) show coseismic subsidence <0.1 m during large earthquakes but particularly during those M_w 7.0 – 7.9 (**table 6.5**). Hence, the sedimentary records of Contacts I and F might represent subsidence caused by shallow ruptures of earthquakes M_w 7.0 – 7.9.

Evidence of subsidence using Holocene sediments is more fragmented and less clear than uplift evidence, possibly because the down-dip limit of most of the ruptures is near or below the coast in the region adjacent to the study site. Alternatively, an explanation for the limited evidence of subsidence is possibly associated with the environmental setting, considering that the Estero Potrero Grande wetland is sheltered by a sandy coastal barrier with minor influence of tides in back-barrier wetlands. These geomorphological features might control the sedimentary signature of subsidence in the back-barrier wetland, limiting the creation threshold of the stratigraphic signature during coseismic subsidence.

6.3.6. The importance of understanding the evolution of the coast in complex sedimentary systems.

This study reveals the evolution of the coast for ~1500 years, from ~2500 to 955 cal. yr BP. Within this period, this sedimentary system evolved rapidly from an open estuary to a restricted coastal lagoon and wetland. Sediments deposited during the last ~300 years, from 1290 to 955 cal. yr BP, allowed to reconstruct earthquake ruptures through land-level changes due to the land surface emerged during this

period, favouring to the development of mangrove peat that experienced two episodes of submergence and one of uplift.

Before this coastal site emerged above the mean tide level, a low intertidal to shallow subtidal environment dominated from 1290 to ~2500 cal. yr BP. During this period, evidence of past earthquakes through the analysis of land-level changes was not possible for two reasons: 1) If subsidence or uplift occurred changes in the lithostratigraphy were not as evident as those occurred in the upper and lower intertidal zones due to the absence of organic sediments, peat or soils, that form in the upper intertidal zone. 2) The linear models used to constrain palaeoelevations contain information of diatom assemblages from above the mean tide level (100 SWLI). Hence, additional evidence of past earthquakes was required.

Through the analysis of diatom assemblages, grain size and CT scanned images it was possible to interpret palaeoenvironmental conditions. Once palaeoenvironments were interpreted, it was possible to select the type of earthquake evidence expected to find. In this case, when this site was a shallow lagoon, the sand deposits S-I and S-II were interpreted based on evidence of palaeotsunamis from coastal lakes (e.g. Kelsey et al., 2005; Kempf et al., 2015, 2017, 2020).

In conclusion, evidence of palaeoearthquakes in sites where palaeoenvironmental context is complex and palaeo-sea level information is inexistent, understanding the evolution of the study sites favour the interpretation of sedimentary evidence associated to palaeoearthquakes.

6.4. Conclusions

Sediments beneath the wetland Estero Potrero Grande show the evidence of this sedimentary system from 2500 to 956 cal. yr BP. The site transitioned from an open estuary to a restricted lagoonal estuary. Sediments beneath this wetland reveal the occurrence of two episodes of abrupt coastal uplift prior to 1820 – 1657 cal. yr BP (S-II) and 1269 – 1219 cal. yr BP (Contact J). These events were possibly caused by earthquakes with ruptures that extended probably to the lowermost limit of the seismogenic zone. Additionally, the coast also experienced three episodes of subsidence in 1710-1541 cal.yr BP (S-II), 1263 – 1151 cal. yr BP (Contact I) and 1108

– 995 cal. yr BP (Contact F). These events were typical of shallow ruptures, similar to those earthquakes occurred in the last century. This study demonstrates variable earthquake rupture depths in the Late Holocene period. Some of these ruptures are deeper and likely larger than those during the last century.

CHAPTER 7

SUMMARY AND FUTURE OUTLOOK

This research contributes to our understanding of megathrust earthquakes using coastal sediments from the wetland Estero Potrero Grande, which is adjacent to the estuarine system of the Marabasco river (**fig. 7.1A**). This is the first study in the Mexican pacific coast, which focuses on quantifying land-level changes using fossil diatoms to reveal the origin, coseismic or non-coseismic, of abrupt stratigraphic changes imprinted in coastal sedimentary sequences. This approach aid on the interpretation of past earthquake rupture dimensions.

Two sites were investigated during two different field seasons, in 2018 and 2019. The coring transect Marabasco-2018 (Chapter 4 and 5; **fig. 7.1**) revealed five abrupt stratigraphic contacts (A to E), produced between 1684 - 2018 cal. AD. In contrast, sediments beneath the site Marabasco-2019 situated nearer the coastline (Chapter 6, **fig. 7.1B)** show five stratigraphic contacts (I to J) and two sand deposits (S-I and S-II) that occurred prior to 995 cal. AD. Based on the detailed chronology developed for each site, there is no overlap between the stratigraphic contacts identified at each site, see the lack of correlation in **figure 7.1**. The results produced in this study reveal a coseismic origin of only some of these events, caused by megathrust earthquakes along the Jalisco subduction zone. The variable patterns of coseismic land-level changes, either subsidence or uplift, indicate that the features and size of past earthquakes, differ from those earthquakes that occurred during the instrumental era. This highlights the importance of geological evidence to understand the spatial and temporal behaviour of the Jalisco subduction zone to refine the earthquake hazard assessment of the region.

This chapter contains a summary of the key findings and specifically addresses each of the research questions (RQ) and research objectives (Ro) established at the beginning of this thesis (**Chapter 1**). This chapter concludes with some recommendations for future palaeoseismic studies along the adjacent coasts of the Jalisco subduction zone.

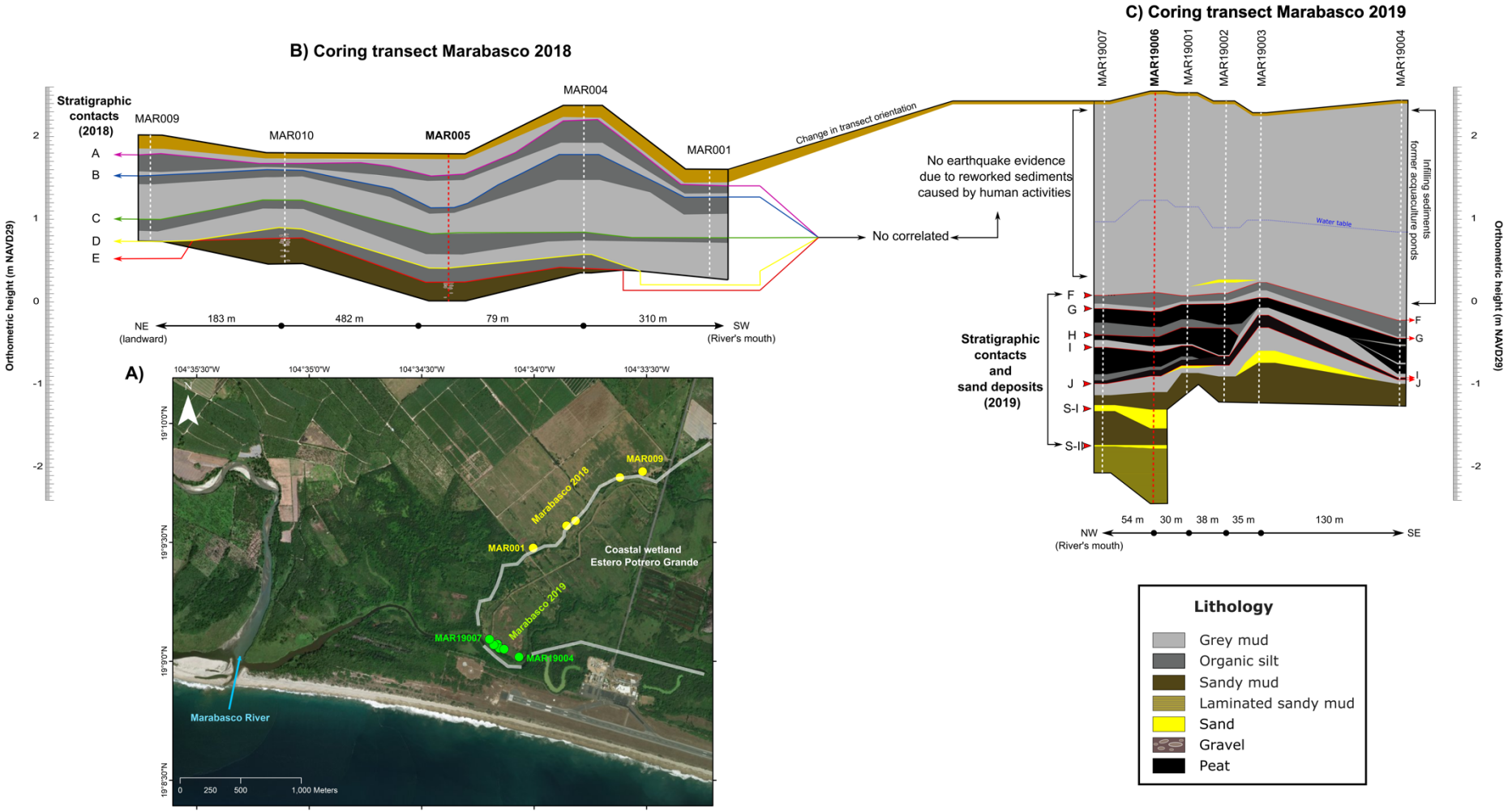

Figure 7.1. *Stratigraphy summary of the coastal wetland Estero Potrero Grande.* ***A)*** *Location of the coring sites within the wetland. B) Cross-stratigraphy of the site Marabasco 2018. C) Cross-stratigraphy of the site Marabasco 2019. Notice the lack of correlation between the stratigraphic contacts at these two coring transects due to human activities.*.

7.1. R.Q. 1: Did the 1995 M_w 8.0 earthquake leave a sedimentary signature in coastal intertidal wetlands of the Mexican Pacific?

The first step in this investigation was to investigate the sedimentary signature of the 1995 M_w 8.0 earthquake. The features of this earthquake are well-constrained because of the availability of datasets from a vast source of instruments, e.g. local and global seismographs, GPS receivers and tide gauges. Finding the signature of this event, would serve as the modern analogue to interpret the sedimentological properties of former events. The findings in Chapter 4: "Quantifying coseismic coastal subsidence caused by the 1995 Colima-Jalisco (M_w 8.0) earthquake using coastal stratigraphic sequences" correspond to the objectives below:

7.1.1. R.o. 1: Identify a coastal wetland that experienced significant coseismic subsidence during the 1995 M_w 8.0 earthquake.

The 1995 earthquake was the first great (M_w 8.0) megathrust earthquake recorded by geodetic GPS receivers in the Jalisco subduction zone. GPS data show widespread coseismic subsidence, < 0.2 m, along the coast adjacent to this earthquake's rupture (Hutton et al., 2001; Melbourne et al., 1997). Within the subsided region is the coastal wetland Estero Potrero Grande. Sediments beneath this wetland reveal a bed of grey silt abruptly overlying a bed of organic black silt for along a 1 km section (**contact A in fig. 7.1**). This stratigraphic sequence is within the upper 30 cm below the land surface.

The age of this sedimentary signature was obtained using Radiocaesium (^{137}Cs) profiling and a Bayesian age-depth model in OxCal. The results of this age-depth model indicate that under a constant sedimentation rate, 1.23 ± 0.01 cm/yr, this stratigraphic transition was produced between 1990 – 2001 cal. AD (2σ), with a mean age 1995 ± 2 AD (1σ). Hence, the modelled age provides strong support for the interpretation of this couplet as the sedimentary signature of the 1995 earthquake.

7.1.2. R.o. 2: Characterise the physical and chemical composition of the sediments that indicate this coseismic subsidence.

Using the elemental ratios S/Zn, Br/Zn and Ca/Zn, geochemistry data reveals the abrupt increase in marine conditions above this stratigraphic contact (**Contact A fig. 7.2**). An organic content XRF-based proxy (inc/coh) also reveals an abrupt change in the composition of the sediments, which rapidly change from an organic-rich underlying unit to an overlying silt bed

Additionally, sediment grain size reveals the occurrence of a thin, < 1 cm, layer of coarse sediments, which is attributed to the 5 m high tsunami that accompanied the 1995 earthquake. This bed of coarse silt with high percentage of sand (~30%) could not be clearly identified in the coring transect, due to its thickness. Hence, this coarse deposit can be the minimum physical evidence of the tsunami, which could penetrate inland through the meandering channels for around > 1 km, limiting the capacity of the tsunami to pick up coarse sediments as it was moving inland. Nonetheless, geochemistry supports the evidence of a marine incursion accompanying this coarse deposit. More evidence within the same estuary needs to be collected in seaward locations to investigate the sedimentological properties of this tsunami.

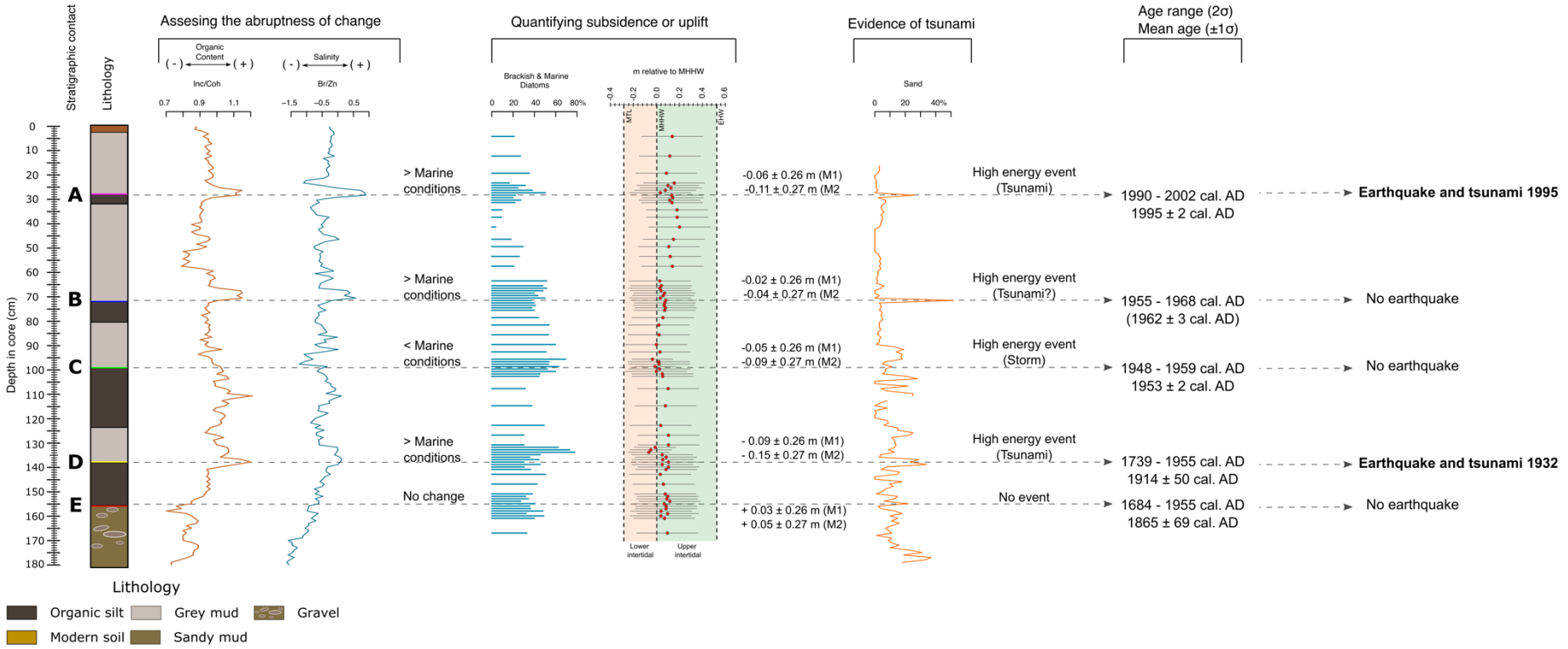

***Figure 7.2**. Summary of the core MAR005. The proxies included are: XRF-based salinity indicator, Br/Zn, the relative abundance of brackish and marine diatoms (%), diatom-based palaeoelevation changes, sand fraction (%). The age of the contacts was estimated from the Bayesian age-depth model. Poxy-based interpretation indicate that the contacts B and E correspond to the stratigraphic signature of the earthquakes in 1932 (M_w 7.8) and 1995 (M_w 8.0).*

7.1.3. R.o. 3: Develop a diatom-based method to quantify coseismic subsidence caused by the 1995 event.

Diatom assemblages show a sudden shift from freshwater to marine diatoms across this stratigraphic contact, suggesting coastal subsidence (**fig. 7.2**). In this chapter, a diatom-based method was developed to quantify the magnitude of this land-level change. This method consisted of using two well-constrained diatom assemblages and their corresponding palaeoelevations, from Alaska and Chile, in order to build a linear regression model, which permitted to estimate palaeoelevations in SWLI units using only the percentage of brackish and marine diatoms.

Using these linear models, it was possible to estimate the magnitude of subsidence during the 1995 earthquake (0.06 ± 0.26 m and 0.11 ± 0. 27 m). These estimations are congruent with observations obtained from GPS receivers, which indicate coastal subsidence between 0.06 and 0.20 m. These results validate the diatom-based palaeoelevation changes produced by the 1995 earthquake.

7.2. R.Q. 2: Can we use coastal sediments from Estero Potrero Grande to constrain earthquake ruptures preceding the 1995 earthquake along the Rivera-North American plate boundary?

Before the 1995 earthquake, the coast adjacent to the Jalisco subduction zone lacked GPS receivers to measure coseismic land-level changes. Hence, the parameters of former earthquakes (location, magnitude, depth, etc.) were estimated using the local network of seismic instruments, which began operations in 1910 (Alcántara et al., 2012; Pérez-Campos et al., 2018), and the global network of seismic instruments, for those earthquake that occurred in the nineteenth century (e.g. Singh et al., 1981). The parameters of these earthquakes show systematic errors, particularly when assessing the location and extension (e.g. Cruz & Wyss, 1983; Hjörleifsdóttir et al., 2016; Singh et al., 1985; Singh & Lermo, 1985). In Chapter 3 “Coastal subsidence caused by the 1932 (M_w 7.8) megathrust earthquake and other marine incursions on the Jalisco-Colima coast, México” the objectives to follow in order to answer the research question were:

7.2.1. R.o. 4: Investigate the sedimentary signature of early (pre-1995 AD) instrumentally recorded earthquakes along the Rivera-North America plate boundary.

Beneath the fingerprint of the 1995 earthquake, four stratigraphic contacts indicate the occurrence of abrupt environmental changes. Three of four stratigraphic contacts resemble the signature of the 1995 earthquake, grey silt over organic-rich sediments (Contacts B to D in **fig. 7.2**). One stratigraphic contact shows the opposite sedimentary sequence, as organic-rich sediments overlying abruptly sandy silt (Contact E in **fig. 7.2**). Based on the well-established criteria to identify megathrust earthquakes using coastal intertidal sediments (e.g. Nelson et al., 1996; Shennan et al., 2016), only one stratigraphic contact, Contact D, fulfils the criteria to be attributed to a megathrust earthquake. The remaining contacts do not entirely fulfil the criteria to conclude that they were produced coseismically and other processes such as hurricanes, hydrological changes, and far-field tsunamis can explain their origin.

Contact D shows the transition from an underlying bed of organic-rich sediments to an overlying bed of silt. Field evidence reveals the lateral continuity of this contact for along ~500 m. Sediment grain size reveal a 3 cm deposit of coarse silt with a high percentage of sand (30%), which is capped by a 2 cm bed of silty clay. CT-scanned images reveal the characteristics of this deposit to be associated to a high-energy event, showing an abrupt basal contact and rip-up clasts. This deposit represents a marine incursion, which is revealed by the increase of the salinity ratios S/Zn and Br/Zn.

After implementing a Bayesian age-depth model, based on ^{14}C and ^{137}Cs dates, the age range of this stratigraphic contact at two-sigma is 1739-1799 cal. AD (5.7%) and 1847-1955 cal. AD (89.8%). The mean age of this event is 1914 ± 50 cal. AD, with a median age centred at 1932 cal. AD. The sedimentological properties and age modelling suggest that this stratigraphic contact represents the sedimentological signal of the 1932 AD earthquake (Mw 7.8).

7.2.2. R.o 5: Reconstruct the magnitude of coseismic land-level changes associated with the earthquakes identified

Diatom-based palaeoelevation models indicate coastal subsidence of 0.09 ± 0.73 m and 0.15 ±74 m across the stratigraphic contact B (**fig. 7.2**). The explanation of this land-level change is a shallow rupture, where most of the coseismic slip occurred offshore, at least in the coast of the Estero Potrero Grande. A shallow rupture contradicts the hypothesis proposed after analysing early instrumentally recorded data (Singh et al., 1985), suggesting a deep rupture. If this were the case, the coast would have been uplifted. The sedimentary evidence here presented highlights the need to continue mapping coseismic land-level changes along the coast to constrain the ruptures of this and former earthquakes, due to the limited historical and geological records.

7.3. R.Q. 3: What is the long-term behaviour of the Rivera-North America megathrust fault?

Instrumental data shows recurrent coastal subsidence during megathrust earthquakes that occurred in the last century along the Jalisco subduction zone (Cumming, 1933; Melbourne et al., 1997; Schmitt et al., 2007). This pattern of crustal deformation suggests that most of the coseismic slip occurred offshore. This type of ruptures indicate that the rupture depths and widths did not extend to the lowermost portion of the seismogenic zone, which extends farther inland. However, Late Holocene geomorphological evidence suggests episodes of abrupt coastal uplift, likely coseismic, along the coast of Jalisco (Ramírez-Herrera et al., 2004). This crustal deformation pattern suggests different rupture modes, with coseismic slip extending inland of the coast. In Chapter 4 “Late Holocene coastal uplift and subsidence during megathrust earthquakes in the Jalisco subduction zone, Mexico”, I investigate Late Holocene coastal sediments following the research objectives below:

7.3.1. R.o. 6: Investigate the late Holocene evolution of this coastline from a coastal wetland on the Rivera-North American plate boundary.

Late Holocene sediments were sampled from the wetland Estero Potrero. These sediments were deposited between 2350 cal. yr BP and the present, 2018 AD.

However, due to human modifications on the stratigraphy, the sediments under study in this chapter correspond to those deposited in the period 2350 - 955 cal. yr BP. Hence, all earthquakes occurred within this years are categorized as palaeoearthquakes because the oldest historical megathrust earthquake occurred in 1563 AD, or 387 yr BP (Castillo-Aja & Ramírez-Herrera, 2017; Suter, 2019).

Sediment grain size and diatoms reveal the evolution from an open estuary, which transitioned, to a lagoonal estuary. Hence, palaeoseismic evidence correspond to records from two different palaeoenvironments.

7.3.2. R.o. 7: Investigate trends and patterns in land-level changes associated with palaeo-earthquakes.

CT scanning images, diatom assemblages and sediment grain size from the recovered sediment cores reveal the occurrence of two events possibly associated with coseismic uplift (**fig. 7.3**). These events occurred before 1820 – 1657 cal. yr BP (Deposit S-II) and before 1269 – 1219 cal. yr BP (Contact J). Palaeoenvironmental interpretations indicate that the oldest event (S-II) occurred when the site was a lagoonal open estuary, and led to the emergence of the site, reducing the influence of marine conditions. A sandy deposit was associated with this uplift event, possibly caused by an accompanying tsunami. Based on the diatom reconstruction, from 2350 – 2154 cal. yr BP the site was below water level; hence it was not possible to estimate the magnitude of uplift as the palaeoelevation models do not extend below MTL. The younger event (Contact J) occurred when the site of coring was a mudflat, between MTL and MHHW. Palaeoelevation models indicate that the coast was uplifted between 0.06 ± 0.47 and 0.11 ± 0.63 m. In contrast with the previous event (S-I), Contact J does not show an accompanying tsunami deposit.

In addition to these uplift events, there is evidence of three events (**deposit S-I, Contacts I and F in fig. 7.3**) showing abrupt increase in salinity, most likely caused by subsidence. The oldest event (S-I) was dated at 1710 – 1541 cal. yr BP. This event is associated with an increase in sand fraction with sedimentary features similar to those produced by tsunami deposition. This event shows a long-lasting increase in salinity after the tsunami deposit, most likely produced by coastal subsidence. Nonetheless, it was not possible to obtain the magnitude of subsidence, as the site is

interpreted to have been below MTL at this time. The remaining two events showing subsidence, Contacts I and F, were dated 1264 – 1151 cal. yr BP and 1112 – 995 cal. yr BP, respectively. The magnitude of land-level change obtained for these two events was < 0.1 m, suggesting that these events could had been produced by earthquakes Mw ~ 7 or, alternatively, these earthquakes' ruptures extended beneath the coast, producing minimum subsidence.

In total five possible earthquakes occurred in a period of 1355 years, between the years 995 cal. yr BP and 2350 cal. yr BP. Among these events, two of them show evidence of coastal uplift.

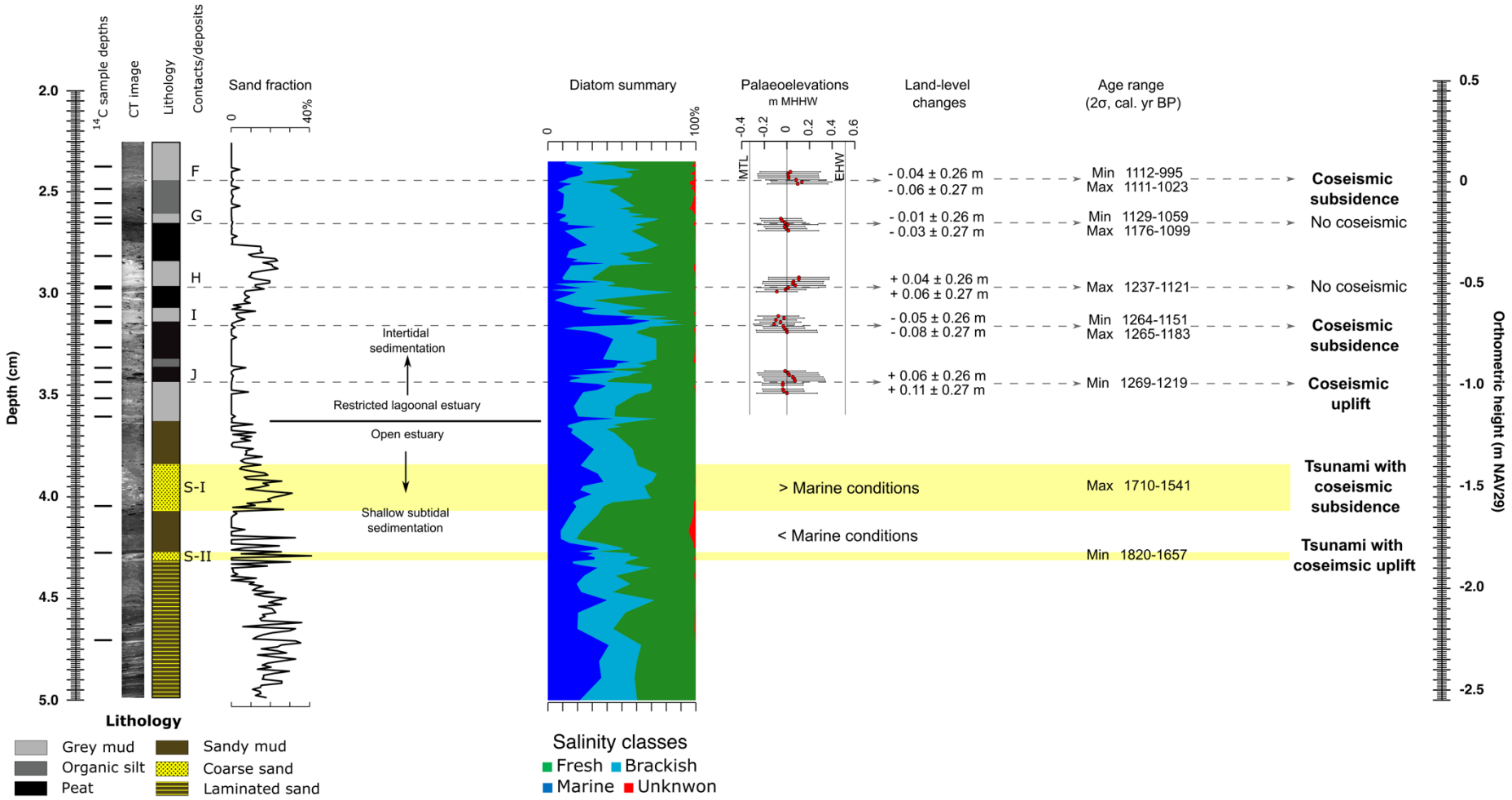

***Figure 7.3**. Record of palaeoearthquakes in the coastal wetland Estero Potrero Grande.*

7.4. Testing the criteria to identify past earthquakes.

The criteria of Nelson et al. (1996) and Shennan et al. (2016) supported this study in the identification of past earthquakes imprinted in the stratigraphy of the wetland Estero Potrero Grande. Due to some non-seismic events left a stratigraphic signal resembling a seismic origin, some criteria received more weight to define the origin of some contacts.

The local stratigraphy shows interbedded organic and minerogenic sediments forming abrupt stratigraphic contacts. The criterion of lateral extent of the abrupt contacts was used to select those cores that better represent the local stratigraphy. This study revealed that seismic and non-seismic events can produce abrupt changes in the stratigraphy, forming contacts correlated between cores >0.5 km. These findings reveal that this wetland is highly sensitive to any change in the creek channels caused by river and estuary modifications, making of this criterion only a guide in the field to identify coring sites that archive the occurrence of extreme events.

The criterion suddenness of submergence or emergence was tested in the field but assisted by analytical methods. X-ray CT scanned images, XRF data and diatom assemblages allowed to assess sudden changes. CT scanned images demonstrated its utility in the identification of abrupt stratigraphic changes downcore, showing changes in the composition of sediments. XRF data and diatom assemblages confirm coastal emergence (subsidence) or emergence (uplift). These two proxies favour the discrimination of the origin of some contacts, considering that flood events and channel abandonment mimic coastal subsidence and uplift respectively.

The amount of submergence or emergence was the most significant criterion in this study. The diatom-based method here developed permitted to quantify the magnitude of deformation during the 1995 earthquake and validate it with instrumental observations. These results indicate that the amount of subsidence for this event was 0.06 - 0.11 m, corresponding to 9 – 15 % of the great diurnal tidal range, according to the tidal datums of the tide gauge at Manzanillo's bay. These values show coherence with the minimum threshold established in Nelson et al. (1996) and Shennan et al. (2016) for the Cascadia and Alaska-Aleutian subduction zones, respectively. Hence, for this study, 0.6 m of land-level change was established as the minimum threshold

to assign a coseismic origin for previous events. Additionally, qualitative features of diatom assemblages confirm long-lasting changes in land-level when values exceed this threshold. However, more evidence needs to be collected within the same estuary to confirm this statement.

The most recent megathrust earthquakes along Jalisco subduction zone demonstrated its capacity of this subduction zone produce tsunamis during earthquakes M > 8.0. Consequently, evidence of tsunamis accompanying either subsidence or uplift was a key criterion in this study. Grain sizes allowed to identify a high energy deposit, XRF data was used to discriminate between a marine a terrestrial origin of high-energy events, while CT scanned images facilitated in the identification of the sedimentological characteristics of tsunami deposits studied worldwide.

The less significant criteria were 1) synchroneity of submergence-emergence due to the restricted evidence of past coseismic deformation along this subducting segment, and 2) evidence of liquefaction concurrent with submergence or emergence, which was used only once (deposits S-I) due to the background sedimentation that favour the identification of liquefaction features.

In conclusion, this tropical coast confirm the fact that more criteria needs to be fulfilled to determine the origin of some abrupt stratigraphic contacts. Additionally, the use of multiple analytical methods favour the identification of sedimentological properties produced coseismically.

7.5. Recommendations for future palaeoseismic studies.

7.5.1. Filling the time gap

Sediments investigated in this study were retrieved from two different sites within the same wetland (**fig. 7.1**)**.** Sedimentary sequences studied in Chapter 3 correspond to fossil records between the present day (2018 AD) and 1684 cal. AD (or 266 cal. yr BP). These sediments were deposited within the earthquake historical and instrumental era. Sediments investigated in Chapter 4 correspond to deposits between 955 - 2350 cal. yr BP. Although a continuous sedimentary sequence was retrieved for chapter 4, the upper 2.75 m is composed of fine-grained siliclastic sediments without significant lithological changes (**fig. 7.1**)**.** These sediments were interpreted as infilling

sediments of former fish tanks. Consequently, these sediments were not considered in this analysis due to potential alterations to the stratigraphic sequences. Hence, in this study there is a sedimentary time gap of ~700 years. However, the gap without evidence of earthquake is longer, ~1000 years, as the oldest earthquake in chapter 3 was dated in 1932 ± 50 AD cal. AD (18 yr cal. BP) and the youngest earthquake in chapter 4 was dated 1111-1023 cal. yr BP. Future investigations should collect sedimentary sequences from other sites within the same estuarine system, less influenced by human activities, to fill this gap and reconstruct a continuous series of earthquakes.

7.5.2. Creating a local diatom-based transfer function.

This study shows the excellent preservation of Late Holocene diatoms in sediments beneath the wetland Estero Potrero Grande. Many of these species live in modern intertidal environments of north-western Mexico (López Fuerte et al., 2010). However, their ecological characteristics were not studied using information at a local scale. Most of their ecological characteristics were assigned from multiple sources worldwide. Future research should focus on understanding the modern ecological conditions of diatom species to provide more accurate palaeoenvironmental reconstructions. Hence, future studies should sample the distribution of modern, surface, diatom species and measure their corresponding elevations in the intertidal zone to build a transfer function and calibrate the fossil record more accurately. This approach would not only solve the constraints of palaeoelevation estimations obtained in this study, but it also would be an excellent test of the method developed here.

7.5.3. Alternative sites for palaeoearthquakes investigations.

Instrumental records show that megathrust earthquakes in the Jalisco subduction zone occurred more frequently in the southern region (e.g. 1932, M_w 7.8; 1995, M_w 8.0; and 2003, M_w 7.6). In this study, the first aim was to find sedimentary evidence of the 1995 earthquake to constrain our diatom-based land-level change estimations with instrumental records. This approach allowed to find evidence of subsidence during the 1932 M_w 7.8 earthquake and an additional five older events during the Late Holocene. This study reveals for the first-time environmental changes produced by palaeoearthquakes (before 1563 AD) in this subduction zone. However, to understand

the size and recurrence of great events, more sites within the same and other estuaries need to be investigated.

The distribution of palaeoseismic studies shows the absence of earthquake records in the central and northern portion of the Jalisco coast. This region need to be investigated because it is experienced a rapid rate of urbanisation and it is adjacent to a seismic gap, where a megathrust earthquake has not occurred in the last 90 years (Singh et al., 1981).

Other seismic gaps outside the domain of the Rivera plate, including the Guerrero and the Tehuantepec gap, highlight the importance to carry out palaeoseismic studies in these areas. In the Guerrero seismic gap earthquakes have not occurred since 1908, along a segment equivalent to an earthquake Mw 8.1 – 8.4 (Suárez et al., 1990). This seismic gap is of is particular interest from the disaster risk reduction point of view due to its proximity to Mexico City (Kanamori et al., 1993). Although, a couple of studies investigate Holocene relative sea-level changes and the role of tectonic activity (e.g. Ramírez-Herrera et al., 2007, 2009), the palaeoseismic history of this seismic gap is unknown. The Tehuantepec seismic gap, which extends over a length equivalent to a Mw ~ 8.5 earthquake, has not experienced any megathrust earthquake in the last two centuries (Suárez, 2021). Along this region, geological records of past earthquakes do not exist. In contrast with the rest of the Mexican Pacific coast, the Gulf of Tehuantepec hosts multiple lower mesotidal estuaries and tidal basins (Flemming, 2012), favouring the chance of this subduction segment to explore the utility of microfossils to quantify coseismic land-level changes.

In conclusion, this study opens the possibility to continue studying megathrust earthquakes using coastal sediments from the Mexican Pacific. Particularly through the analysis of fossil diatoms, which can preserve environmental changes caused by coseismic and interseismic vertical deformation. Future studies might shed light on long-term tectonic processes and seismicity. This approach will open a vast field of opportunities to build models of past ruptures and improve the earthquake hazard assessment of the Mexican Pacific.

REFERENCES

Abbott, E. R., & Brudzinski, M. R. (2015). Shallow seismicity patterns in the northwestern section of the Mexico Subduction Zone. *Journal of South American Earth Sciences*, *63*, 279–292. https://doi.org/10.1016/j.jsames.2015.07.012

Agnew, D. C. (2002). History of Seismology. In W. H. K. Lee (Ed.), *International handbook of earthquake and engineering seismology*. Academic Press.

Alcántara, L., Almora, D., Pérez, C., Torres, M., Macías, M. A., Ramirez-, L., Valdés, C., & Pérez, J. (2012). *Over 100 years of seismic observation at Universidad Nacional Autónoma de México.* https://www.iitk.ac.in/nicee/wcee/fifteenth_conf_purtgal/

Allen, J. R. L. (2000). Morphodynamics of Holocene salt marshes: A review sketch from the Atlantic and Southern North Sea coasts of Europe. *Quaternary Science Reviews*, *19*(12), 1155–1231. https://doi.org/10.1016/S0277-3791(99)00034-7

API Manzanillo. (2012). *Programa Maestro de DesarrolloPortuario del Puerto deManzanillo2012 -2017*. API Manzanillo.

API Salina Cruz. (2016). *Programa Maestro de Desarrollo Portuario del Puerto de Salina Cruz 2017 -2021*. API Salina Cruz.

Arreygue-Rocha, E., & Cortés-Cortes, A. (2007). The catastrophe of the hurricane of 1959 in the towns of Minatitlán and Zacualpan, Colima, México (in spanish). *8th Ibero-American Congress of Mechanical Engineering*.

Atwater, B. F. (1987). Evidence for Great Holocene Earthquakes Along the Outer Coast of Washington State. *Science*, *236*(4804), 942–944. https://doi.org/10.1126/science.236.4804.942

Azúa, B. M., DeMets, C., & Masterlark, T. (2002). Strong interseismic coupling, fault afterslip, and viscoelastic flow before and after the Oct. 9, 1995 Colima-Jalisco earthquake: Continuous GPS measurements from Colima, Mexico. *Geophysical Research Letters*, *29*(8), 122-1-122–124. https://doi.org/10.1029/2002GL014702

Bandy, W., Kostoglodov, V., Díaz, A. H., & Mena, M. (1999). Structure of the southern Jalisco subduction zone, Mexico, as inferred from gravity and seismicity. *Geofísica Internacional*, *38*(3), 127–136.

Bandy, W. L., & Mortera, C. A. (2012). Gas Hydrates in the southern Jalisco subduction zone as evidenced by bottom simulating reflectors in Multichannel Seismic Reflection Data of the 2002 BART/FAMEX campaign. *Geofísica Internacional*, *51*(4), 393–400.

Barlow, N. L. M., Shennan, I., Long, A. J., Gehrels, W. R., Saher, M. H., Woodroffe, S. A., & Hillier, C. (2013). Salt marshes as late Holocene tide gauges. *Global and Planetary Change*, *106*, 90–110. https://doi.org/10.1016/j.gloplacha.2013.03.003

Barron, J. A., & Anderson, L. (2011). Enhanced Late Holocene ENSO/PDO expression along the margins of the eastern North Pacific. *Quaternary International*, *235*(1), 3–12. https://doi.org/10.1016/j.quaint.2010.02.026

Bartolomé, R., Dañobeitia, J., Michaud, F., Córdoba, D., & Delgado-Argote, L. A. (2011). Imaging the Seismic Crustal Structure of the Western Mexican Margin

between 19°N and 21°N. *Pure and Applied Geophysics*, *168*(8–9), 1373–1389. https://doi.org/10.1007/s00024-010-0206-x

Bartolome, R., Górriz, E., Dañobeitia, J., Cordoba, D., Martí, D., Cameselle, A. L., Núñez-Cornú, F., Bandy, W. L., Mortera-Gutiérrez, C. A., Nuñez, D., Castellón, A., & Alonso, J. L. (2016). Multichannel Seismic Imaging of the Rivera Plate Subduction at the Seismogenic Jalisco Block Area (Western Mexican Margin). *Pure and Applied Geophysics*, *173*(10–11), 3575–3594. https://doi.org/10.1007/s00024-016-1331-y

Beltrones, D. A. S., & Fuerte, F. O. L. (2006). Epiphytic diatoms associated with red mangrove (Rhizophora mangle) prop roots in Bahía Magdalena, Baja California Sur, Mexico. *Revista de Biología Tropical*, 287–297. https://doi.org/10.15517/rbt.v54i2.13869

Bender, A. M., Witter, R. C., & Rogers, M. (2015). Testing the use of bulk organic δ13C, δ15N, and Corg:Ntot ratios to estimate subsidence during the 1964 great Alaska earthquake. *Quaternary Science Reviews*, *113*, 134–146. https://doi.org/10.1016/j.quascirev.2014.09.031

Bianchette, T. A., Liu, K., & McCloskey, T. A. (2022). A 4000-year paleoenvironmental reconstruction and extreme event record from Laguna Nuxco, Guerrero, Mexico. *Palaeogeography, Palaeoclimatology, Palaeoecology*, *594*, 110933. https://doi.org/10.1016/j.palaeo.2022.110933

Bianchette, T. A., McCloskey, T. A., & Liu, K. (2016). Re-Evaluating the Geological Evidence for Late Holocene Marine Incursion Events along the Guerrero Seismic Gap on the Pacific Coast of Mexico. *PLOS ONE*, *11*(8), e0161568. https://doi.org/10.1371/journal.pone.0161568

Bianchette, T. A., McCloskey, T. A., & Liu, K. (2017). A 7000-year history of coastal environmental changes from Mexico's Pacific coast: A multi-proxy record from Laguna Mitla, Guerrero. *The Holocene*, *27*(8), 1214–1226. https://doi.org/10.1177/0959683616687379

Bilek, S. L., & Engdahl, E. R. (2007). Rupture characterization and aftershock relocations for the 1994 and 2006 tsunami earthquakes in the Java subduction zone. *Geophysical Research Letters*, *34*(20), L20311. https://doi.org/10.1029/2007GL031357

Birks, H. J. B. (2005). Quantitative palaeoenvironmental reconstructions from Holocene biological data. In H. J. B. Birks, R. Battarbee, A. Mackay, & F. Oldfield (Eds.), *Global Change in the Holocene* (p. 17).

Bitrán Bitrán, D. (2014). *Características del impacto socioeconómico de los principales desastres ocurridos en México en el período 1980-99*. Sistema Nacional de Protecccón Civil, Centro Nacional de Prevención de Desastres. http://catalog.hathitrust.org/api/volumes/oclc/50098182.html

Blott, S. J., & Pye, K. (2001). GRADISTAT: A grain size distribution and statistics package for the analysis of unconsolidated sediments. *Earth Surface Processes and Landforms*, *26*(11), 1237–1248. https://doi.org/10.1002/esp.261

Bodin, P., & Klinger, T. (1986). Coastal Uplift and Mortality of Intertidal Organisms Caused by the September 1985 Mexico Earthquakes. *Science*, *233*(4768), 1071–1073.

Bógalo, M. F., Ramírez-Herrera, M.-T., Goguitchaichvili, A., Rey, D., Mohamed, K. J., Calvo-Rathert, M., & Corona, N. (2017). Magnetic signature of the 22 June 1932 tsunami deposits (Jalisco, Mexican Pacific coast): Magnetic signature of

tsunami deposits. *Geochemistry, Geophysics, Geosystems*, *18*(6), 2370–2387. https://doi.org/10.1002/2016GC006752

Borerro, J., Ortiz, M., Titov, V., & Synolakis, C. (1997). Field survey of Mexican tsunami produces new data, unusual photos. *Eos, Transactions American Geophysical Union*, *78*(8), 85–88. https://doi.org/10.1029/97EO00054

Brader, M., Garrett, E., Melnick, D., & Shennan, I. (2021). Sensitivity of tidal marshes as recorders of major megathrust earthquakes: Constraints from the 25 December 2016 M_w 7.6 Chiloé earthquake, Chile. *Journal of Quaternary Science*, *36*(6), 991–1002. https://doi.org/10.1002/jqs.3323

Briggs, R. W., Engelhart Simon E., Nelson Alan R., Dura Tina, Kemp Andrew C., Haeussler Peter J., Corbett D. Reide, Angster Stephen J., & Bradley Lee-Ann. (2014). Uplift and subsidence reveal a nonpersistent megathrust rupture boundary (Sitkinak Island, Alaska). *Geophysical Research Letters*, *41*(7), 2289–2296. https://doi.org/10.1002/2014GL059380

Broecker, W. S. (2001). Was the Medieval Warm Period Global? *Science*, *291*(5508), 1497–1499. https://doi.org/10.1126/science.291.5508.1497

Bronk Ramsey, C. (1995). Radiocarbon Calibration and Analysis of Stratigraphy: The OxCal Program. *Radiocarbon*, *37*(02), 425–430. https://doi.org/10.1017/S0033822200030903

Bronk Ramsey, C. (2001). Development of the Radiocarbon Calibration Program. *Radiocarbon*, *43*(2A), 355–363. https://doi.org/10.1017/S0033822200038212

Burnett, A. P., Soreghan, M. J., Scholz, C. A., & Brown, E. T. (2011). Tropical East African climate change and its relation to global climate: A record from Lake Tanganyika, Tropical East Africa, over the past 90+ kyr. *Palaeogeography, Palaeoclimatology, Palaeoecology*, *303*(1–4), 155–167. https://doi.org/10.1016/j.palaeo.2010.02.011

Caballero, M., Peinalba, M. C., Martinez, M., Ortega-Guerrerol, B., & Vazquez, L. (2005). A Holocene record from a former coastal lagoon in Bahia Kino, Gulf of California, Mexico. *The Holocene*, *15*(8), 1236–1244. https://doi.org/10.1191/0959683605hl896rr

Cabrera-Paez, Y., Aguilar-Betancourt, C. M., & Sansón, G. G. (2020). Influencia del sustrato en la composición de la ictiofauna en zonas someras de la laguna costera Barra de Navidad, México. *Revista de Biología Tropical*, *68*(4), Article 4. https://doi.org/10.15517/rbt.v68i4.42139

Carrillo-Martínez, M. (1997). Local isosist of the Manzanillo seism of october 9, 1995, 9:36 A.M., states of Colima and Jalisco, Mexico | Revista Mexicana de Ciencias Geológicas. *Revista Mexicana de Ciencias Geológicas*, *14*(1), 110–113.

Castillo-Aja, R., & Ramírez-Herrera, M. T. (2017). Updated Tsunami Catalog for the Jalisco-Colima Coast, Mexico, Using Data from Historical Archives. *Seismological Research Letters*, *88*(1), 144–158. https://doi.org/10.1785/0220160133

Castillo-Aja, R., Ramírez-Herrera, M.-T., Machain-Castillo, M. L., Goguitchaichvili, A., & Cejudo, R. (2019). Sedimentary and microfossil imprint from historical earthquakes and tsunamis, Jalisco coast, Mexican subduction. *Marine Geology*, *407*, 32–43. https://doi.org/10.1016/j.margeo.2018.10.004

Centro Nacional de Prevención de Desastres (CENAPRED). (2005). *Tsunamis* (2nd ed.). Secretaría de Gobernación. http://cenapred.gob.mx/es/Publicaciones/archivos/163-FASCCULOSISMOS.PDF

Centro Nacional de Prevención de Desastres (CENAPRED). (2014). *Sismos* (2nd ed.). Secretaría de Gobernación. http://cenapred.gob.mx/es/Publicaciones/archivos/163-FASCCULOSISMOS.PDF

Černý, J., Ramirez-Herrera, M. T., Bógalo, M. F., Goguitchaichvili, A., Castillo-Aja, R., Morales, J., Sanchez-Cabeza, J. A., & Ruiz-Fernández, A. C. (2015). Magnetic record of extreme marine inundation events at Las Salinas site, Jalisco, Mexican Pacific coast. *International Geology Review*, *58*(3), 342-357,.

Chagué, C. (2020). Applications of geochemical proxies in paleotsunami research. In *Geological Records of Tsunamis and Other Extreme Waves* (pp. 381–401). Elsevier. https://doi.org/10.1016/B978-0-12-815686-5.00018-3

Chagué-Goff, C., Dawson, S., Goff, J. R., Zachariasen, J., Berryman, K. R., Garnett, D. L., Waldron, H. M., & Mildenhall, D. C. (2002). A tsunami (ca. 6300 years BP) and other Holocene environmental changes, northern Hawke's Bay, New Zealand. *Sedimentary Geology*, *150*(1–2), 89–102. https://doi.org/10.1016/S0037-0738(01)00269-X

Chagué-Goff, C., Goff, J., Wong, H. K. Y., & Cisternas, M. (2015). Insights from geochemistry and diatoms to characterise a tsunami's deposit and maximum inundation limit. *Marine Geology*, *359*, 22–34. https://doi.org/10.1016/j.margeo.2014.11.009

Chagué-Goff, C., Schneider, J.-L., Goff, J. R., Dominey-Howes, D., & Strotz, L. (2011). Expanding the proxy toolkit to help identify past events—Lessons from the 2004 Indian Ocean Tsunami and the 2009 South Pacific Tsunami. *Earth-Science Reviews*, *107*(1–2), 107–122. https://doi.org/10.1016/j.earscirev.2011.03.007

Chagué-Goff, C., Szczuciński, W., & Shinozaki, T. (2017a). Applications of geochemistry in tsunami research: A review. *Earth-Science Reviews*, *165*, 203–244. https://doi.org/10.1016/j.earscirev.2016.12.003

Chagué-Goff, C., Szczuciński, W., & Shinozaki, T. (2017b). Applications of geochemistry in tsunami research: A review. *Earth-Science Reviews*, *165*, 203–244. https://doi.org/10.1016/j.earscirev.2016.12.003

Chawchai, S., Kylander, M. E., Chabangborn, A., Löwemark, L., & Wohlfarth, B. (2016). Testing commonly used X-ray fluorescence core scanning-based proxies for organic-rich lake sediments and peat. *Boreas*, *45*(1), 180–189. https://doi.org/10.1111/bor.12145

Cocquyt, C., Ndjombo, E. L., Tsamemba, S. T., & Malale, H. N. S. wa. (2019). Freshwater diatoms in the Democratic Republic of the Congo: A historical overview of the research and publications. *PhytoKeys*, *136*, 107–125. https://doi.org/10.3897/phytokeys.136.47386

Compère, P. (1984). Some algae from the Red Sea Hills in north-eastern Sudan. In H. J. Dumont, A. I. el Moghraby, & L. A. Desougi (Eds.), *Limnology and Marine Biology in the Sudan* (pp. 61–77). Springer Netherlands. https://doi.org/10.1007/978-94-009-6557-7_8

Connell, R., Canevari, L., Bernhardt, C. E., Wright, S., Robertson, J. N., Morgan, W., Cerezo, A., Rivero, A., Ugarte, G., Larson, R., Bronk Ramsey, C., Washington, R., Saucedo, E., Ramírez, E., Olivera, M., Becker, A., Pascual, J., Barandarián, M., Ramírez, G., … Inter American Investment Corporation. (2015). *Port of Manzanillo: Climate Risk Management* (p. 395). Inter-American Development Bank. https://publications.iadb.org/publications/english/document/Port-of-Manzanillo-Climate-Risk-Management-(Executive-Summary).pdf

Corbett, D. R., & Walsh, J. P. (2015). 210-Lead and 137-Cesium: Establishing a chronology for the last century. In I. Shennan, A. J. Long, & B. P. Horton (Eds.), *Handbook of Sea-Level Research* (pp. 361–372). John Wiley & Sons, Ltd. https://doi.org/10.1002/9781118452547.ch24

Corona, N., & Ramírez-Herrera, M. T. (2012). Mapping and historical reconstruction of the great Mexican 22 June 1932 tsunami. *Natural Hazards and Earth System Sciences*, *12*(5), 1337–1352. https://doi.org/10.5194/nhess-12-1337-2012

Costa, P. J., Andrade, C., Cascalho, J., Dawson, A. G., Freitas, M. C., Paris, R., & Dawson, S. (2015). Onshore tsunami sediment transport mechanisms inferred from heavy mineral assemblages. *The Holocene*, *25*(5), 795–809. https://doi.org/10.1177/0959683615569322

Costa, P. J. M., Dawson, S., Ramalho, R. S., Engel, M., Dourado, F., Bosnic, I., & Andrade, C. (2021). A review on onshore tsunami deposits along the Atlantic coasts. *Earth-Science Reviews*, *212*, 103441. https://doi.org/10.1016/j.earscirev.2020.103441

Courboulex, F., Singh, S. K., Pacheco, J. F., & Ammon, C. J. (1997). The 1995 Colima-Jalisco, Mexico, Earthquake (Mw 8): A study of the rupture process. *Geophysical Research Letters*, *24*(9), 1019–1022. https://doi.org/10.1029/97GL00945

Croudace, I. W., Rindby, A., & Rothwell, R. G. (2006). ITRAX: Description and evaluation of a new multi-function X-ray core scanner. *Geological Society, London, Special Publications*, *267*(1), 51–63. https://doi.org/10.1144/GSL.SP.2006.267.01.04

Cruz, G., & Wyss, M. (1983). Large earthquakes, mean sea level, and tsunamis along the Pacific Coast of Mexico and Central America. *Bulletin of the Seismological Society of America*, *73*(2), 553–570.

Cumming, J. L. (1933). Los terremotos de Junio de 1932 en los estados de Colima y Jalisco. *Universidad de Mexico*, *VI (31–32)*, 68–104.

Curray, J. R., & Moore, D. G. (1963). Sedimentos e historia de la costa de Nayarit, Mexico. *Boletin de La Sociedad Geológica Mexicana*, *26*(2), 107–117.

Currie, C. A., Hyndman, R. D., Wang, K., & Kostoglodov, V. (2002). Thermal models of the Mexico subduction zone: Implications for the megathrust seismogenic zone. *Journal of Geophysical Research: Solid Earth*, *107*(B12), 2370. https://doi.org/10.1029/2001JB000886

Dañobeitia, J., Bartolomé, R., Prada, M., Nuñez-Cornú, F., Córdoba, D., Bandy, W. L., Estrada, F., Cameselle, A. L., Nuñez, D., Castellón, A., Alonso, J. L., Mortera, C., & Ortiz, M. (2016). Crustal Architecture at the Collision Zone Between Rivera and North American Plates at the Jalisco Block: Tsujal Project. *Pure and Applied Geophysics*, *173*(10–11), 3553–3573. https://doi.org/10.1007/s00024-016-1388-7

Darienzo, M. E. (1991). *Late Holocene Paleoseismi city along the Northern Oregon Coast* [PhD Thesis, Portland State University]. https://pdxscholar.library.pdx.edu/cgi/viewcontent.cgi?article=2146&context=open_access_etds

Das, S., & Henry, C. (2003). Spatial relation between main earthquake slip and its aftershock distribution. *Reviews of Geophysics*, *41*(3). https://doi.org/10.1029/2002RG000119

Dawson, S., Costa, P. J. M., Dawson, A., & Engel, M. (2020). Chapter 6—Onshore archives of tsunami deposits. In M. Engel, J. Pilarczyk, S. M. May, D. Brill, & E.

Garrett (Eds.), *Geological Records of Tsunamis and Other Extreme Waves* (pp. 95–111). Elsevier. https://doi.org/10.1016/B978-0-12-815686-5.00006-7

De la Lanza Espino, G. J., Ortiz Pérez, M. A., & Carbajal Pérez, J. L. (2013). Diferenciación hidrogeomorfológica de los ambientes costeros del Pacífico, del Golfo de México y del Mar Caribe. *Investigaciones Geográficas*, *81*. https://doi.org/10.14350/rig.33375

DeMets, C., Carmichael, I., Melbourne, T., Sanchez, O., Stock, J., Suarez, G., & Hudnut, K. (1995). Anticipating the successor to Mexico's largest historical earthquake. *Eos, Transactions American Geophysical Union*, *76*(42), 413–413. https://doi.org/10.1029/95EO00255

DeMets, C., & Traylen, S. (2000). Motion of the Rivera plate since 10 Ma relative to the Pacific and North American plates and the mantle. *Tectonophysics*, *318*(1), 119–159. https://doi.org/10.1016/S0040-1951(99)00309-1

Denys L. (1991). *A check-list of the diatoms in the Holocene deposits of the Western Belgian coastal plain with the survey of their apparent ecological requirements. Introduction, ecological code and complete list.* (Vol. 246). Geological Service of Belgium.

DePaolis, J. M., Dura, T., MacInnes, B., Ely, L. L., Cisternas, M., Carvajal, M., Tang, H., Fritz, H. M., Mizobe, C., Wesson, R. L., Figueroa, G., Brennan, N., Horton, B. P., Pilarczyk, J. E., Corbett, D. R., Gill, B. C., & Weiss, R. (2021). Stratigraphic evidence of two historical tsunamis on the semi-arid coast of north-central Chile. *Quaternary Science Reviews*, *266*, 107052. https://doi.org/10.1016/j.quascirev.2021.107052

Di Giacomo, D., Harris, J., Villaseñor, A., Storchak, D. A., Engdahl, E. R., & Lee, W. H. K. (2015). ISC-GEM: Global Instrumental Earthquake Catalogue (1900–2009), I. Data collection from early instrumental seismological bulletins. *Physics of the Earth and Planetary Interiors*, *239*, 14–24. https://doi.org/10.1016/j.pepi.2014.06.003

Dixon, T. H., & Moore, C. (2007). 1 The Seismogenic Zone of Subduction Thrust Faults: Introduction. In T. H. Dixon & C. Moore (Eds.), *The Seismogenic Zone of Subduction Thrust Faults:* (pp. 2–14). Columbia University Press. https://doi.org/10.7312/dixo13866

Dominey-Howes, D. T. M., Humphreys, G. S., & Hesse, P. P. (2006). Tsunami and palaeotsunami depositional signatures and their potential value in understanding the late-Holocene tsunami record. *The Holocene*, *16*(8), 1095–1107. https://doi.org/10.1177/0959683606069400

Dominguez Rivas, J., Singh, S. K., & Sánchez Sesma, F. (1997). Sismología. In A. Tena-Colunga (Ed.), *El macrosismo de Manzanillo del 9 de octubre de 1995: Colima, México, septiembre de 1997*. Universidad de Colima : Gobierno del Estado de Colima : Sociedad Mexicana de Ingeniería Sísmica.

Drexler, J. Z., Fuller, C. C., & Archfield, S. (2018). The approaching obsolescence of 137Cs dating of wetland soils in North America. *Quaternary Science Reviews*, *199*, 83–96. https://doi.org/10.1016/j.quascirev.2018.08.028

Dura, T., & Hemphill-Haley, E. (2020). Diatoms in tsunami deposits. In *Geological Records of Tsunamis and Other Extreme Waves* (pp. 291–322). Elsevier. https://doi.org/10.1016/B978-0-12-815686-5.00014-6

Dura, T., Hemphill-Haley, E., Sawai, Y., & Horton, B. P. (2016). The application of diatoms to reconstruct the history of subduction zone earthquakes and tsunamis. *Earth-Science Reviews*, *152*, 181–197. https://doi.org/10.1016/j.earscirev.2015.11.017

Dura, T., Horton, B. P., Cisternas, M., Ely, L. L., Hong, I., Nelson, A. R., Wesson, R. L., Pilarczyk, J. E., Parnell, A. C., & Nikitina, D. (2017). Subduction zone slip variability during the last millennium, south-central Chile. *Quaternary Science Reviews*, *175*, 112–137. https://doi.org/10.1016/j.quascirev.2017.08.023

Dura, T., Rubin, C. M., Kelsey, H. M., Horton, B. P., Hawkes, A., Vane, C. H., Daryono, M., Pre, C. G., Ladinsky, T., & Bradley, S. (2011). Stratigraphic record of Holocene coseismic subsidence, Padang, West Sumatra. *Journal of Geophysical Research: Solid Earth*, *116*(B11), B11306. https://doi.org/10.1029/2011JB008205

Edwards, R. R. C. (1978). Ecology of a coastal lagoon complex in Mexico. *Estuarine and Coastal Marine Science*, *6*(1), 75–92. https://doi.org/10.1016/0302-3524(78)90043-9

Eissler, H., & McNally, K. (1984). Seismicity and tectonics of the Rivera Plate and implications for the 1932 Jalisco, Mexico, earthquake. *Journal of Geophysical Research: Solid Earth*, *89*(B6), 4520–4530. https://doi.org/10.1029/JB089iB06p04520

Ellison, J. C. (1989). Pollen analysis of mangrove sediments as a sea-level indicator: Assessment from Tongatapu, Tonga. *Palaeogeography, Palaeoclimatology, Palaeoecology*, *74*(3–4), 327–341. https://doi.org/10.1016/0031-0182(89)90068-0

Elwany, M. H. S., Flick, R. E., & Aijaz, S. (1998). Opening and closure of a marginal Southern California lagoon inlet. *Estuaries*, *21*(2), 246–254. https://doi.org/10.2307/1352472

Engdahl, E. R., & Villaseñor, A. (2002). 41 Global seismicity: 1900–1999. In *International Geophysics* (Vol. 81, pp. 665–XVI). Elsevier. https://doi.org/10.1016/S0074-6142(02)80244-3

Engelhart, S. E., Horton, B. P., Nelson, A. R., Hawkes, A. D., Witter, R. C., Wang, K., Wang, P.-L., & Vane, C. H. (2013). Testing the use of microfossils to reconstruct great earthquakes at Cascadia. *Geology*, *41*(10), 1067–1070. https://doi.org/10.1130/G34544.1

Engelhart, S. E., Horton, B. P., Roberts, D. H., Bryant, C. L., & Corbett, D. R. (2007). Mangrove pollen of Indonesia and its suitability as a sea-level indicator. *Marine Geology*, *242*(1), 65–81. https://doi.org/10.1016/j.margeo.2007.02.020

Escobedo, D., Pacheco, J. F., & Suárez, G. (1998). Teleseismic body-wave analysis of the 9 October, 1995 (Mw = 8.0), Colima-Jalisco, Mexico Earthquake, and its largest foreshock and aftershock. *Geophysical Research Letters*, *25*(4), 547–550. https://doi.org/10.1029/98GL00061

Falvard, S., & Paris, R. (2017). X-ray tomography of tsunami deposits: Towards a new depositional model of tsunami deposits. *Sedimentology*, *64*(2), 453–477. https://doi.org/10.1111/sed.12310

Farreras, S., Ortiz, M., & Gonzalez, J. I. (2007). Steps Towards the Implementation of a Tsunami Detection, Warning, Mitigation and Preparedness Program for Southwestern Coastal Areas of Mexico. *Pure and Applied Geophysics*, *164*(2–3), 605–616. https://doi.org/10.1007/s00024-006-0175-2

Figueroa-Rangel, B. L., Valle-Martínez, A., Olvera-Vargas, M., & Liu, K. (2016). Environmental History of Mangrove Vegetation in Pacific West-Central Mexico during the Last 1300 Years. *Frontiers in Ecology and Evolution*, *4*. https://doi.org/10.3389/fevo.2016.00101

Filonov, A. E. (1997). Researchers study tsunami generated by Mexican earthquake. *Eos, Transactions American Geophysical Union*, *78*(3), 21–25. https://doi.org/10.1029/97EO00014

Flemming, B. W. (2012). Siliciclastic Back-Barrier Tidal Flats. In R. A. Davis & R. W. Dalrymple (Eds.), *Principles of Tidal Sedimentology* (pp. 231–267). Springer Netherlands. https://doi.org/10.1007/978-94-007-0123-6_10

Folk, R. L., & Ward, W. C. (1957). *Brazos River Bar: A Study in the Significance of Grain Size Parameters*. 24.

Fujiwara, O., Goto, K., Ando, R., & Garrett, E. (2020). Paleotsunami research along the Nankai Trough and Ryukyu Trench subduction zones – Current achievements and future challenges. *Earth-Science Reviews*, *210*, 103333. https://doi.org/10.1016/j.earscirev.2020.103333

Furukawa, K., & Wolanski, E. (1996). Sedimentation in Mangrove Forests. *Mangroves and Salt Marshes*, *1*(1), 3–10. https://doi.org/10.1023/A:1025973426404

Furukawa, K., Wolanski, E., & Mueller, H. (1997). Currents and sediment transport in mangrove forests. *Estuarine, Coastal and Shelf Science*, *44*(3), 301–310.

García, E. (1964). *Modificaciones al Sistema de Clasificación Climática de Köppen*. Instituto de Geografía, UNAM. https://www.igg.unam.mx/geoigg/biblioteca/archivos/memoria/20190917100949.pdf

Garrett, E., Fujiwara, O., Garrett, P., Heyvaert, V. M. A., Shishikura, M., Yokoyama, Y., Hubert-Ferrari, A., Brückner, H., Nakamura, A., & De Batist, M. (2016). A systematic review of geological evidence for Holocene earthquakes and tsunamis along the Nankai-Suruga Trough, Japan. *Earth-Science Reviews*, *159*, 337–357. https://doi.org/10.1016/j.earscirev.2016.06.011

Garrett, E., Shennan, I., Watcham, E. P., & Woodroffe, S. A. (2013). Reconstructing paleoseismic deformation, 1: Modern analogues from the 1960 and 2010 Chilean great earthquakes. *Quaternary Science Reviews*, *75*, 11–21. https://doi.org/10.1016/j.quascirev.2013.04.007

Garrett, E., Shennan, I., Woodroffe, S. A., Cisternas, M., Hocking, E. P., & Gulliver, P. (2015). Reconstructing paleoseismic deformation, 2: 1000 years of great earthquakes at Chucalén, south central Chile. *Quaternary Science Reviews*, *113*, 112–122. https://doi.org/10.1016/j.quascirev.2014.10.010

Giralt, S., Rico-Herrero, M. T., Vega, J. C., & Valero-Garcés, B. L. (2011). Quantitative climate reconstruction linking meteorological, limnological and XRF core scanner datasets: The Lake Sanabria case study, NW Spain. *Journal of Paleolimnology*, *46*(3), 487–502. https://doi.org/10.1007/s10933-011-9509-x

Goguitchaichvili, A., Ramírez-Herrera, M. T., Calvo-Rathert, M., Reyes, B. A., Carrancho, Á., Caballero, C., Bautista, F., & Contreras, J. M. (2013). Magnetic fingerprint of tsunami-induced deposits in the Ixtapa–Zihuatanejo Area, Western Mexico. *International Geology Review*, *55*(12), 1462–1470. https://doi.org/10.1080/00206814.2013.779781

Gómez-González, J. M., Mendoza, C., Sladen, A., & Guzmán-Speziale, M. (2010). Kinematic source analysis of the 2003 Tecomán, México, earthquake (Mw 7.6) using teleseismic body waves. *Boletín de La Sociedad Geológica Mexicana*, *62*(2), 249–262.

González Villarreal, L. M. (2005). *Guía ilustrada de los gasterópodos marinos de la Bahía de Tenacatita, Jalisco, México*. Universidad de Guadalajara.

Gonzalez-Vazquez, J. A., Silva, R., Mendoza, E., & Delgadillo-Calzadilla, M. A. (2014). Towards Coastal Management of a Degraded System: Barra de Navidad,

Jalisco, Mexico. *Journal of Coastal Research*, *71*, 107–113. https://doi.org/10.2112/SI71-013.1

Goslin, J., & Clemmensen, L. B. (2017). Proxy records of Holocene storm events in coastal barrier systems: Storm-wave induced markers. *Quaternary Science Reviews*, *174*, 80–119. https://doi.org/10.1016/j.quascirev.2017.08.026

Govers R., Furlong K. P., Wiel L., Herman M. W., & Broerse T. (2017). The Geodetic Signature of the Earthquake Cycle at Subduction Zones: Model Constraints on the Deep Processes. *Reviews of Geophysics*, *0*(0). https://doi.org/10.1002/2017RG000586

Guardado Marín, G. (2009). Turismo, globalización y desarrollo local: Puerto Vallarta y los retos del porvenir. *Estudios demográficos y urbanos*, *24*(1), 219–247.

Gugliotta, M., Saito, Y., Ta, T. K. O., Nguyen, V. L., Tamura, T., Wang, Z., La Croix, A. D., & Nakashima, R. (2021). Abandonment and rapid infilling of a tide-dominated distributary channel at 0.7 ka in the Mekong River Delta. *Scientific Reports*, *11*(1), 11040. https://doi.org/10.1038/s41598-021-90268-6

Gutenber, B., & Richter, C. F. (1954). *Seismicity of the Earth and Associated Phenomena*. Princeton University Press ,.

Hagen, A., Morgerman, J., Sereno Trabaldo, E., & Abelardo González, J. (2016). *Re-analysis of the 1959 Manzanillo Mexico Hurricane*. NOAA.

Haltia, E., Leppänen, A.-P., Kallio, A., & Saarinen, T. (2021). Sediment profile dating and reconstructing nuclear events from annually laminated lake sediments in northern Finland. *Journal of Environmental Radioactivity*, *233*, 106611. https://doi.org/10.1016/j.jenvrad.2021.106611

Hamilton, C. A., Kirby, J. R., Lane, T. P., Plater, A. J., & Waller, M. P. (2019). Sediment supply and barrier dynamics as driving mechanisms of Holocene coastal change for the southern North Sea basin. *Quaternary International*, *500*, 147–158. https://doi.org/10.1016/j.quaint.2019.02.028

Hamilton, S., & Shennan, I. (2005). Late Holocene relative sea-level changes and the earthquake deformation cycle around upper Cook Inlet, Alaska. *Quaternary Science Reviews*, *24*(12), 1479–1498. https://doi.org/10.1016/j.quascirev.2004.11.003

Hartley, B., Barber, H. G., Carter, J. R., & Sims, P. A. (1996). *An atlas of British diatoms*. Biopress.

Hawkes, A. D., Horton, B. P., Nelson, A. R., & Hill, D. F. (2010). The application of intertidal foraminifera to reconstruct coastal subsidence during the giant Cascadia earthquake of AD 1700 in Oregon, USA. *Quaternary International*, *221*(1–2), 116–140. https://doi.org/10.1016/j.quaint.2009.09.019

Hayes, G. P., Moore, G. L., Portner, D. E., Hearne, M., Flamme, H., Furtney, M., & Smoczyk, G. M. (2018). Slab2, a comprehensive subduction zone geometry model. *Science*, eaat4723. https://doi.org/10.1126/science.aat4723

Hemphill-Haley, E. (1993). *Taxonomy of recent and fossil (Holocene) diatoms (Bacillariophyta) from northern Willapa Bay, Washington.* (Open-File Report) [Open-File Report]. USGS.

Hemphill-Haley, E. (1996). Diatoms as an aid in identifying late-Holocene tsunami deposits. *The Holocene*, *6*(4), 439–448. https://doi.org/10.1177/095968369600600406

Hernández, J. C. M., Molina, L. M. F., González, F. M.-C., López, V. M. C., & López, J. T. (2013). *Influence of tropical cyclones between 1970 and 2010 in the Bahía de Banderas region, Nayarit-Jalisco, México (in spanish)*. 13.

Hernández Santana, J. R., Ortiz Pérez, M. A., & Zamorano Orozco, J. J. (1995). Regionalización morfoestructural de la Sierra Madre del Sur, México. *Investigaciones geográficas*, *31*, 45–67.

Heuret, A., Lallemand, S., Funiciello, F., Piromallo, C., & Faccenna, C. (2011). Physical characteristics of subduction interface type seismogenic zones revisited. *Geochemistry, Geophysics, Geosystems*, *12*(1), Q01004. https://doi.org/10.1029/2010GC003230

Hill, T. D., Sommer, N. R., Kanaskie, C. R., Santos, E. A., & Oczkowski, A. J. (2018). Nitrogen uptake and allocation estimates for Spartina alterniflora and Distichlis spicata. *Journal of Experimental Marine Biology and Ecology*, *507*, 53–60. https://doi.org/10.1016/j.jembe.2018.07.006

Hjörleifsdóttir, V., Sánchez-Reyes, H. S., Ruiz-Angulo, A., Ramírez-Herrera, M. T., Castillo-Aja, R., Singh, S. K., & Ji, C. (2018). Was the 9 October 1995 Mw 8 Jalisco, Mexico, Earthquake a Near-Trench Event? *Journal of Geophysical Research: Solid Earth*, *123*(10), 8907–8925. https://doi.org/10.1029/2017JB014899

Hjörleifsdóttir, V., Singh, S. K., & Husker, A. (2016). Differences in Epicentral Location of Mexican Earthquakes between Local and Global Catalogs: An update. *Geofísica Internacional*, *55*(1), 79–93.

Hocking, E. P., Garrett, E., & Cisternas, M. (2017). Modern diatom assemblages from Chilean tidal marshes and their application for quantifying deformation during past great earthquakes: A NEW MODERN DIATOM DATASET FOR EARTHQUAKE RECONSTRUCTION IN CHILE. *Journal of Quaternary Science*, *32*(3), 396–415. https://doi.org/10.1002/jqs.2933

Hong, I., Horton, B. P., Hawkes, A. D., O'Donnell, R. J., Padgett, J. S., Dura, T., & Engelhart, S. E. (2021). Diatoms of the intertidal environments of Willapa Bay, Washington, USA as a sea-level indicator. *Marine Micropaleontology*, *167*, 102033. https://doi.org/10.1016/j.marmicro.2021.102033

Horton, B. P., & Sawai, Y. (2010). Diatoms as indicators of former sea levels, earthquakes, tsunamis, and hurricanes. In J. P. Smol & E. F. Stoermer (Eds.), *The Diatoms* (2nd ed., pp. 357–372). Cambridge University Press. https://doi.org/10.1017/CBO9780511763175.020

Horton, B. P., Zong, Y., Hillier, C., & Engelhart, S. (2007). Diatoms from Indonesian mangroves and their suitability as sea-level indicators for tropical environments. *Marine Micropaleontology*, *63*(3), 155–168. https://doi.org/10.1016/j.marmicro.2006.11.005

Hua, Q., Turnbull, J. C., Santos, G. M., Rakowski, A. Z., Ancapichún, S., Pol-Holz, R. D., Hammer, S., Lehman, S. J., Levin, I., Miller, J. B., Palmer, J. G., & Turney, C. S. M. (2021). Atmospheric Radiocarbon For The Period 1950–2019. *Radiocarbon*, 1–23. https://doi.org/10.1017/RDC.2021.95

Hughes, J. F., Mathewes, R. W., & Clague, J. J. (2002). Use of pollen and vascular plants to estimate coseismic subsidence at a tidal marsh near Tofino, British Columbia. *Palaeogeography, Palaeoclimatology, Palaeoecology*, *185*(1), 145–161. https://doi.org/10.1016/S0031-0182(02)00283-3

Hutton, W., DeMets, C., Sánchez, O., Suárez, G., & Stock, J. (2001). Slip kinematics and dynamics during and after the 1995 October 9 Mw = 8.0 Colima–Jalisco earthquake, Mexico, from GPS geodetic constraints. *Geophysical Journal International*, *146*(3), 637–658. https://doi.org/10.1046/j.1365-246X.2001.00472.x

Hyndman, R. D. (2007). 2. The Seismogenic Zone of Subduction Thrust Faults What We Know and Don't Know. In T. H. Dixon & C. Moore (Eds.), *The Seismogenic Zone of Subduction Thrust Faults*. Columbia University Press. https://doi.org/10.7312/dixo13866-002

INEGI. (1975). *Carta uso del suelo, Cihuatlán E-13-B-42* [Map].

Ishizawa, T., Goto, K., Yokoyama, Y., Miyairi, Y., Sawada, C., & Takada, K. (2018). Reducing the age range of tsunami deposits by 14C dating of rip-up clasts. *Sedimentary Geology*, *364*, 334–341. https://doi.org/10.1016/j.sedgeo.2017.09.008

Jagodziński, R., Sternal, B., Szczuciński, W., Chagué-Goff, C., & Sugawara, D. (2012). Heavy minerals in the 2011 Tohoku-oki tsunami deposits—Insights into sediment sources and hydrodynamics. *Sedimentary Geology*, *282*, 57–64. https://doi.org/10.1016/j.sedgeo.2012.07.015

Jaramillo, D., Vélez, M. I., Escobar, J., Pardo-Trujillo, A., Vallejo, F., Villegas, J. C., Acevedo, A. L., Curtis, J., Rincón, H., & Trejos-Tamayo, R. (2021). Mid to late holocene dry events in Colombia's super humid Western Cordillera reveal changes in regional atmospheric circulation. *Quaternary Science Reviews*, *261*, 106937. https://doi.org/10.1016/j.quascirev.2021.106937

Jiménez Román, A. (1980). Estudio hidroclimático de la cuenca del río Marabasco. *Investigaciones geográficas*, *10*, 209–252.

Joo-Chang, J. C., Islebe, G. A., & Torrescano-Valle, N. (2015). Mangrove history during middle- and late-Holocene in Pacific south-eastern Mexico. *The Holocene*, *25*(4), 651–662. https://doi.org/10.1177/0959683614566217

Kanamori, H., Jennings, P. C., Singh, S. K., & Astiz, L. (1993). Estimation of strong ground motions in Mexico City expected for large earthquakes in the Guerrero seismic gap. *Bulletin of the Seismological Society of America*, *83*(3), 811–829. https://doi.org/10.1785/BSSA0830030811

Kelleher, J., Savino, J., Rowlett, H., & McCann, W. (1974). Why and where great thrust earthquakes occur along island arcs. *Journal of Geophysical Research*, *79*(32), 4889–4899. https://doi.org/10.1029/JB079i032p04889

Kelsey, H. M., Nelson, A. R., Hemphill-Haley, E., & Witter, R. C. (2005). Tsunami history of an Oregon coastal lake reveals a 4600 yr record of great earthquakes on the Cascadia subduction zone. *GSA Bulletin*, *117*(7–8), 1009–1032. https://doi.org/10.1130/B25452.1

Kelsey, H. M., Witter, R. C., Engelhart, S. E., Briggs, R., Nelson, A., Haeussler, P., & Corbett, D. R. (2015). Beach ridges as paleoseismic indicators of abrupt coastal subsidence during subduction zone earthquakes, and implications for Alaska-Aleutian subduction zone paleoseismology, southeast coast of the Kenai Peninsula, Alaska. *Quaternary Science Reviews*, *113*, 147–158. https://doi.org/10.1016/j.quascirev.2015.01.006

Kelsey, H. M., Witter, R. C., & Hemphill-Haley, E. (2002). Plate-boundary earthquakes and tsunamis of the past 5500 yr, Sixes River estuary, southern Oregon. *Geological Society of America Bulletin*, *114*(3), 298–314. https://doi.org/10.1130/0016-7606(2002)114<0298:PBEATO>2.0.CO;2

Kemp, A. C., Cahill, N., Engelhart, S. E., Hawkes, A. D., & Wang, K. (2018). Revising Estimates of Spatially Variable Subsidence during the A.D. 1700 Cascadia Earthquake Using a Bayesian Foraminiferal Transfer Function. *Bulletin of the Seismological Society of America*, *108*(2), 654–673. https://doi.org/10.1785/0120170269

Kemp, A. C., Engelhart, S. E., Culver, S. J., Nelson, A., Briggs, R. W., & Haeussler, P. J. (2013). Modern Salt-Marsh and Tidal-Flat Foraminifera From Sitkinak and Simeonof Islands, Southwestern Alaska. *The Journal of Foraminiferal Research*, *43*(1), 88–98. https://doi.org/10.2113/gsjfr.43.1.88

Kemp, A. C., Sommerfield, C. K., Vane, C. H., Horton, B. P., Chenery, S., Anisfeld, S., & Nikitina, D. (2012). Use of lead isotopes for developing chronologies in recent salt-marsh sediments. *Quaternary Geochronology*, *12*, 40–49. https://doi.org/10.1016/j.quageo.2012.05.004

Kemp, A. C., & Telford, R. J. (2015). Transfer functions. In I. Shennan, A. J. Long, & B. P. Horton (Eds.), *Handbook of Sea-Level Research* (pp. 470–499). John Wiley & Sons, Ltd. https://doi.org/10.1002/9781118452547.ch31

Kemp, A. C., Wright, A. J., Barnett, R. L., Hawkes, A. D., Charman, D. J., Sameshima, C., King, A. N., Mooney, H. C., Edwards, R. J., Horton, B. P., & van de Plassche, O. (2017). Utility of salt-marsh foraminifera, testate amoebae and bulk-sediment δ13C values as sea-level indicators in Newfoundland, Canada. *Marine Micropaleontology*, *130*, 43–59. https://doi.org/10.1016/j.marmicro.2016.12.003

Kempf, P., Moernaut, J., Van Daele, M., Pino, M., Urrutia, R., & De Batist, M. (2020). Paleotsunami record of the past 4300 years in the complex coastal lake system of Lake Cucao, Chiloé Island, south central Chile. *Sedimentary Geology*, *401*, 105644. https://doi.org/10.1016/j.sedgeo.2020.105644

Kempf, P., Moernaut, J., Van Daele, M., Vandoorne, W., Pino, M., Urrutia, R., & De Batist, M. (2017). Coastal lake sediments reveal 5500 years of tsunami history in south central Chile. *Quaternary Science Reviews*, *161*, 99–116. https://doi.org/10.1016/j.quascirev.2017.02.018

Kempf, P., Moernaut, J., Van Daele, M., Vermassen, F., Vandoorne, W., Pino, M., Urrutía, R., Schmidt, S., Garrett, E., & De Batist, M. (2015). The sedimentary record of the 1960 tsunami in two coastal lakes on Isla de Chiloé, south central Chile. *Sedimentary Geology*, *328*, 73–86. https://doi.org/10.1016/j.sedgeo.2015.08.004

Khan, N. S., Ashe, E., Horton, B. P., Dutton, A., Kopp, R. E., Brocard, G., Engelhart, S. E., Hill, D. F., Peltier, W. R., Vane, C. H., & Scatena, F. N. (2017). Drivers of Holocene sea-level change in the Caribbean. *Quaternary Science Reviews*, *155*, 13–36. https://doi.org/10.1016/j.quascirev.2016.08.032

Koketsu, K., Yokota, Y., Nishimura, N., Yagi, Y., Miyazaki, S., Satake, K., Fujii, Y., Miyake, H., Sakai, S., Yamanaka, Y., & Okada, T. (2011). A unified source model for the 2011 Tohoku earthquake. *Earth and Planetary Science Letters*, *310*(3), 480–487. https://doi.org/10.1016/j.epsl.2011.09.009

Kostoglodov, V., & Bandy, W. (1995). Seismotectonic constraints on the convergence rate between the Rivera and North American plates. *Journal of Geophysical Research: Solid Earth (1978–2012)*, *100*(B9), 17977–17989. https://doi.org/10.1029/95JB01484

Kostoglodov, V., & Pacheco, J. (1999). *Cien anos de sismicidad en México*. Universidad Nacional Autónoma de México. http://usuarios.geofisica.unam.mx/vladimir/sismos/100a%F1os.html

Krauss, K. W., Lovelock, C. E., McKee, K. L., López-Hoffman, L., Ewe, S. M. L., & Sousa, W. P. (2008). Environmental drivers in mangrove establishment and early development: A review. *Aquatic Botany*, *89*(2), 105–127. https://doi.org/10.1016/j.aquabot.2007.12.014

Lario, J., Spencer, C., Plater, A. J., Zazo, C., Goy, J. L., & Dabrio, C. J. (2002). Particle size characterisation of Holocene back-barrier sequences from North Atlantic coasts (SW Spain and SE England). *Geomorphology*, *42*(1–2), 25–42. https://doi.org/10.1016/S0169-555X(01)00071-X

Lay, T. (2005). The Great Sumatra-Andaman Earthquake of 26 December 2004. *Science*, *308*(5725), 1127–1133. https://doi.org/10.1126/science.1112250

Leira, M., & Sabater, S. (2005). Diatom assemblages distribution in catalan rivers, NE Spain, in relation to chemical and physiographical factors. *Water Research*, *39*(1), 73–82. https://doi.org/10.1016/j.watres.2004.08.034

Leonard, L. J., Currie, C. A., Mazzotti, S., & Hyndman, R. D. (2010). Rupture area and displacement of past Cascadia great earthquakes from coastal coseismic subsidence. *Geological Society of America Bulletin*, *122*(11–12), 2079–2096. https://doi.org/10.1130/B30108.1

Lezilda Carvalho Torgan, & Cristiane Bahi Dos Santos. (2008). *Diadesmis confervacea (Diadesmiaceae-Bacillariophyta): Morfologia externa, distribuição e aspectos ecológicos*. https://doi.org/10.13140/2.1.1702.7208

Liu, X., Colman, S. M., Brown, E. T., Minor, E. C., & Li, H. (2013). Estimation of carbonate, total organic carbon, and biogenic silica content by FTIR and XRF techniques in lacustrine sediments. *Journal of Paleolimnology*, *50*(3), 387–398. https://doi.org/10.1007/s10933-013-9733-7

Lonard, R. I., Judd, F. W., & Stalter, R. (2011). The Biological Flora of Coastal Dunes and Wetlands: Batis maritima C. Linnaeus. *Journal of Coastal Research*, *27*(3), 441. https://doi.org/10.2112/JCOASTRES-D-10-00142.1

Long, A. J., & Shennan, I. (1994). Sea-Level Changes in Washington and Oregon and the 'Earthquake Deformation Cycle'. *Journal of Coastal Research*, *10*(4), 825–838.

Long, A. J., & Shennan, I. (1998). Models of rapid relative sea-level change in Washington and Oregon, USA. *The Holocene*, *8*(2), 129–142. https://doi.org/10.1191/095968398666306493

López Fuerte, F. O., Siqueiros Beltrones, D. A., & Navaro R. Julio Nelson. (2010). *Benthic diatoms associated with mangrove environments in the northwest region of México*. Editorial de CICIMAR.

López-Fuerte, F. O., & Siqueiros Beltrones, D. A. (2016). A checklist of marine benthic diatoms (Bacillariophyta) from Mexico. *Phytotaxa*, *283*(3), 201. https://doi.org/10.11646/phytotaxa.283.3.1

López-Fuerte, F. O., Siqueiros-Beltrones, D. A., & Hernández-Almeida, O. U. (2013). Epiphytic diatoms of Thalassia testudinum (Hydrocharitaceae) from the Mexican Caribbean. *Marine Biodiversity Records*, *6*, e107. https://doi.org/10.1017/S1755267213000857

Manea, V. C., Manea, M., & Ferrari, L. (2013). A geodynamical perspective on the subduction of Cocos and Rivera plates beneath Mexico and Central America. *Tectonophysics*, *609*, 56–81. https://doi.org/10.1016/j.tecto.2012.12.039

Marmolejo-Rodríguez, A. J., Prego, R., Meyer-Willerer, A., Shumilin, E., & Cobelo-García, A. (2007). Total and labile metals in surface sediments of the tropical river-estuary system of Marabasco (Pacific coast of Mexico): Influence of an iron mine. *Marine Pollution Bulletin*, *55*(10–12), 459–468. https://doi.org/10.1016/j.marpolbul.2007.09.008

Márquez González, A. R., & Sánchez Crispín, Á. (2007). Turismo y ambiente: La percepción de los turistas nacionales en Bahía de Banderas, Nayarit, México. *Investigaciones Geográficas*, *64*, 19.

Martin, R. E., Harris, M. S., & Liddell, W. D. (1995). Taphonomy and time-averaging of foraminiferal assemblages in Holocene tidal flat sediments, Bahia la Choya, Sonora, Mexico (northern Gulf of California). *Marine Micropaleontology*, *26*(1–4), 187–206. https://doi.org/10.1016/0377-8398(95)00009-7

Martinez, T., Tejeda, S., Lartigue, J., Zarazua, G., Avila-Perez, P., Ramos, A., Navarrete, M., & Mullller, G. (2014). Chemical composition of marine sediments in the Pacific Ocean from Sinaloa to Jalisco, Mexico. *Journal of Radioanalytical and Nuclear Chemistry*, *299*(1), 827–834. https://doi.org/10.1007/s10967-013-2704-7

Martínez-López, A. (2004). Transport of benthic diatoms across the continental shelf off southern Baja California Peninsula. *Ciencias Marinas*, *30*(4), 503–513. https://doi.org/10.7773/cm.v30i4.347

Masselink, G., Hughes, M., & Knight, J. (2011). *Introduction to Coastal Processes and Geomorphology.* Hodder Education. http://public.eblib.com/choice/publicfullrecord.aspx?p=783997

Masterlark, T., DeMets, C., Wang, H. F., Sánchez, O., & Stock, J. (2001). Homogeneous vs heterogeneous subduction zone models: Coseismic and postseismic deformation. *Geophysical Research Letters*, *28*(21), 4047–4050. https://doi.org/10.1029/2001GL013612

Masters, P. M. (2006). Holocene sand beaches of southern California: ENSO forcing and coastal processes on millennial scales. *Palaeogeography, Palaeoclimatology, Palaeoecology*, *232*(1), 73–95. https://doi.org/10.1016/j.palaeo.2005.08.010

McCalpin, J. P., & Carver, G. A. (2009a). Chapter 5 Paleoseismology of Compressional Tectonic Environments. In *International Geophysics* (Vol. 95, pp. 315–419). Elsevier. https://doi.org/10.1016/S0074-6142(09)95005-7

McCalpin, J. P., & Carver, G. A. (2009b). Chapter 5 Paleoseismology of Compressional Tectonic Environments. In *International Geophysics* (Vol. 95, pp. 315–419). Elsevier. https://doi.org/10.1016/S0074-6142(09)95005-7

McCalpin, J. P., & Nelson, A. R. (2009). Chapter 1 Introduction to Paleoseismology. In *International Geophysics* (Vol. 95, pp. 1–27). Elsevier. https://doi.org/10.1016/S0074-6142(09)95001-X

McCloskey, T. A., Bianchette, T. A., & Liu, K. (2015). Geological and Sedimentological Evidence of a Large Tsunami Occurring ~1100 Year BP from a Small Coastal Lake along the Bay of La Paz in Baja California Sur, Mexico. *Journal of Marine Science and Engineering*, *3*(4), 1544–1567. https://doi.org/10.3390/jmse3041544

McQuoid, M. R., & Hobson, L. A. (1998). Assessment of Palaeoenvironmental Conditions on Southern Vancouver Island, British Columbia, Canada, Using the Marine Tychoplankter Paralia Sulcata. *Diatom Research*, *13*(2), 311–321. https://doi.org/10.1080/0269249X.1998.9705453

McQuoid, M. R., & Nordberg, K. (2003). The diatom Paralia sulcata as an environmental indicator species in coastal sediments. *Estuarine, Coastal and Shelf Science*, *56*(2), 339–354. https://doi.org/10.1016/S0272-7714(02)00187-7

McSweeney, S. L., Kennedy, D. M., Rutherfurd, I. D., & Stout, J. C. (2017). Intermittently Closed/Open Lakes and Lagoons: Their global distribution and boundary conditions. *Geomorphology*, *292*, 142–152. https://doi.org/10.1016/j.geomorph.2017.04.022

Melbourne, T., Carmichael, I., DeMets, C., Hudnut, K., Sanchez, O., Stock, J., Suarez, G., & Webb, F. (1997). The geodetic signature of the M8.0 Oct. 9,1995, Jalisco Subduction Earthquake. *Geophysical Research Letters*, *24*(6), 715–718. https://doi.org/10.1029/97GL00370

Meltzner, A. J., Sieh, K., Abrams, M., Agnew, D. C., Hudnut, K. W., Avouac, J.-P., & Natawidjaja, D. H. (2006). Uplift and subsidence associated with the great Aceh-Andaman earthquake of 2004: THE 2004 EARTHQUAKE. *Journal of Geophysical Research: Solid Earth*, *111*(B2), n/a-n/a. https://doi.org/10.1029/2005JB003891

Méndez Linares, A. P., López-Portillo, J., Hernández-Santana, J. R., Ortiz Pérez, M. A., & Oropeza Orozco, O. (2007). The mangrove communities in the Arroyo Seco deltaic fan, Jalisco, Mexico, and their relation with the geomorphic and physical–geographic zonation. *CATENA*, *70*(2), 127–142. https://doi.org/10.1016/j.catena.2006.05.010

Mendoza, C., & Hartzell, S. (1995). *Fault-Slip Distribution of the 1995 Colima-Jalisco, Mexico, Earthquake*. 7.

Mendoza, C., & Hartzell, S. H. (1988). Aftershock patterns and main shock faulting. *Bulletin of the Seismological Society of America*, *78*(4), 1438–1449. https://doi.org/10.1785/BSSA0780041438

Metcalfe, S. E., O'Hara, S. L., Caballero, M., & Davies, S. J. (2000). Records of Late Pleistocene–Holocene climatic change in Mexico—A review. *Quaternary Science Reviews*, *19*(7), 699–721. https://doi.org/10.1016/S0277-3791(99)00022-0

Milker, Y., Nelson, A. R., Horton, B. P., Engelhart, S. E., Bradley, L.-A., & Witter, R. C. (2016). Differences in coastal subsidence in southern Oregon (USA) during at least six prehistoric megathrust earthquakes. *Quaternary Science Reviews*, *142*, 143–163. https://doi.org/10.1016/j.quascirev.2016.04.017

Misra, V., Groenen, D., Bhardwaj, A., & Mishra, A. (2016). The warm pool variability of the tropical northeast Pacific. *International Journal of Climatology*, *36*(14), 4625–4637. https://doi.org/10.1002/joc.4658

Monecke, K., Finger, W., Klarer, D., Kongko, W., McAdoo, B. G., Moore, A. L., & Sudrajat, S. U. (2008). A 1,000-year sediment record of tsunami recurrence in northern Sumatra. *Nature*, *455*(7217), 1232–1234. https://doi.org/10.1038/nature07374

Monecke, K., Templeton, C. K., Finger, W., Houston, B., Luthi, S., McAdoo, B. G., Meilianda, E., Storms, J. E. A., Walstra, D.-J., Amna, R., Hood, N., Karmanocky, F. J., Nurjanah, Rusydy, I., & Sudrajat, S. U. (2015). Beach ridge patterns in West Aceh, Indonesia, and their response to large earthquakes along the northern Sunda trench. *Quaternary Science Reviews*, *113*, 159–170. https://doi.org/10.1016/j.quascirev.2014.10.014

Moore, A., Nishimura, Y., Gelfenbaum, G., Kamataki, T., & Triyono, R. (2006). Sedimentary deposits of the 26 December 2004 tsunami on the northwest coast of Aceh, Indonesia. *Earth, Planets and Space*, *58*(2), 253–258. https://doi.org/10.1186/BF03353385

Morán-Zenteno, D. J., Martiny, B. M., Solari, L., Mori, L., Luna-González, L., & González-Torres, E. A. (2018). Cenozoic magmatism of the Sierra Madre del Sur and tectonic truncation of the Pacific margin of southern Mexico. *Earth-Science Reviews*, *183*, 85–114. https://doi.org/10.1016/j.earscirev.2017.01.010

Morton, R. A., Gelfenbaum, G., & Jaffe, B. E. (2007). Physical criteria for distinguishing sandy tsunami and storm deposits using modern examples. *Sedimentary Geology*, *200*(3–4), 184–207. https://doi.org/10.1016/j.sedgeo.2007.01.003

Moy, C. M., Seltzer, G. O., Rodbell, D. T., & Anderson, D. M. (2002). Variability of El Niño/Southern Oscillation activity at millennial timescales during the Holocene epoch. *Nature*, *420*(6912), 162–165. https://doi.org/10.1038/nature01194

Muñoz Sevilla, N. P., Azuz Adeath, I., Le Bail, M., & Cortés Ruiz, A. (2019). Coastal Development: Construction of a Public Policy for the Shores and Seas of Mexico. In *Coastal Management* (pp. 21–38). Elsevier. https://doi.org/10.1016/B978-0-12-810473-6.00003-0

Murray-Wallace, C. V., & Woodroffe, C. D. (2014). *Quaternary sea-level changes: A global perspective*. Cambridge University Press.

Nakamura, Y., Nishimura, Y., & Putra, P. S. (2012). Local variation of inundation, sedimentary characteristics, and mineral assemblages of the 2011 Tohoku-oki tsunami on the Misawa coast, Aomori, Japan. *Sedimentary Geology*, *282*, 216–227. https://doi.org/10.1016/j.sedgeo.2012.06.003

National Geophysical Data Center. (2022). *Global Historical Tsunami Database* [Data set]. NOAA National Centers for Environmental Information. https://doi.org/10.7289/V5PN93H7

National Huricane Center (NHC). (1992). *Preliminary report. Hurricane Winifred. 6—10 October 1992.* (p. 8) [Hurricane report]. National Oceanic and Atmospheric Administration.

Nelson, A. R., Briggs, R. W., Dura, T., Engelhart, S. E., Gelfenbaum, G., Bradley, L.-A., Forman, S. L., Vane, C. H., & Kelley, K. A. (2015). Tsunami recurrence in the eastern Alaska-Aleutian arc: A Holocene stratigraphic record from Chirikof Island, Alaska. *Geosphere*, *11*(4), 1172–1203. https://doi.org/10.1130/GES01108.1

Nelson, A. R., & Kashima, K. (1993). Diatom Zonation in Southern Oregon Tidal Marshes Relative to Vascular Plants, Foraminifera, and Sea Level. *Journal of Coastal Research*, *9*(3), 673–697.

Nelson, A. R., Ota, Y., Umitsu, M., Kashima, K., & Matsushima, Y. (1998). Seismic or hydrodynamic control of rapid late-Holocene sea-level rises in southern coastal Oregon, USA? *The Holocene*, *8*(3), 287–299.

Nelson, A. R., Sawai, Y., Jennings, A. E., Bradley, L.-A., Gerson, L., Sherrod, B. L., Sabean, J., & Horton, B. P. (2008). Great-earthquake paleogeodesy and tsunamis of the past 2000 years at Alsea Bay, central Oregon coast, USA. *Quaternary Science Reviews*, *27*(7–8), 747–768. https://doi.org/10.1016/j.quascirev.2008.01.001

Nelson, A. R., Shennan, I., & Long, A. J. (1996). Identifying coseismic subsidence in tidal-wetland stratigraphic sequences at the Cascadia subduction zone of western North America. *Journal of Geophysical Research: Solid Earth*, *101*(B3), 6115–6135. https://doi.org/10.1029/95JB01051

(NHC), N. H. C. (1993). *Preliminary report Hurrican Calvin 4—9 July 1993.* (p. 8) [Hurricane report]. National Hurricane Center. https://www.nhc.noaa.gov/archive/storm_wallets/epacific/ep1993-prelim/calvin/

Novelo, E., Tavera, R., & Ibarra, C. (2007). *Bacillariophyceae from Karstic Wetlands in México*. 137.

Núñez-Cornú, F. J., Córdoba, D., Dañobeitia, J. J., Bandy, W. L., Figueroa, M. O., Bartolome, R., Núñez, D., Zamora-Camacho, A., Espíndola, J. M., Castellón,

A., Escudero, C. R., Trejo-Gómez, E., de Jesús Escalona-Alcázar, F., Suárez Plascencia, C., Alejandro Nava, F., Mortera, C., & TsuJal Working Group. (2016). Geophysical Studies across Rivera Plate and Jalisco Block, Mexico: TsuJal Project. *Seismological Research Letters*, *87*(1), 59–72. https://doi.org/10.1785/0220150144

Núñez-Cornú, F. J., Ortiz, M., & Sánchez, J. J. (2008). The great 1787 Mexican tsunami. *Natural Hazards*, *47*(3), 569–576. https://doi.org/10.1007/s11069-008-9239-1

Obermeier, S. F. (2009). Chapter 7 Using Liquefaction-Induced and Other Soft-Sediment Features for Paleoseismic Analysis. In *International Geophysics* (Vol. 95, pp. 497–564). Elsevier. https://doi.org/10.1016/S0074-6142(09)95007-0

Odériz, I., Silva, R., Mortlock, T. R., & Mori, N. (2020). El Niño-Southern Oscillation Impacts on Global Wave Climate and Potential Coastal Hazards. *Journal of Geophysical Research: Oceans*, *125*(12), e2020JC016464. https://doi.org/10.1029/2020JC016464

Okal, E. A., & Borrero, J. C. (2011). The 'tsunami earthquake' of 1932 June 22 in Manzanillo, Mexico: Seismological study and tsunami simulations. *Geophysical Journal International*, *187*(3), 1443–1459. https://doi.org/10.1111/j.1365-246X.2011.05199.x

Okal, E. A., & Newman, A. V. (2001). Tsunami earthquakes: The quest for a regional signal. *Physics of the Earth and Planetary Interiors*, *124*(1), 45–70. https://doi.org/10.1016/S0031-9201(01)00187-X

Ontiveros-Cuadras, J. F., Ruiz-Fernández, A. C., Pérez-Bernal, L. H., Raygoza-Viera, J. R., & Sanchez-Cabeza, J.-A. (2021). Historical reconstruction of trace element concentrations and fluxes in a tropical coastal lagoon (Mexican Pacific) derived from 210Pb radiochronology. *Continental Shelf Research*, *213*, 104315. https://doi.org/10.1016/j.csr.2020.104315

Ortiz, M., Kostoglodov, V., K. Singh, S., & Pacheco, J. (2000). New constraints on the uplift of October 9, 1995 Jalisco-Colima earthquake (Mw 8) based on the analysis of tsunami records at Manzanillo and Navidad, Mexico. *Geofísica Internacional*, *39*(4), 349–357. https://doi.org/10.22201/igeof.00167169p.2000.39.4.245

Ortiz, M., Singh, S. K., Kostoglodov, V., & Pacheco, J. (2000). Source areas of the Acapulco-San Marcos, Mexico earthquakes of 1962 (M 7.1; 7.0) and 1957 (M 7.7), as constrained by tsunami and uplift records. *Geofísica Internacional*, *39*(4), 337–348.

Ortiz-Huerta, L. G., Ortiz, M., & García-Gastélum, A. (2018). Far-Field Tsunami Hazard Assessment Along the Pacific Coast of Mexico by Historical Records and Numerical Simulation. *Pure and Applied Geophysics*, *175*(4), 1305–1323. https://doi.org/10.1007/s00024-018-1816-y

Otvos, E. G. (2011). Hurricane signatures and landforms—Toward improved interpretations and global storm climate chronology. *Sedimentary Geology*, *239*(1), 10–22. https://doi.org/10.1016/j.sedgeo.2011.04.014

Owen, G., & Moretti, M. (2011). Identifying triggers for liquefaction-induced soft-sediment deformation in sands. *Sedimentary Geology*, *235*(3), 141–147. https://doi.org/10.1016/j.sedgeo.2010.10.003

Pacheco, J. F., Scholz, C. H., & Sykes, L. R. (1992). Changes in frequency–size relationship from small to large earthquakes. *Nature*, *355*(6355), 71–73. https://doi.org/10.1038/355071a0

Pacheco, J. F., Sykes, L. R., & Scholz, C. H. (1993). Nature of seismic coupling along simple plate boundaries of the subduction type. *Journal of Geophysical Research: Solid Earth*, *98*(B8), 14133–14159. https://doi.org/10.1029/93JB00349

Pacheco, J., Singh, S. K., Domínguez, J., Hurtado, A., Quintanar, L., Jiménez, Z., Yamamoto, J., Gutiérrez, C., Santoyo, M., Bandy, W., Guzmán, M., Kostoglodov, V., Reyes, G., & Ramírez, C. (1997). The October 9, 1995 Colima-Jalisco, Mexico Earthquake (Mw 8): An aftershock study and a comparison of this earthquake with those of 1932. *Geophysical Research Letters*, *24*(17), 2223–2226. https://doi.org/10.1029/97GL02070

Padilla Lozoya, R. (2007). Hurricanes in the State of Colima 1573-1999: Occurrence of risk due to hydrometeorological events (in spanish). *Memories of the 6th International Congress and 12th Nacional of en vironmental sciences*, 797–802.

Padilla Lozoya, R., & Luna Montes, E. J. (1995). Post-Disaster Vulnerability in Cuyutlán, Colima 1900-1959 (in spanish). *Revista Culturales*, *6*(1), 1–34. https://doi.org/10.22234/recu.20180601.e371

Padilla y Sotelo, L. S., Juarez Gutierrez, M. del C., Propin Frejomil, E., & Galindo Perez, C. (2009). *Poblacion y economia en el territorio costero de Mexico*. Universidad Nacional Autónoma de México.

Páez, Y. C., Betancourt, C. M. A., Sansón, G. G., Kidd, K. A., Curry, R. A., & Aceves, D. K. (2022). Mercury concentrations and stable isotopes (δ15N and δ13C) in fish muscle indicate human impacts in tropical coastal lagoons. *Marine Pollution Bulletin*, *176*, 113454. https://doi.org/10.1016/j.marpolbul.2022.113454

Paris, R. (2020). Chapter 17—X-ray tomography applied to tsunami deposits. In M. Engel, J. Pilarczyk, S. M. May, D. Brill, & E. Garrett (Eds.), *Geological Records of Tsunamis and Other Extreme Waves* (pp. 365–380). Elsevier. https://doi.org/10.1016/B978-0-12-815686-5.00017-1

Paris, R., Lavigne, F., Wassmer, P., & Sartohadi, J. (2007). Coastal sedimentation associated with the December 26, 2004 tsunami in Lhok Nga, west Banda Aceh (Sumatra, Indonesia). *Marine Geology*, *238*(1), 93–106. https://doi.org/10.1016/j.margeo.2006.12.009

Patiño-Barragán, M., Meyer-Willerer, A. O., Galicia Pérez, M. A., Lezama Cervantes, C., & Lara Chávez, B. (2009). Zone of largest impacts in the port of Manzanillo Colima, Mexico, due to intense hydrometeorological events and their periodicity (in spanish). *Boletín Técnico*, *47*(1), 47–60.

Pérez-Campos, X., Espíndola, V. H., Pérez, J., Estrada, J. A., Monroy, C. C., Bello, D., González-López, A., Ávila, D. G., Esparza, M. G. C. R., Maldonado, R., Tan, Y., Rasilla, I. R., Rosas, M. Á. V., Cruz, J. L., Cárdenas, A., Estrada, F. N., Hurtado, A., Carvajal, A. de J. M., Montoya-Quintanar, E., & Pérez-Velázquez, M. A. (2018). The Mexican National Seismological Service: An Overview. *Seismological Research Letters*, *89*(2A), 318–323. https://doi.org/10.1785/0220170186

Pérez-Cruz, L. (2006). Climate and ocean variability during the middle and late Holocene recorded in laminated sediments from Alfonso Basin, Gulf of California, Mexico. *Quaternary Research*, *65*(3), 401–410. https://doi.org/10.1016/j.yqres.2006.02.003

Peters, R., & Jaffe, B. (2010). *Identification of Tsunami Deposits in the Geologic Record: Developing Criteria Using Recent Tsunami Deposits* (p. 43) [Open-File Report 2010-1239]. U.S. Geological Survey.

Peterson, C. D., & Darienzo, M. E. (1991a). *Discrimination of Climatic, Oceanic and Tectonic Mechanisms of Cyclic Marsh Burial from Alsea Bay, Oregon, U.S.A.* (No. 91–441; Earthquake Hazards in the Pacific Northwest of the United States, p. 53). U.S. Geological Survey. https://books.google.co.uk/books?id=rcEKYgEACAAJ

Peterson, C. D., & Darienzo, M. E. (1991b). *Discrimination of climatic, oceanic and tectonic mechanisms of cyclic marsh burial from Alsea Bay, Oregon, U.S.A.* (USGS Numbered Series No. 91-441–C; Open-File Report). U.S. Geological Survey,. http://pubs.er.usgs.gov/publication/ofr91441C

Pilarczyk, J. E., Dura, T., Horton, B. P., Engelhart, S. E., Kemp, A. C., & Sawai, Y. (2014). Microfossils from coastal environments as indicators of paleo-earthquakes, tsunamis and storms. *Palaeogeography, Palaeoclimatology, Palaeoecology*, *413*, 144–157. https://doi.org/10.1016/j.palaeo.2014.06.033

Pizer, C., Clark, K., Howarth, J., Garrett, E., Wang, X., Rhoades, D., & Woodroffe, S. (2021). Paleotsunamis on the Southern Hikurangi Subduction Zone, New Zealand, Show Regular Recurrence of Large Subduction Earthquakes. *The Seismic Record*, *1*(2), 75–84. https://doi.org/10.1785/0320210012

Plafker, G. (1969). *Tectonics of the March 27, 1964 Alaska earthquake:* (No. 543–I; U.S. Geological Survey Professional Paper 543–I, p. 74). https://pubs.usgs.gov/pp/0543i/pp543i_text.pdf

Polet, J., & Kanamori, H. (2002). Shallow subduction zone earthquakes and their tsunamigenic potential. *Geophysical Journal International*, *142*(3), 684–702. https://doi.org/10.1046/j.1365-246x.2000.00205.x

Qingmin, Y., Kociolek, J. P., & Quanxi, W. (2015). Taxonomic studies of the diatom genus Halamphora (Bacillariophyceae) from the mountainous regions of southwest China, including the description of two new species. *Phytotaxa*, *205*(2), 75. https://doi.org/10.11646/phytotaxa.205.2.1

Rahman, R., & Plater, A. J. (2014). Particle-size evidence of estuary evolution: A rapid and diagnostic tool for determining the nature of recent saltmarsh accretion. *Geomorphology*, *213*, 139–152. https://doi.org/10.1016/j.geomorph.2014.01.004

Ramírez-Herrera, M. T., Bógalo, M. F., Černý, J., Goguitchaichvili, A., Corona, N., Machain, M. L., Edwards, A. C., & Sosa, S. (2016). Historic and ancient tsunamis uncovered on the Jalisco-Colima Pacific coast, the Mexican subduction zone. *Geomorphology*, *259*, 90–104. https://doi.org/10.1016/j.geomorph.2016.02.011

Ramírez-Herrera, M. T., Corona, N., Cerny, J., Castillo-Aja, R., Melgar, D., Lagos, M., Goguitchaichvili, A., Machain, M. L., Vazquez-Caamal, M. L., Ortuño, M., Caballero, M., Solano-Hernandez, E. A., & Ruiz-Fernández, A.-C. (2020). Sand deposits reveal great earthquakes and tsunamis at Mexican Pacific Coast. *Scientific Reports*, *10*(1), 11452. https://doi.org/10.1038/s41598-020-68237-2

Ramírez-Herrera, M. T., Corona, N., Lagos, M., Černý, J., Goguitchaichvili, A., Goff, J., Chagué-Goff, C., Machain, M. L., Zawadzki, A., Jacobsen, G., Carranza-Edwards, A., Lozano, S., & Blecher, L. (2014). Unearthing earthquakes and their tsunamis using multiple proxies: The 22 June 1932 event and a probable fourteenth-century predecessor on the Pacific coast of Mexico. *International Geology Review*, *56*(13), 1584–1601. https://doi.org/10.1080/00206814.2014.951977

Ramírez-Herrera, M. T., Cundy, A. B., Kostoglodov, V., Carranza-Edwards, A., Morales, E., & Metcalfe, S. (2007). Sedimentary record of late-Holocene

relative sea-level change and tectonic deformation from the Guerrero Seismic Gap, Mexican Pacific Coast. *The Holocene*, *17*(8), 1211–1220. https://doi.org/10.1177/0959683607085127

Ramírez-Herrera, M. T., Cundy, A. B., Kostoglodov, V., & Ortiz, M. (2009). Late Holocene tectonic land-level changes and tsunamis at Mitla lagoon, Guerrero, Mexico. *Geofísica Internacional*, *48*(2), 195–209.

Ramírez-Herrera, M. T., Kostoglodov, V., & Urrutia-Fucugauchi, J. (2004). Holocene-emerged notches and tectonic uplift along the Jalisco coast, Southwest Mexico. *Geomorphology*, *58*(1–4), 291–304. https://doi.org/10.1016/j.geomorph.2003.07.004

Ramírez-Herrera, M. T., Lagos, M., Hutchinson, I., Kostoglodov, V., Machain, M. L., Caballero, M., Goguitchaichvili, A., Aguilar, B., Chagué-Goff, C., Goff, J., Ruiz-Fernández, A.-C., Ortiz, M., Nava, H., Bautista, F., Lopez, G. I., & Quintana, P. (2012). Extreme wave deposits on the Pacific coast of Mexico: Tsunamis or storms? — A multi-proxy approach. *Geomorphology*, *139–140*, 360–371. https://doi.org/10.1016/j.geomorph.2011.11.002

Ramírez-Herrera, M. T., & Orozco, J. J. Z. (2002). Coastal Uplift and Mortality of Coralline Algae Caused by a 6.3Mw Earthquake, Oaxaca, Mexico. *Journal of Coastal Research*, *18*(1), 75–81. JSTOR.

Ramirez-Herrera, M. T., & Urrutia-Fucugauchi, J. (1999). Morphotectonic zones along the coast of the Pacific continental margin, southern Mexico. *Geomorphology*, *28*(3), 237–250. https://doi.org/10.1016/S0169-555X(99)00016-1

Ramsey, C. B. (2008). Deposition models for chronological records. *Quaternary Science Reviews*, *27*(1), 42–60. https://doi.org/10.1016/j.quascirev.2007.01.019

Reimer, P. J., Austin, W. E. N., Bard, E., Bayliss, A., Blackwell, P. G., Bronk Ramsey, C., Butzin, M., Cheng, H., Edwards, R. L., Friedrich, M., Grootes, P. M., Guilderson, T. P., Hajdas, I., Heaton, T. J., Hogg, A. G., Hughen, K. A., Kromer, B., Manning, S. W., Muscheler, R., … Talamo, S. (2020). The IntCal20 Northern Hemisphere Radiocarbon Age Calibration Curve (0–55 cal kBP). *Radiocarbon*, *62*(4), 725–757. https://doi.org/10.1017/RDC.2020.41

Rich, A., & Keller, E. A. (2013). A hydrologic and geomorphic model of estuary breaching and closure. *Geomorphology*, *191*, 64–74. https://doi.org/10.1016/j.geomorph.2013.03.003

Roe, H. M., Doherty, C. T., Patterson, R. T., & Swindles, G. T. (2009). Contemporary distributions of saltmarsh diatoms in the Seymour–Belize Inlet Complex, British Columbia, Canada: Implications for studies of sea-level change. *Marine Micropaleontology*, *70*(3), 134–150. https://doi.org/10.1016/j.marmicro.2008.12.001

Rosales Franco, E., & Camargo Soto, C. (2019). *Carta geológico-minera. Cihuatlán. E13-B42* [Map]. Servicio Geológico Mexicano.

Rothwell, R. G., & Croudace, I. w. (2015). Twenty Years of XRF Core Scanning Marine Sediments: What Do Geochemical Proxies Tell Us? In I. W. Croudace & R. G. Rothwell (Eds.), *Micro-XRF Studies of Sediment Cores: Applications of a non-destructive tool for the environmental sciences* (pp. 25–102). Springer Netherlands. https://doi.org/10.1007/978-94-017-9849-5_2

Rovere, A., Stocchi, P., & Vacchi, M. (2016). Eustatic and Relative Sea Level Changes. *Current Climate Change Reports*, *2*(4), 221–231. https://doi.org/10.1007/s40641-016-0045-7

Ruff, L., & Kanamori, H. (1980). Seismicity and the subduction process. *Physics of the Earth and Planetary Interiors*, *23*(3), 240–252. https://doi.org/10.1016/0031-9201(80)90117-X

Ruiz-Fernández, A. C., & Hillaire-Marcel, C. (2009). 210Pb-derived ages for the reconstruction of terrestrial contaminant history into the Mexican Pacific coast: Potential and limitations. *Marine Pollution Bulletin*, *59*(4), 134–145. https://doi.org/10.1016/j.marpolbul.2009.05.006

Ruiz-Fernández, A. C., Hillaire-Marcel, C., Ghaleb, B., Soto-Jiménez, M., & Páez-Osuna, F. (2002). Recent sedimentary history of anthropogenic impacts on the Culiacan River Estuary, northwestern Mexico: Geochemical evidence from organic matter and nutrients. *Environmental Pollution*, *118*(3), 365–377. https://doi.org/10.1016/S0269-7491(01)00287-1

Sabean, J. (2004). *Applications of foraminifera to detecting land level change associated with great earthquakes along the west coast of North America*. Simon Fraser University.

Sachs, H. M., Webb, T., & Clark, D. R. (1977). Paleoecological Transfer Functions. *Annual Review of Earth and Planetary Sciences*, *5*(1), 159–178. https://doi.org/10.1146/annurev.ea.05.050177.001111

Sanchez, A., & Farreras, S. (1993). *Catalogo de Tsunamis (Maremotos) en la Costa Occidental de Mexico Catalog of Tsunamis on the Western Coast of Mexico*. U.S. Dept. of Commerce, Boulder.

Sanchez, A. J., & Farreras, S. F. (1987). Tsunami flooding extension for coastal zones of Mexico. *Marine Geodesy*, *11*(2–3), 127–135. https://doi.org/10.1080/15210608709379555

Sawai, Y. (2001a). Episodic Emergence in the Past 3000 Years at the Akkeshi Estuary, Hokkaido, Northern Japan. *Quaternary Research*, *56*(02), 231–241. https://doi.org/10.1006/qres.2001.2258

Sawai, Y. (2001b). Episodic Emergence in the Past 3000 Years at the Akkeshi Estuary, Hokkaido, Northern Japan. *Quaternary Research*, *56*(2), 231–241. https://doi.org/10.1006/qres.2001.2258

Sawai, Y. (2001c). Distribution of living and dead diatoms in tidal wetlands of northern Japan: Relations to taphonomy. *Palaeogeography, Palaeoclimatology, Palaeoecology*, *173*(3–4), 125–141. https://doi.org/10.1016/S0031-0182(01)00313-3

Sawai, Y. (2020). Subduction zone paleoseismology along the Pacific coast of northeast Japan—Progress and remaining problems. *Earth-Science Reviews*, *208*, 103261. https://doi.org/10.1016/j.earscirev.2020.103261

Sawai, Y., Horton, B., & Nagumo, T. (2004). The development of a diatom-based transfer function along the Pacific coast of eastern Hokkaido, northern Japan?an aid in paleoseismic studies of the Kuril subduction zone. *Quaternary Science Reviews*, *23*(23–24), 2467–2483. https://doi.org/10.1016/j.quascirev.2004.05.006

Sawai, Y., Horton, B. P., Kemp, A. C., Hawkes, A. D., Nagumo, T., & Nelson, A. R. (2016a). Relationships between diatoms and tidal environments in Oregon and Washington, USA. *Diatom Research*, *31*(1), 17–38. https://doi.org/10.1080/0269249X.2015.1126359

Sawai, Y., Horton, B. P., Kemp, A. C., Hawkes, A. D., Nagumo, T., & Nelson, A. R. (2016b). Relationships between diatoms and tidal environments in Oregon and Washington, USA. *Diatom Research*, *31*(1), 17–38. https://doi.org/10.1080/0269249X.2015.1126359

Sawai, Y., & Nasu, H. (2005). A 4500-year record of emergence events at Onnetoh, Hokkaido, northern Japan, reconstructed using plant macrofossils. *Marine Geology*, *217*(1–2), 49–65. https://doi.org/10.1016/j.margeo.2005.02.006

Sawai, Y., Nasu, H., & Yasuda, Y. (2002). Fluctuations in relative sea-level during the past 3000 yr in the Onnetoh estuary, Hokkaido, northern Japan. *Journal of Quaternary Science*, *17*(5–6), 607–622. https://doi.org/10.1002/jqs.708

Sawires, R., Santoyo, M. A., Peláez, J. A., & Corona Fernández, R. D. (2019). An updated and unified earthquake catalog from 1787 to 2018 for seismic hazard assessment studies in Mexico. *Scientific Data*, *6*(1), 241. https://doi.org/10.1038/s41597-019-0234-z

Schmitt, S. V., DeMets, C., Stock, J., Sánchez, O., Márquez-Azúa, B., & Reyes, G. (2007). A geodetic study of the 2003 January 22 Tecomán, Colima, Mexico earthquake. *Geophysical Journal International*, *169*(2), 389–406. https://doi.org/10.1111/j.1365-246X.2006.03322.x

Scholz, C. H. (2002). *The Mechanics of Earthquakes and Faulting* (2nd ed.). Cambridge University Press. https://doi.org/10.1017/CBO9780511818516

Scholz, C. H. (2014). Holocene Earthquake History of Cascadia: A Quantitative Test. *Bulletin of the Seismological Society of America*, *104*(4), 2120–2124. https://doi.org/10.1785/0120140002

Scholz, C. H., & Campos, J. (1995). On the mechanism of seismic decoupling and back arc spreading at subduction zones. *Journal of Geophysical Research: Solid Earth*, *100*(B11), 22103–22115. https://doi.org/10.1029/95JB01869

Sefton, J., Woodroffe, S., Ascough, P., & Khan, N. (2022). Reliability of mangrove radiocarbon chronologies: A case study from Mahé, Seychelles. *The Holocene*, *32*(6), 529–542. https://doi.org/10.1177/09596836221080756

Seminack, C. T., & McBride, R. A. (2018). A life-cycle model for wave-dominated tidal inlets along passive margin coasts of North America. *Geomorphology*, *304*, 141–158. https://doi.org/10.1016/j.geomorph.2017.12.038

Shennan, I. (2009). Late Quaternary sea-level changes and palaeoseismology of the Bering Glacier region, Alaska. *Quaternary Science Reviews*, *28*(17), 1762–1773. https://doi.org/10.1016/j.quascirev.2009.02.006

Shennan, I. (2015). Handbook of sea-level research: Framing research questions. In I. Shennan, A. J. Long, & B. P. Horton (Eds.), *Handbook of Sea-Level Research* (pp. 3–25). John Wiley & Sons, Ltd. https://doi.org/10.1002/9781118452547.ch2

Shennan, I., Barlow, N., Combellick, R., Pierre, K., & Stuart-Taylor, O. (2014). Late Holocene paleoseismology of a site in the region of maximum subsidence during the 1964 Mw 9.2 Alaska earthquake. *Journal of Quaternary Science*, *29*(4), 343–350. https://doi.org/10.1002/jqs.2705

Shennan, I., Bruhn, R., Barlow, N., Good, K., & Hocking, E. (2014). Late Holocene great earthquakes in the eastern part of the Aleutian megathrust. *Quaternary Science Reviews*, *84*, 86–97. https://doi.org/10.1016/j.quascirev.2013.11.010

Shennan, I., Garrett, E., & Barlow, N. (2016). Detection limits of tidal-wetland sequences to identify variable rupture modes of megathrust earthquakes. *Quaternary Science Reviews*, *150*, 1–30. https://doi.org/10.1016/j.quascirev.2016.08.003

Shennan, I., & Hamilton, S. (2006). Coseismic and pre-seismic subsidence associated with great earthquakes in Alaska. *Quaternary Science Reviews*, *25*(1), 1–8. https://doi.org/10.1016/j.quascirev.2005.09.002

Shennan, I., & Hamilton, S. (2010). Holocene sea-level changes and earthquakes around Bering Glacier. In *Geological Society of America Special Papers* (Vol. 462, pp. 275–290). Geological Society of America. https://doi.org/10.1130/2010.2462(14)

Shennan, I., Long, A. J., Rutherford, M. M., Innes, J. B., Green, F. M., & Walker, K. J. (1998). Tidal marsh stratigraphy, sea-level change and large earthquakes—II: Submergence events during the last 3500 years at netarts bay, Oregon, USA. *Quaternary Science Reviews*, *17*(4), 365–393. https://doi.org/10.1016/S0277-3791(97)00055-3

Shennan, I., Scott, D. B., Rutherford, M., & Zong, Y. (1999). Microfossil analysis of sediments representing the 1964 earthquake, exposed at Girdwood Flats, Alaska, USA. *Quaternary International*, *60*(1), 55–73. https://doi.org/10.1016/S1040-6182(99)00007-5

Sherrod, B. L. (1999). Gradient analysis of diatom assemblages in a Puget Sound salt marsh: Can such assemblages be used for quantitative paleoecological reconstructions? *Palaeogeography, Palaeoclimatology, Palaeoecology*, *149*(1), 213–226. https://doi.org/10.1016/S0031-0182(98)00202-8

Silva, H. R. R. (2012). *Una década de participación del Producto Interno Bruto de Puerto Vallarta al estado de Jalisco, 2000–2009*. 11.

Singh, S., Astiz, L., & Havskov, J. (1981). Seismic gaps and recurrence periods of large earthquakes along the Mexican subduction zone: A reexamination. *Bulletin of the Seismological Society of America*, *71*, 827–843.

Singh, S. K., Dominguez, T., Caştro, R., & Rodriguez, M. (1984). P waveform of large, shallow earthquakes along the Mexican subduction zone. *Bulletin of the Seismological Society of America*, *74*(6), 2135–2156.

Singh, S. K., & Lermo, J. (1985). Mislocation of Mexican earthquakes as reported in international bulletins. *Geofísica Internacional*, *24*(2), 333–351. https://doi.org/10.22201/igeof.00167169p.1985.24.2.1047

Singh, S. K., Ponce, L., & Nishenko, S. P. (1985). The great Jalisco, Mexico, earthquakes of 1932: Subduction of the Rivera plate. *Bulletin of the Seismological Society of America*, *75*(5), 1301–1313.

Siqueiros Beltrones, D. A., Lopez-Fuerte, F. O., & Garate-Lizarraga, I. (2005). Structure of Diatom Assemblages Living on Prop Roots of the Red Mangrove (Rhizophora mangle) from the West Coast of Baja California Sur, Mexico. *Pacific Science*, *59*(1), 79–96. https://doi.org/10.1353/psc.2005.0014

Siqueiros-Beltrones, D. A., Argumedo-Hernández, U., & López-Fuerte, F. O. (2017). Diversity of benthic diatoms in the Guerrero Negro Lagoon (El Vizcaíno Biosfere Reserve), Baja California Peninsula, Mexico. *Revista Mexicana de Biodiversidad*, *88*(1), 21–35. https://doi.org/10.1016/j.rmb.2017.01.026

Siqueiros-Beltrones, D. A., López-Mejía, D., & Gutiérrez-Mendieta, F. (2020). High species richness of epiphytic Mastogloia (Mastogloiales: Bacillariophyceae) on Thalassia testudinum along the coast of Campeche, southern Gulf of Mexico. *Revista Mexicana de Biodiversidad*, *91*(0). https://doi.org/10.22201/ib.20078706e.2020.91.2976

Sirkin, L. (1985). Late Quaternary Stratigraphy and Environments of the West Mexican Coastal Plain. *Palynology*, *9*, 3–25.

SMN. (2021). *Manzanillo tide gauge data*. Servicio Mareografico Nacional, México. http://www.mareografico.unam.mx

Soininen, J., & Teittinen, A. (2019). Fifteen important questions in the spatial ecology of diatoms. *Freshwater Biology*, *64*(11), 2071–2083. https://doi.org/10.1111/fwb.13384

Spiske, M. (2020). Chapter 11—The sedimentology and geometry of fine-grained tsunami deposits from onshore environments. In M. Engel, J. Pilarczyk, S. M. May, D. Brill, & E. Garrett (Eds.), *Geological Records of Tsunamis and Other Extreme Waves* (pp. 213–238). Elsevier. https://doi.org/10.1016/B978-0-12-815686-5.00011-0

Suárez, G. (2021). Large earthquakes in the Tehuantepec subduction zone: Evidence of a locked plate interface and large-scale deformation of the slab. *Journal of Seismology*, *25*(2), 449–460. https://doi.org/10.1007/s10950-020-09969-6

Suárez, G., Monfret, T., Wittlinger, G., & David, C. (1990). Geometry of subduction and depth of the seismogenic zone in the Guerrero gap, Mexico. *Nature*, *345*(6273), 336–338. https://doi.org/10.1038/345336a0

Suárez, G., Ruiz-Barón, D., Chico-Hernández, C., & Zúñiga, F. R. (2020). Catalog of Preinstrumental Earthquakes in Central Mexico: Epicentral and Magnitude Estimations Based on Macroseismic Data. *Bulletin of the Seismological Society of America*, *110*(6), 3021–3036. https://doi.org/10.1785/0120200127

Sugawara, D. (2020). Chapter 4—Trigger mechanisms and hydrodynamics of tsunamis. In M. Engel, J. Pilarczyk, S. M. May, D. Brill, & E. Garrett (Eds.), *Geological Records of Tsunamis and Other Extreme Waves* (pp. 47–73). Elsevier. https://doi.org/10.1016/B978-0-12-815686-5.00004-3

Suter, M. (2019). The 1563 MI 8 Puerto de la Navidad Subduction-Zone and 1567 Mw 7.2 Ameca Crustal Earthquakes (Western Mexico): New Insights from Sixteenth-Century Sources. *Seismological Research Letters*, *90*(1), 366–375. https://doi.org/10.1785/0220180304

Switzer, A. D., & Jones, B. G. (2008). Large-scale washover sedimentation in a freshwater lagoon from the southeast Australian coast: Sea-level change, tsunami or exceptionally large storm? *The Holocene*, *18*(5), 787–803. https://doi.org/10.1177/0959683608089214

Szabó, K., Kiss, K. T., Ector, L., Kecskés, M., & Ács, É. (2004). Benthic diatom flora in a small Hungarian tributary of River Danube (Rakos-stream). *Algological Studies/Archiv Für Hydrobiologie, Supplement Volumes*, *111*, 79–94. https://doi.org/10.1127/1864-1318/2004/0111-0079

Takashimizu, Y., Urabe, A., Suzuki, K., & Sato, Y. (2012). Deposition by the 2011 Tohoku-oki tsunami on coastal lowland controlled by beach ridges near Sendai, Japan. *Sedimentary Geology*, *282*, 124–141. https://doi.org/10.1016/j.sedgeo.2012.07.004

Tanner, W. F. (1991). Application of suite statistics to stratigraphy and sea-level changes. In J. P. M. Syvitski (Ed.), *Principles, Methods and Application of Particle Size Analysis* (1st ed., pp. 283–292). Cambridge University Press. https://doi.org/10.1017/CBO9780511626142.026

Tena-Colunga, A., Universidad de Colima, Colima (Mexico : State), & Sociedad Mexicana de Ingeniería Sísmica (Eds.). (1997). *El macrosismo de Manzanillo del 9 de octubre de 1995: Colima, México, septiembre de 1997*. Universidad de Colima : Gobierno del Estado de Colima : Sociedad Mexicana de Ingeniería Sísmica.

Thatcher, W., & Rundle, J. B. (1984). A viscoelastic coupling model for the cyclic deformation due to periodically repeated Earthquakes at subduction zones.

Journal of Geophysical Research: Solid Earth, *89*(B9), 7631–7640. https://doi.org/10.1029/JB089iB09p07631

Thom, B. G. (1967). Mangrove Ecology and Deltaic Geomorphology: Tabasco, Mexico. *Journal of Ecology*, *55*(2), 301–343. https://doi.org/10.2307/2257879

Toonen, W. H. J., Kleinhans, M. G., & Cohen, K. M. (2012). Sedimentary architecture of abandoned channel fills. *Earth Surface Processes and Landforms*, *37*(4), 459–472. https://doi.org/10.1002/esp.3189

Trejo-Gómez, E., Ortiz, M., & Núñez-Cornú, F. J. (2015). Source Model of the October 9, 1995 Jalisco-Colima Tsunami as constrained by field survey reports, and on the numerical simulation of the tsunami. *Geofísica Internacional*, *54*(2), 149–159. https://doi.org/10.1016/j.gi.2015.04.010

Troels-Smith, J. (1955). Karakterisering af lose jordater (Characterisation of Unconsolidated Sediments). *Danmarks Geologiske Undersogelse*, *3*, 39–73.

Vaasma, T. (2008). Grain-size analysis of lacustrine sediments: A comparison of pre-treatment methods. *Estonian Journal of Ecology*, *57*(4), 231. https://doi.org/10.3176/eco.2008.4.01

Vélez, M. I., Hooghiemstra, H., Metcalfe, S., Wille, M., & Berrío, J. C. (2006). Late Glacial and Holocene environmental and climatic changes from a limnological transect through Colombia, northern South America. *Palaeogeography, Palaeoclimatology, Palaeoecology*, *234*(1), 81–96. https://doi.org/10.1016/j.palaeo.2005.10.020

Vidal Zepeda, R. (2005). *Las regiones climáticas de México*. Instituto de Geografía, UNAM.

Vidal Zepeda, R., Cabrera Sánchez, A. L., & Menchaga, S. E. (2007). *Climas* [Map]. Instituto de Geografía, UNAM. http://www.igeograf.unam.mx/Geodig/nvo_atlas/index.html/5_naturaleza_ambiente/4_clima/NA_IV_4.jpg

Vos, P. C., & de Wolf, H. (1993). Diatoms as a tool for reconstructing sedimentary environments in coastal wetlands; methodological aspects. *Hydrobiologia*, *269*(1), 285–296. https://doi.org/10.1007/BF00028027

Wang, K. (2007). 17. Elastic and Viscoelastic Models of Crustal Deformation in Subduction Earthquake Cycles. In T. H. Dixon & C. Moore (Eds.), *The Seismogenic Zone of Subduction Thrust Faults*. Columbia University Press. https://doi.org/10.7312/dixo13866-017

Wang, K., Hu, Y., & He, J. (2012). Deformation cycles of subduction earthquakes in a viscoelastic Earth. *Nature*, *484*(7394), 327–332. https://doi.org/10.1038/nature11032

Ward, R. D. (2020). Sedimentary response of Arctic coastal wetlands to sea level rise. *Geomorphology*, *370*, 107400. https://doi.org/10.1016/j.geomorph.2020.107400

Watcham, E. P., Shennan, I., & Barlow, N. L. M. (2013). Scale considerations in using diatoms as indicators of sea-level change: Lessons from Alaska. *Journal of Quaternary Science*, *28*(2), 165–179. https://doi.org/10.1002/jqs.2592

Whitfield, A., & Elliott, M. (2011). Ecosystem and Biotic Classifications of Estuaries and Coasts. In *Treatise on Estuarine and Coastal Science* (pp. 99–124). Elsevier. https://doi.org/10.1016/B978-0-12-374711-2.00108-X

Wilson, R., Hemphill-Haley, E., Jaffe, B., Richmond, B., Peters, R., Graehl, N., Kelsey, H., Leeper, R., Watt, S., McGann, M., Hoirup, D., Chagué-Goff, C., Goff, J., Caldwell, D., & Loofbourrow, C. (2014). *The search for geologic evidence of distant-source tsunamis using new field data in California* (Open-File Report

No. 229; The SAFRR (Science Application for Risk Reduction) Tsunami Scenario). U.S. Geological Survey.

Witter, R., Briggs, R., Engelhart, S. E., Gelfenbaum, G., Koehler, R. D., Nelson, A., Selle, S. L., Corbett, R., & Wallace, K. (2019). Evidence for frequent, large tsunamis spanning locked and creeping parts of the Aleutian megathrust. *GSA Bulletin*, *131*(5–6), 707–729. https://doi.org/10.1130/B32031.1

Woodward, C. A., & Gadd, P. S. (2019). The potential power and pitfalls of using the X-ray fluorescence molybdenum incoherent: Coherent scattering ratio as a proxy for sediment organic content. *Quaternary International*, *514*, 30–43. https://doi.org/10.1016/j.quaint.2018.11.031

Woodward, C. A., Slee, A., Gadd, P., Zawadzki, A., Hamze, H., Parmar, A., & Zahra, D. (2018). The role of earthquakes and climate in the formation of diamictic sediments in a New Zealand mountain lake. *Quaternary International*, *470*, 130–147. https://doi.org/10.1016/j.quaint.2017.10.051

Yagi, Y., Mikumo, T., Pacheco, J., & Reyes, G. (2004). Source Rupture Process of the Tecomán, Colima, Mexico Earthquake of 22 January 2003, Determined by Joint Inversion of Teleseismic Body-Wave and Near-Source Data. *Bulletin of the Seismological Society of America*, *94*(5), 1795–1807. https://doi.org/10.1785/012003095

Yáñez-Arancibia, A., Day, J. W., Sánchez-Gil, P., Day, J. N., Lane, R. R., Zárate-Lomelí, D., Vásquez, H. A., Rojas-Galaviz, J. L., & Ramírez-Gordillo, J. (2014). Ecosystem functioning: The basis for restoration and management of a tropical coastal lagoon, Pacific coast of Mexico. *Ecological Engineering*, *65*, 88–100. https://doi.org/10.1016/j.ecoleng.2013.03.007

Yao, Q., Liu, K., Wu, Y., Aragón-Moreno, A. A., Rodrigues, E., Cohen, M., de Souza, A. V., Farfán, L. M., & Antinao, J. L. (2021). A multi-proxy record of hurricanes, tsunami, and post-disturbance ecosystem changes from coastal southern Baja California. *Science of The Total Environment*, *796*, 149011. https://doi.org/10.1016/j.scitotenv.2021.149011

Yao, Q., Liu, K.-B., Williams, H., Joshi, S., Bianchette, T. A., Ryu, J., & Dietz, M. (2020). Hurricane Harvey Storm Sedimentation in the San Bernard National Wildlife Refuge, Texas: Fluvial Versus Storm Surge Deposition. *Estuaries and Coasts*, *43*(5), 971–983. https://doi.org/10.1007/s12237-019-00639-6

Ye, L., Kanamori, H., & Lay, T. (2018). Global variations of large megathrust earthquake rupture characteristics. *Science Advances*, *4*(3), eaao4915. https://doi.org/10.1126/sciadv.aao4915

Zobin, V. M., & Ventura-Ramirez, J. F. (1998). The Macroseismic Field Generated by the Mw 8.0 Jalisco, Mexico, Earthquake of 9 October 1995. *Bulletin of the Seismological Society of America*, *88*(3), 703–711.

Zong, Y. (1997). Implications of Paralia Sulcata Abundance in Scottish Isolation Basins. *Diatom Research*, *12*(1), 125–150. https://doi.org/10.1080/0269249X.1997.9705407

Zong, Y., Lloyd, J. M., Leng, M. J., Yim, W. W.-S., & Huang, G. (2006). Reconstruction of Holocene monsoon history from the Pearl River Estuary, southern China, using diatoms and carbon isotope ratios. *The Holocene*, *16*(2), 251–263. https://doi.org/10.1191/0959683606hl911rp

Zong, Y., Shennan, I., Combellick, R. A., Hamilton, S. L., & Rutherford, M. M. (2003). Microfossil evidence for land movements associated with the AD 1964 Alaska earthquake. *The Holocene*, *13*(1), 7–20. https://doi.org/10.1191/0959683603hl590rp

APPENDIX

Contents

List of figures

List of tables

List of scripts

Table A.1. Detailed core sediment descriptions of all the boreholes during the field campaign of 2018. Sediment descriptions were based on the Troels-Smith (1955) classification of unconsolidated sediments. These boreholes correspond to those in Chapters 2 and 3. Only those boreholes marked with a (*) are included in the cross-section diagrams. The rest of the boreholes sampled in the exploratory phase.

Core name	Depth (cm)	Lithology	Throel-Smith description
MAR001 (*)	0-16	Modern soil	Th3, Ag1, As+
19.157946, -104.566730	16-20	Grey silty clay	As4, Ag+
	20-28	Dark grey organic silt	Ag3, Sh1, Sh+
	28-32	Grey silty clay	As3, Ag1
	32-54	Dark grey organic silt	Ag3, Sh1, Sh+
	54-84	Grey silt with clay	As3, Ag1
	84-88	Dark grey organic silt with plant fragments	Ag3, Dh1, Sh1
	88-130	Grey silty clay with very fine sand	As3, Ag1, Ga+
MAR002	0 - 23	Modern soil	Ag2, Th2
19.158599°, -104.567875°	23 - 39	Grey organic clay with silt	As3, Ag1, Sh+, Th+
	39 - 56	Dark grey clay with roots	As4, Th+
	56 - 66	Grey Silty clay with roots	Ag4, Th+, As+
	66 - 115	Dark grey clay with silt and organic matter	As3, Ag1, Sh+
	115 - 130	Grey silty clay	Ag2, As2
	130 - 200	Dark grey silty clay with organic matter	Ag2, As2, Sh+
MAR003	0 - 22	Modern soil	Th3, Ag1, As+
19.159567°, -104.568760°	22 - 44	Brown silty clay with herbaceous roots	As4, Sh+
	44 - 84	Orange silty clay	As3, Ag1, Sh+
	84 - 119	Dark grey organic clay	As4, Dh+
	119 - 140	Brown organic silty clay	As4, Sh+
	140 - 147	Dark grey silty clay with fine sand	As4, Ga+
MAR004 (*)	0 - 13	Modern soil	Th3, Ag1, As+
19.159503, -104.564259	13 - 18	Grey silty clay	Ag3, As1
	18 - 44	Dark grey organic silt with plant fragments	Dh2, Ag2, Sh+, As+,
	44 - 62	Grey silty clay with tiny roots	Ag3, As1, Th+
	62 - 88	Dark grey organic silt	Sh2, Ag2
	88 - 150	Grey silty clay	Ag3, As1
	150 - 161	Dark grey organic silt	Ag3, Sh1, As+
	161 - 178	Grey silty clay and very fine sand	Ag3, As1, Ga+
	178 - 194	Dark grey organic silt	Sh2, Dh1, Ag1, As+
	194 - 202	Grey coarse sand with silt	Ga3, Ag1, As+
MAR005 (*)	0 - 4	Modern soil	Th3, Ag1, As+
19.159857, -104.563600	4 - 28	Grey silty clay	Ag3, As1
	28 - 32	Dark grey organic silt	Sh2, Ag2, As1
	32 - 71	Grey silty clay	Ag3, As1
	71 - 80	Dark grey organic organic silty clay	Sh3, Ag1
	80 - 99	Grey silty clay	Ag3, As1
	99 - 123	Dark grey organic silt with plant fragments	Sh2, Dh1, Ag1, As+
	123 - 138	Grey silt with fine sand	Ag3, Ga1, As+
	138 - 155	Dark grey organic silt with plant and wood fragments	Sh2, Dh1, Dl1, Ag+
	155 - 170	Grey coarse sand with gravel	Ga4, Ag+, As+
	170 - 180	Grey coarse sand with silt	Ga3, Ag1, As+
MAR006	0 - 38	Modern soil	Th2, Ag2, As+
19.161270°, -104.562191°	38 - 57	Grey silty clay	Ag3, As1
	57 - 61	Brown silt	Ag4, As+
	61 - 101	Grey silty clay	Ag3, As1
	101 - 104	Black silt with organic remains	Ag3, Th1, As+
	104 - 113	Fine sandy silt	Ga2, Ag2, As+
	114 - 121	Lost material	
	121 - 207	Brown silty clay with fine sand	Ag3, As1, Ga+
MAR007	0 - 34.5	Modern soil	Th2, Ag2, As+
19.159676°, -104.564404°	34.5 - 45.5	Grey silty clay with fine sand	Ag3, As1, Ga+
	45.5 - 61	Dark brown sandy loam with oxidized organic material	Ga2, Ag1, As1, Sh+
	61 - 67	Brown sand with silt	Ga3, Ag1
	67 - 72	Grey silty clay with humified organic material	Ag3, As1, Sh+
	72 - 100	Brown silty clay with sand	Ag2, Ga2
MAR008	0 - 34.5	Modern soil	Th2, Ag1, As1
19.159860°, -104.564603°	34.5 - 46	Brown silt with fine sand	Ag3, Ga1
	39 - 61	Grey silty clay	Ag2, As2
	61 - 108	Dark brown silty clay and some herbaceous roots	Ag2, As2, Th+
	108 - 117	Grey silty clay with humified organic matter	Ag2, As2, Sh+
	117 - 145	Brown grey silty clay with humified organic matter	Ag2, As2, Sh+
MAR009 (*)	0 - 17	Modern soil	Th3, Ag1, As+
19.163304°, -104.558629°	17 - 24	Grey silt	Ag4, As+
	24 - 44	Dark grey organic silt	Ag3, Sh1, As+
	44 - 49	Grey silty clay	Ag3, As1
	49 - 59	Dark grey organic silty clay	Ag3, Sh1
	59 - 101	Grey silty clay	Ag4, As1
	101 - 115	Dark grey organic silt with plant fragments	Ag2, Sh1, Dh1
	115 - 126	Grey silt with fine sand	Ag4, Ga+
MAR010 (*)	0 - 7	Modern soil	Th2, Ag2, As+
19.162899°, -104.560283°	7 - 13	Grey silty clay	Ag2, As2
	13 - 17	Dark grey organic silty clay	Sh2, Ag2, As+
	17 - 21	Grey silty clay	Ag3, As1
	21 - 29	Dark grey organic silt	Ag2, Sh1, As1
	29 - 57	Grey silty clay	Ag3, As1
	57 - 67	Organic silt with leav and wood fragments	Sh2, Dh1, Ag1, As+
	67 - 89	Grey silty clay with fine sand	Ag3, As1
	89 - 103	Dark grey organic silt with wood and plant fragments	Sh2, Dl1, Dh1, Ag+
	103 - 110	Coarse sand with gravel	Ga4
	110 - 133	Coarse sand with silt	Ga3, Ag1

Table A.2. Raw counts of fossil diatoms of the core MAR005.

Depth in core (cm) -->	4	12	19	23	24	25	26	27	28	29	30	31	34	37	41	46	49	53	57	63	65	66	67	68	69
Achnanthes angustata																									
Achnanthes brevipes						3		2			1			1											1
Achnanthes brevipes var. Intermedia				2	1																				
Achnanthes clevei var. rostrata					1																				
Achnanthes delicatula																								2	1
Achnanthes exigua			*1*	1					2	4		1								1	1		4	4	2
Achnanthes inflata			*3*	7		3	2	1		2		7	15	13	15	2	6	5	3			2	5	3	1
Achnanthes lanceolata var. rostrata											1														
Achnanthes lorenziana																									
Achnanthes marginulata																						1			
Achnanthes parvula																									
Achnanthes promunturi																									
Achnanthes sp1				1				1																	
Achnanthidium exiguum				1	3	1	1	3							1			2							
Achnanthidium minutissimum						1																			
Amphipora ornata																									
Amphora acustiuscula			*1*			1	2									1	4	2	1	5			1		1
Amphora affinis				2			1										3	3							
Amphora arenaria										2															
Amphora bicapitata					2																				
Amphora clevei																	4	1							
Amphora coffeaeformis			*3*		2	1	4		1		1		2			2				1	2		1	2	7
Amphora costata																									1
Amphora gigantea																				4		6			1
Amphora proteus			*1*	2	1						1		1		1	1									
Amphora terroris																									
Astartiella punctifera										1		1													
Aulacoseira sp1																									
Aulacoseira granulata								1				1													
Austariella jamaicensis					1	1																			
Bacillaria paxillifera	*2*	*5*				2	2	3			2	7			1	5			3	1					
Bacillaria socialis								2	5	3															
Biremis ambigua						1																			
Brevisira arentii																									
Caloneis aemula																									
Caloneis bacillum					1	2	1	2		2	1	7	4	4	13	7	7	1	1	1		1			
Caloneis excentrica																	1				1		1	1	
Caloneis permagna																									1
Caloneis sabanicola			*1*			1										3	2								
Caloneis subsalsa																									
Caloneis westii																							1		
Caloneis sp1																									
Ceratulus californicus				7								1						2							1
Cocconeis convexa																									
Cocconeis neodiminuta				1																					
Cocconeis pinnata												1													
Cocconeis placentula		*1*	*4*	6			1						3		2	1	4			1					
Cocconeis placentula var. euglypta			*3*		4		2			1	2		2	1	2	3		3	1			1			
Cocconeis placentula var. lineata																									

Table A.2. (continued)

Depth in core (cm) -->	4	12	19	23	24	25	26	27	28	29	30	31	34	37	41	46	49	53	57	63	65	66	67	68	69
Conticribra weissflogii																									
Coscinodiscus radiatus							1																		
Craticula halophilioides							1			1						1							1		
Cyclotella atomus									3			1									2	2	4	2	1
Cyclotella cryptica																					5				
Cyclotella kuetzingiana																									
Cyclotella litoralis					1																				
Cyclotella meneghiniana	*5*	*3*	*3*	2	2	5	9	10	32	12	5	11	8	5	2	6	2	5	2	25	19	22	21	32	18
Cyclotella ocellata											1														
Cyclotella radiosa					1																	2	2	4	
Cyclotella striata					1																	1			
Cyclotella stylorum																									
Cymbella laevis																									
Denticula kuetzingii			*1*																				2		
Diadesmis confervacea		*2*	*5*	4	10	13	12	5	6	15	3	9	43	45	30	26	3	29	70	2	2	4	17	6	4
Diploneis boldtiana					1																				
Diploneis elliptica										2															3
Diploneis nitecens																									
Diploneis oculata				1																					
Diploneis ovalis				2		1	3						3			1		3			1			2	
Diploneis pseudovalis			*3*		1	1		1	4			1	1	1				1		1					
Diploneis papula												1					3								
Diploneis parma										4															
Diploneis puella																									
Diploneis smithii	*1*		*9*	2	8	1	5	1	1	1	1		1			3	6	14		1			3	2	1
Diploneis sp1.																									
Encyonema montana														1											
Encyonema prostratum									1																
Encyonema silesianum				5	1								1			1	2								
Entomoneis paludosa																									
Eolimna ruttineri																		2				1		1	2
Epithemia adnata														3	1	1		2							
Epithemia argus													2												
Eunotia bidens				2																					
Eunotia flexuosa	*2*	*2*	*10*	1	2	6	9	15	29	16	5	3	2	2	2	22	5	5						1	
Eunotia formica			*4*			2				4	5	2	1		1	8	2	16	2						
Eunotia minor				2																					
Eunotia myrmica					2																				
Eunotia sp1								1			2														
Fallacia auriculata									1																
Fallacia forcipata		*1*							2	3	1						1			6		3	2	6	1
Fragilaria goulardii																2	1	3	1						
Gomphonema acuminatum																									
Gomphonema affine		*5*	*9*	8	20	43	16	6	3	6				1		20	9	20	5		3	1		5	3
Gomphonema angustatum																									
Gomphonema gracile			*1*	1	8		5			12	1		6		4	1			1						2
Gomphonema hebridense						11		2												1				1	1

Table A.2. (continued)

Depth in core (cm) -->	4	12	19	23	24	25	26	27	28	29	30	31	34	37	41	46	49	53	57	63	65	66	67	68	69
Gomphonema parvulum	*1*		*5*	2	2	1	6	1	4	1	3	1	2			4	2	1			2	1			6
Gomphonema subclavatum						2		2	1	3		9	4		1					3				1	3
Grammatophora hamulifera			*1*																						2
Grammatophora marina								1																	
Gyrosigma acuminatum			*6*		1												1			7	1	2	2	1	1
Gyrosigma balticum																									
Halamphora acutiuscula					1				1	1											1	6		1	1
Halamphora exigua																									
Halamphora holsatica						1				2	2														1
Halamphora latecostata																									
Halamphora sp1					1																				
Halamphora submontana	*97*	*85*	*4*	31	14	2	3	1		18	38	11	2	9	3	4	5	5							
Hantzschia amphioxys			*6*	4		1	1						1	5	5	2	7	4	1						
Hantzschia virgata												1					3	1							
Haslea britannica																									
Hippodonta hungarica			*1*										2	1											
Hyalosynedra laevigata							1																		
Karayevia amoena																									
Karayevia clevei																									
Kolbesia suchlandtii					1																				
Luticola goeppertiana							1			3											1				3
Luticola Mutica		*4*	*19*	25	24	10	5	3	7	10	12	28	72	73	67	15	29	20	14		3		2	5	1
Luticola mutica f. intermedia					1	6	1			2	3											1			
Luticola sp1																									
Lyrella lyra																									
Lyrella lyroides																									
Mastogloia decipiens																									
Melosira polaris																					1				
Navicula abunda																					1				
Navicula agatake									1												1		3		
Navicula agnita									1																
Navicula apta																									
Navicula cancellata	*4*	*9*	*7*		1						1					1	2	2	5	15	8	11	8	5	1
Navicula cincta				3			1	3	1	1							1				13	2	1	1	10
Navicula cryptocephala	*1*		*1*	0	1	0	1	3	0	0	0	0	0	0	0	0	0	0	0	0	4	2	0	2	3
Navicula cryptocephala var veneta																									
Navicula cryptotenella											5									2	5	4	3	3	1
Navicula digitoradiata					1															1		5	4		
Navicula duerrenberginiana																									
Navicula eridrigiana																									5
Navicula erifuga				6	2	2	1	6		4	7										2	1			
Navicula exigua var. capitata				1				1																1	
Navicula gregaria												1	1			1	3			6	5	2		1	
Navicula lanceolata								4																	
Navicula lanceolata var minima						5	2															1			2
Navicula longa																					2				
Navicula menisculus																									1
Navicula pennata	*1*		*4*		2	4			1	3											7	15	6	13	14

Table A.2. (continued)

Depth in core (cm) -->	4	12	19	23	24	25	26	27	28	29	30	31	34	37	41	46	49	53	57	63	65	66	67	68	69
Navicula perminuta					1	1				2		2									3			5	
Navicula pupula																								2	
Navicula radiosa					1			1												1					
Navicula recens										1															
Navicula rostellata			1	1		1	2	2	2	1										1		1		2	1
Navicula salinarum	4	5	1	1	7		2	3	1	5	4												4	1	6
Navicula salinicola	3	7	4		3	2		3		2		6						4		1	6	4	5		
Navicula sp1																						1			
Navicula subrostellata				1	2	7			1		4						1	1			1			2	4
Navicula tripunctata		1	2	4	2	5	1			3							1			1	10	6	6	5	6
Navicula vimineoides									1	1											1		3	1	
Navicula viridula var. rostellata																									1
Nitzschia acicularis																				6	2	3			
Nitzschia amphibia		1			3	7			10	14	1					9	3		1					9	
Nitzschia angustata							1																		
Nitzschia bicapitata																									
Nitzschia brevissima	1			1			1				1					1									2
Nitzschia capitellata			0	0	4	0	0	0	1	3	1	0	1	0	1	1	2	2	0	1	2	2	1	0	4
Nitzschia clausii						2	4	8	2	1	26										7		2		2
Nitzschia compressa										1	2														
Nitzschia confinis					1															12	2			1	2
Nitzschia dissipata			2				3				2									2					
Nitzschia distans							1		1																
Nitzschia filiformis			4		2				3																
Nitzschia Fonticola	7	11	7	3	2	1	5		4		4	35	1	13	3	2				7	8	5	1	3	1
Nitzschia frustulum	2	10		16	6	5	2	2	1	8	6	6	1		1		1				6	6	10	6	1
Nitzschia gracilis	21	5				2		7	25	2	1	19			1	4	6	1		25	5	9	4	12	4
Nitzschia grossestriata			2	1		6	33	38	7	1	4	7	4	2		5	1	5	3	12	3	18	7	15	7
Nitzschia hybrida					1																				
Nitzschia inconspicua							2	2	1	1	12														
Nitzschia insignis																									
Nitzschia intermedia																									
Nitzschia lanceolata										2															
Nitzschia lanceolata var. minima				5																					
Nitzschia laevissima								1																	2
Nitzschia linearis										1		1													
Nitzschia microcephala	1	1					4		1		1		1		1	1				1		4			3
Nitzschia obtusa obtusa									1							1		1		2	1		2	1	1
Nitzschia palea	22	13	5	2	2	2		8	15	7	27						5			3	9	17		5	1
Nitzschia panduriformis																									
Nitzschia parvula																									1
Nitzschia perminuta										2	1										2		1		3
Nitzschia plana					1																				
Nitzschia recta																									
Nitzschia scalaris			4							1								3							
Nitzschia scalpelliformis	16	20	4	7	9							12	1	6			14		1	25		5			2
Nitzschia sicula	8	3	1			5	1	1	2	2	3			1		1	1			3	6	3	8		1
Nitzschia sigma	1		6	2	2	1	2	3		1	2									5	1	5	7	8	5

Table A.2. (continued)

Depth in core (cm) -->	4	12	19	23	24	25	26	27	28	29	30	31	34	37	41	46	49	53	57	63	65	66	67	68	69
Nitzschia sp1.			*1*		1					1	4										1				1
Nitzschia thermalis							1									1									
Nitzschia vitrea							1					1						3							4
Opephora marina var. minuta																									
Opephora pacifica																									
Paralia sulcata	*3*	*3*		6			5	23	5		1			2				2	2	5	21	12	29	11	8
Paralia sulcata var. biseriata								1	3													1		1	
Paralia sulcata var. Radiata																					2				
Paralibellus rhombicus																									
Parlibellus calvus			*1*					1																1	
Petroneis sp1						1																			
Petroneis marina							2			1															
Pinnularia acrosphaeria			*3*	1	4	10	15	7	8	8	1	3	2			6	3	12	2			1	2		8
Pinnularia biceps			*1*					1	1	2		3				1									1
Pinnularia biceps var. minor				3	1														1		1				
Pinnularia borealis									1						1			1							
Pinnularia certa			*2*			1			1						1	3		1							1
Pinnularia incognita																									
Pinnularia joculata							2										1								
Pinnularia lattarea																									
Pinnularia microstauron								4																	
Pinnularia neomajor																									
Pinnularia obscura					1		1																		
Pinnularia sp1							1				1		1										2		
Pinnularia streptoraphe var. parva				1																					
Pinnularia subcapitata						2	3																		
Pinnularia turgidula																						1			
Placoneis gastrum	*1*		*3*				2					1	3	2		1		1							
Placoneis hambergii	*1*	*2*									1			2	1								1	1	
Planktoniella sol																									
Planothidium delicatulum					2					1															
Planothidium frequentisimum																									
Planothidium hauckianum							2										1		1					1	
Planothidium lanceolatum																									
Pleurosigma salinarum																									
Pseudogomphonema kamtschaticum																									1
Rhopalodia acuminata			*2*				1						2										1		
Rhopalodia constricta																									
Rhopalodia gibba				3	1				1					2				1							
Rhopalodia gibberula			*5*	3	4	6	3	2		2	1					1		4	1		2			1	
Rhopalodia musculus		*1*	*2*				2					1		2	1	9	1	1	3		1				1
Rhopalodia pacifica					2																				
Sellaphora japponica																									
Sellaphora pupula		*1*	*3*		5	1	2		1	1					2	3				6	1		1	4	3
Sellaphora guyanensis																							1		
Seminavis strigosa			*4*															1				1			
Seminavis ventricosa												1													
Stauroneis amphibia						2	2																2		8

Table A.2. (continued)

Depth in core (cm) -->	4	12	19	23	24	25	26	27	28	29	30	31	34	37	41	46	49	53	57	63	65	66	67	68	69
Stauroneis borrichii								1																	
Stauroneis producta			*6*																						
Staurophora salina				1	1					1															
Staurophora wislouchii								1																	
Staurophora sp1				1																	1				
Staurosirella pinnata											1														
Stephanodiscus hantzschi			*1*																					1	
Stephanodiscus niagarae				1																			1		
Stephanodiscus parvus					1	1	1	3	1	1	1	1										1	1		
Synedra Goulardi				1			1																1		
Tabularia fasciculata									1			1							3						
Tabularia parva																									
Tabularia persuadens																							1		
Thalassionema nitzschioides																					3				
Tryblionella accuminata																									
Tryblionella apiculata									1												1				
Tryblionella compressa								3					3			3	1	5	2				1		
Tryblionella debilis														1	2										
Tryblionella granulata																									
Tryblionella hungarica																									
Tryblionella levidensis		*2*	*1*		1		2	1				1	2	2					1	5	1	2	3	1	
Tryblionella littoralis								1																	
Tryblionella persuadens																									
Ulnaria danica																									
Ulnaria Ulna	*4*	*5*	*8*	4	1	3				1						3	6	4							
Total counts	209	208	202	201	200	208	213	209	210	220	217	206	201	200	166	200	166	205	131	208	203	208	202	208	204

Table A.2. (continued)

Depth in core (cm) -->	70	71	72	73	74	75	78	81	85	89	92	95	96	97	98	99	100	101	102	107	114	122	126	130	131
Achnanthes angustata				1																					
Achnanthes brevipes	2		2	2					2	2		1	1	1					1						
Achnanthes brevipes var. Intermedia								6							4										
Achnanthes clevei var. rostrata																1									
Achnanthes delicatula											1														
Achnanthes exigua	2	3					2	1		2									1				1		
Achnanthes inflata	5	18	10	29	18	14		4	1	7			2	2								1	1	2	
Achnanthes lanceolata var. rostrata																									
Achnanthes lorenziana																			3						
Achnanthes marginulata								2						1											
Achnanthes parvula																									1
Achnanthes promunturi		1																							
Achnanthes sp1															1	1									
Achnanthidium exiguum													1		1	1									
Achnanthidium minutissimum																									
Amphipora ornata										2							8								
Amphora acustiuscula	4													1						10	1	2	1	2	
Amphora affinis												1	1												
Amphora arenaria																									
Amphora bicapitata													4												
Amphora clevei																									
Amphora coffeaeformis	4	4		1	2	3		3	1	2			1		3	3	5		2	4	8	1	12	11	10
Amphora costata																								1	3
Amphora gigantea																									
Amphora proteus	1				2			1		2		3					1		2			2			
Amphora terroris																									
Astartiella punctifera														1											
Aulacoseira sp1												1													
Aulacoseira granulata														1											
Austariella jamaicensis					1								2												
Bacillaria paxillifera		1			5		4	1	6	3	21	22	6	6	5	4	4	8	9	7	9	4	7	10	28
Bacillaria socialis												3	3						2						
Biremis ambigua	3																	3							
Brevisira arentii																1									
Caloneis aemula				4		1																			
Caloneis bacillum		3		1					4	3										2	1				
Caloneis excentrica																									
Caloneis permagna	1			2																					
Caloneis sabanicola			2																						
Caloneis subsalsa												1													
Caloneis westii																									
Caloneis sp1												1													
Ceratulus californicus																									
Cocconeis convexa			1																						
Cocconeis neodiminuta																									
Cocconeis pinnata																									
Cocconeis placentula			1			1		1	1		1	1					1	3	6	15		1	16	5	
Cocconeis placentula var. euglypta		1		1		2	2	1	1	3	1	2							5						3
Cocconeis placentula var. lineata																			1						

Table A.2. (continued)

Depth in core (cm) -->	70	71	72	73	74	75	78	81	85	89	92	95	96	97	98	99	100	101	102	107	114	122	126	130	131
Conticribra weissflogii															1	1									
Coscinodiscus radiatus																									
Craticula halophilioides	3	1																1							
Cyclotella atomus	1	6						3		1			1												
Cyclotella cryptica		1																1							
Cyclotella kuetzingiana	1											1		1	1			1							
Cyclotella litoralis																2		2	3						
Cyclotella meneghiniana	12	7	21	13	11	8	8	12	15	13	32	15	17	26	36	25	35	19	43	76	90	81	94	19	26
Cyclotella ocellata																									
Cyclotella radiosa												2				1			7						
Cyclotella striata			1				2	4			2	5		8	19	7	40	8	4		1	1			1
Cyclotella stylorum	1	1				1							1	1			2								
Cymbella laevis								2							1										
Denticula kuetzingii				1																					
Diadesmis confervacea	9	14	1	4	6	1	1	7	8	9	1			2	3	2	2	3	1	7	4		7	6	6
Diploneis boldtiana																									
Diploneis elliptica	1	1		1			2	1				2													
Diploneis nitecens		1																							
Diploneis oculata					1						2												1	28	
Diploneis ovalis													1	2		1								1	
Diploneis pseudovalis		3	3		1		1	2	1	2		1					1								5
Diploneis papula																						2	1		30
Diploneis parma																									
Diploneis puella																								16	
Diploneis smithii	1	3		4	6	5	1	2	3	3		1	2	1		1	1			1	1	2			
Diploneis sp1.												1													
Encyonema montana																									
Encyonema prostratum																									
Encyonema silesianum																									
Entomoneis paludosa																		3							
Eolimna ruttineri				6	1		1	1		1		1	1			3									
Epithemia adnata							1	1																	
Epithemia argus						2																			
Eunotia bidens																									
Eunotia flexuosa					2			1	2					1	1	1				3		1	1	1	1
Eunotia formica		1					2	1		1					0					1			1		
Eunotia minor																									
Eunotia myrmica																									
Eunotia sp1																									
Fallacia auriculata											3		3											6	
Fallacia forcipata					1	1	1		3	1			2	3	1		1	4		1			1		
Fragilaria goulardii								1												1					
Gomphonema acuminatum													1												
Gomphonema affine	5	6													1		5					1	5	3	
Gomphonema angustatum		1																							
Gomphonema gracile		2			3	2								1						1			1	1	
Gomphonema hebridense	1																2		1						

Table A.2. (continued)

Depth in core (cm) -->	70	71	72	73	74	75	78	81	85	89	92	95	96	97	98	99	100	101	102	107	114	122	126	130	131
Gomphonema parvulum	2	11	1	2	2	4	1		6	3			3		3	3	8	6		2			5	2	2
Gomphonema subclavatum				8	7	1	1		1					1						1		1			
Grammatophora hamulifera			1											1											
Grammatophora marina				1															1						
Gyrosigma acuminatum	2	1							2	2			3		1	2									
Gyrosigma balticum																	2								
Halamphora acutiuscula		10	11	8	12	2	3	8	10	3								7	2						1
Halamphora exigua		1	1	2			2										1								
Halamphora holsatica	4		2								1			1	2			2	4				1		
Halamphora latecostata		3																	1						
Halamphora sp1																									
Halamphora submontana		5	13	26	22	43	40	11	6	3					2										
Hantzschia amphioxys						1				2					1									1	
Hantzschia virgata							2	2	1																
Haslea britannica															5										
Hippodonta hungarica																									16
Hyalosynedra laevigata																									
Karayevia amoena													2												
Karayevia clevei																								1	
Kolbesia suchlandtii																									
Luticola goeppertiana																									
Luticola Mutica	1	4	4	3	6	3	5	11	2	5	1			6	2	1				4		1		2	1
Luticola mutica f. intermedia		1											2												
Luticola sp1																			1						
Lyrella lyra												1													
Lyrella lyroides													2												
Mastogloia decipiens									1						1	1									
Melosira polaris					2				2	2															
Navicula abunda																									
Navicula agatake		1											1						1						
Navicula agnita	2				2																				
Navicula apta									1																
Navicula cancellata	5	2	7	18	8	13	24	9	9	17		1	2	6	2	2		2	4	2	2			7	11
Navicula cincta	9				2				1																
Navicula cryptocephala	9	0	5	0	1	3	2	0	2	1	0	0	2	3	0	5	1	4	1	0	0	0	1	0	
Navicula cryptocephala var veneta		1																							
Navicula cryptotenella	3	1	2					1	1			2	1	3				1							
Navicula digitoradiata	1	2									1	2	1	1	1			2	5						4
Navicula duerrenberginiana												1													
Navicula eridrigiana																									
Navicula erifuga													2	3	2	5									
Navicula exigua var. capitata												1													
Navicula gregaria	2	3	4		1	4		1	1			7	19	13	5	1	2	3							
Navicula lanceolata															1										
Navicula lanceolata var minima												2													
Navicula longa		1																							
Navicula menisculus														1											
Navicula pennata	9	8			2	1	2	1	2			1			1	3						1		1	

Table A.2. (continued)

Depth in core (cm) -->	70	71	72	73	74	75	78	81	85	89	92	95	96	97	98	99	100	101	102	107	114	122	126	130	131
Navicula perminuta		2							1			21		2	1										
Navicula pupula																									
Navicula radiosa										1		1								1				1	
Navicula recens		1																							
Navicula rostellata			1	2			4	1	1	1	1	7			2	2	1					2	4	2	
Navicula salinarum	4				1										1	5	2	2	2		1			1	
Navicula salinicola	1	10	2	1	1	1	1		2				3	3	6	13		5			3			1	1
Navicula sp1												1				1									
Navicula subrostellata	2	2	1					4	3				1		4	6			2						3
Navicula tripunctata	4	5		1	2	11		2	1			1		1		2	4							6	2
Navicula vimineoides				3	1					1															
Navicula viridula var. rostellata																									
Nitzschia acicularis											2								1						
Nitzschia amphibia	8	6	6	3	15	11		1	1			5				1		4	1						2
Nitzschia angustata		2										1							4						
Nitzschia bicapitata		1																							
Nitzschia brevissima	1							2											1						
Nitzschia capitellata	*4*	*0*	*2*	*0*	*0*	*1*	*0*	*0*	*1*	*0*	*0*	*0*	*2*	*2*	*0*	*0*	*1*	*1*	*6*	*1*	*0*	*1*	*0*	*0*	
Nitzschia clausii		3																	1						
Nitzschia compressa														4											
Nitzschia confinis			2	1		2	2	2	1	2	5	4		2	1	2		2	1		3		1		
Nitzschia dissipata				3	2			2			2			3	1	2		8		5	4	1		11	2
Nitzschia distans										2		1		1	4		2						2		
Nitzschia filiformis	1			1		10				1	1			1	1	2		3	2						
Nitzschia Fonticola	1	4	5	5	3	5	13	4	7	6	12	3		7	2	13	1	1		8	5	3	3	12	4
Nitzschia frustulum	5	8	7	2	4		10	2	8		1		3	5	5	10	7	31	12	1				7	
Nitzschia gracilis	7		23	2	6	4	16	14	14	8	15	3	10	4	3	10	5	10	2	5	1	1	2	5	7
Nitzschia grossestriata	12	2	3	2				8	9	8	16	2	1		1			1		1		1			
Nitzschia hybrida			1																						
Nitzschia inconspicua																		9							
Nitzschia insignis	1								1	1									1						
Nitzschia intermedia													1												
Nitzschia lanceolata								1						1											
Nitzschia lanceolata var. minima					3			1	1	3						1									
Nitzschia laevissima																									
Nitzschia linearis	2																								
Nitzschia microcephala	3	3	4		1	2			2		19	1	8	1				1	7		5				2
Nitzschia obtusa obtusa	6	2	4	1	1	1		1	1		2	3	3	2				1				1			
Nitzschia palea			6	3			1		1		3	5	4	5	5	7	12	11	7	4	11	1		2	1
Nitzschia panduriformis																			1						
Nitzschia parvula																									
Nitzschia perminuta													17	4				1							
Nitzschia plana																									
Nitzschia recta																									
Nitzschia scalaris																									
Nitzschia scalpelliformis			13	9	10	19	27	30	23	30		1	3	4	1	5	1	4	1	6		4			3
Nitzschia sicula	2		2	1		2	7	6	4	11	21	14	10	15	7	2	6	4	19	3	30	37	3	4	3
Nitzschia sigma	10	1	5	4	2	8	2	2	6	12	3		1		1	1	1	1		3		1		3	

Table A.2. (continued)

Depth in core (cm) -->	70	71	72	73	74	75	78	81	85	89	92	95	96	97	98	99	100	101	102	107	114	122	126	130	131
Nitzschia sp1.	2	1										1							3						
Nitzschia thermalis		1											1												
Nitzschia vitrea																									
Opephora marina var. minuta																									14
Opephora pacifica	2	1										1													
Paralia sulcata	9	1	4	4	4	1	1	1	4	1	17	22	33	16	35	50	38	23	4	3	13	23	13	4	7
Paralia sulcata var. biseriata	3													1		1		1							
Paralia sulcata var. Radiata																									
Paralibellus rhombicus																			2						
Parlibellus calvus																			1						
Petroneis sp1																									
Petroneis marina																									
Pinnularia acrosphaeria	2	3	1		5	2			1	2				2		1	2					5	1		1
Pinnularia biceps			5	1			3		2	1						2				1			1		
Pinnularia biceps var. minor	1	3		2		2		2											1						
Pinnularia borealis				1																					
Pinnularia certa																				1					
Pinnularia incognita	1																								
Pinnularia joculata																									
Pinnularia lattarea	1											1				1									
Pinnularia microstauron																									
Pinnularia neomajor		1																							
Pinnularia obscura																									
Pinnularia sp1									1										1						
Pinnularia streptoraphe var. parva																									
Pinnularia subcapitata															1										
Pinnularia turgidula																									
Placoneis gastrum		1			3	1	1			1												1		1	1
Placoneis hambergii									2																
Planktoniella sol				1																					
Planothidium delicatulum					1									1	1			1							
Planothidium frequentisimum															1										
Planothidium hauckianum												1		1		1									3
Planothidium lanceolatum														1			1								
Pleurosigma salinarum			4		2																				
Pseudogomphonema kamtschaticum										2															
Rhopalodia acuminata			1	3										4						1					
Rhopalodia constricta		2										3													
Rhopalodia gibba		1						1				3		1			2					2	2	1	
Rhopalodia gibberula	1				6				1		2	6			1								1	1	
Rhopalodia musculus	1	1		2	2	3	2	1	9	6	6	4	5	2			3	1	2	5	3	5	3	1	
Rhopalodia pacifica												1													
Sellaphora japponica					2																				
Sellaphora pupula	1		2					2								1			1				2	1	
Sellaphora guyanensis																								2	
Seminavis strigosa											1										2			2	
Seminavis ventricosa																									
Stauroneis amphibia			1																						

Table A.2. (continued)

Depth in core (cm) -->	70	71	72	73	74	75	78	81	85	89	92	95	96	97	98	99	100	101	102	107	114	122	126	130	131
Stauroneis borrichii																					1				
Stauroneis producta																									
Staurophora salina																									
Staurophora wislouchii												1		1											
Staurophora sp1																									
Staurosirella pinnata																									
Stephanodiscus hantzschi												1													
Stephanodiscus niagarae																									
Stephanodiscus parvus											4	2				1	1	2		1	1	1			3
Synedra Goulardi																									
Tabularia fasciculata								3				1						3	1	5			10	2	7
Tabularia parva						1					4			2					1						
Tabularia persuadens													1	1					2						
Thalassionema nitzschioides	1				1					1						1									
Tryblionella accuminata																				2					
Tryblionella apiculata												3			1	1									
Tryblionella compressa	1			1			1	1		2	1	3	2						2	7	2	9	4	1	
Tryblionella debilis								1																	
Tryblionella granulata															1										
Tryblionella hungarica			1								2		3		1	3	4								
Tryblionella levidensis			3	6	3	1	2	5	1	3	1	7	2	1	5		3	1	1	2				1	1
Tryblionella littoralis																	1								
Tryblionella persuadens												3	2				1							7	
Ulnaria danica		2						1				1	1	2					1						
Ulnaria Ulna									2																
Total counts	206	204	202	203	208	204	203	203	207	201	208	222	207	201	200	226	221	215	205	204	202	201	209	205	216

Table A.2. (continued)

Depth in core (cm) -->	132	133	134	135	136	137	138	139	140	142	146	150	151	152	153	154	155	156	157	158	159	160	166
Achnanthes angustata																							
Achnanthes brevipes		2															1						
Achnanthes brevipes var. Intermedia														1									
Achnanthes clevei var. rostrata																							
Achnanthes delicatula																							
Achnanthes exigua				1		3				1				2				2	1			2	
Achnanthes inflata	3	2	2	4	10	8	5		1	1	1			1	1	3			1	1	2	1	2
Achnanthes lanceolata var. rostrata																							
Achnanthes lorenziana																							
Achnanthes marginulata							1																
Achnanthes parvula																							
Achnanthes promunturi																							
Achnanthes sp1																							
Achnanthidium exiguum																							
Achnanthidium minutissimum																							
Amphipora ornata																							
Amphora acustiuscula			3				19	1		6	4	3				2							1
Amphora affinis																							
Amphora arenaria																							
Amphora bicapitata																							
Amphora clevei																							
Amphora coffeaeformis	4	2	2	1	3	4	3	3	1	2	4	7	5	1		3			3		1	1	1
Amphora costata	4	5		5	2	6			1			1	1	2			2		1		1	1	
Amphora gigantea																	1						
Amphora proteus	4		1	1	2	1		2	4								4	8		1	1	2	
Amphora terroris							1																
Astartiella punctifera			1																				
Aulacoseira sp1																							
Aulacoseira granulata																							
Austariella jamaicensis																							
Bacillaria paxillifera	26	5	3	8	4	6	14	3	3	7	7	8	2	1		3	3	2	2	7	4		4
Bacillaria socialis																							
Biremis ambigua																	1						
Brevisira arentii																							
Caloneis aemula										1													
Caloneis bacillum		1	1	1	2	2				1	1			1	1					3	2	1	1
Caloneis excentrica																							
Caloneis permagna																							
Caloneis sabanicola		1										1					1						
Caloneis subsalsa																							
Caloneis westii																							
Caloneis sp1																							
Ceratulus californicus																							
Cocconeis convexa																							
Cocconeis neodiminuta																							
Cocconeis pinnata				1																			
Cocconeis placentula	2	5	1			9	4	1			8	6	2		1		6	3	1				2
Cocconeis placentula var. euglypta	4	1	1	3	1	1		2					3	1		1		1		1	2		
Cocconeis placentula var. lineata																							

Table A.2. (continued)

Depth in core (cm) -->	132	133	134	135	136	137	138	139	140	142	146	150	151	152	153	154	155	156	157	158	159	160	166
Conticribra weissflogii																							
Coscinodiscus radiatus																							
Craticula halophilioides																				1		3	
Cyclotella atomus				2							2	1											
Cyclotella cryptica																							
Cyclotella kuetzingiana																							
Cyclotella litoralis																							
Cyclotella meneghiniana	13	18	45	26	34	33	25	15	11	9	25	46	34	17	14	64	47	13	8	11	14	11	19
Cyclotella ocellata																							
Cyclotella radiosa																							
Cyclotella striata	9	10	2	4	1		1				1	2	10	1		4	8			1	2	1	
Cyclotella stylorum		1																					
Cymbella laevis																							
Denticula kuetzingii												2				1							
Diadesmis confervacea	10	1	17	17	25	35	23	6			12	11	7	6	3	6	5	1	2	1	3	4	5
Diploneis boldtiana																							
Diploneis elliptica																							
Diploneis nitecens													1										
Diploneis oculata																				1			
Diploneis ovalis																							
Diploneis pseudovalis	23	32		2	5	1		2		1		3		1								2	
Diploneis papula	9	2						1									2	3	2				
Diploneis parma																							
Diploneis puella			1				2				1			1			3				1		2
Diploneis smithii			3						1										5	2	2	3	
Diploneis sp1.																							
Encyonema montana																							
Encyonema prostratum																							
Encyonema silesianum												5											
Entomoneis paludosa																							
Eolimna ruttineri						1																	
Epithemia adnata					1	1																2	
Epithemia argus																							
Eunotia bidens																							
Eunotia flexuosa	2	1		1	3	1	1		2	1	1	1	2	3	2	1	4	9	2	7	3	3	
Eunotia formica	1		1		2				1	1			1							1	3		1
Eunotia minor																							
Eunotia myrmica																							
Eunotia sp1																							
Fallacia auriculata							1	1		1	4												
Fallacia forcipata	1		6	2		3						1	1			1	1			1			
Fragilaria goulardii			1							1	1				1	1							
Gomphonema acuminatum																							
Gomphonema affine			1	1	1		3	1	2	5	1		4	6	3	2	2	4	4	8	4	4	
Gomphonema angustatum																							
Gomphonema gracile											2	1											
Gomphonema hebridense																							

Table A.2. (continued)

Depth in core (cm) -->	132	133	134	135	136	137	138	139	140	142	146	150	151	152	153	154	155	156	157	158	159	160	166
Gomphonema parvulum	1					1	1		4		3		1	2		3	1	4		1		1	3
Gomphonema subclavatum						4		2	2			2			2		1	2			3	2	
Grammatophora hamulifera																							
Grammatophora marina																							
Gyrosigma acuminatum					2	1	2		2	1	1	1	4				1			1			
Gyrosigma balticum																							
Halamphora acutiuscula		20	1	1	4	1							1	1						2		1	
Halamphora exigua																							
Halamphora holsatica			1							1													
Halamphora latecostata																							
Halamphora sp1																							
Halamphora submontana		1	1					70	54	6	3		14	19	2	1	17	23	10	13	8	27	
Hantzschia amphioxys		3	1	2		2	1	2	2	1	1	1	4	5	1	2	5	3	4	1		4	
Hantzschia virgata					1				1												1		
Haslea britannica																							
Hippodonta hungarica			1				1						2										
Hyalosynedra laevigata																							
Karayevia amoena																							
Karayevia clevei											1												
Kolbesia suchlandtii																							
Luticola goeppertiana																							
Luticola Mutica	4	1	4	6	4	9	2	1	2	8	7	3	8	12	2		8	9	9	11	9	10	2
Luticola mutica f. intermedia																							
Luticola sp1																							
Lyrella lyra																							
Lyrella lyroides																							
Mastogloia decipiens																							
Melosira polaris																							
Navicula abunda																							
Navicula agatake											2												
Navicula agnita							1																
Navicula apta																							
Navicula cancellata	5	1	4	10	4	1	6	9	7	2	1		2	2	4	2		4	5	1			1
Navicula cincta				1		2		1	1														
Navicula cryptocephala			4	1			1		2	3	0	0				0				0			0
Navicula cryptocephala var veneta																							
Navicula cryptotenella				2			4				2	3								1	2		1
Navicula digitoradiata	3	2	3	5	2		1		2		1	1									6		1
Navicula duerrenberginiana																							
Navicula eridrigiana																							
Navicula erifuga																							
Navicula exigua var. capitata																							
Navicula gregaria		1									1	2				3	2						
Navicula lanceolata																							
Navicula lanceolata var minima																							
Navicula longa																							
Navicula menisculus																							
Navicula pennata	1	4	3		1			1									1	1			1	2	

Table A.2. (continued)

Depth in core (cm) -->	132	133	134	135	136	137	138	139	140	142	146	150	151	152	153	154	155	156	157	158	159	160	166
Navicula perminuta		1														1			8	1	1	4	
Navicula pupula																							
Navicula radiosa							1																
Navicula recens																							
Navicula rostellata			1				1			2		2				2							
Navicula salinarum	2			2	2	1	1	4	3	8	1	3				6	1	2		5			
Navicula salinicola	1							4	6	4	5	1		2	1	4		1	2	2	2		2
Navicula sp1																							
Navicula subrostellata					2		3		2					2			3	1	4		1	2	
Navicula tripunctata	2		1	2	3	5	8		1				2				1	1	3	1	2		
Navicula vimineoides								1								3	1						
Navicula viridula var. rostellata																							
Nitzschia acicularis																							
Nitzschia amphibia	1	1		6	1	3	3			2	2		2	2	4	1	1			3			1
Nitzschia angustata																							
Nitzschia bicapitata																							
Nitzschia brevissima																							
Nitzschia capitellata			*0*	*2*			*0*			*5*	*5*	*0*		*1*		*0*			*3*	*0*	*3*	*8*	*0*
Nitzschia clausii																							
Nitzschia compressa	2																						
Nitzschia confinis			2									1				2				1			
Nitzschia dissipata			1	1		1	4	3			3	1				5					1		
Nitzschia distans			1																		1		
Nitzschia filiformis		2								2		2					5	8				3	
Nitzschia Fonticola	12	6	20	24	16	11	16	8	13	30	8	9	10	13	17	2	5	20	34	14	10	18	3
Nitzschia frustulum				9		4		4	10		3	6	8	16	6	3	9	8	9	34	9	18	
Nitzschia gracilis							3	5	8	17	7	9	3	9	6	2	7	2	5	3	2	2	
Nitzschia grossestriata	1	1	3		5	6	1			2			1		1	1		3	8		19	9	
Nitzschia hybrida																							
Nitzschia inconspicua																							
Nitzschia insignis																							
Nitzschia intermedia																							
Nitzschia lanceolata									1							2	1						
Nitzschia lanceolata var. minima																							
Nitzschia laevissima																							
Nitzschia linearis						2																	
Nitzschia microcephala										3	3	3			5	1							
Nitzschia obtusa obtusa																1			3		2		
Nitzschia palea		3						9	1	2	3	1	5	5	4	10	3	3		7			1
Nitzschia panduriformis																							
Nitzschia parvula																							
Nitzschia perminuta			1	2							2	5											
Nitzschia plana																							
Nitzschia recta							1																
Nitzschia scalaris			1		1							1											
Nitzschia scalpelliformis	1		3		1	2	4	22	32	26	8	5	16	40	21	5	12	17	23	16	9	18	
Nitzschia sicula		4	16	3	5	3	9	3	2		16	9	14	8	2	14	9	13	8	6	11	6	2
Nitzschia sigma	4		2		3	4	4	2	2	17			2		1			3	9	2	1	7	

Table A.2. (continued)

Depth in core (cm) -->	132	133	134	135	136	137	138	139	140	142	146	150	151	152	153	154	155	156	157	158	159	160	166
Nitzschia sp1.																							
Nitzschia thermalis				6																			
Nitzschia vitrea			1																				
Opephora marina var. minuta	19	35			11												5				1		
Opephora pacifica																							
Paralia sulcata	7	7	12	1	2	3	6		1	9	20	12	2	1		19	5	1	2	6	6	3	7
Paralia sulcata var. biseriata																							
Paralia sulcata var. Radiata																							
Paralibellus rhombicus																							
Parlibellus calvus																							
Petroneis sp1																							
Petroneis marina																							
Pinnularia acrosphaeria					2	3	3	3	1	1		2	4			1		4	1		1	5	
Pinnularia biceps				3									1	1	1		1	2	1			2	1
Pinnularia biceps var. minor																							
Pinnularia borealis					1		1				1												
Pinnularia certa					1		1				1	1	3	2	2			6	1		1		
Pinnularia incognita																							
Pinnularia joculata																							
Pinnularia lattarea																							
Pinnularia microstauron																							
Pinnularia neomajor																							
Pinnularia obscura																							
Pinnularia sp1																							
Pinnularia streptoraphe var. parva																							
Pinnularia subcapitata																							
Pinnularia turgidula																							
Placoneis gastrum	1			1	2		2				1		2		2			1			1		
Placoneis hambergii				1		3			2											3			
Planktoniella sol																							
Planothidium delicatulum			1																				
Planothidium frequentisimum																							
Planothidium hauckianum							2			1				2		1				1			
Planothidium lanceolatum				1																			
Pleurosigma salinarum																					1		
Pseudogomphonema kamtschaticum																							
Rhopalodia acuminata																							
Rhopalodia constricta					2											2							1
Rhopalodia gibba										2			2	3	1			4	1		1	1	
Rhopalodia gibberula				1	3		1					3	3				1	6	4	2	1	7	2
Rhopalodia musculus	4	4	2	2	3	3					2	1						1		2		1	1
Rhopalodia pacifica																							
Sellaphora japponica																							
Sellaphora pupula					1		1	4	2			1		1				2	2	3	1	2	2
Sellaphora guyanensis										3			2	1	1	1				2			
Seminavis strigosa							1									1							
Seminavis ventricosa																	1						
Stauroneis amphibia																			1				

Table A.2. (continued)

Depth in core (cm) -->	132	133	134	135	136	137	138	139	140	142	146	150	151	152	153	154	155	156	157	158	159	160	166
Stauroneis borrichii																							
Stauroneis producta						1																	
Staurophora salina																							
Staurophora wislouchii																							
Staurophora sp1																							
Staurosirella pinnata																1							
Stephanodiscus hantzschi																							
Stephanodiscus niagarae																							
Stephanodiscus parvus											2	2				4	2					1	
Synedra Goulardi																							
Tabularia fasciculata	1	1	1	1	7	2			1	1	5	4	3		2	1	2			5		1	
Tabularia parva																							
Tabularia persuadens																							
Thalassionema nitzschioides																							
Tryblionella accuminata																			2				
Tryblionella apiculata		4			2																		
Tryblionella compressa		4	7	4	1	8	9		3	3		2		1		2	2		1	2		1	
Tryblionella debilis			5	10	8	5	10									1			1				
Tryblionella granulata																							
Tryblionella hungarica	10							2			2	1				1			1		4		
Tryblionella levidensis	11	8	2	6	3	3	4	2		1	2	3		2		1		1			1		
Tryblionella littoralis																							
Tryblionella persuadens																							
Ulnaria danica																							
Ulnaria Ulna			2	5	1		1	2	4				7	3	4			4	5	2	2	1	1
Total counts	**208**	**203**	**200**	**201**	**203**	**209**	**224**	**202**	**201**	**201**	**200**	**202**	**201**	**201**	**118**	**204**	**204**	**206**	**202**	**201**	**170**	**208**	**70**

Table A.3. Summary of fossil diatoms in core MAR005, grouped by salinity classes (%).

Depth (cm)	Fresh (%)	Brackish (%)	Marine (%)	Unclassified (%)
4	78.9	12.9	8.1	0.0
12	73.1	18.3	8.7	0.0
19	60.9	19.3	15.8	4.0
23	76.6	8.5	8.0	6.5
24	66.5	21.5	10.0	2.0
25	74.0	12.5	12.0	1.4
26	61.5	12.2	25.8	0.5
27	48.3	13.9	36.4	1.0
28	76.7	7.1	15.2	1.0
29	79.1	11.8	8.2	0.9
30	69.6	19.8	7.4	3.2
31	77.7	15.0	6.8	0.5
34	89.6	4.0	5.5	1.0
37	90.5	5.5	3.5	0.5
41	96.4	3.0	0.6	0.0
46	80.0	11.0	7.0	2.0
49	68.1	14.5	15.1	2.4
53	72.2	10.2	15.6	2.0
57	79.4	6.9	13.7	0.0
63	48.6	26.4	25.0	0.0
65	50.2	19.2	28.6	2.0
66	47.6	16.3	35.1	1.0
67	47.5	14.4	33.7	4.5
68	59.1	10.6	29.3	1.0
69	54.9	21.1	22.1	2.0
70	49.0	22.8	27.2	1.0
71	62.3	23.5	13.2	1.0
72	59.4	26.2	13.4	1.0
73	54.7	18.2	22.7	4.4
74	61.1	21.6	15.9	1.4
75	60.3	25.5	14.2	0.0
78	55.7	21.7	22.2	0.5
81	45.8	31.0	22.7	0.5
85	46.4	31.4	21.7	0.5
89	39.3	31.3	28.4	1.0
92	49.0	21.2	29.8	0.0
95	26.6	36.5	32.9	4.1
96	44.0	23.2	30.4	2.4
97	45.8	28.4	24.9	1.0
98	36.5	28.5	34.5	0.0
99	45.6	20.4	31.9	1.8
100	40.3	33.9	25.8	0.0
101	54.9	23.3	21.9	0.0
102	51.7	21.0	23.4	3.9
107	68.6	18.1	13.2	0.0
114	62.4	12.9	24.8	0.0
122	50.7	10.0	39.3	0.0
126	69.9	12.0	18.2	0.0
130	69.8	14.6	15.6	0.0
131	37.5	24.5	38.0	0.0
132	26.9	42.8	30.3	0.0
133	21.7	41.9	36.0	0.5
134	54.5	15.0	30.5	0.0
135	64.2	18.9	16.9	0.0
136	55.7	21.7	22.7	0.0
137	68.9	12.9	17.2	1.0
138	54.5	25.9	19.6	0.0
139	69.3	21.3	8.9	0.5
140	63.7	24.9	11.4	0.0
142	49.8	39.3	10.9	0.0
146	56.5	20.5	22.0	1.0
150	58.9	21.3	16.8	3.0
151	68.2	19.4	12.4	0.0
152	65.7	24.4	10.0	0.0
153	72.9	19.5	7.6	0.0
154	57.8	18.6	22.1	1.5
155	63.2	16.7	19.1	1.0
156	63.6	19.4	17.0	0.0
157	52.0	29.2	18.8	0.0
158	67.7	19.9	12.4	0.0
159	51.2	21.2	27.6	0.0
160	60.1	25.5	14.4	0.0
166	67.1	18.6	14.3	0.0

Table A. 4. Summary of fossil diatoms contained in the core MAR005. These species correspond to those with abundance >5% that appear in at least 5 samples.

	Species	Salinity class	Life form	Source
1.-	Achnanthes inflata	Freshwater	Benthic	Denys, 1991
2.-	Bacillaria paxillifera	Brackish	Planktonic	Sawai et al. 2003
3.-	Cyclotella meneghiniana	Freshwater	Planktonic	Denys, 1991; Vos & de Wolf (1993)
4.-	Diadesmis confervacea	Freshwater	Benthic	Kókai et al. 2019
5.-	Gomphonema affine	Freshwater	Benthic	Denys, 1991
6.-	Halamphora submontana	Freshwater	Benthic	Qingmin et al. 2015; Cocquyt et al. 2019
7.-	Luticola Mutica	Freshwater	Benthic	Sawai et al. 2003
8.-	Navicula cancellata	Marine	Benthic	Siqueiros-Beltrones et al. 2017, Siqueiros-Beltrones et al. 2016, Horton et al. Sawai et al. 2003
9.-	Nitzschia Fonticola	Freshwater	Benthic	Denys, 1991; Watchman et al. 2013
10.-	Nitzschia frustulum	Freshwater	Benthic	Watchman et al. 2013, Zong & Sawai, 2015
11.-	Nitzschia gracilis	Freshwater	Benthic	Shennan et al. 2016; Denys, 1991
12.-	Nitzschia grossestriata	Marine	Benthic	Siqueiros-Beltrones et al. 2017
13.-	Nitzschia palea	Freshwater	Benthic	Vos & de Wolf (1988)
14.-	Nitzschia scalpelliformis	Brackish	Benthic	Al-Handal et al. 2014, Sawai et al. 2003
15.-	Nitzschia sicula	Marine	Benthic	Siqueiros-Beltrones et al. 2016
16.-	Paralia sulcata	Marine	Planktonic	Vos & de Wolf (1988)

Table A.5. Datasets from Alaska (Shennan et al 2016) and Chile (Hocking et al. 2017) to build the linear models to estimate palaeoelevations.

Alaska dataset (Model 1)			Chile dataset (Model 2)		
Depth (cm)	SWLI	Marine_&_Brackish (%)	Depth (cm)	SWLI	Marine_&_Brackish (%)
0	221.67	17.31	28.25	210.04	51.85
8	214.57	37.84	30.25	218.19	61.29
16	203.24	75.64	32.25	178.51	72.64
24	201.68	70.00	33.25	171.37	76.59
32	196.03	90.73	35.25	171.00	71.76
40	191.17	100.00	36.25	191.75	47.60
48	202.19	70.07	36.75	178.76	52.27
56	200.28	69.18	37.25	180.58	52.11
64	197.43	82.35	37.75	201.09	55.81
66	193.33	92.36	38.25	209.70	44.00
68	191.20	97.47	44.75	256.01	9.49
69	237.16	35.52	45.25	260.70	6.00
70	237.23	35.32	45.75	269.49	2.79
72	239.13	24.31	46.25	266.90	2.77
76	241.81	12.89	48.25	272.22	3.03
80	241.14	15.58	50.25	266.77	7.39
84	236.52	31.37	51.25	267.25	9.02
88	236.39	25.95	52.25	248.42	20.40
92	239.77	19.14	53.25	217.78	48.80
96	242.65	10.12	53.75	206.67	57.60
100	240.76	10.98	60.25	192.07	77.60
104	240.14	11.92	60.75	194.86	84.00
106	238.03	18.08	61.25	196.79	75.60
108	236.99	31.91	61.75	192.74	78.00
110	233.71	43.61	62.25	193.53	75.30
112	230.85	45.77	64.25	197.74	72.27
116	228.17	25.86	66.25	182.77	74.21
120	224.73	41.33	68.25	197.75	68.80
128	213.56	60.73	70.25	202.06	70.00
136	218.35	52.96	76.25	207.81	49.23
144	206.76	67.67	76.75	208.81	48.02
152	203.24	60.90	77.25	232.34	43.19
160	200.97	72.33	77.75	236.13	29.17
168	192.27	92.81	78.25	226.07	42.31
174	190.87	94.04	79.25	226.34	41.04
176	192.20	93.63	80.25	204.69	49.48
178	211.29	75.82	82.25	190.45	59.50
179	234.75	35.98	83.25	181.15	70.80
180	237.63	23.94	84.25	181.97	69.69
181	239.46	23.51	85.25	186.90	65.20
182	239.64	22.53	89.25	224.15	31.10
183	238.42	23.17	89.75	219.61	33.33
184	236.28	32.27	90.25	216.26	33.59
185	235.33	34.46	90.75	235.12	22.40
186	236.25	32.02	92.25	230.88	30.80
187	236.70	22.56	94.25	228.31	25.57
188	236.97	25.67	96.25	219.55	43.01
189	235.56	38.91			
190	240.12	38.08			
192	239.63	37.85			
194	242.77	27.21			

Table A. 6. Palaeoelevation estimations from Model 1 (Alaska) of core MAR005.

Depth (cm)	B & M (%)	Palaeoelevation in SWLI units			Palaeoelevations transformed in m relative to MHHW			
		SWLI	SWLI_lower	SWLI_upper	m MHHW	Error linear model (e1)	Error Reference Water Level (e2)	Total elevation error (ee)
4	21.05	239.34	12.54	12.54	0.13	0.04	0.26	0.26
12	26.92	235.57	12.50	12.50	0.12	0.04	0.26	0.26
19	35.15	230.27	12.46	12.46	0.10	0.04	0.26	0.26
23	16.42	242.32	12.58	12.58	0.14	0.04	0.26	0.26
24	31.50	232.62	12.48	12.48	0.11	0.04	0.26	0.26
25	24.52	237.11	12.52	12.52	0.12	0.04	0.26	0.26
26	38.03	228.42	12.45	12.45	0.09	0.04	0.26	0.26
27	50.24	220.56	12.45	12.45	0.07	0.04	0.26	0.26
28	22.38	238.49	12.53	12.53	0.13	0.04	0.26	0.26
29	20.00	240.02	12.55	12.55	0.13	0.04	0.26	0.26
30	27.19	235.39	12.50	12.50	0.12	0.04	0.26	0.26
31	21.84	238.83	12.54	12.54	0.13	0.04	0.26	0.26
34	9.45	246.81	12.66	12.66	0.15	0.04	0.26	0.26
37	9.00	247.10	12.66	12.66	0.15	0.04	0.26	0.26
41	3.61	250.57	12.73	12.73	0.17	0.04	0.26	0.26
46	18.00	241.31	12.57	12.57	0.14	0.04	0.26	0.26
49	29.52	233.89	12.49	12.49	0.11	0.04	0.26	0.26
53	25.85	236.25	12.51	12.51	0.12	0.04	0.26	0.26
57	20.61	239.63	12.55	12.55	0.13	0.04	0.26	0.26
63	51.44	219.79	12.45	12.45	0.06	0.04	0.26	0.26
65	47.78	222.14	12.44	12.44	0.07	0.04	0.26	0.26
66	51.44	219.79	12.45	12.45	0.06	0.04	0.26	0.26
67	48.02	221.99	12.44	12.44	0.07	0.04	0.26	0.26
68	39.90	227.21	12.45	12.45	0.09	0.04	0.26	0.26
69	43.14	225.13	12.44	12.44	0.08	0.04	0.26	0.26
70	50.00	220.72	12.45	12.45	0.07	0.04	0.26	0.26
71	36.76	229.23	12.46	12.46	0.10	0.04	0.26	0.26
72	39.60	227.41	12.45	12.45	0.09	0.04	0.26	0.26
73	40.89	226.58	12.45	12.45	0.09	0.04	0.26	0.26
74	37.50	228.76	12.45	12.45	0.09	0.04	0.26	0.26
75	39.71	227.34	12.45	12.45	0.09	0.04	0.26	0.26
78	43.84	224.68	12.44	12.44	0.08	0.04	0.26	0.26
81	53.69	218.34	12.45	12.45	0.06	0.04	0.26	0.26
85	53.14	218.70	12.45	12.45	0.06	0.04	0.26	0.26
89	59.70	214.47	12.47	12.47	0.05	0.04	0.26	0.26
92	50.96	220.10	12.45	12.45	0.07	0.04	0.26	0.26
95	69.37	208.25	12.53	12.53	0.03	0.04	0.26	0.26
96	53.62	218.39	12.45	12.45	0.06	0.04	0.26	0.26
97	53.23	218.64	12.45	12.45	0.06	0.04	0.26	0.26
98	63.00	212.35	12.49	12.49	0.04	0.04	0.26	0.26
99	52.21	219.29	12.45	12.45	0.06	0.04	0.26	0.26
100	59.73	214.45	12.47	12.47	0.05	0.04	0.26	0.26
101	45.12	223.86	12.44	12.44	0.08	0.04	0.26	0.26
102	44.39	224.33	12.44	12.44	0.08	0.04	0.26	0.26
107	31.37	232.70	12.48	12.48	0.11	0.04	0.26	0.26
114	37.62	228.68	12.45	12.45	0.09	0.04	0.26	0.26
122	49.25	221.20	12.44	12.44	0.07	0.04	0.26	0.26
126	30.14	233.49	12.48	12.48	0.11	0.04	0.26	0.26
130	30.24	233.43	12.48	12.48	0.11	0.04	0.26	0.26
131	62.50	212.67	12.49	12.49	0.04	0.04	0.26	0.26
132	73.08	205.86	12.56	12.56	0.02	0.04	0.26	0.26
133	77.83	202.81	12.61	12.61	0.01	0.04	0.26	0.26
134	45.50	223.61	12.44	12.44	0.08	0.04	0.26	0.26
135	35.82	229.84	12.46	12.46	0.10	0.04	0.26	0.26
136	44.33	224.36	12.44	12.44	0.08	0.04	0.26	0.26
137	30.14	233.49	12.48	12.48	0.11	0.04	0.26	0.26
138	45.54	223.59	12.44	12.44	0.08	0.04	0.26	0.26
139	30.20	233.46	12.48	12.48	0.11	0.04	0.26	0.26
140	36.32	229.52	12.46	12.46	0.10	0.04	0.26	0.26
142	50.25	220.55	12.45	12.45	0.07	0.04	0.26	0.26
146	42.50	225.54	12.44	12.44	0.08	0.04	0.26	0.26
150	38.12	228.36	12.45	12.45	0.09	0.04	0.26	0.26
151	31.84	232.40	12.47	12.47	0.11	0.04	0.26	0.26
152	34.33	230.80	12.46	12.46	0.10	0.04	0.26	0.26
153	27.12	235.44	12.50	12.50	0.12	0.04	0.26	0.26
154	40.69	226.71	12.45	12.45	0.09	0.04	0.26	0.26
155	35.78	229.87	12.46	12.46	0.10	0.04	0.26	0.26
156	36.41	229.46	12.46	12.46	0.10	0.04	0.26	0.26
157	48.02	221.99	12.44	12.44	0.07	0.04	0.26	0.26
158	32.34	232.08	12.47	12.47	0.11	0.04	0.26	0.26
159	48.82	221.47	12.44	12.44	0.07	0.04	0.26	0.26
160	39.90	227.21	12.45	12.45	0.09	0.04	0.26	0.26
166	32.86	231.74	12.47	12.47	0.10	0.04	0.26	0.26

2

Table A.7. Palaeoelevation estimations from Model 2 (Chile) of core MAR005.

Depth (cm)	B & M	Palaeoelevation in SWLI units			Palaeoelevations transformed in m relative to MHHW			
		SWLI	SWLI_lower	SWLI_upper	m MHHW	Error linear model (e1)	Error Reference Water Level (e2)	Total elevation error (ee)
4	21.05	242.35	23.63	23.63	0.14	0.08	0.26	0.27
12	26.92	235.94	23.51	23.51	0.12	0.08	0.26	0.27
19	35.15	226.95	23.40	23.40	0.09	0.08	0.26	0.27
23	16.42	247.41	23.74	23.74	0.16	0.08	0.26	0.27
24	31.50	230.94	23.44	23.44	0.10	0.08	0.26	0.27
25	24.52	238.56	23.56	23.56	0.13	0.08	0.26	0.27
26	38.03	223.80	23.37	23.37	0.08	0.08	0.26	0.27
27	50.24	210.46	23.34	23.34	0.03	0.08	0.26	0.27
28	22.38	240.90	23.60	23.60	0.13	0.08	0.26	0.27
29	20.00	243.50	23.65	23.65	0.14	0.08	0.26	0.27
30	27.19	235.65	23.51	23.51	0.12	0.08	0.26	0.27
31	21.84	241.49	23.61	23.61	0.14	0.08	0.26	0.27
34	9.45	255.03	23.94	23.94	0.18	0.08	0.26	0.27
37	9.00	255.52	23.96	23.96	0.18	0.08	0.26	0.27
41	3.61	261.41	24.14	24.14	0.20	0.08	0.26	0.27
46	18.00	245.68	23.70	23.70	0.15	0.08	0.26	0.27
49	29.52	233.10	23.47	23.47	0.11	0.08	0.26	0.27
53	25.85	237.11	23.53	23.53	0.12	0.08	0.26	0.27
57	20.61	242.83	23.64	23.64	0.14	0.08	0.26	0.27
63	51.44	209.15	23.34	23.34	0.03	0.08	0.26	0.27
65	47.78	213.15	23.34	23.34	0.04	0.08	0.26	0.27
66	51.44	209.15	23.34	23.34	0.03	0.08	0.26	0.27
67	48.02	212.89	23.34	23.34	0.04	0.08	0.26	0.27
68	39.90	221.76	23.36	23.36	0.07	0.08	0.26	0.27
69	43.14	218.22	23.34	23.34	0.06	0.08	0.26	0.27
70	50.00	210.73	23.34	23.34	0.04	0.08	0.26	0.27
71	36.76	225.19	23.38	23.38	0.08	0.08	0.26	0.27
72	39.60	222.09	23.36	23.36	0.07	0.08	0.26	0.27
73	40.89	220.68	23.35	23.35	0.07	0.08	0.26	0.27
74	37.50	224.38	23.38	23.38	0.08	0.08	0.26	0.27
75	39.71	221.97	23.36	23.36	0.07	0.08	0.26	0.27
78	43.84	217.46	23.34	23.34	0.06	0.08	0.26	0.27
81	53.69	206.69	23.36	23.36	0.02	0.08	0.26	0.27
85	53.14	207.30	23.35	23.35	0.02	0.08	0.26	0.27
89	59.70	200.13	23.40	23.40	0.00	0.08	0.26	0.27
92	50.96	209.68	23.34	23.34	0.03	0.08	0.26	0.27
95	69.37	189.56	23.55	23.55	-0.03	0.08	0.16	0.18
96	53.62	206.77	23.35	23.35	0.02	0.08	0.26	0.27
97	53.23	207.20	23.35	23.35	0.02	0.08	0.26	0.27
98	63.00	196.52	23.44	23.44	-0.01	0.08	0.16	0.18
99	52.21	208.31	23.35	23.35	0.03	0.08	0.26	0.27
100	59.73	200.10	23.40	23.40	0.00	0.08	0.26	0.27
101	45.12	216.06	23.34	23.34	0.05	0.08	0.26	0.27
102	44.39	216.85	23.34	23.34	0.06	0.08	0.26	0.27
107	31.37	231.08	23.44	23.44	0.10	0.08	0.26	0.27
114	37.62	224.25	23.38	23.38	0.08	0.08	0.26	0.27
122	49.25	211.54	23.34	23.34	0.04	0.08	0.26	0.27
126	30.14	232.42	23.46	23.46	0.11	0.08	0.26	0.27
130	30.24	232.31	23.46	23.46	0.11	0.08	0.26	0.27
131	62.50	197.07	23.44	23.44	-0.01	0.08	0.16	0.18
132	73.08	185.51	23.62	23.62	-0.05	0.08	0.16	0.18
133	77.83	180.32	23.74	23.74	-0.06	0.08	0.16	0.18
134	45.50	215.64	23.34	23.34	0.05	0.08	0.26	0.27
135	35.82	226.22	23.39	23.39	0.09	0.08	0.26	0.27
136	44.33	216.92	23.34	23.34	0.06	0.08	0.26	0.27
137	30.14	232.42	23.46	23.46	0.11	0.08	0.26	0.27
138	45.54	215.60	23.34	23.34	0.05	0.08	0.26	0.27
139	30.20	232.36	23.46	23.46	0.11	0.08	0.26	0.27
140	36.32	225.67	23.39	23.39	0.08	0.08	0.26	0.27
142	50.25	210.45	23.34	23.34	0.03	0.08	0.26	0.27
146	42.50	218.92	23.35	23.35	0.06	0.08	0.26	0.27
150	38.12	223.70	23.37	23.37	0.08	0.08	0.26	0.27
151	31.84	230.56	23.44	23.44	0.10	0.08	0.26	0.27
152	34.33	227.84	23.41	23.41	0.09	0.08	0.26	0.27
153	27.12	235.72	23.51	23.51	0.12	0.08	0.26	0.27
154	40.69	220.90	23.35	23.35	0.07	0.08	0.26	0.27
155	35.78	226.26	23.39	23.39	0.09	0.08	0.26	0.27
156	36.41	225.57	23.39	23.39	0.08	0.08	0.26	0.27
157	48.02	212.89	23.34	23.34	0.04	0.08	0.26	0.27
158	32.34	230.02	23.43	23.43	0.10	0.08	0.26	0.27
159	48.82	212.01	23.34	23.34	0.04	0.08	0.26	0.27
160	39.90	221.76	23.36	23.36	0.07	0.08	0.26	0.27
166	32.86	229.45	23.42	23.42	0.10	0.08	0.26	0.27

Table A.8. Elemental composition and log-ratios of the core MAR005 at 1 cm resolution.

Depth (cm)	Br	Ca	S	Zn	Inc	Coh	ln(Br/Zn)	ln(Ca/Zn)	ln(S/Zn)	ln(Inc/coh)
0	19.860	1193.872	176.796	25.690	3316.679	3766.844	-0.257	3.839	1.929	0.880
1	15.720	813.349	132.304	20.160	3189.110	3665.198	-0.249	3.697	1.881	0.870
2	22.460	1308.071	162.786	26.020	3518.237	3831.700	-0.147	3.917	1.834	0.918
3	29.200	1372.754	184.031	32.730	3614.387	3789.552	-0.114	3.736	1.727	0.954
4	24.660	1405.219	173.018	30.590	3590.913	3911.465	-0.215	3.827	1.733	0.918
5	26.510	1753.505	220.391	32.770	3670.680	3874.749	-0.212	3.980	1.906	0.947
6	27.410	1820.613	221.628	35.020	3749.112	3954.885	-0.245	3.951	1.845	0.948
7	25.240	1724.838	231.005	30.880	3683.924	3805.325	-0.202	4.023	2.012	0.968
8	24.730	1691.834	208.447	29.690	3570.489	3832.797	-0.183	4.043	1.949	0.932
9	25.020	1785.519	210.567	33.010	3643.178	3867.199	-0.277	3.991	1.853	0.942
10	25.970	1695.583	166.052	34.030	3612.221	3753.358	-0.270	3.909	1.585	0.962
11	24.030	1580.383	145.844	32.680	3554.575	3796.119	-0.307	3.879	1.496	0.936
12	28.950	1482.574	170.991	32.280	3703.102	3817.493	-0.109	3.827	1.667	0.970
13	24.390	1815.349	213.263	38.720	3661.727	3944.820	-0.462	3.848	1.706	0.928
14	26.140	1651.333	222.021	35.320	3668.012	3875.465	-0.301	3.845	1.838	0.946
15	24.200	1353.071	206.152	33.250	3549.131	3740.284	-0.318	3.706	1.825	0.949
16	25.160	1317.403	236.702	32.240	3806.516	3913.617	-0.248	3.710	1.994	0.973
17	22.610	1577.284	255.902	32.410	3804.800	3876.710	-0.360	3.885	2.066	0.981
18	25.570	2036.635	502.313	36.650	3795.152	3979.609	-0.360	4.018	2.618	0.954
19	28.180	1798.212	355.579	38.030	3860.187	3987.851	-0.300	3.856	2.235	0.968
20	25.740	1591.735	433.155	34.270	3907.612	3994.211	-0.286	3.838	2.537	0.978
21	21.740	2138.541	874.030	33.350	3848.889	3980.308	-0.428	4.161	3.266	0.967
22	14.360	2030.781	568.819	39.730	3721.235	4022.807	-1.018	3.934	2.661	0.925
23	11.700	1535.296	383.865	35.180	3571.952	3770.229	-1.101	3.776	2.390	0.947
24	19.960	2717.591	1449.963	34.110	3760.623	3820.098	-0.536	4.378	3.750	0.984
25	32.110	2613.209	1577.461	34.590	3903.392	3822.843	-0.074	4.325	3.820	1.021
26	57.160	1528.000	794.857	27.740	4743.901	4119.549	0.723	4.009	3.355	1.152
27	57.550	1095.774	1054.382	24.270	4502.407	4060.186	0.863	3.810	3.771	1.109
28	60.680	900.372	865.064	24.590	4345.158	3895.067	0.903	3.600	3.560	1.116
29	27.300	1151.572	645.099	31.510	3696.360	3797.870	-0.143	3.599	3.019	0.973
30	21.400	1469.280	503.195	42.180	3628.592	3912.206	-0.679	3.551	2.479	0.928
31	19.640	1556.324	320.110	35.510	3535.170	3880.564	-0.592	3.780	2.199	0.911
32	16.340	1378.570	240.944	35.060	3538.358	3894.874	-0.763	3.672	1.928	0.908
33	14.640	1827.238	269.274	35.410	3595.232	3972.868	-0.883	3.944	2.029	0.905
34	16.180	1757.658	232.492	36.560	3526.516	3851.507	-0.815	3.873	1.850	0.916
35	16.270	1552.840	222.208	34.050	3528.611	3885.607	-0.739	3.820	1.876	0.908
36	18.130	1683.793	240.737	36.060	3580.180	3965.961	-0.688	3.844	1.899	0.903
37	25.960	1670.189	256.263	34.500	3511.386	3896.195	-0.284	3.880	2.005	0.901
38	22.010	1306.590	213.050	32.830	3557.292	3894.110	-0.400	3.684	1.870	0.914
39	20.120	1469.984	218.008	31.330	3167.436	3498.849	-0.443	3.848	1.940	0.905
40	17.840	1391.853	343.699	30.280	3346.948	3933.672	-0.529	3.828	2.429	0.851
41	18.680	1400.850	354.925	29.990	3362.230	3740.098	-0.473	3.844	2.471	0.899
42	15.190	1421.061	306.417	28.130	3429.196	3802.265	-0.616	3.922	2.388	0.902
43	17.060	1432.756	250.621	29.260	3137.228	3705.185	-0.539	3.891	2.148	0.847
44	20.890	1736.309	271.380	33.570	3375.919	3837.269	-0.474	3.946	2.090	0.880
45	28.665	1393.580	394.272	31.810	3715.283	3914.007	-0.104	3.780	2.517	0.949
46	33.870	1456.147	574.271	32.650	3828.078	3967.836	0.037	3.798	2.867	0.965
47	24.320	1805.010	643.089	36.195	3642.834	3872.639	-0.398	3.909	2.877	0.941
48	16.795	1444.892	322.442	30.335	3349.288	3806.921	-0.591	3.863	2.364	0.880
49	17.780	1814.807	289.861	38.480	3709.100	3937.722	-0.772	3.854	2.019	0.942
50	17.810	1514.865	358.470	36.600	3722.501	4152.815	-0.720	3.723	2.282	0.896
51	14.640	795.214	358.283	23.470	3084.685	3862.281	-0.472	3.523	2.726	0.799
52	16.950	1123.721	366.598	30.410	3316.371	3948.173	-0.585	3.610	2.489	0.840
53	16.310	1153.542	358.709	28.350	3191.537	3863.928	-0.553	3.706	2.538	0.826
54	15.800	989.924	187.233	27.810	3124.805	3901.226	-0.565	3.572	1.907	0.801
55	16.800	1150.299	378.266	30.740	3302.431	3932.608	-0.604	3.622	2.510	0.840
56	16.690	893.513	326.991	27.300	3179.700	3890.727	-0.492	3.488	2.483	0.817
57	11.490	453.954	183.622	19.840	3003.240	3778.474	-0.546	3.130	2.225	0.795
58	13.150	455.483	266.553	18.180	3294.949	3629.565	-0.324	3.221	2.685	0.908
59	22.640	1697.905	1145.876	25.740	3750.356	3834.912	-0.128	4.189	3.796	0.978
60	18.740	2249.289	1172.176	39.300	3766.970	4023.299	-0.741	4.047	3.395	0.936
61	28.050	2430.061	1107.391	38.080	3828.277	3902.991	-0.306	4.156	3.370	0.981
62	33.980	1857.020	1040.039	39.350	4018.554	4065.510	-0.147	3.854	3.275	0.988
63	28.570	1913.493	978.141	41.850	3890.324	4063.197	-0.382	3.823	3.152	0.957
64	24.470	3057.417	1705.614	42.280	3818.280	3987.090	-0.547	4.281	3.697	0.958
65	21.740	1710.481	856.287	38.820	3575.029	3755.770	-0.580	3.786	3.094	0.952
66	21.890	2384.179	1378.291	40.170	4039.663	3982.502	-0.607	4.083	3.535	1.014
67	43.400	3015.488	1833.280	31.850	4694.951	4127.973	0.309	4.550	4.053	1.137
68	46.630	2870.494	1852.942	31.690	4622.001	4011.123	0.386	4.506	4.069	1.152
69	38.500	5006.824	3339.789	31.280	4517.688	4047.388	0.208	5.076	4.671	1.116
70	45.230	4742.018	3019.163	25.430	4758.777	4130.906	0.576	5.228	4.777	1.152
71	27.650	3191.155	1931.136	33.710	4111.791	4071.544	-0.198	4.550	4.048	1.010
72	23.920	1776.106	521.733	35.710	3574.561	3765.759	-0.401	3.907	2.682	0.949
73	19.800	2087.017	613.447	37.370	3696.383	3888.814	-0.635	4.023	2.798	0.951
74	21.320	4143.142	2398.860	37.130	3746.852	4035.849	-0.555	4.715	4.168	0.928
75	21.380	2290.951	906.723	31.130	3636.895	3860.899	-0.376	4.299	3.372	0.942
76	17.950	2690.543	1111.592	33.720	3812.794	3965.696	-0.631	4.379	3.495	0.961
77	18.850	5016.884	3177.107	34.410	3636.068	3976.621	-0.602	4.982	4.525	0.914
78	18.560	5407.273	3343.403	35.890	3718.418	3935.524	-0.659	5.015	4.534	0.945
79	17.400	3434.383	1709.326	36.140	3710.390	3901.015	-0.731	4.554	3.856	0.951
80	17.820	5270.898	3338.410	36.260	3596.100	3869.174	-0.710	4.979	4.523	0.929
81	22.250	4347.314	2760.355	37.520	3768.822	3907.503	-0.523	4.752	4.298	0.965
82	20.980	2833.238	1191.229	33.650	3539.272	3743.247	-0.472	4.433	3.567	0.946
83	23.360	4665.149	3243.105	34.860	3756.256	3896.503	-0.400	4.897	4.533	0.964
84	24.380	4741.604	2641.705	34.740	3767.326	3969.801	-0.354	4.916	4.331	0.949
85	19.990	3065.380	1364.512	37.530	3655.704	3936.021	-0.630	4.403	3.593	0.929
86	32.050	2608.247	955.059	32.480	3830.523	3968.857	-0.013	4.386	3.381	0.965
87	22.080	2586.009	1210.724	34.290	3520.256	3917.505	-0.440	4.323	3.564	0.899
88	25.390	2694.585	1073.822	36.910	3663.124	3838.766	-0.374	4.291	3.370	0.954
89	18.210	3591.658	1553.105	38.290	3763.972	4025.793	-0.743	4.541	3.703	0.935
90	19.850	2244.747	1363.161	35.325	3633.849	3821.256	-0.576	4.152	3.653	0.951

Table A.8. (continued).

91	30.505	2268.828	1610.341	29.785	3944.360	3840.519	0.024	4.333	3.990	1.027
92	18.700	1580.704	1052.104	29.580	3594.647	3850.833	-0.459	3.979	3.571	0.933
93	10.815	810.485	475.810	31.895	3328.377	3723.580	-1.082	3.235	2.703	0.894
94	10.110	1112.528	581.764	26.530	3702.007	3882.935	-0.965	3.736	3.088	0.953
95	13.290	1784.916	1008.706	29.170	3919.466	4040.763	-0.786	4.114	3.543	0.970
96	12.210	1953.110	869.818	35.430	3788.452	3924.466	-1.065	4.010	3.201	0.965
97	11.190	1763.610	802.504	38.810	3993.226	4054.098	-1.244	3.816	3.029	0.985
98	22.630	1337.481	1079.126	31.700	4093.016	3999.564	-0.337	3.742	3.528	1.023
99	20.570	1137.915	1249.524	36.980	4270.210	4136.073	-0.587	3.427	3.520	1.032
100	19.990	1155.154	1162.963	38.490	4284.026	4128.244	-0.655	3.402	3.408	1.038
101	22.880	1317.105	1190.938	35.880	4236.066	4240.359	-0.450	3.603	3.502	0.999
102	21.270	1234.420	1307.803	30.690	4165.379	3936.325	-0.367	3.694	3.752	1.058
103	20.330	1195.722	955.831	27.860	4295.328	4022.594	-0.315	3.759	3.535	1.068
104	22.770	1012.589	828.548	33.930	4019.633	4106.435	-0.399	3.396	3.195	0.979
105	25.320	967.682	734.538	31.990	3996.688	4032.690	-0.234	3.409	3.134	0.991
106	26.280	1123.047	867.832	32.620	3989.792	4014.043	-0.216	3.539	3.281	0.994
107	31.060	1176.674	738.815	33.410	4209.373	4016.158	-0.073	3.562	3.096	1.048
108	30.740	1396.536	904.405	33.810	4359.795	4033.848	-0.095	3.721	3.287	1.081
109	23.030	1202.530	942.299	33.570	4167.697	3940.093	-0.377	3.579	3.335	1.058
110	32.530	1001.411	782.072	28.960	5120.676	4238.660	0.116	3.543	3.296	1.208
111	28.310	1054.322	605.897	31.520	4313.092	3921.682	-0.107	3.510	2.956	1.100
112	26.050	1111.546	615.636	34.530	4203.613	4091.740	-0.282	3.472	2.881	1.027
113	21.800	825.684	685.154	28.150	4162.728	3896.707	-0.256	3.379	3.192	1.068
114	18.780	1006.554	943.250	34.440	4100.617	3901.075	-0.606	3.375	3.310	1.051
115	19.180	1073.992	1000.776	34.970	3968.173	4007.390	-0.601	3.425	3.354	0.990
116	19.210	1068.322	1172.985	36.440	4032.530	4104.707	-0.640	3.378	3.472	0.982
117	27.450	1008.237	1308.643	37.520	4236.240	4124.676	-0.313	3.291	3.552	1.027
118	20.150	881.141	1241.878	32.250	4324.059	4101.710	-0.470	3.308	3.651	1.054
119	18.510	1225.405	1328.449	37.250	4184.142	4016.178	-0.699	3.493	3.574	1.042
120	16.021	1205.540	1639.236	35.206	3855.348	3778.788	-0.787	3.533	3.841	1.020
121	15.400	1103.416	1394.994	36.770	4174.004	4049.196	-0.870	3.401	3.636	1.031
122	16.010	1031.532	1551.271	27.630	3918.556	3876.646	-0.546	3.620	4.028	1.011
123	15.510	901.282	940.837	32.120	3856.897	4010.235	-0.728	3.334	3.377	0.962
124	20.420	973.010	906.776	31.270	3732.320	3911.318	-0.426	3.438	3.367	0.954
125	16.070	875.877	730.596	31.760	3691.976	3984.824	-0.681	3.317	3.136	0.927
126	18.500	1089.182	1182.284	36.960	4100.075	4119.709	-0.692	3.383	3.465	0.995
127	20.450	1130.767	1281.038	32.560	4175.437	4031.624	-0.465	3.548	3.672	1.036
128	19.190	980.061	1145.937	35.500	3839.849	3919.187	-0.615	3.318	3.474	0.980
129	21.570	1206.872	1054.729	38.810	3956.048	3982.522	-0.587	3.437	3.302	0.993
130	18.250	1245.165	1238.028	33.360	4111.092	4118.181	-0.603	3.620	3.614	0.998
131	32.310	883.395	1004.056	32.560	4332.359	4098.085	-0.008	3.301	3.429	1.057
132	36.710	1035.158	1492.035	36.720	4307.630	4012.765	0.000	3.339	3.705	1.073
133	31.120	1240.818	1076.304	32.025	4331.482	4033.741	-0.029	3.657	3.515	1.074
134	30.630	1237.207	983.321	34.320	4267.828	4053.572	-0.114	3.585	3.355	1.053
135	36.680	1278.276	972.682	34.505	4124.660	4036.104	0.061	3.612	3.339	1.022
136	32.405	967.636	859.580	28.555	4675.222	4076.498	0.126	3.523	3.405	1.147
137	26.245	985.193	732.051	24.380	4900.700	4067.327	0.074	3.699	3.402	1.205
138	20.555	753.132	405.148	20.435	4218.776	3799.732	0.006	3.607	2.987	1.110
139	23.130	1424.125	679.637	32.160	4064.564	3998.869	-0.330	3.791	3.051	1.016
140	22.800	1185.801	415.611	33.040	3757.226	3990.007	-0.371	3.580	2.532	0.942
141	25.300	1631.426	399.571	36.800	3804.306	4014.534	-0.375	3.792	2.385	0.948
142	27.960	1580.195	352.007	35.470	3685.638	3860.371	-0.238	3.797	2.295	0.955
143	23.840	1471.165	331.265	36.260	3792.027	4022.367	-0.419	3.703	2.212	0.943
144	20.930	1543.528	335.351	33.830	3656.367	3823.818	-0.480	3.820	2.294	0.956
145	20.020	1449.462	349.413	35.310	3809.391	4065.633	-0.567	3.715	2.292	0.937
146	22.110	1641.991	396.467	34.340	3816.806	3960.253	-0.440	3.867	2.446	0.964
147	19.880	1337.890	332.458	32.930	3646.403	3877.395	-0.505	3.704	2.312	0.940
148	16.890	1463.573	297.602	35.820	3741.963	3916.365	-0.752	3.710	2.117	0.955
149	20.010	1710.563	375.489	36.370	3766.049	4012.699	-0.598	3.851	2.334	0.939
150	18.030	1769.922	426.244	37.330	3748.403	4009.624	-0.728	3.859	2.435	0.935
151	20.320	1486.485	351.031	32.990	3684.462	4017.876	-0.485	3.808	2.365	0.917
152	15.090	1256.197	251.948	31.120	3450.783	3921.841	-0.724	3.698	2.091	0.880
153	15.920	1076.918	222.036	29.020	3351.421	3921.844	-0.600	3.614	2.035	0.855
154	12.780	900.382	202.894	23.750	3165.296	3735.334	-0.620	3.635	2.145	0.847
155	11.060	1597.769	322.112	28.000	2901.654	3829.956	-0.929	4.044	2.443	0.758
156	10.380	1968.183	341.795	26.710	3092.022	3901.256	-0.945	4.300	2.549	0.793
157	8.990	1640.655	270.581	23.940	2749.704	3925.110	-0.979	4.227	2.425	0.701
158	13.290	889.679	158.607	24.870	3171.475	3882.068	-0.627	3.577	1.853	0.817
159	12.580	943.372	144.550	26.270	3289.870	3864.871	-0.736	3.581	1.705	0.851
160	14.120	1356.331	147.974	33.160	3484.573	3984.971	-0.854	3.711	1.496	0.874
161	15.880	1408.045	163.190	31.990	3563.646	3982.673	-0.700	3.785	1.629	0.895
162	12.150	1326.738	277.136	30.900	3514.860	3976.204	-0.933	3.760	2.194	0.884
163	11.140	1173.803	148.990	28.600	3293.734	4009.022	-0.943	3.715	1.650	0.822
164	9.690	1169.897	151.192	27.690	3328.633	3918.273	-1.050	3.744	1.697	0.850
165	9.050	871.687	98.033	22.830	3157.536	3940.101	-0.925	3.642	1.457	0.801
166	9.520	912.216	92.072	26.230	3197.512	3876.139	-1.014	3.549	1.256	0.825
167	8.030	972.628	83.365	24.380	3146.148	3914.647	-1.111	3.686	1.229	0.804
168	9.020	1292.689	105.513	28.330	3212.286	4004.078	-1.144	3.821	1.315	0.802
169	5.820	1249.789	85.701	28.460	3115.525	3917.885	-1.587	3.782	1.102	0.795
170	7.670	1611.066	85.737	33.190	3451.039	4010.354	-1.465	3.882	0.949	0.861
171	7.920	1668.942	70.468	34.470	3546.798	3999.892	-1.471	3.880	0.715	0.887
172	9.050	1789.128	83.996	32.960	3225.449	3631.386	-1.293	3.994	0.935	0.888
173	8.780	1981.609	81.474	35.630	3545.665	4053.186	-1.401	4.018	0.827	0.875
174	6.900	1554.559	62.254	29.690	3410.828	3967.431	-1.459	3.958	0.740	0.860
175	6.550	1474.651	67.980	32.080	3397.864	3936.721	-1.589	3.828	0.751	0.863
176	7.710	1672.038	72.735	31.140	3322.130	4022.004	-1.396	3.983	0.848	0.826
177	5.560	1455.604	76.479	26.110	3084.422	3961.385	-1.547	4.021	1.075	0.779
178	4.810	1193.080	70.338	24.870	2925.052	4027.526	-1.643	3.871	1.040	0.726
179	5.360	1253.551	53.052	25.410	2942.080	4026.725	-1.556	3.899	0.736	0.731

Table A. 9. Downcore concentrations of ^{137}Cs

Depth (cm)	Cs-137 (mBq g-1)	Error (1σ) (mBq g-1)
4	0.008	0.008
12	0.006	0.006
20	0.600	0.661
28	0.091	0.848
32	0.373	0.803
36	0.634	0.324
40	0.542	0.210
44	0.556	0.200
48	0.357	0.880
52	0.695	0.242
56	0.073	1.159
60	0.969	0.247
64	1.249	0.866
66	0.664	0.945
68	1.788	0.988
70	0.579	1.273
72	1.578	1.221
76	1.472	0.796
80	0.694	1.048
88	0.295	0.525
100	0.006	0.006
108	0.004	0.004

Figure A.1. Example of material sampled from the Core MAR005 for radiocarbon dating. A to C) different types of leaf fragments. D) Different types of seed.

A)

B)

C)

D)

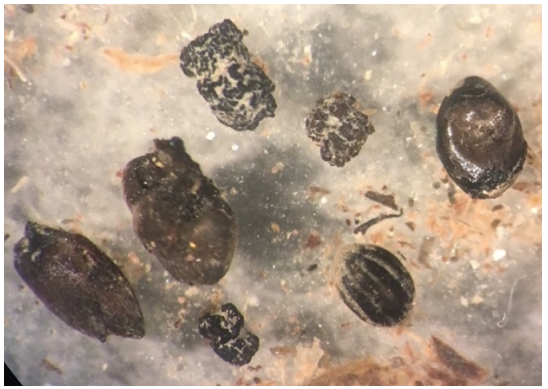

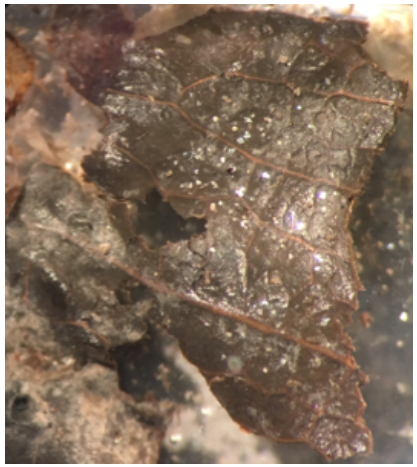

Script. 1. Input in OxCal to build the age-depth model of Chapter 2 and identify the year 1995 AD in core MAR005.

```
Plot()
{
};
P_Sequence ("", 10, 1)
{Boundary ("Base")
 { };
  C_Date ("137-Cs",1963,1){z=68;};
  C_Date ("Top surface",2018,1){z=0.5;};
  Boundary ("Top")
  {};
};
```

Script. 2. Input in OxCal to build the age-depth model of Chapter 3.

```
Plot()
{
Curve(“Bomb”,"Bomb21NH2.14c");
Curve ("Atmospheric","intcal20.14c");
Mix_Curves(“Mixed”,"Bomb", "Atmospheric", U(0,100));
P_Sequence ("", 0.05)
{Boundary ("Contact A MAR005") {  };
R_Date("SUERC-90544", 126, 37){z=155.5;};
Boundary ("Contact B MAR005") {z=136;};
R_Date("Beta - 535426", 190, 30){z=129.5;};
R_F14C("SUERC-90543", 1.0063, 0.0047){ z=99.5;};
Boundary ("Contact C MAR005") {z=99;};
R_F14C("SUERC-90542", 1.0051, 0.0046) { z=98.5;};
Boundary ("Contact D MAR005") {z=71;};
R_F14C("SUERC-90541", 1.3156, 0.0061){z=68.5;};
C_Date ("137-Cs",1963,1){z=68;};
R_F14C("SUERC-90540", 1.249, 0.0058){z=67;};
C_Date ("Contact E MAR005", 1995,1) {z=28;};
C_Date ("Top surface",2018,1){z=0;};
Boundary ("Top"){ z = 0};
```

```
    };
    };
```

Table A.10. Output of the P_sequence age-depth model from OxCal for Chapter 2 to identify the depth corresponding to the 1995 earthquake.

Depth (cm)	Modelled age (cal. AD)					Sed. Rate
	mu	sigma	median	from (2-sigma)	to (2-sigma)	(cm/yr)
0	2018	1	2018	2015	2020	1.23
1	2018	2	2018	2011	2023	1.23
2	2017	2	2017	2011	2021	1.23
3	2015	2	2014	2011	2021	1.23
4	2014	2	2014	2009	2021	1.23
5	2014	1	2014	2009	2018	1.23
6	2013	1	2014	2008	2018	1.23
7	2013	2	2013	2006	2018	1.22
8	2012	2	2012	2006	2016	1.23
9	2010	2	2009	2006	2016	1.23
10	2009	2	2009	2004	2016	1.23
11	2009	1	2009	2004	2013	1.23
12	2008	1	2009	2004	2013	1.23
13	2008	2	2008	2001	2013	1.23
14	2007	2	2007	2001	2011	1.24
15	2006	2	2005	2001	2011	1.23
16	2004	2	2004	1999	2011	1.23
17	2004	1	2004	1999	2010	1.23
18	2003	1	2004	1998	2008	1.23
19	2003	2	2003	1996	2008	1.24
20	2002	2	2003	1996	2008	1.23
21	2001	3	2001	1995	2006	1.23
22	2000	2	1999	1994	2006	1.23
23	1999	1	1999	1994	2006	1.23
24	1999	1	1999	1992	2005	1.23
25	1998	2	1998	1991	2003	1.22
26	1997	2	1997	1991	2003	1.23
27	1996	3	1996	1991	2001	1.23
28	1995	2	1994	1990	2001	1.23
29	1994	2	1993	1989	2001	1.23
30	1994	1	1994	1986	1999	1.24
31	1993	2	1993	1986	1998	1.23
32	1992	2	1993	1986	1998	1.22
33	1991	3	1990	1986	1997	1.23
34	1990	2	1989	1984	1996	1.22
35	1989	2	1989	1984	1996	1.22
36	1989	1	1989	1983	1995	1.23
37	1988	1	1988	1981	1994	1.23
38	1987	2	1988	1981	1993	1.23
39	1986	3	1986	1981	1992	1.24
40	1985	2	1985	1980	1991	1.22
41	1984	2	1984	1979	1991	1.23
42	1984	1	1984	1979	1991	1.23
43	1983	1	1984	1976	1988	1.22
44	1983	2	1983	1976	1988	1.23
45	1981	2	1982	1976	1987	1.22
46	1980	2	1980	1975	1986	1.22
47	1979	2	1979	1974	1986	1.23
48	1979	1	1979	1974	1986	1.23
49	1978	1	1979	1971	1984	1.22
50	1978	2	1978	1971	1983	1.22
51	1977	2	1977	1971	1982	1.22
52	1975	2	1975	1970	1981	1.23
53	1974	2	1974	1969	1981	1.23
54	1974	1	1974	1969	1980	1.23
55	1973	1	1974	1968	1978	1.23
56	1973	2	1973	1966	1978	1.23
57	1972	2	1972	1966	1978	1.23
58	1970	2	1970	1965	1976	1.23
59	1969	2	1969	1964	1976	1.23
60	1969	1	1969	1964	1974	1.22
61	1968	1	1969	1964	1973	1.22
62	1968	2	1968	1961	1973	1.22
63	1967	2	1967	1961	1973	1.22
64	1966	2	1964	1961	1971	1.23
65	1964	2	1964	1959	1971	1.23
66	1964	1	1964	1959	1970	1.22
67	1963	1	1964	1960	1968	1.22
68	1963	1	1963	1960	1965	1.23

Table A. 11. Output of the P_sequence age-depth model from OxCal for core MAR005 in Chapter 3.

Depth (cm)	Modelled age (cal. AD)					Sed. Rate
	mu	sigma	median	from (2-sigma)	to (2-sigma)	(cm/yr)
0	2018	1	2018	2015	2020	1.25
1	2017	1	2017	2014	2019	1.25
2	2016	1	2016	2013	2018	1.25
3	2015	1	2015	2013	2018	1.25
4	2014	1	2014	2012	2017	1.25
5	2013	1	2013	2011	2016	1.25
6	2013	1	2013	2010	2015	1.25
7	2012	1	2012	2009	2014	1.25
8	2011	1	2011	2008	2013	1.25
9	2010	1	2010	2008	2013	1.25
10	2009	1	2009	2007	2012	1.25
11	2008	1	2008	2006	2011	1.25
12	2008	1	2008	2005	2010	1.25
13	2007	1	2007	2004	2009	1.25
14	2006	1	2006	2004	2009	1.25
15	2005	1	2005	2003	2008	1.25
16	2004	1	2004	2002	2007	1.25
17	2004	1	2004	2001	2006	1.25
18	2003	1	2003	2000	2005	1.25
19	2002	1	2002	1999	2004	1.25
20	2001	1	2001	1999	2004	1.25
21	2000	1	2000	1998	2003	1.25
22	1999	1	1999	1997	2002	1.25
23	1999	1	1999	1996	2001	1.25
24	1998	1	1998	1995	2000	1.25
25	1997	1	1997	1994	1999	1.25
26	1996	1	1996	1994	1999	1.25
27	1995	1	1995	1993	1998	1.25
28	1995	1	1995	1992	1997	1.25
29	1994	1	1994	1991	1996	1.25
30	1993	1	1993	1990	1996	1.25
31	1992	1	1992	1989	1995	1.25
32	1991	1	1991	1989	1995	1.25
33	1991	1	1991	1988	1994	1.25
34	1990	1	1990	1987	1994	1.25
35	1989	1	1989	1986	1993	1.25
36	1988	1	1988	1985	1992	1.25
37	1988	1	1987	1984	1992	1.25
38	1987	1	1987	1984	1991	1.25
39	1986	2	1986	1983	1991	1.25
40	1985	2	1985	1982	1990	1.25
41	1984	2	1984	1981	1990	1.25
42	1984	2	1983	1980	1989	1.26
43	1983	2	1983	1979	1989	1.26
44	1982	2	1982	1978	1988	1.26
45	1981	2	1981	1978	1987	1.26
46	1980	2	1980	1977	1987	1.26
47	1980	2	1979	1976	1986	1.26
48	1979	2	1979	1975	1986	1.26
49	1978	2	1978	1974	1985	1.26
50	1977	2	1977	1973	1985	1.26
51	1977	2	1976	1973	1984	1.26
52	1976	2	1975	1972	1983	1.26
53	1975	2	1975	1971	1983	1.26
54	1974	2	1974	1970	1982	1.26
55	1973	2	1973	1969	1982	1.26
56	1973	2	1972	1968	1981	1.26
57	1972	2	1971	1967	1981	1.26
58	1971	2	1971	1967	1980	1.26
59	1970	2	1970	1966	1980	1.26
60	1969	2	1969	1965	1979	1.26
61	1969	2	1968	1964	1978	1.26
62	1968	2	1967	1963	1978	1.26
63	1967	2	1967	1962	1977	1.26
64	1966	2	1966	1962	1977	1.26
65	1966	2	1965	1961	1976	1.26
66	1965	3	1964	1960	1976	1.26
67	1964	3	1964	1959	1975	1.26
68	1963	1	1963	1961	1965	1.46
69	1963	3	1963	1957	1968	2.98
70	1962	3	1962	1956	1968	3
71	1962	3	1962	1955	1968	3.02
72	1961	3	1961	1955	1968	3.02
73	1961	3	1961	1954	1967	3.03
74	1961	3	1961	1954	1967	3.03
75	1961	3	1960	1954	1967	3.03
76	1960	3	1960	1954	1966	3.04
77	1960	3	1960	1953	1966	3.04

Table A. 11. (continued)

78	1960	3	1959	1953	1966	3.04
79	1959	3	1959	1953	1965	3.05
80	1959	3	1959	1953	1965	3.05
81	1959	3	1959	1952	1965	3.05
82	1958	3	1958	1952	1964	3.06
83	1958	3	1958	1952	1964	3.06
84	1958	3	1958	1952	1964	3.07
85	1957	3	1957	1951	1963	3.07
86	1957	3	1957	1951	1963	3.07
87	1957	3	1957	1951	1963	3.08
88	1956	3	1957	1951	1962	3.08
89	1956	3	1956	1950	1962	3.08
90	1956	3	1956	1950	1962	3.09
91	1955	3	1956	1950	1961	3.09
92	1955	3	1955	1950	1961	3.09
93	1955	3	1955	1949	1961	3.1
94	1954	3	1955	1949	1960	3.1
95	1954	3	1955	1949	1960	3.11
96	1954	3	1954	1949	1960	3.11
97	1954	3	1954	1948	1959	3.11
98	1953	3	1954	1948	1959	3.12
99	1953	3	1953	1948	1959	2.7
100	1952	3	1952	1945	1958	0.988
101	1951	5	1952	1938	1958	0.987
102	1950	6	1951	1931	1958	0.985
103	1949	8	1951	1924	1958	0.984
104	1948	9	1950	1917	1958	0.982
105	1947	10	1950	1910	1957	0.981
106	1946	12	1949	1904	1957	0.979
107	1945	13	1949	1897	1957	0.978
108	1944	15	1948	1890	1957	0.976
109	1943	16	1948	1883	1957	0.975
110	1942	18	1947	1876	1957	0.973
111	1941	19	1947	1869	1957	0.972
112	1940	20	1946	1863	1957	0.97
113	1939	22	1946	1856	1957	0.969
114	1938	23	1945	1849	1957	0.967
115	1937	25	1945	1842	1956	0.966
116	1936	26	1944	1835	1956	0.964
117	1935	28	1944	1828	1956	0.963
118	1934	29	1943	1822	1956	0.961
119	1933	30	1943	1815	1956	0.96
120	1932	32	1942	1808	1956	0.958
121	1931	33	1942	1801	1956	0.956
122	1930	35	1941	1794	1956	0.955
123	1929	36	1941	1787	1956	0.953
124	1928	38	1940	1781	1956	0.952
125	1927	39	1940	1774	1955	0.95
126	1926	41	1939	1767	1955	0.949
127	1925	42	1939	1760	1955	0.947
128	1924	43	1938	1753	1955	0.946
129	1923	45	1938	1746	1955	0.944
130	1921	46	1937	1743	1955	0.906
131	1920	47	1936	1742	1955	0.832
132	1919	47	1935	1741	1955	0.757
133	1918	48	1935	1741	1955	0.682
134	1916	49	1934	1740	1955	0.607
135	1915	49	1933	1740	1955	0.533
136	1914	50	1932	1739	1955	0.458
137	1911	51	1930	1736	1954	0.458
138	1909	52	1927	1733	1954	0.458
139	1906	53	1925	1731	1953	0.458
140	1904	54	1923	1728	1953	0.458
141	1901	55	1921	1725	1952	0.458
142	1899	56	1918	1722	1952	0.458
143	1896	57	1916	1719	1951	0.458
144	1894	58	1914	1716	1951	0.458
145	1891	59	1911	1714	1950	0.458
146	1889	60	1909	1711	1950	0.458
147	1886	61	1907	1708	1949	0.458
148	1884	62	1905	1705	1949	0.458
149	1881	62	1902	1702	1948	0.458
150	1879	63	1900	1700	1948	0.458
151	1876	64	1898	1697	1947	0.458
152	1874	65	1895	1694	1947	0.458
153	1871	66	1893	1691	1946	0.458
154	1869	67	1891	1688	1946	0.458
155	1866	68	1889	1685	1945	0.458

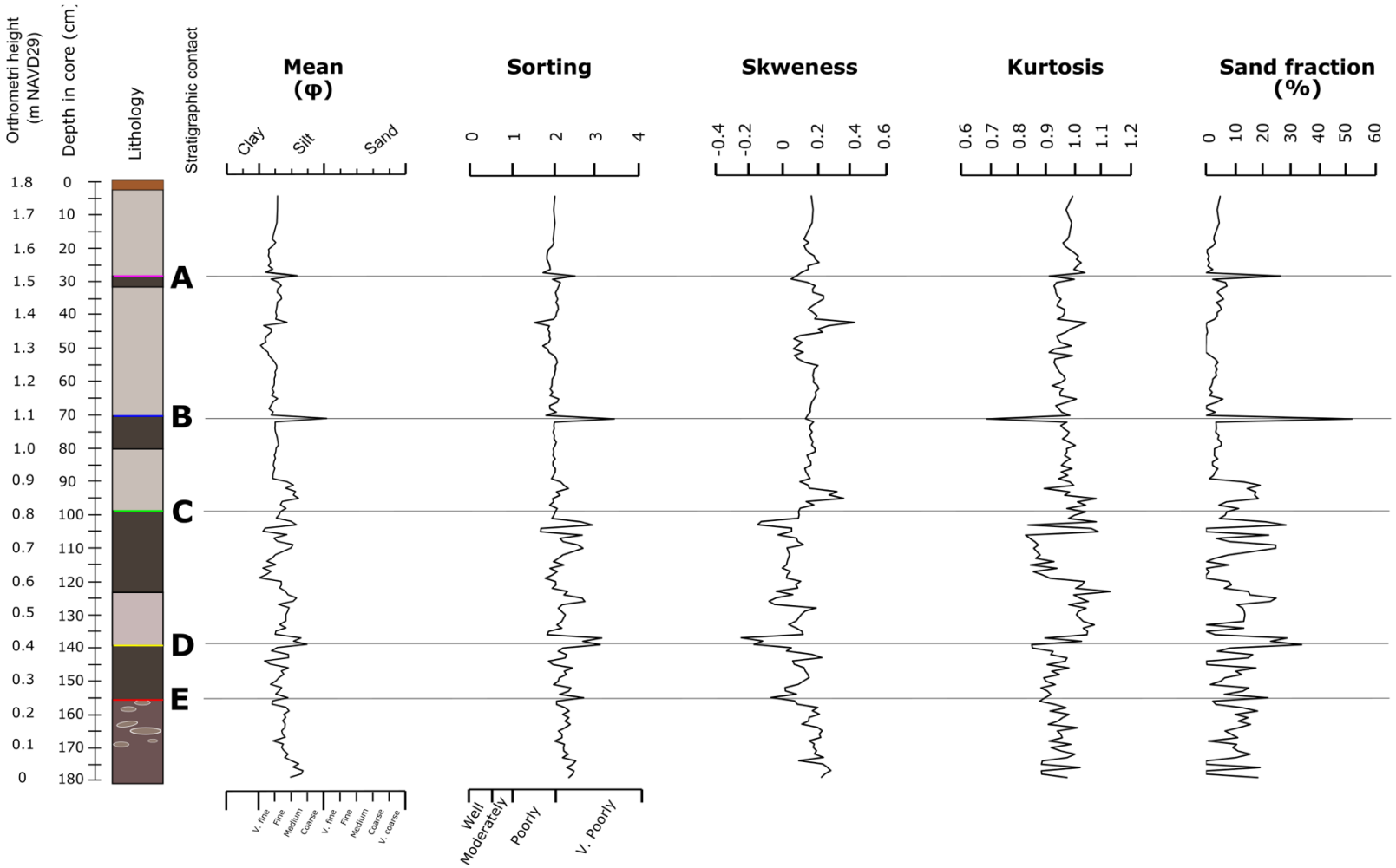

Figure A. 2. Sediment grain size parameters of the core MAR005.

Table A.12. Detailed core sediment descriptions of those boreholes sampled during the field campaign of 2019. Descriptions were based on the Troels-Smith (1955) classification of unconsolidated sediments. These boreholes correspond to those in Chapters 4.

Core name	Depth (cm)	Lithology	Throel-Smith description
MAR19001	0 - 80	Grey silty clay	Ag3, As1
19.151222°, -104.569389°	80 - 85	Organe silty clay	Ag2, As2
	85 - 129	Grey silty clay	Ag3, As1
	129 - 139	Grey clay	As4
	139 - 235	Grey silty clay with rootlets	Ag3, As1, Th+
	235 - 245	Grey silty clay	Ag3, As1
	245 - 252	Organic silty clay	Sh2, Ag1, As1
	252 - 266	Grey silty clay	Ag3, As1
	266 - 274	Peat	Sh2, Dh2
	274 - 284	Organic silty clay	Ag2, Sh1, As1, Dh+
	284 - 304	Peat	Sh2, Dh2, Th+
	304 - 306	Organic silty clay	Sh2, Ag1, As1
	306 - 319	Peat	Sh2, Th1, Dh1
	319 - 323	Grey silty clay	Ag2, As2
	329 - 333	Coarse sand	Ga3, Ag1
	333 - 339	Grey clay	As4
	339 - 357	Brown sandy mud	Ga2, Ag1, As1
MAR19002	0 - 27	Grey silty clay	Ag2, As2
19.150917°, -104.569222°	27 - 31	Orange silty clay	Ag3, As1
	31 - 90	Grey silty clay	Ag2, As2
	90 - 95	Orange silty clay	Ag3, As1
	95 -106	Grey silty clay	Ag2, As2
	106 - 147	Grey silt	Ag4, As+
	147 - 151	Grey clay	As4
	151 - 210	Grey silty clay with rootlets	Ag2, As2, Th+
	210 - 216	Grey silt	Ag4
	216 - 219	Coarse sand	Ga4, Ag+
	219 - 233	Grey silty clay	Ag2, As2
	233 - 245	Grey organic silt	Sh2, Ag12
	245 - 270	Peat	Sh2, Dh2, Th+
	270 - 275	Organic silt	Ag2, Sh2, As+
	275 - 306	Peat	Sh2, Dh1, Dl1, Th+
	306 - 308.5	Grey silty clay	Ag2, As2
	308.5 - 319	Peat	Sh2, Dl1, Dh1
	319 - 333	Grey clay	As4
	333 - 364	Brown sandy mud	Ga2, Ag1, As1
MAR19003	0 -75	Grey silty clay	Ag2, As2
19.150861°, -104.568889°	75 - 77	Orange silty clay	Ag3, As1
	77 - 103	Grey silty clay	Ag2, As2
	103 - 104	Orange silty clay	Ag3, As1
	104 - 122.5	Grey silty clay	Ag2, As2
	122.5 - 129	Grey clay	As4
	129 - 202	Grey silty clay with rootlets	Ag2, As2, Th+
	202 - 205	Grey silty clay	Ag2, As2
	205 - 214	Organic silty clay	Ag2, Th1, As1
	214 - 224	Grey silty clay	Ag2, As2
	224 - 235	Peat	Sh2, Dh1, Dl1, Th+
	235 - 245	Organic silty clay	Ag2, Sh1, As1
	245 - 259	Peat	Sh2, Dl1, Dh1
	259 - 287	Grey clay	As4
	287 - 302	Coarse sand	Ga4, Ag+

Table A.12 (Continued)

MAR19004	0 -98	Grey silty clay	Ag2, As2
19.150306, -104.56777	98 -103	Organge silty clay	Ag3, As1
	103 - 150	Grey silty clay	Ag2, As2
	150 - 158	Grey clay	Ag3, As1
	158 - 254	Grey silty clay with rootlets	Ag2, As2, Th+
	254 - 266	Grey silty clay	Ag2, As2
	266 - 285	Dark grey organic silty clay	Ag2, Sh1, As1
	285 - 288	Grey organic silt	Ag3, Sh1, As+
	288 - 295	Peat	Sh2, Dh2
	295 - 297	Grey silty clay	Ag3, As1
	297 - 317	Peat	Sh2, Dh2
	317 - 319	Grey silty clay	Ag2, As2
	319 - 330	Peat	Sh2, Dh1, Dl1
	330 - 335	Grey silty clay	Ag2, As2
	335 - 338	Peat	Sh2, Dl1, Dh1
	338 - 343	Grey clay	As4
	343 - 370	Brown sandy mud	Ga2, Ag1, As1
MAR19006	0 - 8	Grey silty clay	Ag2, As2
19.151167°, -104.569667°	8 - 11	Orange silty clay	Ag3, As1
	11 - 40	Grey silty clay	Ag2, As2
	40 - 65	Grey silt with rootlets	Ag2, As2, Th+
	65 - 111	Grey silty clay	Ag
	111 - 115	Orange silty clay	Ag3, As1
	115 - 122	Grey silty clay	Ag2, As2
	122 - 132	Grey clay	As4
	132 - 225	Grey silty clay with rootlets	Ag2, As2, Th+
	225 - 244	Grey silty clay	Ag2, As2
	244 - 262	Organic silt	Sh2, Ag2
	262 - 266	Grey silt	Ag3, As1
	266 - 285	Peat	Sh2, Dh2, Th+
	285 - 297	Grey silty clay with fine sand	Ag2, Ga1, As1
	297 - 308	Peat	Sh2, Dh2
	308 - 315	Grey silty clay with fine sand	Ag2, As1, ga1
	315 - 333	Peat	Sh2, Dl2, Dh1
	333 - 337	Organic silty clay	Ag2, Sh1, As1
	337 - 344	Peat	Sh2 Dh1, Dl1
	344 - 364	Clay	Ag4
	364 - 384	Brown sandy mud	Ga2, Ag1, As1
	384 - 408	Coarse sand with silt	Ga4, Ag+
	408 - 428	Brown sandy mud	Ga2, Ag1, As1
	428 - 432	Coarse sand	Ga4
	432 - 500	Sandy mud	Ga2, Ag2, As+
MAR19007	0 - 23	Grey silty clay	Ag2, As2
19.151556°, -104.569972°	23 - 27	Orange silty clay	Ag3, As1
	27 - 43	Grey silty clay	Ag2, As2
	43 - 47	Orange silty clay	Ag3, As1
	47 - 86	Grey silty clay with rootlets	Ag2, As2, Th+
	86 - 89	Organge silty clay	Ag3, As1
	89 - 136	Grey silty clay with rootlets	Ag2, As2, Th+
	136 - 146	Grey clay	As4
	146 - 223	Grey silt with rootlets	Ag4, Th+
	223 -235	Grey silt	Ag4
	235 - 244.5	Organic silt	Ag3, Sh1
	244.5 - 251	Grey silty clay	Ag2, As2
	251 - 268	Peat with silt	Sh2, Dh1, Ag1
	268 - 283	Grey silt with fine sand	Ag3, Ga1
	283 - 289	Peat	Sh2, Dh1, Th1
	289 - 298	Grey silty clay with fine sand	Ag2, As1, ga1
	298 - 330	Peat	Sh2, Dh1, Dl1
	330 - 337	Grey silty clay	Ag3, As1
	337 - 342	Peat with silt	Sh2, Dh1, Ag1, Dl+
	342 - 355	Grey clay	As4
	355 - 367	Brown sandy mud	Ga2, Ag1, As1
	367 - 375	Coarse sand with silt	Ga3, Ag1
	375 - 415	Brown sandy mud	Ga2, Ag1, As1
	415 - 417	Coarse sand	Ga4
	417 - 450	Brown sandy mud	Ga2, Ag2, As+

Table A. 13. Raw counts of fossil diatoms of the core MAR005.

Depth in core (cm) -->	235	236	237	238	239	240	241	242	243	244	245	246	247	248	249	250	251	257	258	259	260	261	262	263	264	265	266	267	268	269	276	277
Achnanthes angustata																																
Achnanthes brevipes						2		2															4		1							
Achnanthes brevipes var. intermedia								1											1										1			
Achnanthes clevei var. rostrata																													1	2		
Achnanthes delicatula																										1				1		
Achnanthes exigua	3	4	1		1	4	3			1	6	4	2	1			1		2				2	1					2	3	1	
Achnanthes inflata	2	1		1	2	6	1	5	1	2			1	5	7	3	4				1	3			3	2	5	6	1			
Achnanthes lanceolata var. rostrata																							1									
Achnanthes lorenziana																																
Achnanthes marginulata																							1			1						
Achnanthes parvula																																
Achnanthes promunturi																																
Achnanthes sp1																																
Achnanthidium exiguum																					1											
Achnanthidium minutissimum																							1									
Amphipora ornata																																
Amphipora gigantea																																
Amphora acustiuscula																																
Amphora affinis															1														1			
Amphora arenaria																																
Amphora bicapitata																																
Amphora clevei																																
Amphora coffeaeformis	3	3	4	2	5	2	6	3	2	3	2	2	9	1	5	2	2	2	4	1	3		1	3	1	2	2	1		7	3	
Amphora costata		1				1				2	2			1	1		1	1	2	2			1			2				2		
Amphora gigantea																																
Amphora proteus				4			1		1					1				2	2					1	1		1	3	3	2	2	
Amphora terroris																																
Astartiella punctifera																																
Aulacoseira sp1																																
Aulacoseira granulata																																
Austariella jamaicensis																										1	3					
Bacillaria paxillifer	21	4	24	13	17	12	12	39	51	11	4	8	25	17	18	20	12	8	3	13	8	27	14	5	9		4		9	11	2	
Bacillaria socialis																																
Biremis ambigua																															2	
Brevisira arentii																																
Caloneis aemula								3			7															1						
Caloneis bacillum	6	4	4		2	1	3	7	5	1	1	5	4	2	4	3	2		4		1	1	1					1	6	2		
Caloneis excentrica																			2													
Caloneis permagna																																
Caloneis sabanicola																																
Caloneis subsalsa																																
Caloneis westii																																
Caloneis sp1																																
Ceratulus californicus																																
Cocconeis convexa																												1				
Cocconeis fluviatilis													3																			
Cocconeis neodiminuta																																
Cocconeis pinnata							1							1											1	1	2	5	16	12	2	7	
Cocconeis placentula	2	8	6	10	9	8	3	2	6	4	8	6	4	14	20	20	19	8	8	4	3	10	5	9	11	18	10	15	21	19	4	
Cocconeis placentula var. euglypta	1	1				5		2	1	2		2	2	3	5	4	2	1	2				1				2	8		1	2	
Cocconeis placentula var. lineata																																
Conticribra weissflogii																																
Coscinodiscus radiatus																																
Craticula halophiliioides								1				2							1											1		
Cyclotella atomus	5		3	2			1	1					1	1	1			2	4	2	3	4	1		2					4		
Cyclotella cryptica																																
Cyclotella kuetzingiana																																
Cyclotella litoralis																										7		15	3	3		
Cyclotella meneghiniana	18	20	54	33	9	15	12	22	9	31	38	32	37	28	26	12	29	20	12	25	28	15	33	27	19	17	10	5	6	13	6	
Cyclotella ocellata																																

Table A.13 (Continued)

Depth in core (cm) -->	235	236	237	238	239	240	241	242	243	244	245	246	247	248	249	250	251	257	258	259	260	261	262	263	264	265	266	267	268	269	276	277
Cyclotella radiosa																																
Cyclotella striata		1	7	8	3	3	12	5		8	2	3	8	22	26	20	24	61	36	33	26	29	47	120	89	86	60	38	42	50	81	
Cyclotella stylorum																								1				3				
Cymbella laevis																													1			
Denticula kuetzingii										1			1																			
Denticula elegans				2																												
Denticula subtilis						1			2				5							1							2					
Diadesmis confervacea	3	4	4	3	3	1	6	2	7	3	4	4		4	3	6	5		1	4	1		3			1		1		3		
Diadesmis contenta																													2			
Diploneis boldtiana																																
Diploneis elliptica																														6		
Diploneis finnica													1																			
Diploneis fusca																												1				
Diploneis nitecens			1																													
Diploneis oculata																																
Diploneis ovalis																	1															
Diploneis pseudovalis																							1				1		1			
Diploneis papula																																
Diploneis parma																																
Diploneis puella				1			1											1				1	1		1	3		1	7		7	
Diploneis smithii																1										1	1		1	1	1	
Diploneis subovalis																						1										
Diploneis sp1.																																
Encyonema hebridicum																										1						
Encyonema montana																																
Encyonema prostratum																																
Encyonema silesianum					1	2				1		4		1	1				3									1				
Entomoneis paludosa																																
Eolimna ruttineri							2																									
Epithemia adnata	2				1	3		1	3	3	2		2			3	2		1	1		1		2		2		3	3		4	
Epithemia argus																		2														
Eunotia bidens																																
Eunotia flexuosa	7		1			1	3	2			2					1	2													1		
Eunotia formica	1						1	3		3		2	1										2		1	1				1	1	
Eunotia minor																																
Eunotia myrmica														1																		
Eunotia sp1																																
Fallacia auriculata					2		1											2														
Fallacia forcipata																			1								2					
Fragilaria goulardii	1	4		3	2	3		6	3	7	10	8	1	3	3	2	6	3	6	3	3	1		1	1	3	7	1	4	2		
Fragilaria famelica																			3		3	3										
Frustulia interposita																											1					
Gomphonema acuminatum																																
Gomphonema affine			1	1	1			1	3		3		1	1		1	4		3		2	2				1					2	
Gomphonema angustatum																																
Gomphonema gracile			1	2							2	1			1	1							1	7	1		1					
Gomphonema hebridense	2									2																		3				
Gomphonema parvulum	2	4	4	2	2	2	2	3	3	4	3	3	3	3	3	4	1	3	3	3	2	3					2	5			2	
Gomphonema subclavatum				2			1				4			1						2							3	1	5	2		
Grammatophora hamulifera																																
Grammatophora marina																																
Gyrosigma acuminatum								1														2							1			
Gyrosigma balticum																																
Gyrosigma lanceolatum		1																														
Halamphora acutiuscula	1	7	3	2	2	6	3	1		6	5	6		1								1					1	3		1		
Halamphora exigua								3																						1		
Halamphora holsatica																	3										1	2	5			
Halamphora latecostata											1																					
Halamphora sp1																																
Halamphora submontana																																

Table A.13 (Continued)

Depth in core (cm) -->	235	236	237	238	239	240	241	242	243	244	245	246	247	248	249	250	251	257	258	259	260	261	262	263	264	265	266	267	268	269	276	277
Hantzschia amphioxys	11	24		5	5	3	7	6	2	4	8	7	3	6	5	6	2	6	3	6	5	1	1	2		2	2	7	3	2		
Hantzschia virgata		1	2	1	1																									1		
Haslea britannica																														1		
Hippodonta hungarica				1				1		2				2			1			1			1		1		1					
Hyalosynedra laevigata																																
Karayevia amoena																																
Karayevia clevei																																
Kolbesia suchlandtii																																
Luticola goeppertiana												1													1							
Luticola Mutica	7	24	1	14	4	3	3	2	5	5	8	6	4	3	4	10	11	2	6	2	4		5	2	3	8	3	5	6	7		
Luticola mutica f. intermedia																																
Luticola sp1																																
Lyrella lyra																																
Lyrella lyroides																																
Mastogloia decipiens																																
Mastogloia lineata																														1		
Mastogloia apiculata																																
Melosira polaris																				1												
Navicula abunda																																
Navicula agatake																																
Navicula agnita																																
Navicula apta																																
Navicula cancellata	4	1	3	4	6	6	25	9	10	5	2	3	4	2		3	6		1		1	1							1		3	
Navicula cincta								1						2				2	3	2							2					
Navicula cryptocephala		3	2			1	1		2	2	1	1						1			1							1		1		
Navicula cryptocephala var veneta																																
Navicula cryptotenella			1									1								2												
Navicula directa																									1							
Navicula digitoradiata	1	2		1	3	3	2	3				2	1		1		2	1	2	3			1	1			3	1				
Navicula duerrenberginiana																																
Navicula eridrigiana																																
Navicula erifuga																																
Navicula exigua var. capitata																																
Navicula gregaria									1												1											
Navicula lanceolata																																
Navicula lanceolata var minima													1																			
Navicula longa									1								2													1		
Navicula menisculus																																
Navicula pennata		1			2	1				1	2	1		1	1							1	1	4			1	1			1	
Navicula peregrina		1																														
Navicula perminuta																														1		
Navicula pupula																																
Navicula radiosa				1					1			2		1	2		1														3	
Navicula recens																																
Navicula rostellata										1						4	7	2											2			
Navicula salinarum		1				1	3	1		2	1							2														
Navicula salinicola	3	5	1	1	2	2			1	2										1												
Navicula sp1																													1			
Navicula subrostellata		4	2	5	7	5	7	4	5	8		12	4	3	3			1		2					1							
Navicula tripunctata	4			1	2	1	6	1	4	2	3	3	4	2	1	1	1		1			1	1	3		1	2		1		6	
Navicula vimineoides							1		1																							
Navicula viridula var. rostellata																																
Nitzschia acicularis																						1										
Nitzschia amphibia	1						1		1			5			2				1								5					
Nitzschia angustata																																
Nitzschia bicapitata																																
Nitzschia brevissima																																
Nitzschia capitellata			2		6	5					1		4	3		1		2	1											1		
Nitzschia clausii			2																													
Nitzschia confinis	2						2	2		1	2		1	2		1		1	1	2										1		

Table A.13 (Continued)

Depth in core (cm) -->	235	236	237	238	239	240	241	242	243	244	245	246	247	248	249	250	251	257	258	259	260	261	262	263	264	265	266	267	268	269	276	277
Nitzschia dissipata			1							1			1			1	1	4		5	1		1								1	
Nitzschia distans									3																					2		
Nitzschia filiformis		3	2	2	9			1							1		2															
Nitzschia fluminensis																									1					1		
Nitzschia fonticola	5	5	4	2	4	7	4	4	8	7	5	2	4	6	4		1	1		1		12	12	1	1	3	12	4	3	4	1	
Nitzschia frustulum		1		3	8		2		4								1	1		2	1	2	6		2		1		4	3		
Nitzschia gracilis	6	8	4		6	15	9	5	5	17	10	5	1		1	4	2		4	8	6	2	3		1			1		2		
Nitzschia grossestriata	8	9	9	9	7	5	6	13	2	2	6	9	6	3	4	4	5	4	6	6	2	2	10	4	2	8		9	2	2		
Nitzschia hybrida																																
Nitzschia inconspicua																																
Nitzschia insignis					3													1	1			1		1		1						
Nitzschia intermedia																																
Nitzschia lanceolata						1																										
Nitzschia lanceolata var. minima																																
Nitzschia laevissima																																
Nitzschia linearis																										1		4		1		
Nitzschia microcephala	1							3																								
Nitzschia obtusa obtusa																																
Nitzschia palea		3			1				1	2	1					4	3							1	1	1	2				2	
Nitzschia panduriformis																																
Nitzschia parvula																																
Nitzschia pellucida									3					1																		
Nitzschia perminuta						1	2																									
Nitzschia plana																																
Nitzschia recta																									2							
Nitzschia scalaris	2				1							2				1								4	3		4					
Nitzschia scalpelliformis	1		1	5	6	7	1						1				2		1	4		1							1			
Nitzschia sicula																		2			1			1	2	2	1					
Nitzschia sigma			1	1	1		1	3	1	1			1	3					1		3	4	2			1	2	3	4	1	4	
Nitzschia sp1.																																
Nitzschia thermalis																	1															
Nitzschia vitrea								2	1																		3			1		
Opephora marina var. minuta				1																												
Opephora pacifica																																
Orthoseira roseana																										1						
Paralia sulcata	7	2	17	24	14	24	1	22	3	3	2	6	7	4	3	5	2	3	3	5	7	17	4		1			1			15	
Paralia sulcata var. biseriata																																
Paralia sulcata var. Radiata																																
Paralibellus rhombicus																																
Parlibellus calvus	5									1																1						
Petroneis sp1																																
Petroneis marina																																
Pinnularia acrosphaeria	1	4										1																	1			
Pinnularia biceps						1						1		1				1	1				1									
Pinnularia biceps var. minor					2																									6		
Pinnularia borealis	1	4									1	2		1	2													2				
Pinnularia certa	6	3	1	3	1					1	2		1		2	1		1			4	1		1	2	1						
Pinnularia gibba																			1	2	5							1				
Pinnularia incognita																																
Pinnularia joculata																1													1			
Pinnularia lattarea																																
Pinnularia microstauron																			3						1							
Pinnularia neomajor																																
Pinnularia obscura																																
Pinnularia sp1																																
Pinnularia streptoraphe var. parva																																
Pinnularia subcapitata																														1		
Pinnularia turgidula																																
Placoneis gastrum		4					1		3	2	2	1	1	1	2				4		2	2			2	3	4			1		
Placoneis hambergii													1	1		1													1		3	

Table A.13 (Continued)

Depth in core (cm) -->	235	236	237	238	239	240	241	242	243	244	245	246	247	248	249	250	251	257	258	259	260	261	262	263	264	265	266	267	268	269	276	277
Plankton iella sol																																
Planothidium delicatulum														1		1										1						
Planothidium frequentisimum		1		2			1			1	3		2		1			2	3	3	2			1	1							
Planothidium hauckianum	1	2	2			4			1		1				1								2		2	2						
Planothidium lanceolatum	1	2	1	1		2			1			1			3	1	2					1	2									
Pleurosigma salinarum																																
Podosira stelligera																																
Pseudogomphonema kamtschaticum																																
Rhopalodia acuminata																																
Rhopalodia constricta																																
Rhopalodia gibba				3	6	2	1	5	3	9	10	4	3		1	10	9	5	5			1	1	2		1				3		
Rhopalodia gibberula	5	3	8	6	14	4	5	5	4	6	7	7	16	7	6	6	5	4	4	5	20	10	6	7	15	14	4	8	3	2		
Rhopalodia musculus	3	2		2	3	2	7	1		3	1			3	7	7	9	9		6	4		1	10	7	3	1	3	3			
Rhopalodia pacifica																																
Sellaphora japponica																																
Sellaphora pupula	4	2	6	2	1	3		4	5	6	6	5	6	2	4	8	1		4	2	4			1	1	2			1	1	1	
Sellaphora guyanensis		3																														
Seminavis strigosa					1																									1		
Seminavis ventricosa													2				1															
Stauroneis amphibia									1	1			3																			
Stauroneis borrichii																				1												
Stauroneis producta					1																								1			
Staurophora salina																																
Staurophora wislouchii																																
Staurophora sp1																																
Staurosirella pinnata	1																						2									
Staurosirella lapponica																													2	1		
Stephanodiscus hantzschi																					2	1										
Stephanodiscus niagarae																																
Stephanodiscus parvus					1		1	2	2				2	1	2		3	9	2	4	7	2	7	1			5	3			5	
Synedra Goulardi																							1									
Synedra nana																									3							
Surirella fastuosa																									1	1	1					
Tabularia fasciculata	30	3	4	4	10	11	16	13	14	8	8	6	12	15	6	8	12	9	20	24	30	27	2	5	5		4			4	6	
Tabularia investiens																																
Tabularia parva																											3		10	3		
Tabularia persuadens																																
Thalassionema nitzschioides																														1		
Tryblionella accuminata							2																									
Tryblionella apiculata								1														1					1					
Tryblionella coarctata																																
Tryblionella compressa		1																2				1	2				6	8	5	3	13	
Tryblionella debilis		1																														
Tryblionella granulata																			1							2						
Tryblionella hungarica										2						2						1		1				1	1		1	
Tryblionella levidensis			2	2	2	2	2	2					1	2				1	1	1		2	4	5	1	1	3	11	8		12	
Tryblionella littoralis																											2	1				
Tryblionella persuadens																																
Ulnaria danica																				1									1	1		
Ulnaria acus var. angustissima	2	1	6			2	5	1	2	2	9	8		7	3	2	1	6	9	4	3	1										
Ulnaria Ulna	2	5	7	12	3	5	2	6	2	6	5	4	2	2	4	6	3		3	2									1		6	
Total counts	205	206	210	209	205	207	202	239	200	211	213	200	210	200	201	202	219	201	200	202	201	201	200	236	205	214	202	209	204	204	210	0

Table A.13 (Continued)

Depth in core (cm) -->	278	279	280	281	282	283	284	285	286	292	293	294	295	296	297	298	299	303	306	307	308	309	310	311	312	313	314	315	316	317	318	319
Achnanthes angustata																																
Achnanthes brevipes										1			4																			
Achnanthes brevipes var. intermedia																																
Achnanthes clevei var. rostrata																																
Achnanthes delicatula											1																					
Achnanthes exigua	1		2			1	4	2					2		1		1				1											
Achnanthes inflata							2								1			1			2					1						
Achnanthes lanceolata var. rostrata											2																					
Achnanthes lorenziana																																
Achnanthes marginulata										2							3															
Achnanthes parvula																																
Achnanthes promunturi																																
Achnanthes sp1																																
Achnanthidium exiguum			1																													
Achnanthidium minutissimum																																
Amphipora ornata																																
Amphipora gigantea																																
Amphora acustiuscula																																
Amphora affinis																																
Amphora arenaria																																
Amphora bicapitata																																
Amphora clevei																																
Amphora coffeaeformis	2	2	3		3	5	6	3	1				2	1	1	2		11	4		4	3	4	5	3	2	2		2			
Amphora costata			2			1		2	6					4	3			1	4	6	2	3		1		4				2	1	1
Amphora gigantea																									1							
Amphora proteus						1	1													1	1											
Amphora terraris			1																													
Astartiella punctifera																																
Aulacoseira sp1																																
Aulacoseira granulata																																
Austariella jamaicensis																																
Bacillaria paxillifer	10	9	10			13	8	7	6	10			21	21	9		5	3	4	1	5	11	4	4	4	12	11		2		2	2
Bacillaria socialis																																
Biremis ambigua	2	2	1																													
Brevisira arentii																																
Caloneis aemula																																
Caloneis bacillum					2	1												11					1					1				
Caloneis excentrica																																
Caloneis permagna																																
Caloneis sabanicola																																
Caloneis subsalsa																																
Caloneis westii																																
Caloneis sp1																																
Ceratulus californicus																																
Cocconeis convexa																																
Cocconeis fluviatilis																																
Cocconeis neodiminuta																																
Cocconeis pinnata	6	3			1		2	1								1			4	3	4	2	6	7	4	13	8	3	3	1	5	8
Cocconeis placentula	6	1	9		8	13	1	1	3	2			9	4	2	29	5	8	17	10	5	14	12	3	4	3	3		1	8	9	12
Cocconeis placentula var. euglypta	1	4	3		4	2	1	6						1	5			15	3		5	1	2	1	4							2
Cocconeis placentula var. lineata																																
Conticribra weissflogii																																
Coscinodiscus radiatus																																
Craticula halophiliioides			2																													
Cyclotella atomus			1		2		5	2	8	3	30		3					1								1				4	3	1
Cyclotella cryptica											3	8																				
Cyclotella kuetzingiana			9							3																						
Cyclotella litoralis			7						3	9	21		4	3			36	3	4	22	11	11	21	43	46	32	34	40				
Cyclotella meneghiniana	11	3	10		16	24	30	5	47	56	108	102	77	53	55	35	11	24	27	35	53	50	49	17	40	6	11	14	42	37	35	41
Cyclotella ocellata																																

Table A.13 (Continued)

Depth in core (cm) -->	278	279	280	281	282	283	284	285	286	292	293	294	295	296	297	298	299	303	306	307	308	309	310	311	312	313	314	315	316	317	318	319
Cyclotella radiosa										1			4																			
Cyclotella striata	65	30	22		28	15	43	28	27	14	38		36	18	50	115	150	6	52	66	28	26	36	23	14	6	4	76	104	107	60	42
Cyclotella stylorum										2																						
Cymbella laevis																																
Denticula kuetzingii			1													1																
Denticula elegans																							1									
Denticula subtilis									1																							
Diadesmis confervacea						1	2							4				4				2				1		1	1			
Diadesmis contenta							1		1												1	1			1							
Diploneis bolditiana																																
Diploneis elliptica			1				1																									
Diploneis finnica																																
Diploneis fusca																																
Diploneis nitecens																																
Diploneis oculata																																
Diploneis ovalis			2			1																										
Diploneis pseudovalis																					1											
Diploneis papula																					1				1							
Diploneis parma																																
Diploneis puella	7	1			1														3	3		4		2	2		2					
Diploneis smithii	1																							2	1							
Diploneis subovalis																																
Diploneis sp1.																																
Encyonema hebridicum																																
Encyonema montana																																
Encyonema prostratum																																
Encyonema silesianum																																
Entomoneis paludosa																																
Eolimna ruttineri																																
Epithemia adnata	4	4			14		2	4	1					1				5				1		1		1	1				1	
Epithemia argus																																
Eunotia bidens																																
Eunotia flexuosa			1										1						1				1									
Eunotia formica							1								2		1						1	1								
Eunotia minor																																
Eunotia myrmica																																
Eunotia sp1																																
Fallacia auriculata																					1						1					
Fallacia forcipata																	1	1			1											
Fragilaria goulardii		6						1		2						3	2				1									1		
Fragilaria famelica																																
Frustulia interposita																																
Gomphonema acuminatum		6																	1													
Gomphonema affine	3	11				1	1								3			1	2												
Gomphonema angustatum																																
Gomphonema gracile			1																													
Gomphonema hebridense																																
Gomphonema parvulum	6				1	2	1	1	3		3		1		2	5	1	3			2	2		1			1		1		2	2
Gomphonema subclavatum			1		2					2									2		1	1										
Grammatophora hamulifera																																
Grammatophora marina																																
Gyrosigma acuminatum	3		1							1			2													2				2	1	
Gyrosigma balticum																																
Gyrosigma lanceolatum														2																		
Halamphora acutiuscula						2		1			1							8	3							2						
Halamphora exigua			1									1																				
Halamphora holsatica			2								1																					
Halamphora latecostata																																
Halamphora sp1																																
Halamphora submontana																		2														

Table A.13 (Continued)

Depth in core (cm) -->	278	279	280	281	282	283	284	285	286	292	293	294	295	296	297	298	299	303	306	307	308	309	310	311	312	313	314	315	316	317	318	319
Hantzschia amphioxys	4		1		1	1	3	1	1	2				5	1			6	2		1	4		4	5	1	3		3			
Hantzschia virgata		2	1																													
Haslea britannica																																
Hippodonta hungarica							1	2						1																	3	
Hyalosynedra laevigata																																
Karayevia amoena																																
Karayevia clevei																	1															
Kolbesia suchlandtii										1																						
Luticola goeppertiana										1						3	1															
Luticola Mutica			9		2	1	1	1	2			2	2	3			2	8	7	6	4	3	10	8	1	4	4		4	1	3	2
Luticola mutica f. intermedia																																
Luticola sp1																																
Lyrella lyra																																
Lyrella lyroides																																
Mastogloia decipiens																																
Mastogloia lineata										1																						
Mastogloia apiculata																																
Melosira polaris										2						1																
Navicula abunda																																
Navicula agatake																																
Navicula agnita																																
Navicula apta																																
Navicula cancellata						6	9	6	1					1	2				1				1	1	4	2	3	3	1			
Navicula cincta																																
Navicula cryptocephala			5			2																	1								2	
Navicula cryptocephala var veneta																																
Navicula cryptotenella						1															1				1							
Navicula directa																																
Navicula digitoradiata			4			2		2		3		2	7	1		6	6		1		2	1		1	1		1				2	
Navicula duerrenberginiana																																
Navicula eridrigiana																																
Navicula erifuga																																
Navicula exigua var. capitata																																
Navicula gregaria											1			2				2					1									3
Navicula lanceolata												2																				
Navicula lanceolata var minima																																
Navicula longa																																
Navicula menisculus																																
Navicula pennata			3		2		5		2					1					1	2	2	5	2	4	3							1
Navicula peregrina						1																										
Navicula perminuta			1																												1	2
Navicula pupula										2																						
Navicula radiosa			4							3							1				2											
Navicula recens													2																			
Navicula rostellata			1							3						1																
Navicula salinarum						1	3	1	2			4	1						1		1	1					2					
Navicula salinicola			1			1	5	2	3	2				2				1														
Navicula sp1																																
Navicula subrostellata	2		3				3	3				1	1	4	1									1								
Navicula tripunctata	1	2			2	4		3	1					4	1			6			2	1	2				2				1	1
Navicula vimineoides																																
Navicula viridula var. rostellata																																
Nitzschia acicularis								4				2									1											
Nitzschia amphibia	2	1	2			2	2					8	7	2				2	1													1
Nitzschia angustata																																
Nitzschia bicapitata																																
Nitzschia brevissima										1																				1		
Nitzschia capitellata	2							1	8			1													2							
Nitzschia clausii										3							1															
Nitzschia confinis			1			1		4					3	1									1				1	1	3		1	1

Table A.13 (Continued)

Depth in core (cm) -->	278	279	280	281	282	283	284	285	286	292	293	294	295	296	297	298	299	303	306	307	308	309	310	311	312	313	314	315	316	317	318	319
Nitzschia dissipata			3			6	2						2	2	2		1	2	6	3	4	1	1	1					1		1
Nitzschia distans								1		3												1				1						
Nitzschia filiformis			3			2																										
Nitzschia fluminensis																																
Nitzschia fonticola	7	1	12		2	4	23	8	6		7	5	2	15	1	1		4	8	3	9	18	6			4	7		6	11	15	12
Nitzschia frustulum			3					1														1		1	3	3	1	2	1			3
Nitzschia gracilis	4		1				4	1	4	11		7	1	8	1			6		3	3	3	3		1	1	2		2	2	1	2
Nitzschia grossestriata			1		2	4	1		2					4	2	1			4	4	5	7	3	7	3	8	15	3				3
Nitzschia hybrida																																
Nitzschia inconspicua																																
Nitzschia insignis																																
Nitzschia intermedia																																
Nitzschia lanceolata																																
Nitzschia lanceolata var. minima																																
Nitzschia laevissima																																
Nitzschia linearis										3					2				2													
Nitzschia microcephala								1																								
Nitzschia obtusa obtusa																																
Nitzschia palea	1	3	2			11		4	3	4		4			3		3	8	2			1			4			1				
Nitzschia panduriformis																																
Nitzschia parvula																																
Nitzschia pellucida																																
Nitzschia perminuta						5						1															1					1
Nitzschia plana																																
Nitzschia recta												1																				
Nitzschia scalaris																																
Nitzschia scalpelliformis							1		2	1									1								1					
Nitzschia sicula	1	1					1		1						1				1	1		3	4	1	1		2	3	1			2
Nitzschia sigma	6	13	2		1	11	2	1											1		2	1		1								
Nitzschia sp1.																																
Nitzschia thermalis																					1											
Nitzschia vitrea			1																							1	1					
Opephora marina var. minuta																																
Opephora pacifica			1																										1			
Orthoseira roseana																																
Paralia sulcata	7	2	5			22	5	64	8		2	77	5	6	39		9		11	20	13	8	21	39	25	63	43	68	31	14	46	51
Paralia sulcata var. biseriata																																
Paralia sulcata var. Radiata																																
Paralibellus rhombicus																																
Parlibellus calvus																																
Petroneis sp1																																
Petroneis marina																																
Pinnularia acrosphaeria					1				1	5								1											1			1
Pinnularia biceps					2																											
Pinnularia biceps var. minor									1																							
Pinnularia borealis																																
Pinnularia certa		1												1				4														
Pinnularia gibba																																
Pinnularia incognita																																
Pinnularia joculata																																
Pinnularia lattarea																																
Pinnularia microstauron						1											1															
Pinnularia neomajor																																
Pinnularia obscura																																
Pinnularia sp1																																
Pinnularia streptoraphe var. parva																																
Pinnularia subcapitata										2																						
Pinnularia turgidula																																
Placoneis gastrum		3			1		1			3				3				6	2				2				2		1		1	
Placoneis hambergii																																

Table A.13 (Continued)

Depth in core (cm) -->	278	279	280	281	282	283	284	285	286	292	293	294	295	296	297	298	299	303	306	307	308	309	310	311	312	313	314	315	316	317	318	319
Planktoniella sol							1		1			3								4	1	1		2	2		19					
Planothidium delicatulum														1																		
Planothidium frequentisimum									2																							
Planothidium hauckianum	1																				1					1						
Planothidium lanceolatum					1			1													1	1					1					
Pleurosigma salinarum																																
Podosira stelligera																																
Pseudogomphonema kamtschaticum																																
Rhopalodia acuminata													2					3														
Rhopalodia constricta																																
Rhopalodia gibba		1						1									3															
Rhopalodia gibberula	2		2		3	4	12	2		4			3	3	2	1	2	4	2		5	7		1	2	2	2			1	1	
Rhopalodia musculus	2					2										4	2	4	1		2	2				2	2					
Rhopalodia pacifica																																
Sellaphora japponica																																
Sellaphora pupula	3				1	2			3	3			1			1		12		2				1	1	4				1	1	
Sellaphora guyanensis		1													2																	
Seminavis strigosa																																
Seminavis ventricosa							2										1															
Stauroneis amphibia																																
Stauroneis borrichii																																
Stauroneis producta																																
Staurophora salina																																
Staurophora wislouchii																																
Staurophora sp1																																
Staurosirella pinnata													1																			
Staurosirella lapponica								2																								
Stephanodiscus hantzschi																																
Stephanodiscus niagarae																																
Stephanodiscus parvus		1	14			2		4	16	16	3				3				3	3	8						9					
Synedra Goulardi																																
Synedra nana										3																						
Surirella fastuosa																																
Tabularia fasciculata	4	13	1		10	5	6	10	13			4	10	3	4			6	4			2	4	9	4	4	4		1	2	4	2
Tabularia investiens							2		1																							
Tabularia parva			4			1				1							1		1													
Tabularia persuadens																																
Thalassionema nitzschioides																																
Tryblionella accuminata																																
Tryblionella apiculata																			3													
Tryblionella coarctata																						2	2							1	2	
Tryblionella compressa	7	5			2	2	1	1	7		1			0	0	1	3	5	7	6	5	10	7	15	13	20	5	5	3	5	1	3
Tryblionella debilis			1																													
Tryblionella granulata																																
Tryblionella hungarica	4	10	3			2		4																								
Tryblionella levidensis	6	9	1		7	4	1							2		1			2						3							
Tryblionella littoralis					3																											
Tryblionella persuadens																																
Ulnaria danica			4							8																						
Ulnaria acus var. angustissima							1		3						2				1										1	1		1
Ulnaria Ulna	6	17			10	4	1	2	9	2			3	17	1			11					1		1		1		2		1	2
Total counts	200	168	194	0	135	200	211	202	210	201	222	235	219	204	204	212	254	209	207	204	206	216	210	208	205	207	212	221	218	203	205	206

Table A.13 (Continued)

Depth in core (cm) -->	322	332	333	334	335	336	337	338	339	340	341	342	343	344	345	347	348	349	355	360	361	362	363	364	365	366	368	376	384	388	392	394
Achnanthes angustata				2																												
Achnanthes brevipes													1		1				2		1											
Achnanthes brevipes var. intermedia																																
Achnanthes clevei var. rostrata																																
Achnanthes delicatula										1																						
Achnanthes exigua		1		1													1		1							1						1
Achnanthes inflata													1																	1		
Achnanthes lanceolata var. rostrata																																
Achnanthes lorenziana																																
Achnanthes marginulata																																
Achnanthes parvula																																
Achnanthes promunturi																																
Achnanthes sp1																																
Achnanthidium exiguum																																
Achnanthidium minutissimum																1																
Amphipora ornata																																
Amphipora gigantea	1				1								2					2	2	1		2									1	
Amphora acustiuscula																																
Amphora affinis						1										1																
Amphora arenaria																																
Amphora bicapitata																																
Amphora clevei																																
Amphora coffeaeformis				3	8	2		2	6	4	15	6	9	2	1	3	6	6	7	1	1		1	8	7	5	12	5	3	4	1	1
Amphora costata			3	1	5		10	11	14	2	18	10	4	3		4		4	2	1		2	5	1	2	3	5	6	4	5	3	1
Amphora gigantea																																
Amphora proteus				2	1		2	1	1	3			3	12	16	10			2		2	1			1			1		3	5	2
Amphora terraris																																
Astartiella punctifera																																
Aulacoseira sp1																																
Aulacoseira granulata																																
Austariella jamaicensis																																
Bacillaria paxillifer		4	7	10	4	5	14	11	8	14	4	8	9	10	9	8	20	11	10	15	27	29	21	12	9	5	7	4	24	21	14	19
Bacillaria socialis																																
Biremis ambigua																	4															
Brevisira arentii																																
Caloneis aemula																																
Caloneis bacillum							1					1	4																	2	4	3
Caloneis excentrica																																
Caloneis permagna																																
Caloneis sabanicola																																
Caloneis subsalsa																																
Caloneis westii																																
Caloneis sp1																																
Ceratulus californicus																1																
Cocconeis convexa																																
Cocconeis fluviatilis																																
Cocconeis neodiminuta																																
Cocconeis pinnata	6	2	59	48	44	3	9	21	2			1	1	15	14	11	8	14	2	5	23	11	4	2	4	3	1	6	14	13	23	6
Cocconeis placentula	2		11	13	14		16	5	10	7	12	15	15	9	5	9	12	10	9	19	7	2	1	3	1	2	8	2	11	9	4	13
Cocconeis placentula var. euglypta	1	6	21	19	8	12	14	13	9	3	6	3		7	5	8		11	27	9	10	27	19	12	47	31	49	70	33	11	6	8
Cocconeis placentula var. lineata																																
Conticribra weissflogii																																
Coscinodiscus radiatus																																
Craticula halophiliioides																		1	2													
Cyclotella atomus						9				3							3															
Cyclotella cryptica																																
Cyclotella kuetzingiana																																
Cyclotella litoralis	48	19	14	6	7	4	20	30	15	5	11	10	3	13	11	10	8	2	5		24	6	11	11	3	4	6	1	7	14	14	3
Cyclotella meneghiniana	40	30	5	8	7	10	21	13	23	9	24	24	22	6	13	6	5	29	24	36	19	16	52	73	41	36	28	9	14	9	23	27
Cyclotella ocellata																																

Table A.13 (Continued)

Depth in core (cm) -->	322	332	333	334	335	336	337	338	339	340	341	342	343	344	345	347	348	349	355	360	361	362	363	364	365	366	368	376	384	388	392	394
Cyclotella radiosa																																
Cyclotella striata	51	55	3	4	10		4	14	17	12	18	21	20	50	47	44	40	49	18	13	16	24	20	30	28	15	10	12	16	12	17	22
Cyclotella stylorum																																
Cymbella laevis																																
Denticula kuetzingii																					2											
Denticula elegans																																
Denticula subtilis													2																			
Diadesmis confervacea							3									3		1		1									1	1	5	3
Diadesmis contenta			2		1																											
Diploneis boldtiana																																
Diploneis elliptica																																
Diploneis finnica																																
Diploneis fusca																																
Diploneis nitecens																																
Diploneis oculata																																
Diploneis ovalis																																
Diploneis pseudovalis			1		1																											1
Diploneis papula														1			1													1		
Diploneis parma																																
Diploneis puella	1		1	5	2		4	8	2		2	6	4	5	2	4			1						2	1	1	3				
Diploneis smithii							1							3	2	7	4	2			15	2					1			1		1
Diploneis subovalis																																
Diploneis sp1.																																
Encyonema hebridicum																																
Encyonema montana																																
Encyonema prostratum																																
Encyonema silesianum																																
Entomoneis paludosa																																
Eolimna ruttineri																																
Epithemia adnata					1		1	1			1			1	1			2		1												
Epithemia argus																																
Eunotia bidens																																
Eunotia flexuosa																																
Eunotia formica							1																									1
Eunotia minor																																
Eunotia myrmica																																
Eunotia sp1																																
Fallacia auriculata											1		2															1			1	
Fallacia forcipata			1					1	1				3	1	1	1	3	5		1	1	1									
Fragilaria goulardii	1				1			1			1			1	1	1															
Fragilaria famelica																																
Frustulia interposita																																
Gomphonema acuminatum																				2												
Gomphonema affine			1		3			1			3		1	1							2	5	1	1					2	2	1	3
Gomphonema angustatum																																
Gomphonema gracile															2	2		1	1													
Gomphonema hebridense						1																										
Gomphonema parvulum	2		1	1		1	1				5	3			2	1		2	4			2	1									
Gomphonema subclavatum	1			3	2		1	1		2	1		1	5	3	2			3		3				3	1	3			2	3	
Grammatophora hamulifera																																
Grammatophora marina																																
Gyrosigma acuminatum										1							1															
Gyrosigma balticum														1																		
Gyrosigma lanceolatum																									5	2	7		1		1	
Halamphora acutiuscula									6	1		1	1				1		1	1	1			1			1		4	4	2	2
Halamphora exigua																																
Halamphora holsatica																	2															
Halamphora latecostata																																
Halamphora sp1																																
Halamphora submontana																																

Table A.13 (Continued)

Depth in core (cm) -->	322	332	333	334	335	336	337	338	339	340	341	342	343	344	345	347	348	349	355	360	361	362	363	364	365	366	368	376	384	388	392	394
Hantzschia amphioxys	4		2	3	4		2	2					2	3	3				1													
Hantzschia virgata																																
Haslea britannica																																
Hippodonta hungarica																1														2		
Hyalosynedra laevigata																																
Karayevia amoena																																
Karayevia clevei																																
Kolbesia suchlandtii																																
Luticola goeppertiana																																
Luticola Mutica	1	5		3	2	1	5	5	1		3	4	1	1	1	2	2	2	2		1							1			2	
Luticola mutica f. intermedia																																
Luticola sp1																																
Lyrella lyra																																
Lyrella lyroides																																
Mastogloia decipiens																																
Mastogloia lineata																																
Mastogloia apiculata																																
Melosira polaris																																
Navicula abunda																																
Navicula agatake																																
Navicula agnita																																
Navicula apta																																
Navicula cancellata				2	4			3	5	2	2	2	2	1	3	2	1	2	3	2	3						2					1
Navicula cincta					1	2		2	1				2					2	2													
Navicula cryptocephala		1								2							27	9	3							1	1		1	1		
Navicula cryptocephala var veneta																																
Navicula cryptotenella							1									1		4								1						
Navicula directa						1																										
Navicula digitoradiata			4	4	4	2	7	3	6	2	5	3	4	2	1	4	1		1	4	1	1		1					1	1		1
Navicula duerrenberginiana																																
Navicula eridrigiana																																
Navicula erifuga																																
Navicula exigua var. capitata																																
Navicula gregaria		1										1					2															
Navicula lanceolata													1				1															
Navicula lanceolata var minima																																
Navicula longa					2		1																									
Navicula menisculus																																
Navicula pennata	5	4	13	8	3	2	3	1	5			1	2	1		3	3	3	6	6	3	4				4		1	1	4	6	5
Navicula peregrina																																
Navicula perminuta																										1						
Navicula pupula																																
Navicula radiosa										1				1																		
Navicula recens																																
Navicula rostellata																	2															
Navicula salinarum			1	3	2	3							3	2			4	1	1			1				4			1	1		
Navicula salinicola		2			1				1			2	2	1		1					2	1	1		1		2	1				
Navicula sp1																																
Navicula subrostellata					1	1		1	1				1		2	1						3	2									
Navicula tripunctata					1					1	4	4	6	4	7	5	2	3	1	5	1		1		1	4			1			3
Navicula vimineoides																																
Navicula viridula var. rostellata																																
Nitzschia acicularis						1																										
Nitzschia amphibia							1										2					1				2						1
Nitzschia angustata																																
Nitzschia bicapitata																																
Nitzschia brevissima																																
Nitzschia capitellata						2									3																	
Nitzschia clausii																																
Nitzschia confinis											1						2															

Table A.13 (Continued)

Depth in core (cm) -->	322	332	333	334	335	336	337	338	339	340	341	342	343	344	345	347	348	349	355	360	361	362	363	364	365	366	368	376	384	388	392	394
Nitzschia dissipata			1	3	1	10	7	3	4	14	11	3	12	1	2	2	6	4	8	7		1	5	3	6	14	1		12	3		
Nitzschia distans																1	2			1												
Nitzschia filiformis																																
Nitzschia fluminensis																																
Nitzschia fonticola		1	13	13	17	11	33	18	32	41	28	45	27	10	4	6	4	5	19	25	10	12	12	20	9	20	16		9	8	3	5
Nitzschia frustulum		2				24				41			3				10		14													
Nitzschia gracilis	1	4	1	3	1	5	3	1		1	1				2			1	1	2		1		2	1	4	2					1
Nitzschia grossestriata	1	9			3	21		3	4	1	10	2	3	3	9		2			1	2		4	4						1	5	12
Nitzschia hybrida																	3															
Nitzschia inconspicua																																
Nitzschia insignis																																
Nitzschia intermedia						3																										
Nitzschia lanceolata								2												2												
Nitzschia lanceolata var. minima																																
Nitzschia laevissima																																
Nitzschia linearis						1																										
Nitzschia microcephala		3								3											2	2							1		1	
Nitzschia obtusa obtusa																																
Nitzschia palea		1	1	2							7	7	6																			
Nitzschia panduriformis																																
Nitzschia parvula																																
Nitzschia pellucida																																
Nitzschia perminuta																																
Nitzschia plana																																
Nitzschia recta																																
Nitzschia scalaris																		2			1								1			
Nitzschia scalpelliformis			2					1				1							1	1						1						
Nitzschia sicula	1	1	1			2				4		2							3	1	4			1			1		1	1		2
Nitzschia sigma		1		1			3		1							2		2						1					1	2		
Nitzschia sp1.																																
Nitzschia thermalis																																
Nitzschia vitrea																																
Opephora marina var. minuta																2																
Opephora pacifica		1																														
Orthoseira roseana																																
Paralia sulcata	27	44	18	22	12	51		20	14	6	4			3	19	11	4	7	7	18	16	17	13	9	13	13	8	9	10	13	17	9
Paralia sulcata var. biseriata																																
Paralia sulcata var. Radiata																																
Paralibellus rhombicus																																
Parlibellus calvus										1										1												
Petroneis sp1																																
Petroneis marina								1																								
Pinnularia acrosphaeria												1	3	1		1																
Pinnularia biceps																																
Pinnularia biceps var. minor																																
Pinnularia borealis			1																													
Pinnularia certa							2																									
Pinnularia gibba							1		1																							
Pinnularia incognita																																
Pinnularia joculata																																
Pinnularia lattarea																																
Pinnularia microstauron																																
Pinnularia neomajor																																
Pinnularia obscura																																
Pinnularia sp1																																
Pinnularia streptoraphe var. parva																																
Pinnularia subcapitata																																
Pinnularia turgidula																																
Placoneis gastrum													2		1													1		1		
Placoneis hambergii							1							5																		

Table A.13 (Continued)

Depth in core (cm) -->	322	332	333	334	335	336	337	338	339	340	341	342	343	344	345	347	348	349	355	360	361	362	363	364	365	366	368	376	384	388	392	394
Plankoniella sol																																3
Planothidium delicatulum										2		1																			2	1
Planothidium frequentisimum																													1	1		
Planothidium hauckianum						1	1										1															2
Planothidium lanceolatum				1				1	1				1		1	4		1	3		2		3				1			1	1	1
Pleurosigma salinarum																			1													
Podosira stelligera																												40	9	6	2	1
Pseudogomphonema kamtschaticum																																
Rhopalodia acuminata																																
Rhopalodia constricta																																
Rhopalodia gibba																				2							1				1	
Rhopalodia gibberula		4	2	3			3	2		2		2				7			1								6	1	1	1	9	14
Rhopalodia musculus	1		1		5			2	3		1	4					1	2	2	5		2	4	3	17		5	2	1	6		5
Rhopalodia pacifica																																
Sellaphora japponica																																
Sellaphora pupula	2		1		1		1	1	1		1		6												2	1						2
Sellaphora guyanensis															1																	
Seminavis strigosa																																
Seminavis ventricosa					1			3			1	1		3																		
Stauroneis amphibia																1	1												1			
Stauroneis borrichii																																
Stauroneis producta																																
Staurophora salina																																
Staurophora wislouchii																																
Staurophora sp1																																
Staurosirella pinnata																																
Staurosirella lapponica																																
Stephanodiscus hantzschi																																
Stephanodiscus niagarae																																
Stephanodiscus parvus		1	1	1	1	6				3		1		1	2				1	4		7	4	4							2	
Synedra Goulardi																																
Synedra nana																																
Surirella fastuosa																1																
Tabularia fasciculata	8	2	1	1	5	2				1	1			2	3	1	3	5	2	6	12	20	12	4	17	16	11	27	31	23	20	22
Tabularia investiens		6			1		1	1	3			2			1	4		2		1	1	1	8	4	2	2	5	1		5	2	
Tabularia parva										1	1											1										
Tabularia persuadens																																
Thalassionema nitzschioides																																
Tryblionella accuminata																																
Tryblionella apiculata	3				1												1				2											
Tryblionella coarctata		2	4					1				1			2		1					1										
Tryblionella compressa	7	0	5	1	7	1	0	2	3	1	1	2	1	1	5	3	3	5	1	0	5	2	2	2	0	0	1	0	0	0	0	1
Tryblionella debilis																																
Tryblionella granulata																																
Tryblionella hungarica			1										1	3	1								1						1			
Tryblionella levidensis				2	2			3	1	3		1	1	7	1	2	1		2	4	2				2	1				2		2
Tryblionella littoralis																														3		
Tryblionella persuadens																																
Ulnaria danica		2																														
Ulnaria acus var. angustissima																															1	
Ulnaria Ulna	2		1	1			2	1																1		2					2	2
Total counts	217	214	205	203	203	201	201	217	202	200	204	202	200	202	210	205	211	214	209	204	224	208	208	213	224	200	202	204	219	201	204	213

Table A.13 (Continued)

Depth in core (cm) -->	396	398	400	402	404	408	416	420	422	424	425	426	427	428	429	430	431	432	433	434	438	442	446	450	456	464	472	480	488	499
Achnanthes angustata																		3												
Achnanthes brevipes																				4	1				2	1				5
Achnanthes brevipes var. Intermedia																														
Achnanthes clevei var. rostrata																		1												
Achnanthes delicatula																														
Achnanthes exigua				1																1	3				2				1	1
Achnanthes inflata													4	1					1			1		1						2
Achnanthes lanceolata var. rostrata																													1	1
Achnanthes lorenziana																														
Achnanthes marginulata																														
Achnanthes parvula																														
Achnanthes promunturi																														
Achnanthes sp1																														
Achnanthidium exiguum																														
Achnanthidium minutissimum																														
Amphipora ornata																														
Amphipora gigantea	1			1																										
Amphora acustiuscula																														
Amphora affinis																										1				
Amphora arenaria																														
Amphora bicapitata																														
Amphora clevei																														
Amphora coffeaeformis	7		4	3	3	4	1	1	4	5	2	2	3	3	6	3	7	12	14	6	9	4	1	1	2	1	2		2	2
Amphora costata	1	4	1	1		2			1	2	3	3	2		6	4	1	6	2	2	3		2							2
Amphora gigantea																														
Amphora proteus	7	5	6	5	2	3				4							4		4	27	4	4	15	26	6					2
Amphora terroris																														
Astartiella punctifera																														
Aulacoseira sp1																														
Aulacoseira granulata																														
Austariella jamaicensis																														
Bacillaria paxillifer	12	17	15	8	5	7	5	5	12	8	6	4	6	4	12	6	6	4	6	9	3	30	7	12	24	7	14	17	10	8
Bacillaria socialis																														
Biremis ambigua																									1					
Brevisira arentii																														
Caloneis aemula																							1					1	1	1
Caloneis bacillum						5	1		2	1	1			1		2	2					1	2					1		3
Caloneis excentrica																														
Caloneis permagna																														
Caloneis sabanicola																														
Caloneis subsalsa																														
Caloneis westii																														
Caloneis sp1																														
Ceratulus californicus																														
Cocconeis convexa																														
Cocconeis fluviatilis																														
Cocconeis neodiminuta																														
Cocconeis pinnata	5	12	8	3	1	4				3	2		1		3	4	2	2	6	2	3			3	1					
Cocconeis placentula	1	7	10	5					3	11	9	7	36	19	16	13	17	9	8	5	14	16	8	3	24	8		6	7	11
Cocconeis placentula var. euglypta	6	7	5	11		15	1	3	3	8	11	17	10	29	20	8	2	14	13	11	26	4	7	10	6	4		5	5	5
Cocconeis placentula var. lineata																														
Conticribra weissflogii																														
Coscinodiscus radiatus																														
Craticula halophilioides						1																								
Cyclotella atomus													1					2	1	3	2							2		1
Cyclotella cryptica																														
Cyclotella kuetzingiana																														
Cyclotella litoralis	10	5	7	1	3				1	27	26	8	12	12	12	22	13	15	18	14	9	11	3	16	6	1		4	8	3
Cyclotella meneghiniana	28	26	24	54	88	58	86	111	78	58	41	68	7	13	13	22	26	36	17	15	33	35	34	17	30	24	32	40	41	2
Cyclotella ocellata																														

Table A.13 (Continued)

Depth in core (cm) -->	396	398	400	402	404	408	416	420	422	424	425	426	427	428	429	430	431	432	433	434	438	442	446	450	456	464	472	480	488	499
Cyclotella radiosa																														
Cyclotella striata	20	23	27	8	2	4	2	2	8	3	6	2	5	12	15	26	46	33	30	38	16	25	20	43	6		11	15	16	27
Cyclotella stylorum																														
Cymbella laevis																														
Denticula kuetzingii																														
Denticula elegans																														
Denticula subtilis														1			1			1					2		1		2	
Diadesmis confervacea	2		2	4	2		3	2	1		4	2			1	4	1		2	1		1						1	3	10
Diadesmis contenta							1		1				1									1	1							
Diploneis boldtiana																														
Diploneis elliptica																									1		2			
Diploneis finnica																														
Diploneis fusca																														
Diploneis nitecens																														
Diploneis oculata																														
Diploneis ovalis																														2
Diploneis pseudovalis	2	1	1								1		1					1			1		1		1					
Diploneis papula																				1										
Diploneis parma																														
Diploneis puella		1		1					1							1	1	1					6		1			1		
Diploneis smithii	3	1	3		1					2	1		2	2		1				2	2	1		5	1		1		3	3
Diploneis subovalis																														
Diploneis sp1.																														
Encyonema hebridicum																														
Encyonema montana																														
Encyonema prostratum																														
Encyonema silesianum																														
Entomoneis paludosa																														2
Eolimna ruttineri																									1					
Epithemia adnata	2	1	3		1							1	2		1	1		1	1	2	2	2	1							
Epithemia argus																														
Eunotia bidens																														
Eunotia flexuosa					1		3		4					1		2	1	1					1						1	8
Eunotia formica	1						2					1		1	1	2		3	2	3	1				1		1			3
Eunotia minor																														
Eunotia myrmica																														
Eunotia sp1																														
Fallacia auriculata		1		1							1			1				1			1				1					
Fallacia forcipata		1			1							2	1								1	1	2	3	5			3	24	
Fragilaria goulardii					1				1	1			1	3										1		1	2		1	
Fragilaria famelica																														
Frustulia interposita																														
Gomphonema acuminatum																														
Gomphonema affine	3	6	6	5	3	1		1	4	1			7	7	2	2	1	1	4				2	3						4
Gomphonema angustatum																														
Gomphonema gracile																													1	
Gomphonema hebridense																					1	3	1	3						
Gomphonema parvulum	1	1			1	2		1	2		1	1		1	3		9	2	3	3	6	9	4	6	1		1	1		
Gomphonema subclavatum	3	2		4	1	2				1	4		2	1	1		2			1		1	4	6						4
Grammatophora hamulifera																														
Grammatophora marina																														
Gyrosigma acuminatum																														
Gyrosigma balticum																														
Gyrosigma lanceolatum														1					1											
Halamphora acutiuscula		1					1		2		3	2		3		1	1		1	3	2	1	2	1	2			3	1	
Halamphora exigua												1		1	2															
Halamphora holsatica																									1			3		
Halamphora latecostata																														
Halamphora sp1																														
Halamphora submontana																														

Table A.13 (Continued)

Depth in core (cm) -->	396	398	400	402	404	408	416	420	422	424	425	426	427	428	429	430	431	432	433	434	438	442	446	450	456	464	472	480	488	499
Hantzschia amphioxys									2		1						2					2	1	1						1
Hantzschia virgata								1																						
Haslea britannica																														
Hippodonta hungarica	1				1					1			2	1						1										1
Hyalosynedra laevigata																														
Karayevia amoena																														
Karayevia clevei																														
Kolbesia suchlandtii																														
Luticola goeppertiana																														
Luticola Mutica						1			1					1		3	1	2	1	1		3		2						2
Luticola mutica f. intermedia																														
Luticola sp1																														
Lyrella lyra																														
Lyrella lyroides																														
Mastogloia decipiens																														
Mastogloia lineata																														
Mastogloia apiculata																					3									
Melosira polaris																														
Navicula abunda																														
Navicula agatake																														
Navicula agnita																														
Navicula apta																														
Navicula cancellata					2						1						1		1					2						
Navicula cincta																	1	1												
Navicula cryptocephala				3	1													1							2			2	1	
Navicula cryptocephala var veneta																														
Navicula cryptotenella										1															1	2				
Navicula directa																														
Navicula digitoradiata	2				1		1					1	3			1			1	2		1		1	8		1	2	2	
Navicula duerrenberginiana																														
Navicula eridrigiana																														
Navicula erifuga																														
Navicula exigua var. capitata																														
Navicula gregaria																						4	1			1	3	1		1
Navicula lanceolata																														
Navicula lanceolata var minima																														
Navicula longa																														
Navicula menisculus										3	2	1	5	7	11	2	2	2	1	1				2				1	1	
Navicula pennata	3	1		3	4	2		2	4	2	2	1	1	1	1	1		1	1	3	1	3	4	1	3		3	26	10	2
Navicula peregrina																														
Navicula perminuta																												1		
Navicula pupula																														
Navicula radiosa																														
Navicula recens																														
Navicula rostellata																														
Navicula salinarum																														1
Navicula salinicola			1		1				1		3			1				2\	11									2	6	2
Navicula sp1																														
Navicula subrostellata	3		1	1	3	1				1	2		1			2									4			1		
Navicula tripunctata	1		1	2	4		1	4	1	1	1	6	4	3	5	1				2	1	1	10		2			1	2	1
Navicula vimineoides																														
Navicula viridula var. rostellata																														
Nitzschia acicularis																									1	6	7			
Nitzschia amphibia	2			1	4	2	3		1	1		2	8	2	1		3	3	5		4	5	3	2	4		2	3	5	1
Nitzschia angustata																														
Nitzschia bicapitata																														
Nitzschia brevissima																														
Nitzschia capitellata					2																					1	1		1	
Nitzschia clausii																														
Nitzschia confinis																														

Table A.13 (Continued)

Depth in core (cm) -->	396	398	400	402	404	408	416	420	422	424	425	426	427	428	429	430	431	432	433	434	438	442	446	450	456	464	472	480	488	499
Nitzschia dissipata	3		1			4		1	2		1	1		1			1	2	1		1				2	8	6	7	4	
Nitzschia distans																				1										
Nitzschia filiformis																														
Nitzschia fluminensis																														
Nitzschia fonticola	11	12	12	15	7	20	12	4	3	7	9	11	4	5	7	12	13	9	16	7	11	3	15	3	10	49	10	13	8	6
Nitzschia frustulum																									9	34	6	2	1	
Nitzschia gracilis				2		5	7	10	2	2					2	2	1		2	2		1	3			17	6			
Nitzschia grossestriata	5	3	5	10	10	7	2	4	8	19	11	15	39	33	40	13	7	5	2	11	13	11	11	24	4	19	19	21	18	9
Nitzschia hybrida																											1			
Nitzschia inconspicua																														
Nitzschia insignis																														
Nitzschia intermedia																														
Nitzschia lanceolata																													1	
Nitzschia lanceolata var. minima																														
Nitzschia laevissima																														
Nitzschia linearis																														
Nitzschia microcephala																										1	1	2	1	
Nitzschia obtusa obtusa																													1	
Nitzschia palea						1	4	2	1		4	6				2	1	3	3				2		1	1	1	2		3
Nitzschia panduriformis																														
Nitzschia parvula																														
Nitzschia pellucida																														
Nitzschia perminuta																														
Nitzschia plana																														
Nitzschia recta																														
Nitzschia scalaris		1	1			1					5	1	1	1		3			3			2	1	1						7
Nitzschia scalpelliformis																														
Nitzschia sicula			1										1				2	1	1						1	2				
Nitzschia sigma	1		3	3																	1		2	1	1	1	1		1	12
Nitzschia sp1.																														
Nitzschia thermalis																											1			
Nitzschia vitrea																														
Opephora marina var. minuta	2					2					1																			
Opephora pacifica																														
Orthoseira roseana																														
Paralia sulcata	4	12	4	10	9	6	5	5	13	6	15	11	2	3	3	14	5	2	7	6	12	10	2	5	2	24	67	23	13	5
Paralia sulcata var. biseriata																														
Paralia sulcata var. Radiata																														
Paralibellus rhombicus																														
Parlibellus calvus																									2					
Petroneis sp1																														
Petroneis marina																														
Pinnularia acrosphaeria											2	1	1				1			1		3								4
Pinnularia biceps																														
Pinnularia biceps var. minor																														
Pinnularia borealis																				2	3		2							
Pinnularia certa									1									2								1				
Pinnularia gibba					3	1	3	1	2						1	1	3													
Pinnularia incognita																														
Pinnularia joculata																														
Pinnularia lattarea																														
Pinnularia microstauron																														
Pinnularia neomajor																														
Pinnularia obscura																														
Pinnularia sp1																														
Pinnularia streptoraphe var. parva																														
Pinnularia subcapitata																														
Pinnularia turgidula																														
Placoneis gastrum	3																													
Placoneis hambergii			1	1	1						1										1	2								1

Table A.13 (Continued)

Depth in core (cm) -->	396	398	400	402	404	408	416	420	422	424	425	426	427	428	429	430	431	432	433	434	438	442	446	450	456	464	472	480	488	499
Planktoniella sol	1	4			1		1			1	2																		2	
Planothidium delicatulum	1	2		1														4	3	3	1				1			4		
Planothidium frequentisimum		1		2									11	17	5	3	3	1		3	2	6			1	4				
Planothidium hauckianum		4	1									1				1									5		2			
Planothidium lanceolatum	1				1	3	3			6	3	6				1	1	3	1	4	2	2		2	2		1		1	
Pleurosigma salinarum																														
Podosira stelligera	1	4	5	1														2	1	1										
Pseudogomphonema kamtschaticum																														
Rhopalodia acuminata			1																		1	3			4		1			1
Rhopalodia constricta																														
Rhopalodia gibba				4						1				1							1		2	2						3
Rhopalodia gibberula	12	5	9	18	15	10	5	7	11	8	3	4	1	1	1	1	9	8	1		4	1	2	5			1	1	3	13
Rhopalodia musculus	2	2	8	2	3	2	1			3	1		2		1	7				1	1	5	3	3	1		1	2		7
Rhopalodia pacifica																														
Sellaphora japponica																			1	1										
Sellaphora pupula		1		3		2		1	1	1	1				2				2			4	2	1			2	1		1
Sellaphora guyanensis																	1													
Seminavis strigosa												1																		
Seminavis ventricosa						1																								
Stauroneis amphibia	1																									2				
Stauroneis borrichii																														
Stauroneis producta																														
Staurophora salina																														
Staurophora wislouchii																														
Staurophora sp1																														
Staurosirella pinnata																		1												
Staurosirella lapponica																														
Stephanodiscus hantzschi																									1					
Stephanodiscus niagarae																														
Stephanodiscus parvus					1	1		1		1	1	3	1			4		2	1			1					7		2	
Synedra Goulardi																														
Synedra nana																														
Surirella fastuosa		1	2																2	2				1						
Tabularia fasciculata	36	23	25	12	4	9	2		2	5	6	1	12	10	7	2	1	4	6	4		1	4	6		7		1		5
Tabularia investiens		2	1		1		1					7			1		1				1							2		
Tabularia parva																											5	1		
Tabularia persuadens																														
Thalassionema nitzschioides																														
Tryblionella accuminata																														
Tryblionella apiculata																	2	1	1											1
Tryblionella coarctata																1					1					2				
Tryblionella compressa	2	3	0	0	1	0	0	0	0	1	0	0	0	0	0	0	0	2	2	0	1	2	5	2	0	0	0	0	0	1
Tryblionella debilis																1													1	
Tryblionella granulata																	1													
Tryblionella hungarica																												1		
Tryblionella levidensis			1			1			1	1				4				1					2	5						10
Tryblionella littoralis																														
Tryblionella persuadens																														
Ulnaria danica																														
Ulnaria acus var. angustissima				10	9	11	41	24	12	3					2	1		1			1									
Ulnaria Ulna	5	2		4	3	9	10	9	10	3	3	3	1	2		3	7	1	5		1	2	5	2						4
Total counts	218	205	206	224	208	210	208	202	207	213	203	204	204	211	204	206	213	213	216	213	211	229	207	234	200	230	223	224	215	217

Table A.14. Summary of fossil diatoms in core MAR19006, grouped by salinity classes (%).

Depth (cm)	Fresh (%)	Brackish (%)	Marine (%)	Unclassified (%)
235	51.71	34.15	13.17	0.98
236	69.90	17.96	11.65	0.49
237	52.86	26.19	18.10	2.86
238	51.20	24.88	23.92	0.00
239	37.56	40.98	21.46	0.00
240	47.34	28.02	23.67	0.97
241	38.61	33.66	23.76	3.96
242	42.68	35.56	21.34	0.42
243	43.00	41.00	14.50	1.50
244	61.61	25.59	11.85	0.95
245	72.30	15.96	7.51	4.23
246	62.50	17.00	16.50	4.00
247	50.00	37.14	11.43	1.43
248	52.00	35.00	9.50	3.50
249	56.72	35.32	6.47	1.49
250	55.94	34.16	8.91	0.99
251	53.88	34.70	10.96	0.46
257	38.31	48.26	10.45	2.99
258	47.50	38.00	10.00	4.50
259	42.08	47.52	8.42	1.98
260	44.28	48.76	5.47	1.49
261	34.33	52.74	12.44	0.50
262	45.50	42.50	12.00	0.00
263	25.00	65.68	9.32	0.00
264	27.32	64.39	7.80	0.49
265	33.64	51.40	14.02	0.93
266	40.10	45.05	13.37	1.49
267	34.45	32.06	33.49	0.00
268	38.24	43.14	18.14	0.49
269	43.14	45.10	11.27	0.49
276	25.24	48.10	26.67	0.00
278	32.50	51.00	16.50	0.00
279	37.50	48.21	14.29	0.00
280	52.06	34.02	13.92	0.00
282	43.70	43.70	12.59	0.00
283	46.50	33.00	20.50	0.00
284	41.23	41.71	16.59	0.47
285	28.71	32.18	39.11	0.00
286	56.19	26.67	15.71	1.43
292	69.65	20.40	9.95	0.00
293	69.37	19.82	10.81	0.00
294	56.17	7.66	36.17	0.00
295	54.34	40.64	5.02	0.00
296	60.78	25.98	13.24	0.00
297	42.16	33.33	23.53	0.98
298	36.79	60.38	2.83	0.00
299	14.96	65.35	19.69	0.00
303	69.86	25.36	4.78	0.00
306	42.03	38.16	19.32	0.48
307	33.33	32.84	33.82	0.00
308	52.91	23.79	23.30	0.00
309	49.54	25.46	24.07	0.93
310	44.76	23.33	30.95	0.95
311	18.75	22.12	59.13	0.00
312	32.68	15.12	52.20	0.00
313	12.56	17.87	69.57	0.00
314	24.06	14.15	61.79	0.00
315	8.14	35.29	56.56	0.00
316	30.73	50.46	18.35	0.46
317	32.51	55.67	10.84	0.99
318	38.05	35.12	25.85	0.98
319	39.81	26.21	33.50	0.49

Table A.14. (continued).

322	26.73	29.03	44.24	0.00
332	25.70	35.98	37.38	0.93
333	31.22	10.73	56.10	1.95
334	39.41	13.79	46.80	0.00
335	33.00	20.20	46.80	0.00
336	37.31	17.91	44.78	0.00
337	60.20	16.42	23.38	0.00
338	35.02	17.97	46.54	0.46
339	42.08	25.25	32.67	0.00
340	45.50	40.50	14.00	0.00
341	54.41	22.55	23.04	0.00
342	57.92	25.74	15.84	0.50
343	60.00	25.50	14.50	0.00
344	30.20	35.64	34.16	0.00
345	28.57	30.95	39.52	0.95
347	29.76	36.10	33.66	0.49
348	31.75	43.60	24.17	0.47
349	40.19	36.92	22.90	0.00
355	54.07	28.23	17.70	0.00
360	54.90	24.51	20.59	0.00
361	26.34	28.57	45.09	0.00
362	36.54	37.98	25.00	0.48
363	47.60	32.69	19.71	0.00
364	55.87	30.05	14.08	0.00
365	50.45	36.16	13.39	0.00
366	60.50	22.50	17.00	0.00
368	54.95	29.21	15.84	0.00
376	42.65	25.98	31.37	0.00
384	39.27	38.36	22.37	0.00
388	26.37	39.80	33.83	0.00
392	28.92	32.84	37.75	0.49
394	34.74	41.31	23.94	0.00
396	33.49	44.50	22.02	0.00
398	32.20	38.05	29.76	0.00
400	30.10	47.57	22.33	0.00
402	54.02	25.45	16.07	4.46
404	60.10	17.31	18.27	4.33
408	63.33	17.14	14.29	5.24
416	67.31	9.13	3.85	19.71
420	74.75	7.43	5.94	11.88
422	61.35	19.32	13.53	5.80
424	49.77	16.43	32.39	1.41
425	48.77	16.26	34.98	0.00
426	66.18	12.75	21.08	0.00
427	44.12	25.00	30.88	0.00
428	45.02	27.96	27.01	0.00
429	36.76	30.39	31.86	0.98
430	41.26	26.21	31.55	0.97
431	46.48	36.62	16.90	0.00
432	47.42	34.74	17.37	0.47
433	41.20	35.19	23.61	0.00
434	30.52	35.68	33.80	0.00
438	53.08	21.33	24.64	0.95
442	44.10	36.24	19.65	0.00
446	56.04	21.26	22.71	0.00
450	27.78	32.05	40.17	0.00
456	47.00	32.00	20.50	0.50
464	54.78	24.35	20.00	0.87
472	36.77	21.97	41.26	0.00
480	39.73	25.45	34.82	0.00
488	41.40	22.33	36.28	0.00
499	39.63	38.71	21.66	0.00

Table A. 15. Summary of fossil diatoms contained in the core MAR19006. These species correspond to those with abundance >5% that appear in at least 5 samples.

No.	Species	Living	Salinity class	Halobian class	Source
1	Cyclotella meneghiniana	Tychoplanktonic, benthic origin	Freshwater	Oh	Denys, 1991; Vos & de Wolf (1993)
2	Nitzschia fonticola	Benthic	Freshwater	OI	Denys, 1991; Watchman et al. 2013
3	Cocconeis placentula	Epiphytes	Freshwater	OI	Denys, 1991; Vos & de Wolf (1993)
4	Cocconeis placentula var. euglypta	Epiphytes	Freshwater	OI	Denys, 1991; Vos & de Wolf (1993)
5	Nitzschia dissipata	Benthic	Freshwater	OI	Horton et al.
6	Ulnaria Ulna	Epontic	Freshwater	OI	Denys, 1991; Novelo et al. 2007
7	Cyclotella striata	tychoplanktonic, benthic origin	Brackish	M	Denys, 1991
8	Bacillaria paxillifer	Tychoplanktonic, epontic origin	Brackish	M	Denys, 1991; Sawai et al. 2003
9	Tabularia fasciculata	Epontic	Brackish	M	Hartley et al. 1996
10	Rhopalodia gibberula	Epiphytes	Brackish	M	Vos & de Wolf, 1993
11	Amphora coffeaeformis	Epontic and benthic	Brackish	M	Denys, 1991; Horton et al.
12	Paralia sulcata	Tychoplanktonic, both epontic and benthic origin	Marine	P	Vos & de Wolf, 1993; Denys, 1991; Ramírez-Herrera et al. 2014
13	Cyclotella litoralis	Benthic	Marine	P	Siqueiros-Beltrones et al. 2017
14	Nitzschia grossestriata	Benthic	Marine	P	Siqueiros-Beltrones et al. 2017
15	Cocconeis pinnata	Epontic	Marine	P	Denys, 1991
16	Amphora proteus	Benthos epipelon	Marine	P	Denys, 1991; Vos & de Wolf, 1993; Hartley et al., 1996; Horton et al.

Oh: Oligohalobous-halophite
Oi: Oligohlobous-indifferent
M: Mesohalobous
P: Polyhalobous

Table A.16. Palaeoelevation estimations from Model 1 (Alaska) of core MAR19006.

Depth (cm)	B & M (%)	Palaeoelevation in SWLI units			Palaeoelevations transformed in m relative to MHHW			
		SWLI	SWLI_lower	SWLI_upper	m MHHW	Error linear model (e1)	Error Water Level (e2)	Total elevation error (ee)
235	47.32	222.44	12.44	12.44	0.07	0.04	0.26	0.26
236	29.61	233.83	12.49	12.49	0.11	0.04	0.26	0.26
237	44.29	224.39	12.44	12.44	0.08	0.04	0.26	0.26
238	48.80	221.49	12.44	12.44	0.07	0.04	0.26	0.26
239	62.44	212.71	12.49	12.49	0.04	0.04	0.26	0.26
240	51.69	219.63	12.45	12.45	0.06	0.04	0.26	0.26
241	57.43	215.94	12.47	12.47	0.05	0.04	0.26	0.26
242	56.90	216.27	12.46	12.46	0.05	0.04	0.26	0.26
243	55.50	217.18	12.46	12.46	0.06	0.04	0.26	0.26
244	37.44	228.80	12.45	12.45	0.09	0.04	0.26	0.26
245	23.47	237.78	12.52	12.52	0.12	0.04	0.26	0.26
246	33.50	231.33	12.47	12.47	0.10	0.04	0.26	0.26
247	48.57	221.63	12.44	12.44	0.07	0.04	0.26	0.26
248	44.50	224.25	12.44	12.44	0.08	0.04	0.26	0.26
249	41.79	226.00	12.45	12.45	0.09	0.04	0.26	0.26
250	43.07	225.17	12.44	12.44	0.08	0.04	0.26	0.26
251	45.66	223.51	12.44	12.44	0.08	0.04	0.26	0.26
257	58.71	215.11	12.47	12.47	0.05	0.04	0.26	0.26
258	48.00	222.00	12.44	12.44	0.07	0.04	0.26	0.26
259	55.94	216.89	12.46	12.46	0.06	0.04	0.26	0.26
260	54.23	217.99	12.45	12.45	0.06	0.04	0.26	0.26
261	65.17	210.95	12.50	12.50	0.04	0.04	0.26	0.26
262	54.50	217.82	12.46	12.46	0.06	0.04	0.26	0.26
263	75.00	204.63	12.58	12.58	0.02	0.04	0.26	0.26
264	72.20	206.43	12.56	12.56	0.02	0.04	0.26	0.26
265	65.42	210.79	12.51	12.51	0.04	0.04	0.26	0.26
266	58.42	215.30	12.47	12.47	0.05	0.04	0.26	0.26
267	65.55	210.71	12.51	12.51	0.04	0.04	0.26	0.26
268	61.27	213.46	12.48	12.48	0.04	0.04	0.26	0.26
269	56.37	216.62	12.46	12.46	0.05	0.04	0.26	0.26
276	74.76	204.78	12.58	12.58	0.02	0.04	0.26	0.26
278	67.50	209.46	12.52	12.52	0.03	0.04	0.26	0.26
279	62.50	212.67	12.49	12.49	0.04	0.04	0.26	0.26
280	47.94	222.04	12.44	12.44	0.07	0.04	0.26	0.26
282	56.30	216.66	12.46	12.46	0.05	0.04	0.26	0.26
283	53.50	218.46	12.45	12.45	0.06	0.04	0.26	0.26
284	58.29	215.38	12.47	12.47	0.05	0.04	0.26	0.26
285	71.29	207.02	12.55	12.55	0.02	0.04	0.26	0.26
286	42.38	225.62	12.44	12.44	0.08	0.04	0.26	0.26
292	30.35	233.36	12.48	12.48	0.11	0.04	0.26	0.26
293	30.63	233.18	12.48	12.48	0.11	0.04	0.26	0.26
294	43.83	224.69	12.44	12.44	0.08	0.04	0.26	0.26
295	45.66	223.51	12.44	12.44	0.08	0.04	0.26	0.26
296	39.22	227.65	12.45	12.45	0.09	0.04	0.26	0.26
297	56.86	216.30	12.46	12.46	0.05	0.04	0.26	0.26
298	63.21	212.22	12.49	12.49	0.04	0.04	0.26	0.26
299	85.04	198.17	12.69	12.69	-0.01	0.04	0.16	0.17
303	30.14	233.49	12.48	12.48	0.11	0.04	0.26	0.26
306	57.49	215.90	12.47	12.47	0.05	0.04	0.26	0.26
307	66.67	209.99	12.51	12.51	0.03	0.04	0.26	0.26
308	47.09	222.59	12.44	12.44	0.07	0.04	0.26	0.26
309	49.54	221.01	12.44	12.44	0.07	0.04	0.26	0.26
310	54.29	217.96	12.45	12.45	0.06	0.04	0.26	0.26
311	81.25	200.61	12.65	12.65	0.00	0.04	0.26	0.26
312	67.32	209.57	12.52	12.52	0.03	0.04	0.26	0.26
313	87.44	196.62	12.73	12.73	-0.01	0.04	0.16	0.17
314	75.94	204.02	12.59	12.59	0.01	0.04	0.26	0.26
315	91.86	193.78	12.79	12.79	-0.02	0.04	0.16	0.17
316	68.81	208.61	12.53	12.53	0.03	0.04	0.26	0.26
317	66.50	210.10	12.51	12.51	0.03	0.04	0.26	0.26
318	60.98	213.65	12.48	12.48	0.04	0.04	0.26	0.26

Table A.16 (continued)

319	59.71	214.47	12.47	12.47	0.05	0.04	0.26	0.26
322	73.27	205.74	12.57	12.57	0.02	0.04	0.26	0.26
332	73.36	205.68	12.57	12.57	0.02	0.04	0.26	0.26
333	66.83	209.89	12.52	12.52	0.03	0.04	0.26	0.26
334	60.59	213.90	12.48	12.48	0.05	0.04	0.26	0.26
335	67.00	209.78	12.52	12.52	0.03	0.04	0.26	0.26
336	62.69	212.55	12.49	12.49	0.04	0.04	0.26	0.26
337	39.80	227.28	12.45	12.45	0.09	0.04	0.26	0.26
338	64.52	211.38	12.50	12.50	0.04	0.04	0.26	0.26
339	57.92	215.62	12.47	12.47	0.05	0.04	0.26	0.26
340	54.50	217.82	12.46	12.46	0.06	0.04	0.26	0.26
341	45.59	223.55	12.44	12.44	0.08	0.04	0.26	0.26
342	41.58	226.13	12.45	12.45	0.09	0.04	0.26	0.26
343	40.00	227.15	12.45	12.45	0.09	0.04	0.26	0.26
344	69.80	207.97	12.54	12.54	0.03	0.04	0.26	0.26
345	70.48	207.54	12.54	12.54	0.02	0.04	0.26	0.26
347	69.76	208.00	12.54	12.54	0.03	0.04	0.26	0.26
348	67.77	209.28	12.52	12.52	0.03	0.04	0.26	0.26
349	59.81	214.40	12.48	12.48	0.05	0.04	0.26	0.26
355	45.93	223.33	12.44	12.44	0.08	0.04	0.26	0.26
360	45.10	223.87	12.44	12.44	0.08	0.04	0.26	0.26
361	73.66	205.49	12.57	12.57	0.02	0.04	0.26	0.26
362	62.98	212.36	12.49	12.49	0.04	0.04	0.26	0.26
363	52.40	219.17	12.45	12.45	0.06	0.04	0.26	0.26
364	44.13	224.49	12.44	12.44	0.08	0.04	0.26	0.26
365	49.55	221.00	12.44	12.44	0.07	0.04	0.26	0.26
366	39.50	227.47	12.45	12.45	0.09	0.04	0.26	0.26
368	45.05	223.90	12.44	12.44	0.08	0.04	0.26	0.26
376	57.35	215.98	12.46	12.46	0.05	0.04	0.26	0.26
384	60.73	213.81	12.48	12.48	0.05	0.04	0.26	0.26
388	73.63	205.51	12.57	12.57	0.02	0.04	0.26	0.26
392	70.59	207.47	12.54	12.54	0.02	0.04	0.26	0.26
394	65.26	210.90	12.51	12.51	0.04	0.04	0.26	0.26
396	66.51	210.09	12.51	12.51	0.03	0.04	0.26	0.26
398	67.80	209.26	12.52	12.52	0.03	0.04	0.26	0.26
400	69.90	207.91	12.54	12.54	0.03	0.04	0.26	0.26
402	41.52	226.17	12.45	12.45	0.09	0.04	0.26	0.26
404	35.58	230.00	12.46	12.46	0.10	0.04	0.26	0.26
408	31.43	232.67	12.48	12.48	0.11	0.04	0.26	0.26
416	12.98	244.54	12.62	12.62	0.15	0.04	0.26	0.26
420	13.37	244.29	12.61	12.61	0.15	0.04	0.26	0.26
422	32.85	231.75	12.47	12.47	0.10	0.04	0.26	0.26
424	48.83	221.47	12.44	12.44	0.07	0.04	0.26	0.26
425	51.23	219.92	12.45	12.45	0.07	0.04	0.26	0.26
426	33.82	231.12	12.47	12.47	0.10	0.04	0.26	0.26
427	55.88	216.93	12.46	12.46	0.06	0.04	0.26	0.26
428	54.98	217.51	12.46	12.46	0.06	0.04	0.26	0.26
429	62.25	212.83	12.49	12.49	0.04	0.04	0.26	0.26
430	57.77	215.72	12.47	12.47	0.05	0.04	0.26	0.26
431	53.52	218.45	12.45	12.45	0.06	0.04	0.26	0.26
432	52.11	219.36	12.45	12.45	0.06	0.04	0.26	0.26
433	58.80	215.06	12.47	12.47	0.05	0.04	0.26	0.26
434	69.48	208.18	12.54	12.54	0.03	0.04	0.26	0.26
438	45.97	223.31	12.44	12.44	0.08	0.04	0.26	0.26
442	55.90	216.92	12.46	12.46	0.06	0.04	0.26	0.26
446	43.96	224.60	12.44	12.44	0.08	0.04	0.26	0.26
450	72.22	206.42	12.56	12.56	0.02	0.04	0.26	0.26
456	52.50	219.11	12.45	12.45	0.06	0.04	0.26	0.26
464	44.35	224.35	12.44	12.44	0.08	0.04	0.26	0.26
472	63.23	212.20	12.49	12.49	0.04	0.04	0.26	0.26
480	60.27	214.11	12.48	12.48	0.05	0.04	0.26	0.26
488	58.60	215.18	12.47	12.47	0.05	0.04	0.26	0.26
499	60.37	214.04	12.48	12.48	0.05	0.04	0.26	0.26

Table A. 17. Palaeoelevation estimations from Model 2 (Chile) of core MAR19006.

Depth (cm)	B & M (%)	Palaeoelevation in SWLI units			Palaeoelevations transformed in m relative to MHHW			
		SWLI	SWLI_lower	SWLI_upper	m MHHW	Error linear model (e1)	Error Water Level (e2)	Total elevation error (ee)
235	47.32	213.66	23.34	23.34	0.04	0.08	0.26	0.27
236	29.61	233.00	23.47	23.47	0.11	0.08	0.26	0.27
237	44.29	216.97	23.34	23.34	0.06	0.08	0.26	0.27
238	48.80	212.03	23.34	23.34	0.04	0.08	0.26	0.27
239	62.44	197.14	23.44	23.44	-0.01	0.08	0.16	0.18
240	51.69	208.88	23.35	23.35	0.03	0.08	0.26	0.27
241	57.43	202.61	23.38	23.38	0.01	0.08	0.26	0.27
242	56.90	203.18	23.38	23.38	0.01	0.08	0.26	0.27
243	55.50	204.72	23.37	23.37	0.02	0.08	0.26	0.27
244	37.44	224.45	23.38	23.38	0.08	0.08	0.26	0.27
245	23.47	239.70	23.58	23.58	0.13	0.08	0.26	0.27
246	33.50	228.75	23.42	23.42	0.09	0.08	0.26	0.27
247	48.57	212.29	23.34	23.34	0.04	0.08	0.26	0.27
248	44.50	216.73	23.34	23.34	0.05	0.08	0.26	0.27
249	41.79	219.69	23.35	23.35	0.06	0.08	0.26	0.27
250	43.07	218.30	23.34	23.34	0.06	0.08	0.26	0.27
251	45.66	215.46	23.34	23.34	0.05	0.08	0.26	0.27
257	58.71	201.21	23.39	23.39	0.00	0.08	0.26	0.27
258	48.00	212.91	23.34	23.34	0.04	0.08	0.26	0.27
259	55.94	204.24	23.37	23.37	0.01	0.08	0.26	0.27
260	54.23	206.11	23.36	23.36	0.02	0.08	0.26	0.27
261	65.17	194.15	23.48	23.48	-0.02	0.08	0.16	0.18
262	54.50	205.81	23.36	23.36	0.02	0.08	0.26	0.27
263	75.00	183.41	23.67	23.67	-0.05	0.08	0.16	0.18
264	72.20	186.48	23.61	23.61	-0.04	0.08	0.16	0.18
265	65.42	193.88	23.48	23.48	-0.02	0.08	0.16	0.18
266	58.42	201.53	23.39	23.39	0.01	0.08	0.26	0.27
267	65.55	193.74	23.48	23.48	-0.02	0.08	0.16	0.18
268	61.27	198.41	23.42	23.42	-0.01	0.08	0.16	0.18
269	56.37	203.76	23.37	23.37	0.01	0.08	0.26	0.27
276	74.76	183.67	23.66	23.66	-0.05	0.08	0.16	0.18
278	67.50	191.61	23.51	23.51	-0.03	0.08	0.16	0.18
279	62.50	197.07	23.44	23.44	-0.01	0.08	0.16	0.18
280	47.94	212.98	23.34	23.34	0.04	0.08	0.26	0.27
282	56.30	203.85	23.37	23.37	0.01	0.08	0.26	0.27
283	53.50	206.90	23.35	23.35	0.02	0.08	0.26	0.27
284	58.29	201.66	23.39	23.39	0.01	0.08	0.26	0.27
285	71.29	187.47	23.59	23.59	-0.04	0.08	0.16	0.18
286	42.38	219.05	23.35	23.35	0.06	0.08	0.26	0.27
292	30.35	232.19	23.46	23.46	0.11	0.08	0.26	0.27
293	30.63	231.89	23.45	23.45	0.10	0.08	0.26	0.27
294	43.83	217.47	23.34	23.34	0.06	0.08	0.26	0.27
295	45.66	215.46	23.34	23.34	0.05	0.08	0.26	0.27
296	39.22	222.51	23.36	23.36	0.07	0.08	0.26	0.27
297	56.86	203.23	23.38	23.38	0.01	0.08	0.26	0.27
298	63.21	196.30	23.45	23.45	-0.01	0.08	0.16	0.18
299	85.04	172.45	23.95	23.95	-0.09	0.08	0.16	0.18
303	30.14	232.42	23.46	23.46	0.11	0.08	0.26	0.27
306	57.49	202.55	23.38	23.38	0.01	0.08	0.26	0.27
307	66.67	192.52	23.50	23.50	-0.02	0.08	0.16	0.18
308	47.09	213.91	23.34	23.34	0.05	0.08	0.26	0.27
309	49.54	211.23	23.34	23.34	0.04	0.08	0.26	0.27
310	54.29	206.04	23.36	23.36	0.02	0.08	0.26	0.27
311	81.25	176.59	23.83	23.83	-0.08	0.08	0.16	0.18
312	67.32	191.81	23.51	23.51	-0.03	0.08	0.16	0.18
313	87.44	169.82	24.03	24.03	-0.10	0.08	0.16	0.18
314	75.94	182.38	23.69	23.69	-0.06	0.08	0.16	0.18
315	91.86	165.00	24.18	24.18	-0.11	0.08	0.16	0.18
316	68.81	190.18	23.54	23.54	-0.03	0.08	0.16	0.18
317	66.50	192.70	23.50	23.50	-0.02	0.08	0.16	0.18
318	60.98	198.73	23.42	23.42	0.00	0.08	0.26	0.27

Table A.17. (continued).

319	59.71	200.12	23.40	23.40	0.00	0.08	0.26	0.27
322	73.27	185.30	23.63	23.63	-0.05	0.08	0.16	0.18
332	73.36	185.20	23.63	23.63	-0.05	0.08	0.16	0.18
333	66.83	192.34	23.50	23.50	-0.03	0.08	0.16	0.18
334	60.59	199.16	23.41	23.41	0.00	0.08	0.26	0.27
335	67.00	192.16	23.51	23.51	-0.03	0.08	0.16	0.18
336	62.69	196.87	23.44	23.44	-0.01	0.08	0.16	0.18
337	39.80	221.87	23.36	23.36	0.07	0.08	0.26	0.27
338	64.52	194.87	23.47	23.47	-0.02	0.08	0.16	0.18
339	57.92	202.07	23.39	23.39	0.01	0.08	0.26	0.27
340	54.50	205.81	23.36	23.36	0.02	0.08	0.26	0.27
341	45.59	215.55	23.34	23.34	0.05	0.08	0.26	0.27
342	41.58	219.92	23.35	23.35	0.07	0.08	0.26	0.27
343	40.00	221.65	23.36	23.36	0.07	0.08	0.26	0.27
344	69.80	189.09	23.56	23.56	-0.04	0.08	0.16	0.18
345	70.48	188.36	23.57	23.57	-0.04	0.08	0.16	0.18
347	69.76	189.14	23.56	23.56	-0.04	0.08	0.16	0.18
348	67.77	191.31	23.52	23.52	-0.03	0.08	0.16	0.18
349	59.81	200.01	23.41	23.41	0.00	0.08	0.26	0.27
355	45.93	215.17	23.34	23.34	0.05	0.08	0.26	0.27
360	45.10	216.08	23.34	23.34	0.05	0.08	0.26	0.27
361	73.66	184.88	23.64	23.64	-0.05	0.08	0.16	0.18
362	62.98	196.54	23.44	23.44	-0.01	0.08	0.16	0.18
363	52.40	208.10	23.35	23.35	0.03	0.08	0.26	0.27
364	44.13	217.14	23.34	23.34	0.06	0.08	0.26	0.27
365	49.55	211.21	23.34	23.34	0.04	0.08	0.26	0.27
366	39.50	222.20	23.36	23.36	0.07	0.08	0.26	0.27
368	45.05	216.13	23.34	23.34	0.05	0.08	0.26	0.27
376	57.35	202.69	23.38	23.38	0.01	0.08	0.26	0.27
384	60.73	199.00	23.42	23.42	0.00	0.08	0.26	0.27
388	73.63	184.91	23.64	23.64	-0.05	0.08	0.16	0.18
392	70.59	188.23	23.57	23.57	-0.04	0.08	0.16	0.18
394	65.26	194.06	23.48	23.48	-0.02	0.08	0.16	0.18
396	66.51	192.68	23.50	23.50	-0.02	0.08	0.16	0.18
398	67.80	191.27	23.52	23.52	-0.03	0.08	0.16	0.18
400	69.90	188.98	23.56	23.56	-0.04	0.08	0.16	0.18
402	41.52	219.99	23.35	23.35	0.07	0.08	0.26	0.27
404	35.58	226.48	23.39	23.39	0.09	0.08	0.26	0.27
408	31.43	231.01	23.44	23.44	0.10	0.08	0.26	0.27
416	12.98	251.17	23.84	23.84	0.17	0.08	0.26	0.27
420	13.37	250.75	23.82	23.82	0.17	0.08	0.26	0.27
422	32.85	229.46	23.42	23.42	0.10	0.08	0.26	0.27
424	48.83	212.01	23.34	23.34	0.04	0.08	0.26	0.27
425	51.23	209.38	23.34	23.34	0.03	0.08	0.26	0.27
426	33.82	228.40	23.41	23.41	0.09	0.08	0.26	0.27
427	55.88	204.30	23.37	23.37	0.01	0.08	0.26	0.27
428	54.98	205.29	23.36	23.36	0.02	0.08	0.26	0.27
429	62.25	197.34	23.43	23.43	-0.01	0.08	0.16	0.18
430	57.77	202.24	23.39	23.39	0.01	0.08	0.26	0.27
431	53.52	206.88	23.35	23.35	0.02	0.08	0.26	0.27
432	52.11	208.42	23.35	23.35	0.03	0.08	0.26	0.27
433	58.80	201.12	23.40	23.40	0.00	0.08	0.26	0.27
434	69.48	189.44	23.55	23.55	-0.03	0.08	0.16	0.18
438	45.97	215.13	23.34	23.34	0.05	0.08	0.26	0.27
442	55.90	204.29	23.37	23.37	0.01	0.08	0.26	0.27
446	43.96	217.32	23.34	23.34	0.06	0.08	0.26	0.27
450	72.22	186.45	23.61	23.61	-0.04	0.08	0.16	0.18
456	52.50	207.99	23.35	23.35	0.03	0.08	0.26	0.27
464	44.35	216.90	23.34	23.34	0.06	0.08	0.26	0.27
472	63.23	196.27	23.45	23.45	-0.01	0.08	0.16	0.18
480	60.27	199.51	23.41	23.41	0.00	0.08	0.26	0.27
488	58.60	201.33	23.39	23.39	0.00	0.08	0.26	0.27
499	60.37	199.40	23.41	23.41	0.00	0.08	0.26	0.27

Figure A. 3. Organic material sampled from core MAR19006 for radiocarbon dating. A) Leaf fragments. B) Seeds of Distichlis spicata.

A)

B)

Script. 3. Input in OxCal to build the age-depth model of the core MAR19006.

```
Plot()
{
};
P_Sequence ("", 10, 1)
{
  Boundary ("Base")
  {
  };
  R_Date ("Beta- 574924",2280.00,30){z=470.5;};
  R_Date ("SUERC-97309",1784.87,35){z=427.5;};
  Boundary ("Base sand 1") {z=418;};
  R_Date ("Beta-574923",1700.00,30){z=404.5;};
  Boundary ("Base sand 2") {z=404;};
  Boundary ("Shell bed") {z=364;};
  R_Date ("UCIAMS-244081",1295.00,15){z=360.5;};
  R_Date ("SUERC-97310",1250.74,37){z=351.5;};
  R_Date ("SUERC-97315",1222.40,35){z=343.5;};
  R_Date ("SUERC-97316",1296.76,37){z=336.5;};
  R_Date ("SUERC-97317",1259.02,37){z=326.5;};
```

```
 R_Date ("SUERC-97318",1253.09,35){z=314.5;};
Boundary ("Contact 1 3") {z=314;};
R_Date ("SUERC-97319",1202.28,35){z=313.5;};
R_Date ("SUERC-97320",1318.44,37){z=306.5;};
R_Date ("SUERC-97324",1244.26,37){z=297.5;};
Boundary ("Contact 2") {z=297;};
R_Date ("SUERC-97325",1282.49,37){z=296.5;};
R_Date ("SUERC-97326",1194.15,37){z=281.5;};
R_Date ("SUERC-97327",1206.67,37){z=265.5;};
R_Date ("SUERC-97328",1145.94,37){z=262.5;};
R_Date ("SUERC-97329",1168.98,37){z=255.5;};
R_Date ("SUERC-97330",1125.45,37){z=248.5;};
R_Date ("SUERC-97334",1130.82,37){z=237.5;};
Boundary ("Top")
 {
 };
};
```

Table A. 18. Output of the P_sequence age-depth model from OxCal for core MAR19006.

Depth (cm)	Modelled age (cal. yr BP)					sed. rate
	mu	sigma	median	from (2-sigma)	to (2-sigma)	(cm/yr)
237.5	1017	33	1017	1108	955	0.371
238.5	1020	32	1020	1109	958	0.371
239.5	1023	32	1023	1109	962	0.372
240.5	1025	31	1025	1110	966	0.371
241.5	1028	30	1028	1111	969	0.371
242.5	1031	30	1031	1112	973	0.371
243.5	1033	29	1033	1111	976	0.371
244.5	1036	28	1036	1113	980	0.371
245.5	1039	28	1039	1112	984	0.371
246.5	1041	27	1042	1111	987	0.371
247.5	1044	26	1044	1112	991	0.37
248.5	1047	26	1047	1112	995	0.37
249.5	1050	25	1049	1100	998	0.369
250.5	1052	25	1052	1103	1002	0.369
251.5	1055	24	1055	1104	1006	0.369
252.5	1058	23	1057	1107	1010	0.369
253.5	1060	23	1060	1109	1014	0.369
254.5	1063	22	1062	1109	1018	0.369
255.5	1066	22	1065	1111	1023	0.369
256.5	1069	22	1067	1114	1027	0.37
257.5	1071	21	1070	1114	1031	0.37
258.5	1074	21	1073	1116	1034	0.37
259.5	1077	21	1075	1119	1038	0.37
260.5	1079	20	1078	1119	1043	0.37
261.5	1082	20	1081	1122	1046	0.37
262.5	1085	20	1084	1123	1050	0.37
263.5	1087	20	1086	1124	1053	0.37
264.5	1090	19	1089	1127	1056	0.37
265.5	1093	19	1092	1129	1059	0.37
266.5	1096	19	1095	1131	1062	0.371
267.5	1098	19	1097	1134	1064	0.371
268.5	1101	19	1100	1136	1067	0.371
269.5	1104	19	1103	1139	1069	0.371
270.5	1106	19	1106	1142	1071	0.371
271.5	1109	20	1109	1145	1074	0.371
272.5	1112	20	1112	1148	1076	0.371
273.5	1114	20	1114	1150	1079	0.371
274.5	1117	20	1117	1155	1080	0.371
275.5	1120	21	1120	1157	1084	0.37
276.5	1123	21	1123	1160	1085	0.371
277.5	1125	21	1126	1164	1088	0.371
278.5	1128	22	1129	1167	1091	0.371
279.5	1131	22	1132	1170	1092	0.371
280.5	1133	23	1135	1174	1095	0.371
281.5	1136	23	1138	1176	1099	0.37
282.5	1139	24	1140	1180	1099	0.371
283.5	1141	24	1143	1183	1101	0.37
284.5	1144	25	1146	1187	1103	0.37
285.5	1147	25	1149	1190	1105	0.37
286.5	1150	26	1152	1194	1106	0.37
287.5	1152	27	1155	1197	1108	0.37
288.5	1155	27	1158	1201	1109	0.37
289.5	1158	28	1161	1206	1111	0.37
290.5	1160	29	1164	1210	1112	0.37
291.5	1163	29	1167	1214	1113	0.37
292.5	1166	30	1170	1219	1114	0.37
293.5	1168	31	1173	1222	1116	0.37
294.5	1171	31	1176	1227	1116	0.37
295.5	1174	32	1178	1230	1120	0.37
296.5	1177	33	1181	1235	1120	0.371
297.5	1179	32	1184	1235	1125	0.347
298.5	1182	31	1186	1236	1129	0.346
299.5	1185	29	1189	1236	1135	0.345
300.5	1188	27	1191	1237	1141	0.345
301.5	1191	26	1193	1239	1144	0.345
302.5	1194	24	1195	1240	1150	0.345
303.5	1197	23	1198	1242	1155	0.345
304.5	1200	22	1200	1245	1163	0.346
305.5	1203	20	1203	1245	1170	0.346
306.5	1205	19	1206	1247	1176	0.346
307.5	1208	19	1208	1247	1179	0.347
308.5	1211	18	1211	1250	1183	0.347
309.5	1214	17	1215	1252	1185	0.347
310.5	1217	17	1218	1255	1189	0.347
311.5	1220	17	1222	1257	1162	0.347
312.5	1223	18	1225	1259	1150	0.347
313.5	1226	18	1228	1263	1151	0.347

Table A.18. (continued)

314.5	1227	18	1230	1264	1153	1.48
315.5	1228	18	1230	1264	1155	1.48
316.5	1229	17	1231	1264	1158	1.48
317.5	1229	17	1232	1264	1161	1.48
318.5	1230	17	1233	1265	1161	1.48
319.5	1231	17	1233	1265	1163	1.48
320.5	1231	16	1234	1265	1165	1.48
321.5	1232	16	1234	1265	1169	1.48
322.5	1233	16	1235	1265	1170	1.48
323.5	1233	15	1236	1264	1175	1.48
324.5	1234	15	1236	1265	1176	1.48
325.5	1235	15	1237	1265	1180	1.48
326.5	1235	15	1238	1265	1183	1.48
327.5	1236	14	1238	1265	1198	1.48
328.5	1237	14	1239	1265	1208	1.48
329.5	1237	14	1239	1265	1209	1.48
330.5	1238	14	1240	1265	1210	1.48
331.5	1239	13	1241	1266	1210	1.48
332.5	1240	13	1241	1266	1211	1.48
333.5	1240	13	1242	1266	1211	1.48
334.5	1241	13	1243	1266	1212	1.48
335.5	1242	13	1243	1266	1212	1.48
336.5	1242	13	1244	1265	1213	1.48
337.5	1243	12	1245	1265	1214	1.49
338.5	1244	12	1245	1265	1215	1.49
339.5	1244	12	1246	1266	1216	1.48
340.5	1245	12	1246	1267	1218	1.48
341.5	1246	12	1247	1267	1219	1.48
342.5	1246	12	1247	1268	1219	1.48
343.5	1247	12	1248	1269	1219	1.48
344.5	1248	12	1249	1269	1220	1.48
345.5	1248	12	1250	1270	1220	1.48
346.5	1249	12	1250	1270	1222	1.48
347.5	1250	12	1251	1272	1224	1.48
348.5	1250	12	1252	1273	1225	1.48
349.5	1251	12	1252	1274	1224	1.48
350.5	1252	12	1253	1275	1224	1.48
351.5	1252	13	1253	1275	1223	1.48
352.5	1253	13	1254	1277	1227	1.48
353.5	1254	13	1255	1278	1225	1.48
354.5	1254	13	1255	1279	1222	1.48
355.5	1255	13	1256	1280	1221	1.48
356.5	1256	13	1257	1280	1220	1.47
357.5	1256	14	1258	1282	1224	1.47
358.5	1257	14	1258	1283	1224	1.48
359.5	1258	14	1259	1284	1223	1.47
360.5	1258	14	1260	1285	1221	1.47
361.5	1259	14	1260	1286	1233	1.47
362.5	1260	15	1261	1288	1230	1.47
363.5	1260	15	1261	1289	1223	0.945
364.5	1265	15	1266	1293	1228	0.154
365.5	1272	15	1273	1301	1239	0.132
366.5	1280	15	1281	1309	1248	0.132
367.5	1287	15	1288	1317	1256	0.132
368.5	1295	15	1296	1324	1264	0.132
369.5	1303	15	1304	1332	1272	0.132
370.5	1310	15	1311	1340	1280	0.132
371.5	1318	15	1319	1348	1287	0.132
372.5	1325	15	1326	1356	1294	0.132
373.5	1333	15	1333	1364	1301	0.132
374.5	1341	15	1341	1372	1308	0.131
375.5	1348	16	1349	1381	1315	0.131
376.5	1356	16	1356	1389	1321	0.131
377.5	1363	16	1364	1398	1328	0.131
378.5	1371	16	1371	1406	1336	0.132
379.5	1379	17	1379	1414	1344	0.132
380.5	1386	17	1386	1422	1352	0.132
381.5	1394	18	1394	1431	1359	0.132
382.5	1401	18	1401	1440	1365	0.132
383.5	1409	18	1408	1449	1373	0.132
384.5	1417	19	1416	1458	1380	0.132
385.5	1424	19	1423	1466	1387	0.132
386.5	1432	20	1431	1474	1395	0.132
387.5	1439	20	1438	1482	1402	0.131
388.5	1447	21	1446	1490	1409	0.132
389.5	1455	21	1453	1499	1416	0.132
390.5	1462	22	1461	1507	1424	0.132
391.5	1470	22	1468	1516	1431	0.132
392.5	1477	23	1476	1524	1438	0.131
393.5	1485	24	1483	1532	1446	0.131

Table A.18. (continued)

394.5	1493	24	1491	1540	1454	0.132
395.5	1500	25	1498	1548	1462	0.132
396.5	1508	25	1506	1557	1468	0.132
397.5	1515	26	1513	1566	1475	0.132
398.5	1523	27	1521	1575	1482	0.132
399.5	1531	27	1528	1584	1489	0.132
400.5	1538	28	1536	1592	1497	0.131
401.5	1546	29	1543	1600	1504	0.132
402.5	1553	29	1551	1608	1512	0.131
403.5	1561	30	1558	1617	1519	0.143
404.5	1566	30	1564	1623	1525	0.323
405.5	1569	29	1566	1626	1528	0.325
406.5	1572	29	1570	1630	1530	0.325
407.5	1576	29	1573	1635	1532	0.325
408.5	1579	29	1576	1641	1533	0.325
409.5	1582	30	1579	1647	1534	0.326
410.5	1585	30	1582	1654	1535	0.326
411.5	1588	31	1584	1662	1535	0.326
412.5	1591	32	1587	1670	1536	0.325
413.5	1594	33	1590	1676	1538	0.325
414.5	1597	35	1592	1683	1540	0.325
415.5	1600	36	1595	1690	1540	0.325
416.5	1603	38	1597	1700	1540	0.325
417.5	1606	40	1600	1707	1541	0.247
418.5	1614	40	1607	1713	1548	0.0916
419.5	1626	39	1619	1726	1561	0.0838
420.5	1638	39	1631	1737	1574	0.0839
421.5	1650	38	1643	1748	1586	0.0838
422.5	1661	37	1655	1759	1599	0.0838
423.5	1673	36	1667	1770	1612	0.0838
424.5	1685	36	1679	1785	1624	0.0837
425.5	1697	35	1690	1797	1635	0.0837
426.5	1709	34	1703	1809	1646	0.0839
427.5	1721	34	1715	1820	1657	0.0826
428.5	1733	34	1727	1830	1670	0.0815
429.5	1746	33	1740	1838	1685	0.0815
430.5	1758	33	1752	1846	1697	0.0815
431.5	1770	33	1765	1856	1711	0.0816
432.5	1782	33	1778	1866	1721	0.0816
433.5	1795	33	1790	1876	1733	0.0816
434.5	1807	33	1803	1887	1744	0.0816
435.5	1819	33	1815	1899	1755	0.0815
436.5	1832	34	1827	1909	1769	0.0816
437.5	1844	34	1840	1922	1780	0.0816
438.5	1856	34	1852	1933	1792	0.0817
439.5	1868	35	1864	1944	1804	0.0817
440.5	1880	35	1876	1958	1815	0.0817
441.5	1893	36	1889	1969	1828	0.0816
442.5	1905	36	1901	1983	1839	0.0815
443.5	1917	37	1913	1995	1851	0.0815
444.5	1930	37	1925	2008	1863	0.0816
445.5	1942	38	1937	2021	1875	0.0815
446.5	1954	39	1949	2033	1887	0.0815
447.5	1966	40	1961	2045	1898	0.0815
448.5	1979	40	1972	2058	1910	0.0815
449.5	1991	41	1984	2070	1922	0.0815
450.5	2003	42	1995	2085	1933	0.0816
451.5	2015	43	2006	2097	1945	0.0816
452.5	2028	44	2018	2110	1956	0.0816
453.5	2040	45	2029	2123	1968	0.0815
454.5	2052	46	2040	2136	1979	0.0816
455.5	2064	47	2052	2149	1992	0.0816
456.5	2077	48	2063	2163	2002	0.0815
457.5	2089	49	2074	2178	2013	0.0816
458.5	2101	50	2086	2192	2022	0.0816
459.5	2113	51	2097	2206	2032	0.0816
460.5	2126	52	2108	2221	2043	0.0816
461.5	2138	54	2120	2233	2054	0.0815
462.5	2150	55	2131	2246	2066	0.0816
463.5	2162	56	2142	2260	2076	0.0818
464.5	2175	57	2154	2274	2087	0.0817
465.5	2187	58	2165	2286	2098	0.0815
466.5	2199	59	2176	2299	2109	0.0814
467.5	2212	61	2188	2312	2120	0.0815
468.5	2224	62	2199	2325	2131	0.0815
469.5	2236	63	2211	2337	2143	0.0815
470.5	2248	64	2222	2350	2154	0.0815

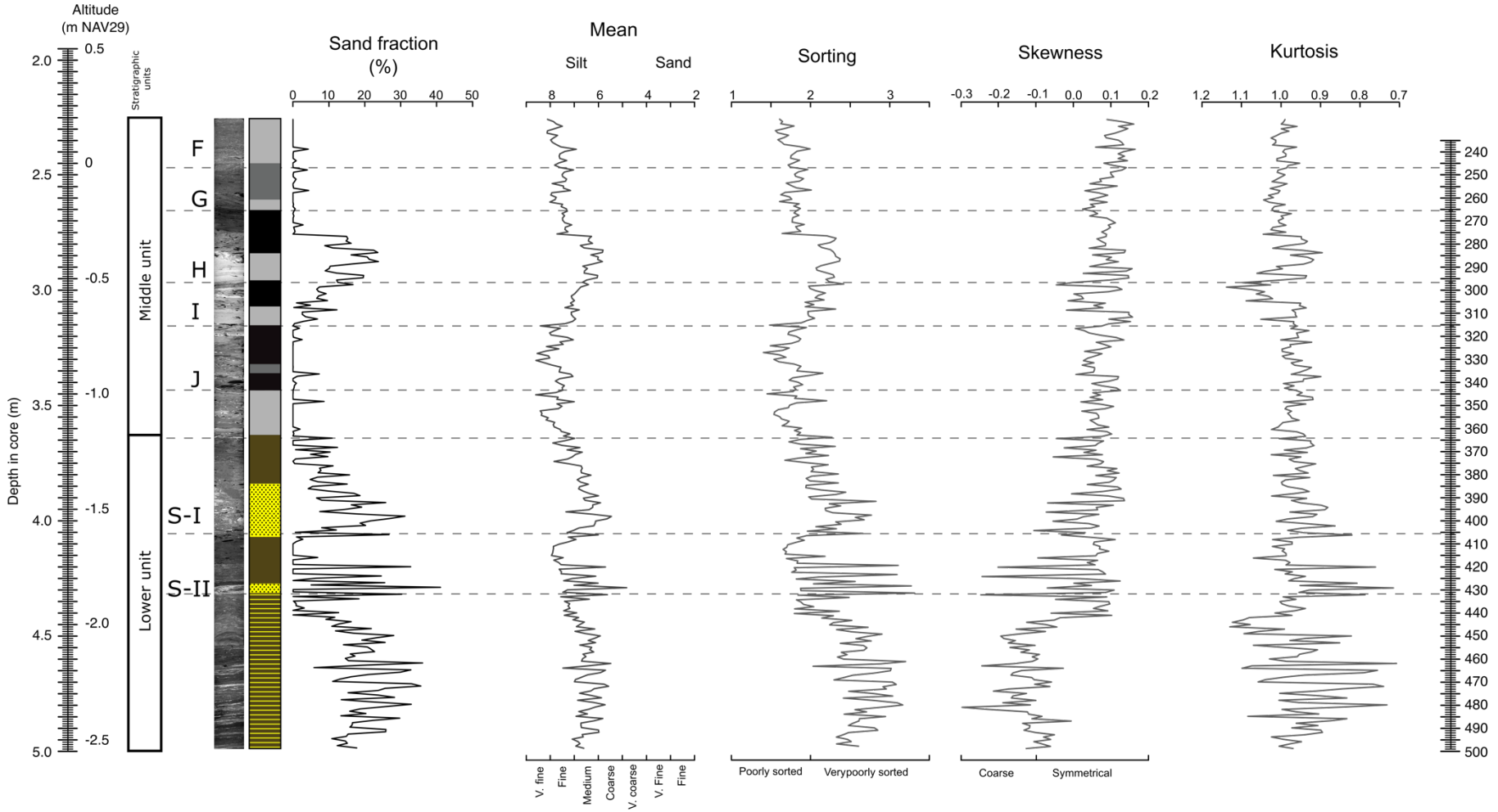

Figure A. 4. Sediment grain size parameters of the core MAR19006.